Université du Québec
Institut National de la Recherche Scientifique
Centre Énergie, Matériaux et Télécommunications

NANOSTRUCTURED FUNCTIONAL METAL OXIDE-BASED CATALYSTS FOR DIRECT ETHANOL FUEL CELLS

Par

Youling Wang, M.Sc.

Thèse présentée pour l'obtention
du grade de *Philosophiæ Doctor*, Ph.D.
en sciences de l'énergie et des matériaux

Jury d'évaluation

Président du jury et examinateur interne	Shuhui Sun Professeur à l'INRS-ÉMT
Examinateur externe	Sasha Omanovic Professeur à l'Université de McGill
Examinateur externe	Dominic Rochefort Professeur à l'Université de Montréal
Directeur de recherche	Mohamed Mohamedi Professeur à l'INRS-ÉMT

ACKNOWLEDGEMENTS

ABSTRACT

Rising energy demands, depletion of fossil fuel reserves and environmental deteriorations, have spurred great interest in searching for energy conversion devices with high efficiency and low greenhouse gas emissions. Fuel cells powered by hydrogen (H_2) or H-rich fuels (such as methanol, ethanol, ethylene glycol, etc.) have been regarded as promising alternative energy conversion devices to ease our concerns about fossil energy and the environment. Among various available fuels, ethanol becomes a more attractive fuel compared with H_2 and other organic fuels. At room temperature, ethanol is in the liquid state and, unlike hydrogen, can be easily stored and transported using the current gasoline infrastructure with only slight modifications. Furthermore, it has more advantages than other liquid fuels including low toxicity, high energy density (8.0 kWh/kg), biocompatibility and wide availability from renewable resources like from sugar cane, wheat, corn, or even straw and algae. Despite these advantages, the use of ethanol in fuel cells and ultimately realizing the commercialization of direct ethanol fuel cells (DEFCs) are still being hampered by several challenges, especially the difficulties from the development of anode catalysts which are listed as follows: (i) high cost of electrocatalysts. Platinum (Pt) is the most commonly used catalysts for ethanol oxidation, but as Pt is scarce and expensive, the high loading of Pt in electrodes becomes a critical obstacle limiting the successful commercialization of DEFCs; (ii) sluggish electrochemical kinetics; (iii) low poisoning resistance to reaction intermediates (like CO_{ads}); and (iv) difficulties associated with breaking the C-C bond in order to achieve the complete ethanol oxidation to CO_2. Therefore, more active, selective and durable electrocatalysts have to be developed, and the preparation of multi-component (binary, ternary, or even quaternary) catalysts has been regarded as a promising strategy to meet the demands of the complicated process of ethanol oxidation.

So far, a great deal of effort has been centered on modifying platinum by adding transition metals (M: Ru, Sn, Mo, Pd, Ir, etc.) to form Pt-M binary catalysts. It was found that the added metal can definitely enhance Pt activity for alcohol oxidation by the bifunctional mechanism or electronic effect between Pt and foreign metals. Alternatively, the combination of nanostructured Pt with functional metal oxides (FMO: such as CeO_2, SnO_2, TiO_2) has recently originated a distinctive class of electrocatalysts for DEFCs applications. The interaction between Pt and metal oxides was proved to have a critical influence on the chemisorption properties and ultimate catalytic behavior. Indeed, FMOs' role has been claimed to improve Pt nanoparticles dispersion, and/or to supply hydroxyl species at lower potentials than Pt to accomplish the oxidative removal

of CO_{ads} (bi-functional effect), and/or to alter the electronic structure of Pt and thus lessens the adsorption strength of CO_{ads} on Pt (the electronic effect). In this project, the work centers on developing advanced binderless, nanoarchitectured catalysts layers composed of the substrate (carbon paper, CP), the catalyst support (CNTs), Pt and FMO for DEFC applications. Two dissimilar materials (Pt and FMO) could be directly deposited onto the substrate by means of pulsed laser deposition. Four different FMOs (CeO_2, SnO_2, MnO_2, and TiO_2) have been selected and incorporated respectively in our binderless catalyst layer. It is well known that interactions of Pt with FMO can radically improve the catalytic performance of the Pt-FMO composites. In order to gain insight of the role of FMO in the catalytic behavior of Pt-based composites, FMO was incorporated into catalyst layer in two manners, namely layer-by-layer architecture and co-deposition architecture. The first architecture is fabricated by depositing Pt layer onto a layer of FMO. The second architecture is the co-deposition structure of Pt and FMO obtained by ablating both targets of Pt and FMO simultaneously. Furthermore, the optimization of each type of architecture was undertaken by varying the background gas pressure in the deposition chamber. Afterward, the prepared electrodes were firstly characterized by various physicochemical techniques including scanning electron microscopy (SEM), transmission electron microscopy (TEM) and high-resolution TEM (HR-TEM), X-ray diffraction (XRD), X-ray photoelectron spectroscopy (XPS), and micro-Raman spectroscopy. The electrocatalytic performance of synthesized electrodes towards ethanol oxidation was investigated by using cyclic voltammetry (CV), linear scanning voltammetry (LSV) and chronoamperometry (CA). Based on the results obtained, the correlation between physiochemical characterization and the electrochemical performance of corresponding Pt-FMO catalysts have been discussed and established. Specifically, as for the LOL structured catalyst layer, the porosity of the top Pt layer is varied with the morphologies of the underlying FMO layer which could be tuned by varying the gas background pressure. As a result, the catalytic performance of FMO/Pt towards EOR is affected due to the variation of the microstructure of FMO layer. Similarly, the gas pressure plays an important role on the physic-chemical properties of the co-deposits of Pt and FMO. The interactions between Pt and FMO have been found to be varied with gas pressure during deposition, and thus leading to different catalytic behaviors in the electrooxidation reaction for ethanol. Comparing the FMO-based catalysts of two different architectures, co-deposited catalysts exhibited superior EOR performance with respect to catalysts with LOL structure. This is mainly related to the higher interaction degree of Pt-FMO in co-deposited structure compared with LOL structure.

Based on the results of binary Pt-FMO catalysts, ternary catalysts composed of Pt, CeO_2 and SnO_2 were prepared in an attempt to further enhance the activity and durability with respect to that of binary catalysts. The catalytic activity of our optimized ternary catalysts under low potentials is enhanced compared with optimized Pt-CeO_2 co-deposits but is still inferior to Pt-SnO_2 co-deposits. Further optimization work needs to be carried out.

Furthermore, cathode catalysts for oxygen reduction reactions composed of Pt and FMO catalysts have been widely investigated, owing to the outstanding proton conductivity and the promoting effect of FMO demonstrated by the spillover phenomena of FMO to Pt. As is well known, synthesis method of catalysts plays a significant role in the catalytic properties of the resulting catalysts. Therefore, it would be an interesting study to examine the PLD-synthesized Pt-FMO catalysts for oxygen reduction reaction. In this doctoral project, it was found that the TiO_2 films synthesized under different gas atmosphere dramatically increased the electroactive surface area of Pt and enhanced its electroactivity towards oxygen reduction reaction as compared with bare Pt electrode. Unfortunately, I could not complete studies on all synthesized FMO-based catalysts towards ORR due to the limitation of my Ph.D. period. However, the initial work presented in this thesis could intrigue further studies on PLD synthesized FMO-based catalysts towards ORR.

_____   _____

   Youling Wang, étudiante   Professeur Mohamedi Mohamed

                                        Directeur de recherche

TABLE OF CONTENTS

LIST OF FIGURES

LIST OF TABLES

LIST OF ABBREVIATIONS

AA	Acetic Acid
AAL	Acetaldehyde
AFCs	Alkaline Fuels Cells
AFM	Atomic Force Microscopy
ASA	Area Specific Activity
Ag/AgCl	Silver/Silver Chloride
BE	Binding Energy
CBPLD	Cross-Beam Pulsed Laser Deposition
CNF	Carbon Nanofiber
CNTs	Carbon Nanotubes
CP	Carbon Paper
CV	Cyclic Voltammetry
CVD	Chemical Vapour Deposition
DEFCs	Direct Ethanol Fuel Cells
DEGFCs	Direct Ethylene Glycol Fuel Cells
DEMS	Differential Electrochemical Mass Spectrometry
DFAFCs	Direct Formic Acid Fuel Cells
DFT	Density Functional Theory
DMFCs	Direct Methanol Fuel Cells
EELS	Electron Energy Loss Spectroscopy
EIA	U.S. Energy Information Administration
EMF	Electromotive force
EOR	Ethanol Oxidation Reaction
ESCA	Electron Spectroscopy for Chemical Analysis
ESA	Electroactive Surface Area
FCC	Face-Centered Cubic
FCs	Fuel Cells
FCEVs	Fuel Cell Electric Vehicles
FMOs	Functional Metal Oxides
FTIR	Fourier Transform Infrared spectroscopy
FWHM	Full Width at Half Maximum
GC	Gas Chromatography

GDL	Gas Diffusion Layer
GS	Graphene Sheet
Hg/HgO	Mercury/Mercury Oxide
HPLC	High Performance Liquid Chromatography
HR-TEM	High-Resolution Transmission Electron Microscopy
IRRAS	Infrared Reflection-Absorption Spectroscopy
JCPDS	Joint Committee for Powder Diffraction Standards
KE	Kinetic Energy
LSV	Linear Scan Voltammetry
MCFCs	Molten Carbonate Fuel Cells
MEA	Membrane Electrode Assembly
MOR	Methanol Oxidation Reaction
MWCNTs	Multi-Walled Carbon Nanotubes
NAA	Neutron Activation Analysis
NMR	Nuclear Magnetic Resonance spectroscopy
ORR	Oxygen Reduction Reaction
OCP	Open Circuit Potential
PAFCs	Phosphoric Acid Fuels Cells
PDF	Powder Diffraction File
PEMFCs	Polymer Electrolyte Membrane or Proton Exchange Membrane Fuels Cells
PLAL	Pulsed Laser Ablation in Liquid
PLD	Pulsed Laser Deposition
PSPD	Position-Sensitive Photodiode
RDE	Rotating Disc Electrodes
RDS	Rate-Determining Step
RF	Roughness Factor
SAED	Selected Area Electron Diffraction
SEM	Scanning Electron Microscopy
SERS	Surface Enhanced Raman Spectroscopy
SOFCs	Solid Oxide Fuels Cells
STM	Scanning Tunnelling Microscope
SWCNTs	Single-Walled Carbon Nanotubes
TEM	Transmission Electron Microscopy
TOF	Time of Flight

WE	Working Electrode
XPS	X-ray Photoelectron Spectroscopy
XRD	X-Ray Diffraction
RE	Reference Electrode
RHE	Reversible Hydrogen Electrode
CE	Counter Electrode
SHE	Standard Hydrogen Electrode
NHE	Normal Hydrogen Electrode
SCE	Saturated Calomel Electrode
PTFE	Polytetrafluoroethylene
RDE	Rotating Disk Electrode

CHAPTER 1 INTRODUCTION AND BACKGROUND

1.1 General introduction

Energy can be recognized as one of the most important pillars of our modern way of life. It is integral to our lives, it cooks our meals, keeps us warm, cools us down, lights our nights, propels our cars and connects us with others near and far. By far, the dominant sources of our consumed energy come from the combustion of fossil fuels which mainly refer to petroleum (crude oil), coal and natural gas. As is well known, fossil fuels are considered as non-renewable resources, since they don't renew themselves at a sufficient rate within time frame meaningful to humans. Inevitably, they will eventually run out, which is an undisputed fact and is only a matter of time due to their finite reserves and human's rising demand for energy. British Petroleum has reported in its 2016 statistical review of world energy that global proved reserves of oil, natural gas and coal are only respectively sufficient for 50.7, 52.8 and 114 years at the current production rate [1]. Except for the depletion concerns of fossil fuels, burning fossil fuels has caused a wide variety of environmental problems, such as global warming, air pollutions, acid rains, and so forth. The consequences of these environmental crises, in particular from the global warming due to excessive CO_2 emission, are catastrophic and will ultimately affect the entire planet including human existence. The U.S. Energy Information Administration (EIA) has projected energy-related CO_2 emissions over the period from 2012 to 2040 [2]. It has reported that the CO_2 emissions are going to rise from 32.2 billion metric tons in 2012 to 35.6 billion metric tons in 2020, and to 43.2 billion metric tons in 2040. Much of the growth is contributed by high populated, developing countries including China and India, as a result of their fast-paced growth of energy demand. By 2040, developing countries account for approximately 60% of the world's primary energy consumption due to their fast growth rates of economies and populations.

In response to the growing energy demand, the depletion of fossil fuels and the rapid deterioration of the environment, a dynamic change takes place in the energy supply. It is getting increasingly diversified, enabling us to reduce the excessive reliance on low efficient and high polluted traditional ones, in particular, the combustion of fossil fuels. In this context, exploring economically viable, clean and renewable energy is recognized as a long-term solution, and their developments are already underway. Based on the statistic of EIA's energy projection report, renewable energy is regarded as the world's fastest-growing source of energy that is increased

at an average of 2.6% per year, as shown in Figure 1.1 [3]. These sources include solar, wind, biomass (bio-ethanol), geothermal, hydropower, and so forth. Each of them exhibits their unique benefits and constraints. For example, solar and wind energy have abundant energy resources but they are intermittent and geographically restricted.

Note: Dotted lines for coal and renewables show projected effects of the U.S. Clean Power Plan.
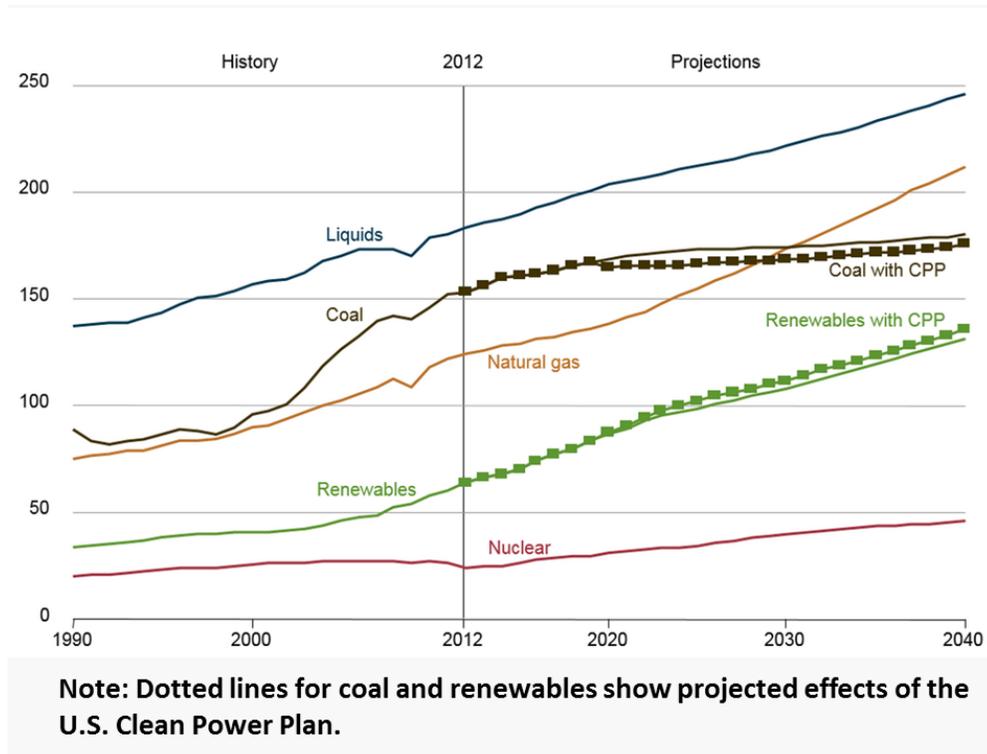
Figure 1.1 World energy consumption by energy sources, 1990-2040 (quadrillion Btu) [3].

Furthermore, electrochemical power sources including batteries, fuel cells (FCs) and electrochemical capacitors appear to be promising as power supplies for automotive, portable and stationary applications [4]. In the past decades, FCs have aroused tremendous attention due to their attractive features, such as the fuel flexibility, high energy density, high efficiency, low-to-zero CO_2 emissions and quiet operation. FCs can be viewed as scalable power plants with wide applications ranging from transportation to stationary prime/backup power to portable electronics [5]. In 2014, the revenue from fuel cell (FC) system grew by around $ 1 billion, getting to 2.2 billion in sales. By 2014, the most viable market for FCs remains stationary distributed power that has been widely used for prime or backup power for residential and commercial operations [6]. As indicated in fuel cell technologies market report of 2014, nearly 10% of Fortune 500 companies currently use fuel cells for stationary or motive power generation [6]. As of 2015, reinforced by several countries' FC-support policies, automakers such as Honda, Hyundai, and Toyota, started to deliver fuel cell electric vehicles (FCEVs) that are currently available to customers in numbers

of regions (U.S., Germany, France, the UK, South Korea, Canada) around the world. With the mass production of FCEVs and their expanding in vehicles markets, the cost of FCEVs is projected to keep decreasing and in turn, will accelerate FCEVs' commercialization. As for portable power application, micro-FCs from the size of thumbnail to handhold even to small-bread-box-scale are able to meet different power requirements of various portable devices. To date, several companies such as Intelligent energy UPP, MyFC, Brunton and Neah power systems, sell hydrogen cartridges and micro fuel cell units that can give you power on the go. From a long-term disruptive vision, micro FCs are expected to be the personal power for the entire planet, which frees us from connections to electrical sockets and grids. To date, the micro fuel cell market is still in a nascent stage so we would need to see both incremental and breakthrough performance gains in order to arrive at this scenario.

1.2 The background and problematics

What has driven the above developments in FCs and what are the major challenges facing FCs today? Firstly, we need to know what exactly a FC is and how it works.

1.2.1 What is fuel cell?

A FC is a galvanic cell which, with the assist of catalysts, converts the chemical energy stored in a fuel directly into electrical energy through an electrochemical reaction between the fuel and an oxidant [5]. Taking the classic H_2/O_2 FCs as an example, in which H_2 gas is the fuel and O_2 gas serves as the oxidant. The overall reaction of H_2/O_2 FCs resembles the simple combustion reaction of H_2, given in equation 1.1.

$$Overall\ reaction: 2H_2\ +\ O_2\ \rightarrow 2H_2O + Energy\ (Heat\ or\ electricity) \qquad (1.1)$$
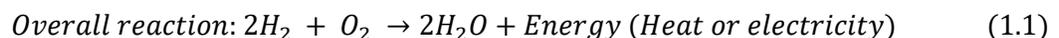
The hydrogen combustion reaction is an exothermic reaction. When igniting H_2 in the air, the energy is released in a disorder explosion. Specifically, at the atomic level, H-H bonds and O-O bonds are broken, while H-O bonds are formed during the collisions between H_2 molecules and O_2 molecules. During the above bonding reconfiguration processes, the energy difference between the initial and final states is released within picoseconds which can only be recoverable in the form of heat energy. To produce electricity, the heat energy must first be transformed into mechanical energy and then converted into electrical energy. The multi-steps (shown in Figure

1.2) significantly lower the energy efficiency owing to the energy loss in each step and the Carnot cycle limitation of heat engine.
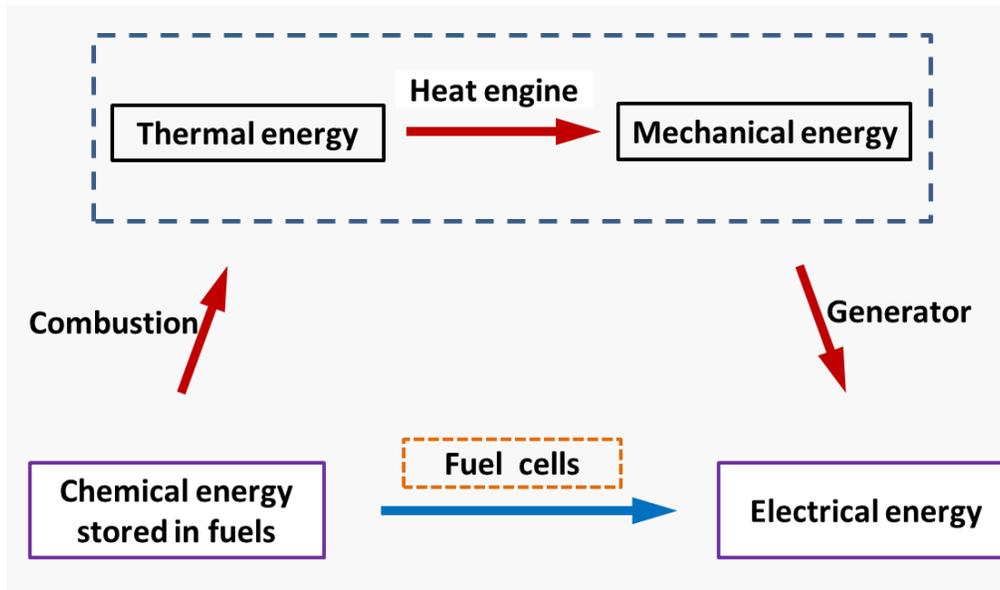
Figure 1.2 Graphical illustration of the difference in energy conversion between fuel cells and traditional combustion processes [7].

In comparison, FCs offer an alternative way to harness electrons during the processes of bonding reconfiguration between high-energy reactant and low-energy product, enabling to more efficiently convert the chemical energy of the fuel directly into electricity. FCs break the above overall reaction into two halves by using a membrane to keep two gases apart so that electron transfer is necessary to complete the bonding reconfiguration occurring over a greatly extended length scale. Briefly, on one side (anode), as shown in equation 1.2, H_2 molecules lose electrons to form protons which travel across the membrane. On the other side (cathode), these protons react with O_2 molecules and gain the electrons from the cathode to produce water as represented in equation 1.3.

$$Anode\ reaction: 2H_2\ \rightarrow 4H^+ + 4e^- \tag{1.2}$$

$$Cathode\ reaction: O_2\ +\ 4H^+ + 4e^-\ \rightarrow 2H_2O \tag{1.3}$$
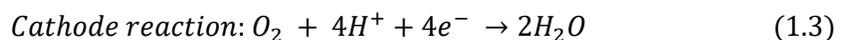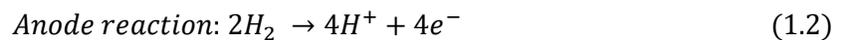
In essence, both reactions on two electrodes take place on the surface of catalysts which enable to lower energy barrier of reactions and thereby improve the overall kinetics. The electricity can be produced by harnessing the electrons as they flow from the anode to the cathode via an external circuit. In FCs, the whole process excludes the conversion of heat to mechanical energy,

enabling high conversion efficiency up to 60%. This value is 2-3 times higher than that of the combustion reaction.

Compared with other electrochemical power sources, FCs are able to deliver much higher energy capacity as presented in Ragone plot (Figure 1.3). FCs work similarly to batteries, as both of them generate electricity through electrochemical reactions. However, FCs are not consumed when they generate electricity, which can be viewed as shells of factory that take fuels as raw materials and chunk out electricity as product. They can constantly and instantly supply power as long as fuel is continuously supplied in contrast to batteries needing longer time to be recharged.
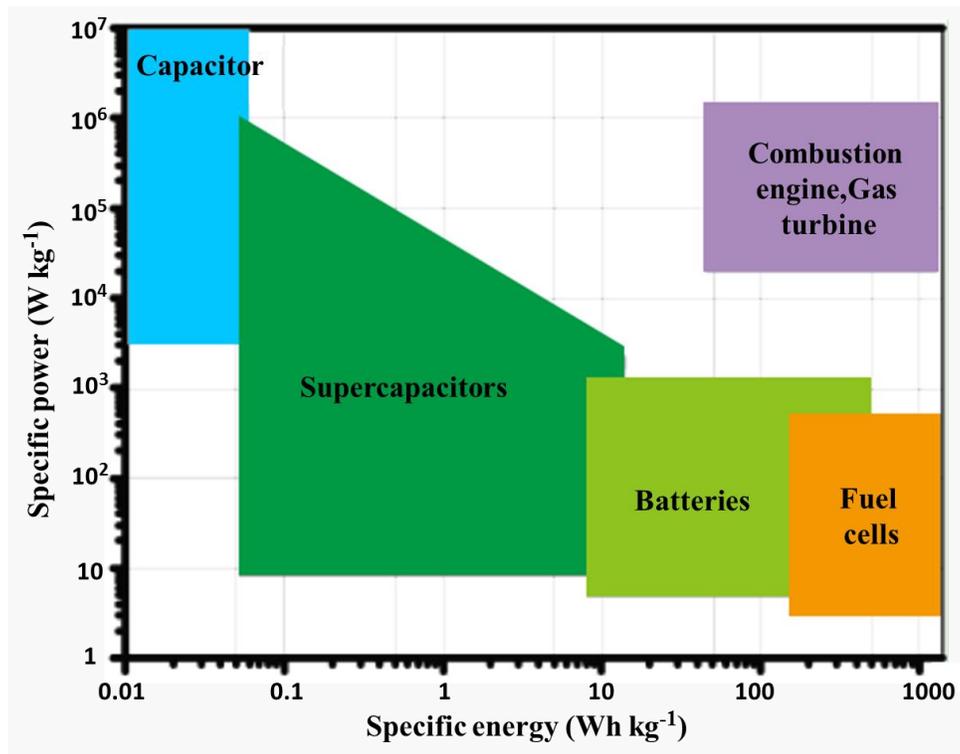
Figure 1.3 Ragone plot representing specific energy vs. specific power for traditional power source and electrochemical power sources [4].

1.2.2 Types of fuel cells

At present, many types of FCs are currently under development. The most common classification of FCs is by the type of electrolyte employed in individual cells, mainly including five categories: polymer electrolyte membrane or proton exchange membrane FCs (PEMFCs), solid oxide FCs (SOFCs), molten carbonate FCs (MCFCs), phosphoric acid FCs (PAFCs) and the alkaline FCs (AFCs). The type of electrolyte determines the kind of electrochemical reactions taking place in FCs, the kinds of catalysts qualified, the fuel required, the operation temperature

range, and other factors. These characteristics, in turn, determine the applications for which each type of FCs is most suitable. A brief summary of these five FCs is given in Table 1.1.

Among these five main categories of FCs, PEMFCs are regarded as one of the most promising power sources in portable and transportation applications due to low operating temperature and rapid start-up features [8]. The essential part of the PEMFCs is known as membrane electrode assembly (MEA) which consists of two electrodes (anode and cathode) and a proton exchange membrane (such as Nafion ionomer) sandwiched in between. To get a desired electrical power, several MEAs can be combined together to form a fuel cell stack. With respect to fuels, there are varieties of choices which can be gaseous H_2 or liquid H-rich organic molecules such as methanol, ethanol, formic acid and ethylene glycol, etc. Accordingly, based on the type of fuel used in the cell, PEMFCs can be further categorized into H_2-PEMFCs [9], direct methanol FCs (DMFCs) [10, 11], direct ethanol FCs (DEFCs) [12], direct formic acid FCs (DFAFCs) [13] and direct ethylene glycol FCs (DEGFCs) [14], and so forth.

Table 1.1 The comparison of different types of FCs [8, 15].

Fuel cell type	Common Electrolyte	Operation temperature range (°C)	Charge carrier	Electrode reactions	Applications
PEMFC	Solid polymer (Nafion)	50 – 100	H^+	Anode: $2H_2 \rightarrow 4\,H^+ + 4e^-$ Cathode: $O_2 + 4H^+ + 4e^- \rightarrow 2H_2O$	Backup power Portable power Transportation
SOFC	Yttria-stablized Zirconina (YSZ)	600 – 1000	O^{2-}	Anode: $H_2 + O^{2-} \rightarrow H_2O + 2e^-$ Cathode: $\frac{1}{2}O_2 + 2e^- \rightarrow O^{2-}$	Auxiliary power Electric utility Large distributed generation
MCFC	Molten salt consisting of a binary or ternary mixture of lithium, potassium and/or sodium carbonate	600 – 700	$CO_3^{\,2-}$	Anode: $H_2 + CO_3^{\,2-} \rightarrow H_2O + CO_2 + e^-$ Cathode: $\frac{1}{2}O_2 + CO_2 + 2e^- \rightarrow CO_3^{\,2-}$	Electric utility Large distributed generation
PAFC	Phosphoric acid soaked in a matrix	150 – 200	H^+	Anode: $2H_2 \rightarrow 4H^+ + 4e^-$ Cathode: $O_2 + 4H^+ + 4e^- \rightarrow 2H_2O$	Distributed generation
AFC	Aqueous solution of potassium hydroxide soaked in a matrix	60 – 90	OH^-	Anode: $2H_2 + 4OH^- \rightarrow 4H_2O + 4e^-$ Cathode: $O_2 + H_2O \rightarrow 4e^- + 4OH^-$	Military Space Backup power, transportation

1.2.3 Introduction of DEFCs

In the past few decades, DEFCs have attracted significant attention owing to the attractive attributes of ethanol [12, 16-18]. Ethanol, at room temperature and ambient pressure, is in liquid state and, unlike hydrogen, can be easily handled, stored and transported. In DEFCs, ethanol is not reformed into hydrogen gas but is oxidized directly. As shown in table 1.2, ethanol and other liquid fuels show much higher volumetric energy density than gaseous H_2, which makes the system to be more compact and appears high potential application as power sources for portable devices, such as cellular phones, notebook computers, and portable power suppliers. In addition, the use of liquid ethanol enables to utilize the current gasoline infrastructure in contrast to spending a large sum of money on building hydrogen infrastructure.

Table 1.2 The Volumetric and gravimetric energy densities of different small organic fuels [19, 20]

Fuels	Volumetric energy density (kWh L^{-1})	Gravimetric energy density (kWh kg^{-1})
Hydrogen	0.18 (@1000 psi, 25 oC)	-
Methanol	4.82 (100 wt.%)	6.09
Ethanol	6.28 (100 wt.%)	8.00
Formic acid	1.75 (88 wt.%)	1.74 [21]
Ethylene Glycol	5.87 (100 wt.%)	5.3

Compared with the most popular liquid alcohol (methanol), ethanol displays numerous advantages including less toxicity, higher theoretical energy density, biocompatibility and wide availability from renewable biomasses such as sugar cane, wheat, corn, straw, or even algae [22]. Brazil that is considered as the bioethanol industry leader and a policy model for other countries, has the world's first sustainable biofuels economy. In 2015, Brazil produced 7093 million gallons of ethanol, is the world's second largest ethanol producer behind the United States [23]. Canada is a nation of renewable opportunity, and according to Natural Resources Canada [24], Canadian farmers grow millions of tons of crops every year that can be used to produce clean, renewable fuels in the form of bio-ethanol without hurting the nation's food supply. This huge energy source is equal to an annual supply of 436 million gallons of renewable fuels that are largely untapped today [23]. Thus, the rapid growth of bio-ethanol industry has laid a solid foundation for the development of DEFCs.

With respect to the performance of ethanol in FCs, ethanol oxidation shows similar kinetics to that of methanol at low temperatures. On the other hand, compared with methanol, ethanol has

smaller permeability through Nafion membrane [18, 25]. Therefore, ethanol presents a lower crossover rate than methanol and thus influences less severely on the energy conversion efficiency than methanol.
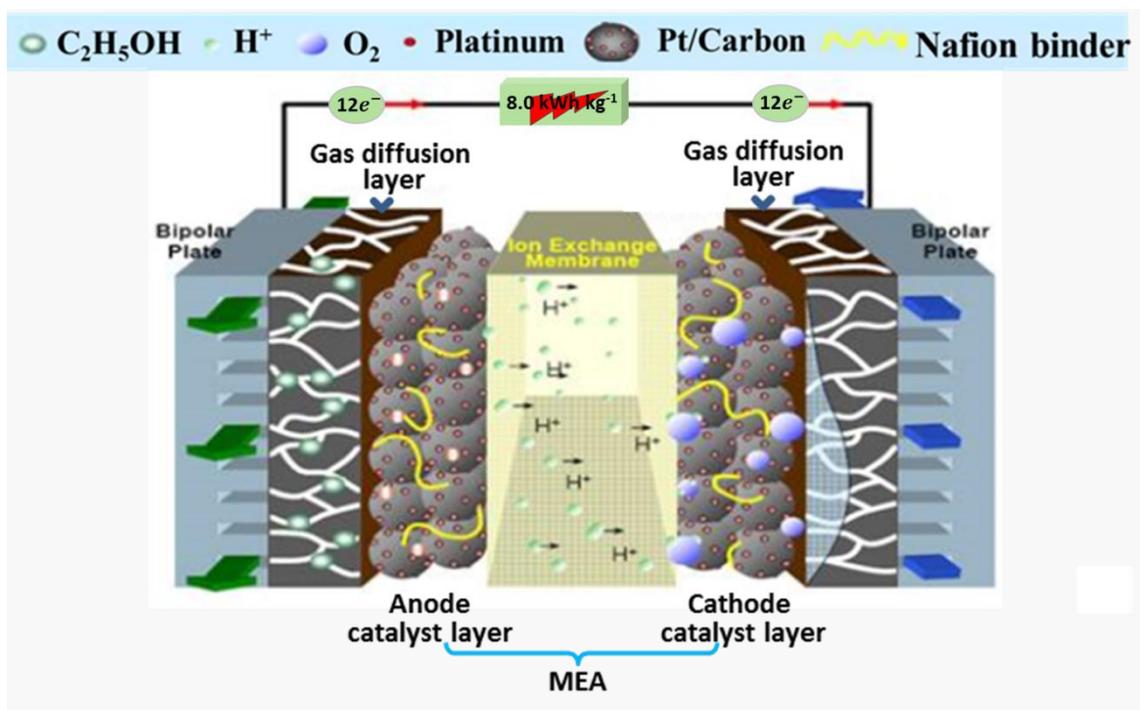
Figure 1. 4 Schematic diagram of a typical MEA in DEFCs [26].

As with other PEM-based FCs, the pivotal part of DEFCs is the MEA with a sandwich-like structure [8]. As depicted in Figure 1.4, a single MEA consists of a proton-exchange membrane in contact with an anode and a cathode electrode on either side. So far, the most mature, commercially available, performance-durability membrane employed for PEM-based FCs is Nafion® membrane made by DuPont which is in charge of transporting protons generated from the anode to the cathode and spatially separating two electrodes. As for the anode and cathode electrodes, catalysts must be used for these reactions to occur effectively. The energy conversion efficiency of DEFCs largely depends on the catalytic performance of the catalysts on the anode and cathode. Till now, Pt-based catalysts are considered to be the most practical catalysts for both anode and cathode reaction in terms of both performance and durability.

In comparison to H_2 oxidation, as shown in equation 1.4, the ethanol oxidation reaction (EOR) at the anode is a more complex, multiple-electron process. It involves the cleavage of C-H, C-O, and C-C bonds and the complete oxidation of ethanol delivers 12 electrons, surpassing 6 electrons in DMFCs and 2 electrons in H_2-PEMFCs [27]. Resembling H_2-PEMFCs, gaseous O_2

is supplied to cathode of DEFCs, and oxygen reduction reaction (ORR) occurs by combining O_2 with electrons and protons generated on the anode (equation 1.5) [22, 27]. As a result, the overall reaction of DEFCs is presented by equation 1.6, with the enthalpy change (ΔH^0), Gibbs free energy (ΔG^0), and equilibrium standard electromotive force (*emf*) of -1367.9 kJ mol^{-1}, -1326.7 kJ mol^{-1} and 1.145 V, respectively [22, 27].

$$Anode\ reaction: CH_3CH_2OH + 3\ H_2O \rightarrow 2CO_2 + 12H^+ + 12e^-\ \ E^0 = 0.084\ V\ vs\ SHE \quad (1.4)$$

$$Cathode\ reaction: 3O_2\ +\ 12H^+ + 12e^-\ \rightarrow 6H_2O \qquad\qquad E^0 = 1.229\ V\ vs\ SHE \quad (1.5)$$

$$Overall\ reaction: CH_3CH_2OH + 3O_2\ \rightarrow 2CO_2 + 3\ H_2O \qquad\qquad E^0 = 1.145\ V\ vs\ SHE \quad (1.6)$$
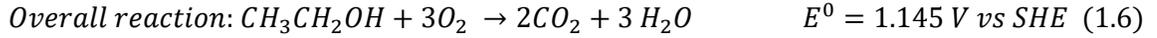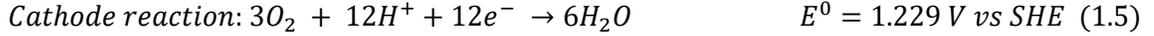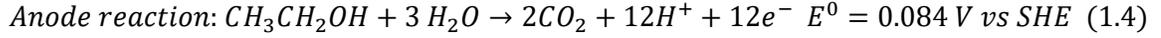
Under reversible standard conditions, the theoretical energy efficiency defined as the ratio between the usable energy ΔG^0 and the total energy from the chemical reaction, ΔH^0, can be determined with equation 1.7.

$$\eta_{theo} = \frac{\Delta G^0}{\Delta H^0} \times 100\% = \frac{1326.7}{1367.9} \times 100\% = \ 97\% \qquad\qquad (1.7)$$

Although the thermodynamic data of DEFCs is promising, the kinetics of ethanol oxidation is more difficult that leads to a high overpotential and a low current density. Under operating conditions, the cell voltage measured at a current density *j* becomes smaller than the equilibrium potential E^0 as a result of three primary potential losses [28]. The actual cell voltage E_{cell} is defined as [28]

$$E_{cell} = \ E^0 - \Delta E_{acti} - \Delta E_{ohmic} - \Delta E_{conc} \qquad\qquad (1.8)$$

where ΔE_{acti} is the activation loss or activation overpotential resulted from the need to move electrons and to break/form chemical bonds in both EOR and ORR; ΔE_{ohmic} is the ohmic loss primarily due to material and interface resistances; ΔE_{conc} is the concentration loss or concentration polarization caused by the decrease in concentration of reactants on both the anode and the cathode as they are consumed in reactions. Figure 1.5 shows a typical polarization curve of a DEFC, displaying the above mentioned losses in potential. At low current densities, there is a sharp drop in potential and activation loss is the most important cause due to the sluggish kinetic rates of both EOR and ORR. To lower activation losses, more active catalysts are demanded on both electrodes. So far, Pt-based catalysts have been widely used as catalysts for both EOR and ORR in DEFCs [29]. At intermediate current densities, ohmic losses become more

pronounced. As current intensity keeps increasing, the cell voltage declines dramatically due to the mass transport limit of reactants accessible to the reactive sites in catalysts layers.
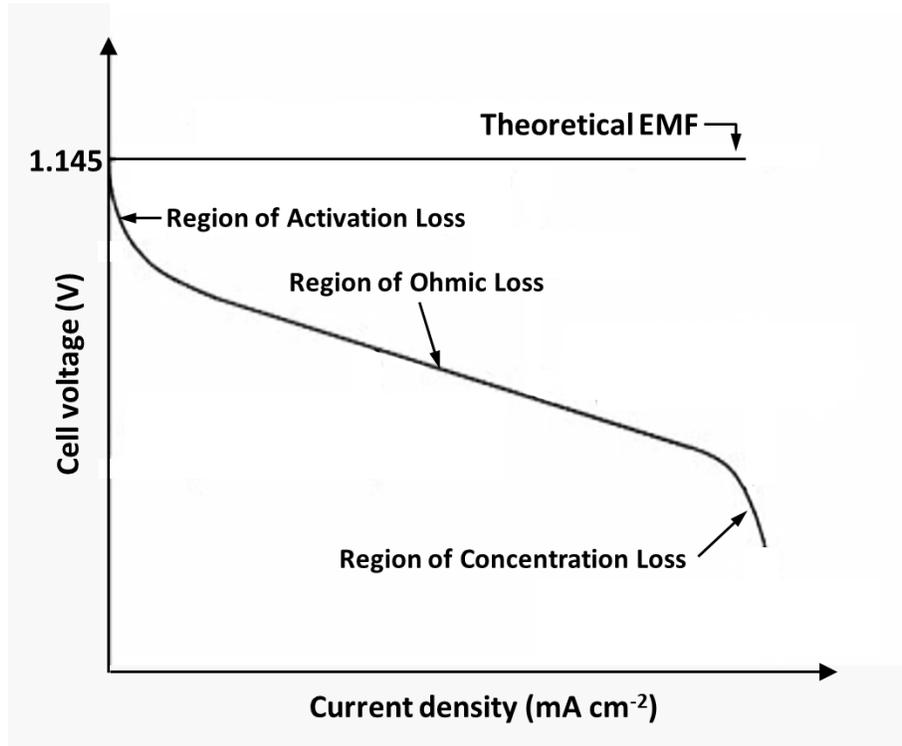
Figure 1.5 Schematic of an ideal polarization curve with the corresponding regions and ovepotentials [28].

Therefore, the potential efficiency must to be taken into account when calculate the overall efficiency of a DEFC. The potential efficiency is defined as follows:

$$\eta_{potential} = \frac{E_{cell}}{1.145} \times 100\% \qquad (1.9)$$

For the complete oxidation reaction of ethanol to CO_2, under operating conditions, the practical energy efficiency for a DEFC is defined as follows:

$$\eta = \eta_{theo} \times \eta_{potential} = 97\% \times \frac{E_{cell}}{1.145} \times 100\% \qquad (1.10)$$

Given E_{cell} of a DEFC is 0.5 V, the energy efficiency is 42%.

However, in addition to the aforementioned losses in efficiency, there are still other significant issues need to be addressed. For example, the problem related to the complicated reaction process of EOR and ORR occurring on anode and cathode, respectively. On the anode,

11

instead of complete oxidation to CO_2 releasing 12 electrons, other by-products such as acetic acid and acetaldehyde are often yielded via incomplete reaction paths, leading to a considerable loss in energy efficiency. On the cathode, H_2O_2 is often formed other than H_2O, further contributing to the decrease in energy efficiency. Another significant issue is the ethanol crossover effect [17], even though less severe than methanol. Ethanol crosses through the polymer membrane to the cathode, leading to the cathode experiencing a mixed potential as both EOR and ORR taking place at the same electrode. As a result, the cathode potential gets lower, causing a further decrease in the potential efficiency beside of the aforementioned three potential losses.

Therefore, how to overcome these efficiency losses become the main objectives and working directions for the study and development of DEFCs. Briefly, it includes exploring highly active, selective and durable catalysts for EOR and ORR; and developing high proton-conductive, stable membrane with low ethanol permeability. In the context of the present work, the materials which have been developed are Pt-based catalysts mainly for the EOR in acid medium. However, it is also within our interest to discover the potential application of synthesized catalysts of this doctoral project for ORR.

REFERENCES

[1] BP. BP Statistical Review of World Energy 2016, London, BP, (2016) pp. 7 (oil), p. 21(gas), p. 31 (coal) http://www.bp.com/energyoutlook (Accessed November 7th, 2016).

[2] U.S. Department of Energy, U.S. Energy Information Administration (EIA), Independent Statistics & Analysis. International energy outlook 2016, Washington, DC, (2016) pp. 5 http://www.eia.gov/forecasts/ieo/ (Accessed November 7th, 2016).

[3] U.S. Department of Energy, U.S. Energy Information Administration (EIA), Independent Statistics & Analysis. International energy outlook 2016, Washington, DC, (2016) pp. 9 http://www.eia.gov/forecasts/ieo/ (Accessed November 7th, 2016).

[4] M. Winter, R.J. Brodd. Chem. Rev., 104 (2004) 4245-4270.

[5] G. Hoogers. Fuel cell technology handbook, CRC press, Boca Raton, FL, 2003.

[6] U.S. Department of Energy, Office of Energy Efficiency & Renewable Energy, Fuel Cell Technologies Office. Fuel Cell Technologies Market Report 2014, Washington, D.C, (2015) pp. 13 http://energy.gov/eere/fuelcells/market-analysis-reports (Accessed November 7th, 2016).

[7] S. Sun. DEVELOPMENT OF NOVEL NANOMATERIALS FOR HIGH-PERFORMANCE AND LOW-COST FUEL CELL APPLICATIONS PhD Dissertation in Mechanical and Materials Engineering (The University of Western Ontario, London, Ontario, Canada) (2011) 263 p.

[8] J. Zhang. PEM fuel cell electrocatalysts and catalyst layers: fundamentals and applications, Springer Science & Business Media, 2008.

[9] H.A. Gasteiger, S.S. Kocha, B. Sompalli, F.T. Wagner. Appl. Catal. B, 56 (2005) 9-35.

[10] S. Basri, S.K. Kamarudin, W.R.W. Daud, Z. Yaakub. Int. J. Hydrogen Energy, 35 (2010) 7957-7970.

[11] V. Neburchilov, J. Martin, H. Wang, J. Zhang. J. Power Sources, 169 (2007) 221-238.

[12] E. Antolini. J. Power Sources, 170 (2007) 1-12.

[13] X. Yu, P.G. Pickup. J. Power Sources, 182 (2008) 124-132.

[14] A. Serov, C. Kwak. Appl. Catal. B, 97 (2010) 1-12.

[15] A. Brouzgou, A. Podias, P. Tsiakaras. J. Appl. Electrochem., 43 (2013) 119-136.

[16] J. Friedl, U. Stimming. Electrochim. Acta, 101 (2013) 41-58.

[17] S. Song, P. Tsiakaras. Appl. Catal. B, 63 (2006) 187-193.

[18] M.Z.F. Kamarudin, S.K. Kamarudin, M.S. Masdar, W.R.W. Daud. Int. J. Hydrogen Energy, 38 (2013) 9438-9453.

[19] B. Pignataro. Ideas in Chemistry and Molecular Sciences: Advances in Nanotechnology,

Materials and Devices, John Wiley & Sons, 2010.

[20] J. Zhang, H. Liu. Electrocatalysis of direct methanol fuel cells: from fundamentals to applications, John Wiley & Sons, 2009.

[21] C. Rice, S. Ha, R. Masel, A. Wieckowski. J. Power Sources, 115 (2003) 229-235.

[22] S. Badwal, S. Giddey, A. Kulkarni, J. Goel, S. Basu. Applied Energy, 145 (2015) 80-103.

[23] Renewable Fuels Association. World Fuel Ethanol Production. http://ethanolrfa.org/resources/industry/statistics/#1454098996479-8715d404-e546 (Accessed November 7th, 2016).

[24] Natural Resources Canada,. Ethanol. http://www.nrcan.gc.ca/energy/alternative-fuels/fuel-facts/ethanol/3493 (Accessed November 7th, 2016).

[25] S. Song, W. Zhou, Z. Liang, R. Cai, G. Sun, Q. Xin, V. Stergiopoulos, P. Tsiakaras. Appl. Catal. B, 55 (2005) 65-72.

[26] C. Lamy, A. Lima, V. LeRhun, F. Delime, C. Coutanceau, J.M. Léger. J. Power Sources, 105 (2002) 283-296.

[27] C. Lamy, A. Lima, V. LeRhun, F. Delime, C. Coutanceau, J. Léger. J. Power Sources, 105 (2002) 283-296.

[28] C. Lamy, C. Coutanceau, J.M. Leger. Catalysis for sustainable energy production, (2009) 1-46.

[29] C. Lamy, E.M. Belgsir, J.M. Léger. J. Appl. Electrochem., 31 (2001) 799-809.

CHAPTER 2 LITERATURE REVIEW

2.1 Introduction to anode catalysts for DEFCs

Catalysts play a significant role in the cost, performance, and durability of DEFCs. In terms of the catalytic performance and durability, Pt and Pt-based catalysts are the most commonly used and extensively investigated anode and cathode catalysts for DEFCs operated in acidic medium [1-8]. Due to the high cost and limited sources of Pt, reducing the loading of Pt in catalysts layer is of critical importance to overcome the cost barrier for the commercialization of DEFCs [8]. Therefore, in order to maximize the utilization of Pt, the most common approach is to disperse nanostructured Pt catalysts on high-surface-area support materials such as carbon black (e.g. Vulcan XC-72) [9, 10]. To date, Vulcan XC-72 supported Pt is widely used as anode and cathode catalysts in DEFCs. Indeed, Vulcan XC-72 support greatly improves the catalytic activity of catalysts. While over long term operation of FCs, it undergoes severe corrosion, causing the agglomeration, dissolution, and isolation of Pt nanoparticles, in turn largely impairing the performance and durability of DEFCs [5, 11].

It is well known that Pt as anode catalysts is very active towards C-H bonding cleavage and dissociative adsorption of ethanol, but it cannot accomplish the complete oxidation of ethanol to CO_2 releasing 12 electrons by effectively breaking C-O and C-C bonds at low temperatures. Through incomplete oxidation of ethanol (2-electron and 4-electron oxidation), undesired by-products acetaldehyde (CH_3CHO, AAL) and acetic acid (CH_3COOH, AA) are formed, respectively. The incomplete oxidation of ethanol not only lowers the energy efficiency due to fewer electrons exchanged relative to the complete oxidation reaction, but also gives rise to acetate or (bi)sulfate that strongly adsorbs on the surface of catalysts and significantly affects the reactivity of the catalysts [12, 13]. In addition, Pt itself has low resistance to poisoning, since intermediate species such as CO_{ads} could be strongly adsorbed on its surface, poisoning the catalysts and consequently leading to a sluggish reaction rate and even an irreversible degradation of the catalytic performance [14].

To address the above challenges in DEFCs, a great deal of work has been focused on exploring multi-component catalysts in comparison to pure Pt, aimed to obtain highly active, selective and durable catalysts. In recent years, many attempts have been made, such as combining Pt with non-noble transition metals to form binary/ternary catalysts, incorporating

transition metal oxides to Pt to form nanocomposite catalysts. A detailed literature review concerning the studies on Pt-transition metal (Pt-M) and Pt-transition metal oxides catalysts is elaborated in the following section. According to the scope of this thesis, catalysts applied in the acidic medium will be exclusively presented and discussed.

2.2 Ethanol oxidation on Pt-M bimetallic catalysts

With regard to Pt-based bimetallic catalyst for ethanol oxidation reaction, different transition metals have been introduced such as Ru [15-18], Sn [16, 19-24], Rh [18, 25], Au [26, 27], Mo [28] in order to enhance the activity, durability and selectivity of Pt. As in the case of the methanol oxidation, there are two widely accepted mechanisms to account for the improvement in catalytic performance for EOR: bifunctional mechanism [29, 30] and electronic (ligand) effect [1, 31, 32].

The bifunctional mechanism was proposed in the 70s by Watanabe and Motoo to explain the promotion of CO oxidation on PtRu catalysts [29]. According to bifunctional mechanism, two kinds of active sites are required for the EOR. One kind of active site on Pt surface is responsible for adsorbing and dissociating ethanol molecules. The other kind of active site on transition metals is for water adsorption and activation to provide oxygenated species (OH) at lower potentials. The OH species facilitate the oxidative removal of adsorbed carbonaceous generated on neighboring Pt sites, giving an enhanced catalytic performance. The whole process can be briefly depicted by equation 2.1 and 2.2 [10]:

$$M + H_2O \rightarrow M - OH + H^+ + e^- \tag{2.1}$$

$$Pt - CO + M - OH \rightarrow Pt + M + CO_2 + H^+ + e^- \tag{2.2}$$
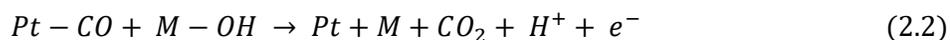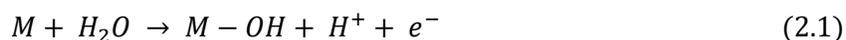
With regard to electronic effect, the presence of certain transition metals alters the electronic structure of Pt, which can be described as the change in the location of d-band center. According to the proposal of Nørskov and his co-workers, the shift of d-band center leads to the variation in the bond strength between reactive surface and adsorbates [33, 34]. A higher-lying d-band center with respect to the Fermi level indicates a more reactive surface which tends to bond with adsorbates more strongly, and conversely, a surface with a lower-lying d-band center tends to form weaker bonds with adsorbates. As for the EOR on pure Pt, a relatively high d-band center of Pt facilitates the dissociative chemisorption of ethanol molecules, giving rise to a higher coverage of CO species which are strongly bonded to active sites of Pt and thus rapidly poison

16

the catalysts. In the case of EOR on Pt-M (e.g. Ru, Sn) catalysts, a downshift of Pt surface d-band center could lower the adsorption energy of CO poisoning species, facilitating the removal of CO_{ads} [35]. Whereas if the d-band center is too low, it would diminish the adsorption ability of Pt with ethanol molecules, and thus the reactive intermediates are too low to enable a high turnover rate of the EOR. Therefore, an optimal d-band center of a catalyst is required to achieve the highest catalytic activity. The location of d-band center of Pt-based catalysts is largely affected by the nature of foreign metal alloyed to Pt (or used to modify Pt) and the composition of alloy.

Among investigated Pt-based bimetallic electrocatalysts, Pt-Sn catalysts were found to be the most active catalyst for the EOR in acidic medium [14, 20-22, 36-39], which contrasts with the case of MOR in which PtRu catalysts are known to be the most effective one [40-42]. In single DEFC test, compared to pure Pt, the enhancement of Pt-Sn catalysts in electrocatalytic activity is demonstrated in Figure 2.1 [19]. At the current density of $100\,mA\,cm^{-2}$, the overpotential of ethanol oxidation on pure Pt is about 0.6 V which is 200-300 mV higher than that on Pt-Sn bimetallic catalysts and can be further reduced on Pt-Sn-X (X: Ni) catalyst [1].
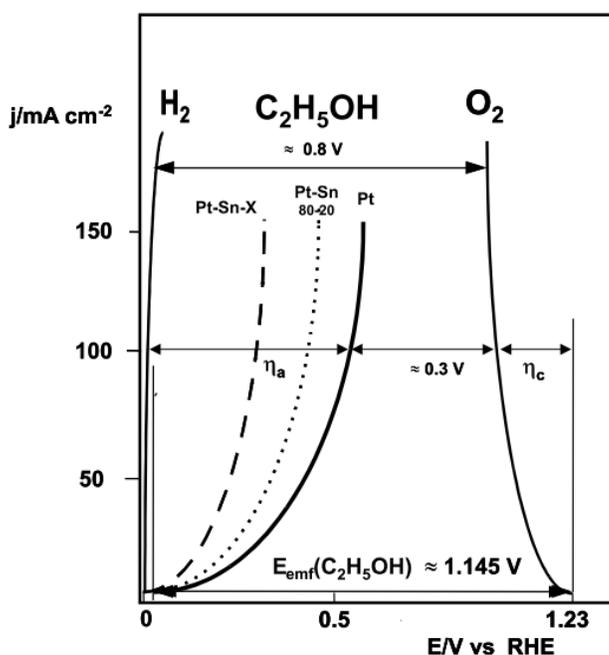
Figure 2.1 j/E curves of DEFCs with Pt-based material as anode catalysts, compared to that of a H₂ PEMFC with Pt catalysts as anode catalysts [19].

Therefore, particular attention of the study of bimetallic catalysts is given to Pt-Sn based catalysts, including the main effect on EOR activity, the oxidation mechanism investigation on Pt-Sn. The catalyst composition, the degree of alloying and the content of Sn oxides were identified to be the main factors influencing the catalytic performance towards the electrooxidation of

ethanol [1]. However, so far there is no common agreement on the optimum conditions for Pt-Sn towards EOR. Sometimes, the results are even contradictory. Regarding the composition effect, Zhou and co-workers synthesized Pt-Sn/C catalysts with varied Pt:Sn atomic ratios (1:1, 3:2, 2:1, 3:1 and 4:1) and the optimum composition of Sn was in the range 33-40 at.% depending on the operating temperature [22, 43]. Similarly, Kim et al. prepared PtSn/C catalyst with the same variations in Pt:Sn ratio (Pt:Sn = 1:1, 3:2, 2:1, 3:1, 4:1) by reducing Pt salt and Sn salt precursors with borohydride and followed by freeze-drying procedure [44]. They found that the charge transfer from Sn to Pt could mitigate the poisoning of catalysts by partially filling Pt 5d band vacancies. PtSn/C with 33 at.% of Sn exhibited the highest current density for EOR with CV characterization. With an alcohol reduction process, Spinacé et al. reported Pt-Sn/C electrocatalysts with the Pt:Sn atomic ratio of 1:1 was better than two other compositions (1:3 and 3:1) [45]. Asgardi et al. prepared a series of PtSn catalysts with different Pt:Sn atomic ratio (1:1 and 3:1) by using formic acid, supported on two kinds of carbon materials, carbon Vulcan XC-72R and carbon nanofibers (CNF) [46]. It was found that Pt_1Sn_1 anodes exhibited higher activity toward EOR in half-cell experiments than Pt_3Sn_1, irrespective of support materials. The authors ascribed it to higher content of Pt_3Sn_1 crystallite phase in catalysts with Pt:Sn atomic ratio of 1:1 with respect to that of 3:1, which was determined by the extended lattice parameters from XRD. On the contrary, Lamy et al reported the optimum content of Sn for Pt-Sn catalysts in the range 10–20 at.% is much lower than the values reported by the above authors [38, 47]. Bommersbach et al. prepared Pt-Sn catalysts by using crossed beam pulse laser deposition (CBPLD) [24]. Four compositions were investigated, namely, Pt_9Sn_1, Pt_3Sn_1, Pt_1Sn_1, and Pt_3Sn_7. Pt_3Sn_1 displayed the best catalytic activity and durability characterized by cyclic voltammetry (CV) and chronoamperometry (CA) techniques. However, we still get conclude that compositions richer in platinum are favored for electro-oxidation of ethanol. The large range in the optimal composition of Pt-Sn catalysts towards EOR could be attributed to the preparation approaches. Song et al. have prepared two kinds of PtSn/C catalysts with different preparation procedures, a modified polyol approach and co-precipitation [37]. PtSn/C-a catalysts were prepared by the directly depositing Sn on Pt/C via a modified polyol process and PtSn/C-b catalysts were obtained by simultaneous deposition of Pt and Sn on the carbon supports via a co-precipitation process. From single DEFC tests, the cell using PtSn/C-b as anode catalysts displayed a higher electrocatalytic activity at high current density than that using PtSn/C-a, despite both catalysts showed a similar initial activity. The authors attributed the inferior performance of PtSn/C-a to a higher content of Sn oxides which led to higher internal cell resistance and part coverage of Pt active sites. Indeed, it has been reported by many groups that in most cases Sn in PtSn catalyst is present in two

states: non-alloyed oxidized state (Sn oxides), and alloyed metallic state which forms faced-centered-cubic (fcc) solid solution with Pt atoms. The content of Sn oxides and the degree of alloying have been reported to be of importance for the catalytic performance of binary Pt-Sn catalyst toward EOR. However, so far, controversial results regarding the effect of the degree of alloying on the EOR activity of Pt alloy catalysts have been reported. Colmenares et al. compared the EOR catalytic activities of polyol-type Pt/C, PtRu/C and Pt_3Sn/C catalysts with those of commercial Pt/C, PtRu/C and Pt_3Sn/C (E-Tek) catalysts [48]. All polyo-type catalysts displayed inferior performance than their commercial counterparts in terms of the mass activity and active surface area specific activity, which was ascribed to the lower alloying degree of Sn in polyol-type catalysts. In agreement with the observations of Colmenares, Zhu et al. reported that PtSn catalysts with high degree of alloying (denoted as PtSn/C-B) showed better EOR activity than that with low alloying degree (denoted as PtSn/C-EG) and the catalysts with only non-alloyed oxidized Sn (denoted as $PtSnO_2/C$) [49]. They found that the $PtSnO_2/C$ catalyst could only enhance the EOR activity below 0.36 V due to readily forming OH species on SnO_2 at lower potentials which is favorable for the removal of CO_{ads} species, whereas catalyst with high alloying degree could promote the activity over the entire potential range owing to the changes in electronic and geometric structure. Similar results have also been reported by other researchers. Godoi et al. prepared Pt-Sn/C catalysts with varied amount of oxidized and alloyed form of tin but the identical overall composition (Pt:Sn=7:3) and nearly the same particle sizes (around 3 nm) [50]. In the absence of the composition and size effect, it was found that the Pt-Sn/C catalysts displayed an increase in EOR catalytic activity by increasing the amount of metallic Sn at the expense of the oxides, attributed to a more filled Pt d-band in PtSn alloy facilitating the effective removal of CO_{ads}.

Conversely, Antoniassi et al. observed that the catalysts with higher content of Sn oxides displayed superior EOR performance than the PtSn catalysts with high alloying degree [51]. They observed almost 70% more power density on $Pt_3(SnO_2)/C$ than Pt_3Sn/C (alloy) electrode in single DEFC tests. The product distribution results evaluated with gas chromatography (GC) technique, indicated that $Pt_3(SnO_2)/C$ catalysts had a higher selectivity for AA production (4 electrons releasing) while Pt_3Sn/C mainly produced AAL by releasing 2 electrons. Alternatively, Jiang et al. prepared two types of catalysts with the same nominal Pt:Sn ratio, $PtSnO_x$ and PtSn alloy, by using a modified polyol approach [20]. From the results of chronoamperometry and single DEFC tests, $PtSnO_x$ catalysts better performed than PtSn alloy toward EOR. The authors deduced that the unchanged lattice constant of Pt in the $PtSnO_x$ catalyst enables the effective adsorption of ethanol, and simultaneously the SnO_x in the vicinity of Pt could supply OH species which facilitate the removal of poisoning CO_{ads} residues from Pt active sites. They also proposed that an ideal

PtSn anode catalyst for DEFCs should contain both PtSn alloy and $PtSnO_x$ components with optimum compositions. In similar, Colmati et al. have also demonstrated that the activity of Pt-Sn/C catalysts seems to be dependent on the amount of both non-alloyed and alloyed phase of Sn [52]. The DEFCs operating conditions (such as DEFC operation temperatures) affect the rate-determining step (rds) of EOR and thus the optimal content of each form of Sn are varied accordingly. They found that the oxidation of CO_{ads} species was the rds at low temperatures of electrochemical experiments, and the presence of tin oxides were favorable to increase the DEFC performance by offering adequate OH species. Whereas at high temperatures, the rds was the dissociative adsorption of ethanol and/or the oxidation of AAL to AA: both reactions could be increased with the increase of the amount of alloyed Sn.

The discrepancies among various studies on Pt-Sn catalysts could be attributed to a variety of influencing factors such as size, crystallinity, shape, composition of the catalysts, the content of each kind of phase for Sn (alloyed or non-alloyed). Furthermore, different synthesize methods may also bring impurities such as organic solvent and reducing agent that affect the catalytic behaviors of catalysts as well. Besides, the electrochemical testing conditions such as temperature, concentration of ethanol, and so forth could also play a critical role in the catalytic performance of investigated catalysts. The complexity of ethanol oxidation process is another important reason. Regarding the oxidation mechanism of ethanol on Pt-Sn catalysts, conflicting results have also been reported, including reaction paths, product distribution, and so on.

From the studies on Pt-Sn binary catalyst, there is no question that the addition of Sn does improve the catalytic performance towards ethanol oxidation, lower reaction overpotential, and boost output energy. While a consensus gained from the research on Pt-Sn catalyst is that Pt-Sn cannot accomplish the complete oxidation of ethanol at low temperatures and low potentials, but helps to produce AAL and AA as main products through 2- and 4-electron transfer, respectively. It is crucial and necessary to develop novel catalysts that exhibit high activity and selectively for the EOR.

2.3 Ethanol oxidation on functional metal oxide–based catalysts

In addition to extensive studies on Pt-M catalysts, much effort has been made to explore novel Pt-based catalyst by introducing diverse functional metal oxides (FMOs) such as CeO_2, SnO_2, MnO_2, TiO_2, WO_3, etc. As is well known, these FMOs are cheap and abundant compared with Pt, and thus the incorporation of high specific-surface-area FMOs could largely reduce the

cost of catalysts. Furthermore, these FMOs also possess the following important characteristics qualifying their potential applications in DEFCs:

1) High chemical and electrochemical stability under fuel cell operating conditions, reducing the agglomeration or coalescence of catalysts nanoparticles and thus increasing their durability.

2) The Strong interaction of catalyst nanoparticles with oxide supports (metal-support interaction, SMSI) could immobilize catalysts nanoparticles on the surfaces of support materials, preventing from the growth and sintering of catalyst nanoparticles, and could also alter the electron distribution of catalysts enabling to diminish the CO poisoning effect [53].

3) Readily forming abundant hydroxyl (OH) groups on their surfaces, which could promote the catalytic performance on the basis of bifunctional mechanism [54].

It has been reported that FMOs in DEFCs serve as support materials to increase the utilization of Pt, and/or as co-catalysts (promoter) to assist certain catalytic processes [10]. However, most FMOs have a low electronic conductivity which could be enhanced by Nano-structuring them or by combining them with highly conductive carbon materials to form composites or by doping foreign elements. In the composites, nanostructured carbons are considered as the primary supports, such as carbon nanotubes, graphene, mesoporous carbon, and so forth. FMOs are considered as the secondary supports which are generally used to promote and modify the primary supports [9].

In the following part, several FMOs are particularly chosen to be introduced in detail, including their structure, properties, emerging features relevant to the DEFCs application, and the studies conducted on Pt-FMOs systems for ethanol oxidations.

2.3.1 CeO₂–based catalysts
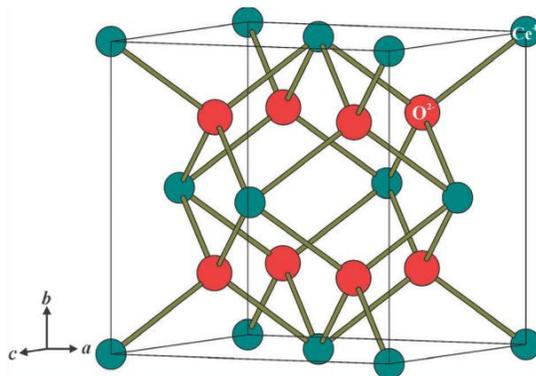
Figure 2.2 The crystal structure of CeO₂.

CeO₂, named cerium (di)oxide or ceria, is the most abundant rare earth oxide which exhibits a fluorite (CaF₂) crystal structure (space group $Fm\bar{3}m$) with lattice constant a = 5.4113 Å. Figure 2.2 presents a unit cell of CeO₂, where each cerium cation is coordinated by eight equivalent nearest-neighbor oxygen anions, whereas each oxygen anions is coordinated by four equivalent cerium cations [55].

Ceria is not only a technologically important functional material in the industry but also one of the most actively investigated materials in academia. From 1950 to 2015, the publication number concerning "CeO₂" or "ceria" exceeds 26000 covering a wide range of applications including catalysis [53, 56-60], solid oxide fuel cells (SOFCs) [60, 61], photocatalysis [62, 63], oxygen sensors [64, 65], glass polishing [66], ultraviolet absorbent, ceramics, electrochromic thin-film application, environmental chemistry etc., owing to its diverse properties, such as electronic (high oxygen ion conductivity), optical (high refractive index, high transmission, violet and blue emission), mechanical (high adhesion, hardness, stability towards abrasion), etc. [55, 58]. Owing to the catalytic property, ceria is an important constituent in SOFCs and three-way catalysts in the automotive industry, which is considered to be mainly related to its exceptional redox property (oxygen storage capacity) and oxygen transport property (oxygen ion conductivity). Redox property refers to its ability to repeatedly pass through redox cycles rapidly while retaining its fluorite structure, which is related to the ease in forming and eliminating oxygen vacancies at the surface of solid ceria, endowing ceria a high oxygen storage property [55]. Specifically, when exposed to a reducing atmosphere at elevated temperatures (above 685 ℃), CeO₂ could be readily transformed into non-stoichiometric CeO₂₋ₓ oxides ($0 < x \leq 0.286$) by forming a continuum

of oxygen-deficiencies accompanied by the reduction of Ce(IV) to Ce(III), which can be expressed following the Kröger-Vink notation as:

$$2Ce_{Ce}^{\times} + O_O^{\times} \rightarrow V_O^{\cdot\cdot} + 2Ce_{Ce}' + \frac{1}{2}O_2(gas) \tag{2.3}$$
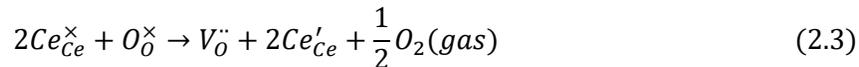
where $Ce_{Ce}^{\times}$, $O_O^{\times}$, $V_O^{\cdot\cdot}$, Ce_{Ce}' represent cerium ions in the lattice, oxygen ions in the lattice, doubly charged oxygen vacancies, and cerium anions on the lattice site with single negative charge, respectively. On the contrary, under oxidizing conditions at lower temperatures, the partially reduced ceria can be re-oxidized back to CeO_2 and remaining its fluorite structure. The non-stoichiometric form at elevated temperatures exhibits both electronic and ionic conduction, and ionic conduction becomes dominant at a temperature above 500 °C mainly due to increased oxygen vacancies. The concentration of oxygen vacancies is usually determined by using X-ray photoelectron spectroscopy (XPS) to compare the ratio of Ce^{3+} to Ce^{4+}.

It has been reported that the concentration of oxygen vacancy defect in ceria plays an important role in the conductivity and the reactivity of ceria for different catalytic reactions such as the CO oxidation, SO_2 reduction by CO. Compared with bulk material, there are high densities of interfaces in nanocrystalline ceria which substantially reduces the energetics for the formation of defects (oxygen vacancies), resulting in remarkably increased degrees of non-stoichiometry. As a consequence, nanostructured ceria displays an improved oxygen storage capacity and oxygen ion conductivity with respect to its bulk counterpart. These features appear to contribute to the unusual catalytic activity of nanostructured ceria. In the last decades, nanostructured CeO_2 have been extensively studied either as co-catalysts or as modifier/promoter of primary carbon support materials of noble catalysts for electro-oxidations of small organic molecules (like CO, methanol, and ethanol) and the reduction reaction of oxygen in fuel cell (FC) applications. Pronounced improvements in catalytic activity and durability have been widely observed towards different electrocatalytic reactions including ORR [67], MOR [68-70], EOR [71, 72], and so on.

The promotion effect of CeO_2 in Pt-CeO_2 systems for catalytic reactions can be summarized as follows:

1) The strong interaction between Pt and ceria, not only inhibits the growth and sintering of Pt metal particles but also alters the electronic structure of Pt improving CO poisoning resistance, leading to the enhanced activity and durability of the catalysts. By combining density functions theory (DFT) calculations (theoretical study) and synchrotron-radiation photoelectron spectroscopy (experimental study), Vayssilov identified two types of oxidative metal-oxide interaction coexist when nanostructured CeO_2 is in close contact

with Pt: (i) electron transfer from the Pt nanoparticle to the ceria, and (ii) activated oxygen transfer from ceria to Pt (called oxygen reverse spillover) [53]. They found the oxygen reverse spillover phenomenon is a nanoscale effect: it is operative on nanostructured ceria only, but not on the surface of ordered bulk ceria. Their finding rationalized the significant promotion on the catalytic activity of nanostructured ceria. Ou et al demonstrated the presence of strong metal-oxide interaction via electron energy loss spectroscopy (EELS) on Pt-CeO$_2$/C catalysts, and the interaction was enhanced with the increasing of Pt:Ce atomic ratio [70]. They found that the redox reaction took place between Pt and CeO$_2$, resulting in the formation of Ce$_{1-y}$Pt$_y$O$_{2-z}$ - type solid solution. The microstructural and chemical features due to the interaction between Pt and ceria can account for the promotion effect of ceria on MOR.

2) According to bifunctional mechanism, OH groups could readily form on the surfaces of ceria, facilitating the removal of CO species generated by the ethanol oxidation on the neighboring Pt, leading to improved activity and durability of the catalysts.

3) In the presence of CeO$_2$, catalysts show higher selectivity to CO$_2$ for EOR. Neto et al. prepared PtSn/CeO$_2$-C by an alcohol-reduction process and the best results were found on the catalyst with 15 wt% CeO$_2$ which exhibits much higher EOR performance than the PtSn/C catalysts [72, 73]. Their Fourier Transform Infrared (FTIR) spectroscopy studies showed that the main products were CO$_2$ and AA on PtSn/CeO$_2$–C catalysts, in comparison to AAL and AA on PtSn/C catalysts [73].

2.3.2 SnO$_2$–based catalysts

SnO$_2$, tin dioxide, crystallises in a tetragonal rutile structure (space group P4$_2$mnm) with lattice parameters: a = 4.738 Å and c = 3.187 Å [74]. As shown in Figure 2.3, the tin cations are surrounded by an octahedron of 6 oxygen atoms, and the oxygen anions form a trigonal planar coordination. SnO$_2$ is commonly regarded as an oxygen-deficient n-type semiconductor with a wide band gap (ca. 3.6 eV for bulk at room temperature) [74]. Owing to its remarkable electrical, optical, and electrochemical properties, SnO$_2$ is an important component in various applications such as solar cells, solid-state chemical sensors [75-77], lithium ion batteries [78, 79], and fuel cell applications [80-87].
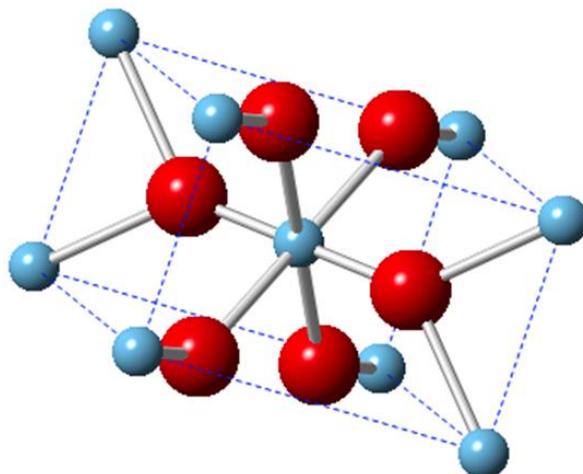
Figure 2.3 The crystal structure of SnO₂.

As discussed in the previous part about Pt-Sn binary catalysts, two phases (alloyed Sn and Sn oxides) mostly coexist in the binary catalysts and the promoting effect of tin oxide in Pt-Sn catalysts for EOR has been demonstrated by several researchers [20, 52]. The role of SnO_2 is believed to active H_2O dissociation at low potentials and to provide OH species for the efficient oxidative removal of CO_{ads} poisoning species adsorbed on neighbouring Pt active sites, according to the bifunctional mechanism [74, 88]. Additionally, Zhou et al. have reported the importance of interface sites between Pt and SnO_x towards EOR [89]. Via reactive layer assisted deposition (RLAD), they deposited nanoislands of SnO_x onto Pt (111) disk and the coverage of SnO_x layer was varied. According to CV and CA results, the SnO_x/Pt(111) catalysts exhibited enhanced EOR activities with respect to bare Pt(111) and a "volcano" dependence of EOR activity on the SnO_x coverage was observed. As the available reactive sites on Pt were decreased after the deposition of SnO_x, the enhanced electrochemical activity with less active Pt sites was attributed to the "ensemble" effect controlled by the presence of actives sites at the boundary between Pt and SnO_x. To date, nanostructured SnO_2 is generally introduced either as independent support material [82, 83] or to form hybrid/composite supports by combining primary supports (such as carbon materials) [84, 85], or as promoting additives for carbon supported Pt-based catalysts [81, 86, 87]. Silva et al has reported a study on core–shell structured SnO_2@Pt/C for ethanol oxidation. The Pt/C prepared in the same manner and commercial PtSn/C E-TEK are used for comparison. Electrochemical results demonstrated a promoted mass-specific activity towards EOR compared with Pt/C and PtSn/C E-TEK. They ascribed the catalytic promotion to the following factors: (i) an increase in the Pt surface, (ii) a modification in the electronic structure of Pt induced by a foreign core and (iii) the removal of CO species by exposed core SnO_2 by pinholes in the incomplete Pt

shell. With hydrothermal method, Zhang et al. synthesized SnO_2 nanoflowers and nanorods which were used as the support of Pt nanocatalysts for MOR and EOR [90]. It was found that the Pt/SnO_2 (flower) catalyst exhibited a higher electrocatalytic activity and better stability than that of Pt catalysts supported on SnO_2 nanorods and carbon black, due to the multidimensional active sites and radial channels of liquid diffusion provided by SnO_2 flower-shape support. Jiang et al. prepared uniform tin oxide nanoparticles with controlled particle size by heating ethylene glycol solutions containing $SnCl_2$ at atmospheric pressure, and then loaded Pt nanoparticles on pre-formed SnO_2 particles by a modified polyol method [91]. The resulting PtSnO$_2$/C catalysts containing uniform Pt and SnO_2 nanoparticles, displayed a surprisingly promoted catalytic activity for EOR than Pt/C. Following this work, they fabricated Pt/SnO_x/C catalysts with varied Pt:Sn atomic ratios (5:5, 6:4, 7:3 and 8:2) by the same method [86]. All Pt/SnO_2 catalyst presented higher DEFC performance than pure Pt, and $Pt_7/(SnO_2)_3$/C showed an optimal performance due to the highest yield of AA and lowest production of AAL compared with other catalysts. By means of alcohol reduction processes, Antoniassi et al. prepared PtSnO$_2$/C catalysts with different Pt:SnO_2 molar ratios (9:1, 3:1 and 1:1) and their catalytic performance were compared with commercial Pt_3Sn/C (alloy) and Pt/C catalysts based on the results of single FC tests and corresponding products distribution analysis using ethanol, AAL, AA and mixtures of ethanol/AAL and ethanol/AA as fuels [51]. PtSnO$_2$/C with Pt:SnO_2 molecular ratio of 3:1 exhibited a superior EOR performance than PtSnO$_2$/C with other compositions, commercial Pt_3Sn/C(alloy) and Pt/C, ascribed to an increased selectivity for AA production (release 4 electrons) at the cost of AAL production. Du et al. prepared mesoporous SnO_2 coated CNT core–sheath nanocomposites (CNT@SnO_2) by a hydrothermal method. CNT@SnO_2 was found to be more corrosion resistant than CNT support, which was considered as a promising support material for use in PEM-based FCs [80]. Pang et al. grew Pt nanoparticles on CNT@SnO_2 core-shell composites through a two-step strategy [85]. CV and CA results indicated that Pt/(CNT@SnO_2) catalysts had much higher catalytic activity and CO-tolerance for ethanol electro-oxidation compared with that of Pt/CNT, owing to the synergetic interaction between Pt and SnO_2. Similarly, Ryan et al. coated SnO_2 on single-walled nanotube (SWNT) bundles by a chemical-solution route and followed by the loading of Pt nanocatalysts via an ethylene glycol reduction method [84]. With respect to Pt/SWNT, the Pt/SnO_2–SWNTs exhibited promoted electrocatalytic activity for EOR in acid medium.

Zignani et al. added nanostructured SnO_2 and TiO_2 to PtRu/C catalysts as promoters for ethanol oxidation (named as PtRh/C+SnO_2 and PtRh/C+TiO_2, respectively). From electrochemical tests carried out in 3-electrode cell and single DEFC, PtRh/C+ MO_2 (M: Sn, Ti) catalysts performed better than bare PtRu/C catalyst, and PtRh/C+SnO_2 is superior to

PtRh/C+TiO$_2$ in terms of lower onset potential, higher oxidation current density, and higher maximum powder density. From the Tafel plot analysis, it was found that the presence of metal oxides (MO) promoted the intrinsic activity of PtRu/C catalysts at low potentials based on the increased exchange current density on PtRh/C+MO$_2$. Furthermore, in-situ adsorbed ethanolic residues stripping voltammetry was exploited to get insight into the promoting effect of metal oxide additives. Similar coulombic charges under ethanol stripping peak were obtained for the composite electrodes with TiO$_2$ and SnO$_2$, but higher than that of PtRu/C, indicating the increase of coverage of ethanolic residues in the presence of metal oxide additives.

2.3.3 TiO$_2$–based catalysts
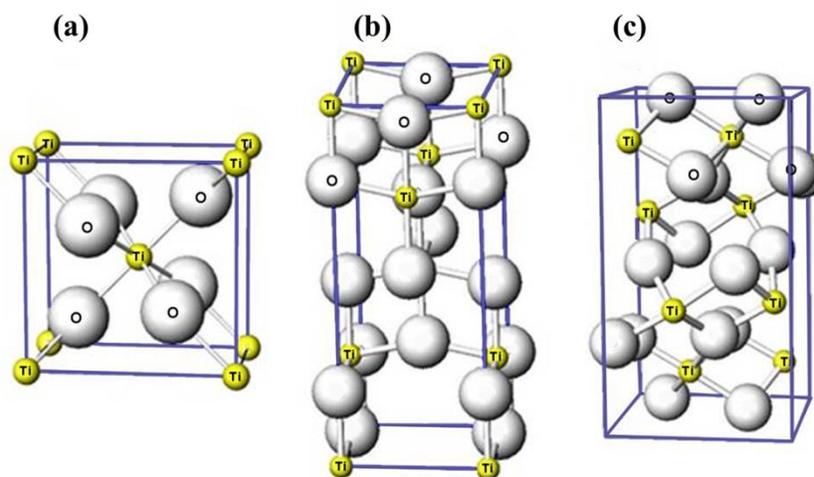
Figure 2.4 The crystal structure of TiO$_2$ in phase: a) Rutile, b) anatase, c) brookite.

Titanium dioxide, also known as titanium (IV) oxide, is the naturally occurring oxide of titanium. Titanium dioxide occurs in nature in three main phases: rutile, anatase, and brookite, [92]. The unit cells of the three phases of TiO$_2$ are presented in Figure 2.4. Rutile phase is the most common natural form of TiO$_2$. Rutile has a body-centred tetragonal unit cell, with unit cell parameters $a=b=4.584$ Å, and $c=2.953$ Å. Each titanium cation is surrounded by an octahedron of 6 oxygen atoms. The oxygen anions have a co-ordination number of 3 resulting in a trigonal planar co-ordination. Rutile also shows a screw axis when the octahedra are viewed sequentially [93]. Anatase crystallizes in the tetragonal system. The common pyramid of anatase, parallel to the faces of which there are perfect cleavages, has an angle over the polar edge of 82°9', the corresponding angle of rutile being 56°52½' [94]. Brookite belongs to the orthorhombic dipyramidal crystal class 2/m 2/m 2/m. The unit cell parameters are: $a=5.4558$ Å, $b=9.1819$ Å

and c=5.1429 Å. The formula is TiO_2, with 8 formula units per unit cell (Z=8). The brookite structure is built up of distorted octahedra with a titanium ion at the center and oxygen ions at each of the six vertices. Each octahedron shares three edges with adjoining octahedra, forming an orthorhombic structure [95]. A general consensus places the bandgaps of rutile and anatase TiO_2 at 3.03 and 3.20 eV, respectively [96].

For fuel cell application, nanostructured Ti oxides have been incorporated to improve the performance either as membrane or as catalyst support or as catalyst itself. The wide applications in each aspect are reviewed by Pu et al [97]. Under UV excitation, TiO_2 was reported to be an excellent photocatalysts for the degradation of organic contaminants present in different environments such as water or air, due to its high redox activity [98]. In the literature, Pt-TiO_2 electrodes were mostly reported as photocatalysts for photo-electrochemical cells [92, 99]. Park et al. reported a significantly improved MOR performance of Pt-TiO_2 nanostructure electrode under UV illumination in comparison with that without UV illumination [100]. The authors attributed the remarkably enhanced performance under UV illumination to the photocatalysis of methanol oxidation by photo-generated holes in TiO_2. Hosseini reported photocatalytic and UV-cleaning properties of Pt nanoparticle-decorated titania nanotubes (Pt-NPs/TNT) towards electrooxidation reaction of methanol [101]. Pt-NPs/TNT electrode was swept in 0.1 M H_2SO_4 + 0.1 M methanol aqueous solution for 250 cycles in the potential range of 0.0 -1.0V vs. SCE. Inevitably, the current density got decreased with increasing cycling numbers, mainly due to the CO poisoning effect. After exposing the electrode to UV for 5 min, interestingly, authors found that the cycle voltammograms of Pt-NPs/TNT could return to its original shape and magnitude, which was ascribed to the self-cleaning properties of TiO_2. In addition, the peak current density of MOR with UV illumination was reported to be approximately 2.1 times with respect to that without UV illumination. On the basis of the experiments and relevant literature, authors concluded that the electrooxidation of methanol on Pt-NPs and the photoelectrooxidation of methanol on TiO_2 took place simultaneously under UV illumination and contributed to the enhanced peak current density in CV tests. TiO_2 have also been proposed as potential cathodes for ORR due to its higher durability in relation to conventional carbon supports [102-104]. Various mechanisms have been discussed for the role of TiO_2 and the electrocatalytic activity of Pt-TiO_2 towards ORR. For cathodic electrodes, TiO_2 helps mitigate the aggregation of Pt particles and protect the Nafion membrane against peroxide radicals formed during ORR [104, 105].

On the other hand, several works have reported that TiO_2 can enhance the electrocatalytic activity of Pt towards methanol oxidation and ethanol oxidation in darkness by mitigating CO

poisoning effect [106]. Kamat et al. found that TiO_2 can improve the performance of the Pt–Ru catalyst for methanol oxidation without UV excitation by diminishing CO poisoning effects [107]. Yu et al. prepared composite anode catalyst (Pt/C+TiO_2) in a very simple manner by ultrasonically mixing commercial Pt/C and TiO_2 nanoparticles, and effect of the size and the content of TiO_2 were investigated [106]. Pt/C+TiO_2 electrocatalyst with 20 wt% of TiO_2 (10 nm in diameter) displayed the best catalytic performance for ethanol oxidation which is much higher than the pristine Pt/C. The promoted catalytic performance of Pt/C+TiO_2 was ascribed to the presence of TiO_2 which could promote CO oxidative removal verified by CO stripping test, and the optimum content and size of TiO_2 which could guarantee an optimized TiO_2-Pt-C interfaces and good electronic conductivity for composite catalysts. The synergistic effect of Pt catalysts with submicrometer-sized TiO_2 sphere support has been reported by Hua et al [108], which lowered the onset potential towards MOR and EOR compared with Pt supported by carbon black demonstrating enhanced reaction kinetics. By means of thermal decomposition of chloride precursors H_2PtCl_6 and $TiCl_3$ at high temperature, Hasa et al. prepared Pt-TiO_2 binary electrocatalysts with different Pt:TiO_2 molar ratios for EOR and MOR [109]. Pt(50%)-TiO_2(50%) was found to be the optimal composition, which presented dramatically enhanced EOR and MOR activity than pure Pt. The addition of TiO_2 was reported to be favorable for the formation of smaller Pt nanoparticles and their uniform dispersion, which was considered as the main reason for the improved electrocatalytic performance of Pt-TiO_2 binary electrode instead of bifunctional effect.

2.3.4 MnO_2–based catalysts

Because of appealing properties of MnO_2 such as good proton conductivity, structural diversity, and variable oxidation states, it has been widely employed in many electrochemical applications including electrochemical capacitors [110-113], Lithium batteries [114-116], FCs [117-123], etc.

MnO_2 presents in diverse polymorphic forms over a wide compositional range. All crystalline Mn(IV) oxides are constructed by the same building block ([MnO_6] octahedron) [124, 125]. According to how [MnO_6] unit are linked, Mn(IV) oxides present different crystalline structures (such as α-, β-, γ-, δ-type). α-MnO_2 has a very open tunnel structure constructed by 2 × 2 octahedral units. β-MnO_2 is formed with 1×1 octahedral units, which is the most stable and densest polymorph. γ-MnO_2 is a highly disordered material due to the random intergrowth of 1 × 2 and 1 × 1 tunnels. δ-MnO_2 has a lamellar structure due to loosely bound layers of edge shared [MnO_6] octahedra. The interlayer spacing of δ-MnO_2 sheets is about 0.7 nm, which are commonly

29

separated by hydroxyl groups or water molecules. Figure 2.5 shows the crystal structures of α-, β-, γ-, and δ-MnO_2 [125]. In addition to crystallized forms, amorphous MnO_2 is present in a highly porous microstructure with a lower electrical conductivity. The structure variation of MnO_2 phase leads to dramatically different performances in electrochemical applications, such as catalytic activities for the oxidations small molecules [126, 127], capacitive behaviors and cycling stability in supercapacitances and lithium ion batteries [125].
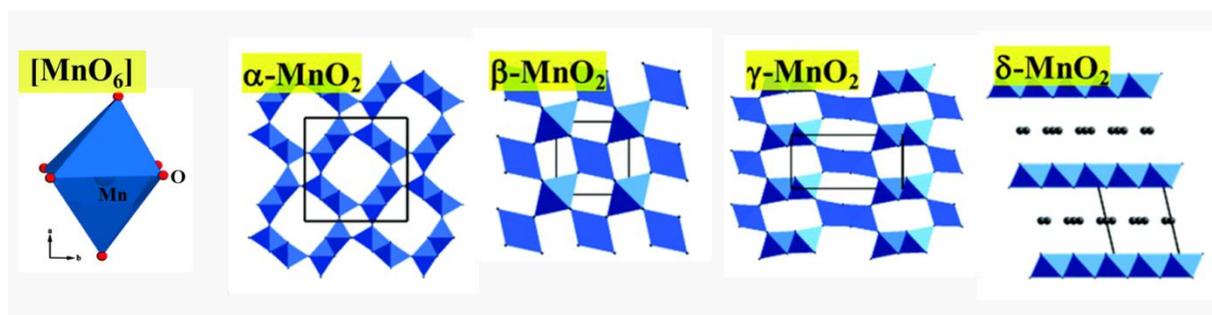
Figure 2.5 Polyhedral representations of the crystal structures of different MnO_2 and [MnO_6] octahedron.

As for the application in FCs, MnO_2 was found to show enhancing effects similar to SnO_2, CeO_2, and TiO_2, towards the electrooxidation reactions of small molecules (methanol [117-119, 121, 122, 128], formic acid [123] and ethanol [120, 129, 130]) when incorporated into noble nanoparticle catalysts. Zhao prepared MnO_2 nanowires by an anodic deposition technique, followed by the deposition of Pt nanoparticles with a cathode deposition approach [121]. MnO_2 nanowire supported Pt catalyst show 2.1-fold enhanced voltammetric forward peak current and 110 mV decreased overpotential. MnO_2/CNTs were used by Zhou et al. as the support of Pt (or PtRu alloy) catalysts, which could effectively increase the proton conductivity and utilization of Pt leading to a remarkable enhancement in catalytic performance to MOR [117]. Huang et al. functionalized 2-dimensional graphene sheets (GS) with hydrous MnO_2 as the support of Pt catalysts for MOR [118]. Due to the unique and critical function offered by each component, the ternary Pt/MnO_2/GS electrocatalysts with high electronic and proton conductivity showed higher electrocatalytic activity, better anti-poisoning ability and stability than Pt/GS, Pt/XC-72 and Pt/MnO_2/XC-72 catalysts.

Due to the excellent proton conductivity of MnO_x and the synergistic effect between Pt and MnO_x, Pt-MnO_x system has also been used as the catalyst for EOR [120, 129, 130]. Cai et al. dispersed Pt nanoparticles on MnO_x-CNT by a microwave-assisted polyol approach [129]. Their results showed the incorporation of MnO_x in the catalyst largely improved the EOR activity, stability and anti-poisoning ability of Pt catalysts. By hydrothermal synthesis, Meher et al.

prepared α-MnO$_2$ with different microstructures (nanorod and microcube) and the effects of MnO$_2$ microstructure in Pt/MnO$_2$/C on the performance for EOR and MOR have been studied [120]. MnO$_2$-nanorod-modified Pt/C catalyst outperformed than that modified by MnO$_2$-microcubes, in terms of CO tolerance, EOR (MOR) activity and durability. It was ascribed to higher triple-phase interfaces on MnO$_2$-nanorod-modified Pt/C which provide high amount of OH species for the effective removal of poisoning species on Pt, and thus boosted the alcohol electrooxidation performance.

2.4 Reaction mechanism of EOR

It is well known that the complete oxidation of ethanol leads to the breakdown of C-C bond and generates adsorbed CO species that are finally oxidized to CO$_2$. The whole process involves 12-electron transfer per ethanol molecule, giving rise to an energy density of 8.0 kWh kg^{-1}. However, under low temperatures, it was found that the breakdown of C-C bond is not easily accomplished on currently available Pt catalysts. Various intermediates (e.g. CH$_{x,ads}$, CO$_{ads}$, CH$_3$COH$_{ads}$) and products (e.g. AAL, AA, CO$_2$ and methane) are formed through numbers of parallel reactions, which largely lowers the exploitable energy density (8.0 kWh kg^{-1}) of ethanol. Therefore, a comprehensive understanding of the reaction mechanism for the oxidation of ethanol is valuable and critical for the designing of novel catalysts with high activity, selectivity, and stability.

In this context, numerous studies have been devoted to elucidating the reaction mechanism of ethanol oxidation by identifying the adsorbed intermediates and quantifying the reaction products and by-products [131, 132]. To achieve this, some traditional electrochemical methods, such as CV, CA and rotating disc electrodes (RDE) have been combined with other physicochemical techniques including *in situ* FTIR [133, 134], (on line) differential electrochemical mass spectrometry (DEMS) [133-135], high performance liquid chromatography (HPLC) [136], gas chromatography (GC) [37, 87, 137], *in situ* nuclear magnetic resonance spectroscopy (NMR) [138], and surface enhanced Raman spectroscopy (SERS) [139]. Furthermore, theoretical studies with DFT calculations have been conducted to provide a fundamental basis for the understanding of experimental observations and to give a further experimental guidance [140-143].

To date, it has been generally accepted that the major oxidation products during the EOR are AAL, AA, and CO$_2$. The global mechanism of the ethanol electro-oxidation on Pt-based catalysts in acid medium can be simply represented as Figure 2.6, which is composed of several

parallel reactions [131, 139, 144]. The desired path leads to the formation of CO_2 exchanging 12 electrons during the entire process. It goes through the breakdown of C-C bond from ethanol or AAL, the generation of adsorbed intermediates $C1_{ads}$ which represent hydrocarbon fragments with one carbon atom (such as CO_{ads}, $CH_{x,ads}$ species), and finally the oxidation of $C1_{ads}$ intermediates to CO_2 with the aid of OH species [139]. However, it has been found that most of the ethanol molecules undergo partial oxidations on Pt electrodes, in which C-C bond is preserved forming AAL (or AA) involving 2-electron (or 4-electron) exchange. Meanwhile, some AAL could re-adsorb on the surface of catalysts, and be further decomposed to form $C1_{ads}$ intermediates and eventually be oxidized to CO_2, or be directly oxidized to AA which is found to be a dead-end product.
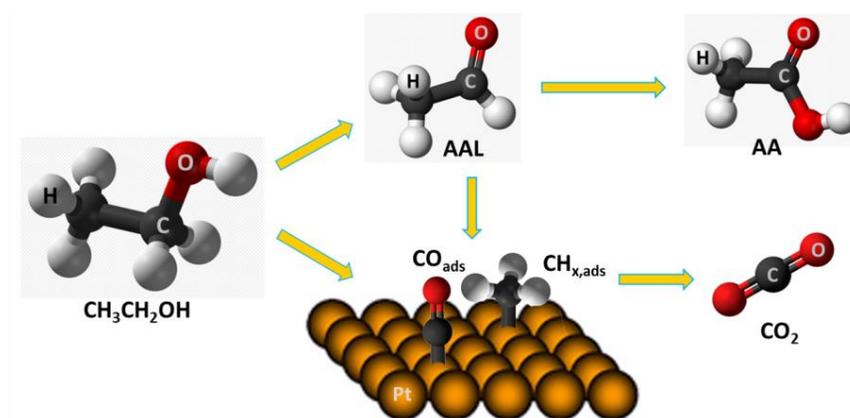
Figure 2.6 Schematic of the global reaction mechanism for the electro-oxidation of ethanol on Pt electrodes in acidic medium [131, 139, 144].

The product yield of the EOR on Pt catalysts was found to be largely dependent on ethanol concentration [144, 145], electrode potential at which the reaction occurs. These studies allow us to improve our understanding on the reaction mechanism of EOR. Wang et al. investigated the effect of the ethanol concentration on product yields for carbon-supported Pt catalysts by combining on-line mass spectrometric analysis and electrochemical current measurements [145]. Under room temperature, it was found that ethanol oxidation to AAL was favoured at high ethanol concentrations, whereas at low concentrations the formation of AA prevailed. The yield of CO_2 was low at all concentrations ranged from 0.001 M to 0.5 M. By using FTIR, the results on polycrystalline Pt obtained by Camara et al., that is in accordance with that reported by Wang et al. [144]. At low ethanol concentrations (< 0.1 M), it was found that AA was the main product, whereas AAL was not detected, and the yield of CO_2 was detected to be 6 times lower than that of AA. When the ethanol concentration above 0.1 M, the pathways generating AA and CO_2 were significantly inhibited, probably owing to the limited availability of free sites for the H_2O adsorption, which is the O-donor in the formation reactions for CO_2 and AA. When the concentration was

increased over 0.2 M, the formation of AAL became dominant. Hitmi and coworkers found the same variation from AA to AAL with the increase of ethanol concentration [137]. As for the electrode potential, Hitmi et al. have studied its effect on the production yield via chromatographic techniques (HPLC, GC) in 0.025 M ethanol + 0.1 M $HClO_4$ [137]. At potentials lower than 0.8 V vs. RHE, AAL was detected to be the dominant product. At potentials above 0.8 V where the dissociation of water was initiated to form oxygenated species, AA became the major product.

In case of the most active binary catalyst (Pt-Sn) for EOR, there is a general agreement that the addition of Sn in binary catalysts could promote the overall activity for EOR, due to the bifunctional effect and electronic (ligand) effect. According to bifunctional mechanism, the neighboring Sn atoms (or Sn oxides) could activate H_2O at potentials (0.4-0.6 V vs. RHE) lower than Pt alone (0.8 V vs. RHE) to form OH_{ads} which facilitates the removal of CO species that are strongly adsorbed on Pt active sites. In addition, alloyed Sn could modify the electronic properties of the neighboring Pt atoms, leading to a weaker bonding strength between Pt and CO_{ads}. However, it was found that the addition of Sn to Pt catalyst inhibited the cleavage of C-C bond and only facilitated the partial oxidation of ethanol [37, 38, 47-49, 134, 135]. By means of *in situ* FTIR and DEMS, Wang et al. found that Pt/C catalyst exhibited higher selectivity to CO_2 through dissociative adsorption of ethanol within the potential range suitable for practical applications (<0.6 V vs. RHE) compared with Pt_3Sn/C and PtRu/C catalysts, whereas Pt/C was found to be rapidly poisoned by CO adlayer [134]. By combining chronoamperometry and chronopotentiometry techniques, Vigier et al. reported that PtSn catalysts showed higher selectivity towards AA formation compared to Pt at low potentials (E < 0.5 V vs. RHE), leading to the enhanced EOR performance on PtSn catalysts [47].

As for the FMOs modified Pt catalysts, mechanistic studies have also been performed by several groups. Jiang et al. investigated the catalytic behavior and reaction product distributions on Pt/SnO_x/C catalysts with various compositions and alloyed $PtSnO_x$/C catalysts [86]. $PtSnO_x$/C catalysts exhibited a slightly higher selectivity towards CO_2 in comparison with PtSn alloy, which was attributed the presence of both sufficiently large Pt ensembles for ethanol dehydrogenation and C–C bond splitting and of SnO_x for the formation of OH. While on PtSn alloy, alloying Sn induces a partial filling of the d band vacancies of Pt, which reduces the rate for the dehydrogenation and C-C bond breaking on Pt. However, even on the more active $PtSnO_x$/C catalysts, CO_2 formation contributed only 1–3% to the reaction current, and AAL and AA were detected to be dominant reaction products. Similarly, Antoniassi et al. compared the reactivity and selectivity for EOR of $PtSnO_2$/C, commercial Pt_3Sn/C (alloy) and Pt/C catalysts [51]. By using GC

analysis, AAL were found to be main product on Pt_3Sn/C (alloy) and Pt/C, while AA was dominantly produced on $PtSnO_2/C$ with the same Pt:Sn atomic ratio. In the DEFCs tests, $Pt_3(SnO_2)/C$ catalysts produced 70% more power density relative to Pt_3Sn/C (alloy), which was attributed to a higher oxidation extent of ethanol on $Pt_3(SnO_2)/C$ involving 4-electron exchange than that on Pt_3Sn/C (2-electron releasing). In addition, the authors found the AA/AAL ratio of $PtSnO_2/C$ catalysts was varied with the Pt:Sn atomic ratio, which was 15.8%, 92.3% and 53.8% for $Pt_9(SnO_2)/C$, $Pt_3(SnO_2)/C$ and $Pt(SnO_2)/C$, respectively. By means of *in situ* FTIR, Neto and coworkers reported that the addition of CeO_2 to PtSn catalysts caused the formation of CO_2 and AA as main products, in comparison to AAL and AA as major products on PtSn [73]. In general, FMOs are regarded as good sources of OH species at low potential being critical for the formation of AA and CO_2.

It has been recently claimed that rhodium (Rh) exhibits a great potential to break C-C bond at low temperatures during the EOR [141, 146-149]. De Souza et al. found the CO_2 yield of $Pt_{73}Rh_{27}$ and $Pt_{55}Rh_{45}$ catalysts is higher than that on the pure Pt and $Pt_{90}Rh_{10}$, and the $Pt_{73}Rh_{27}$ catalyst being the highest [150]. Whereas in CV test, the normalized current of investigated catalysts is in the following order: $Pt \approx Pt_{90}Rh_{10} > Pt_{55}Rh_{45} > Pt_{73}Rh_{27} > Rh$. This suggests that the addition of Rh is not enough to produce a good catalyst even though Rh could facilitate the C-C bond splitting, since Rh does not help in decreasing the barrier for CO oxidation. The author proposed that Ru could be a good candidate to add to the PtRh catalysts in order to facilitate the oxidation of CO_{ads} to CO_2. In the literature, SnO_2 is regarded to function as Ru does in Pt-Ru catalysts for EOR. In specific, SnO_2 could active water at low potentials to generate oxygen-containing species which helps the removal of CO_{ads} from Pt surface according to bifunctional mechanism. Kowal et al. prepared $PtRhSnO_2/C$ ternary catalysts by employing a cation-adsorption-reduction-galvanic-displacement synthetic method [141]. Both EOR reactivity and selectivity toward CO_2 production of the ternary catalysts were found to be higher than that of commercial Pt/C, $PtSnO_2/C$ and PtRh/C catalysts. It was found that the C-C bond was directly broken on the ternary catalysts without going through the step involving AAL, which was verified by the high yield of CO_2 and low yield of AAL and AA identified by using *in situ* infrared reflection-absorption spectroscopy (IRRAS). This is different from what has been observed on the surface of Pt and $PtSnO_2$ on which AA and AAL were dominantly generated. Furthermore, DFT calculations demonstrated that the addition of Rh was essential for the generation and adsorption of oxametallacyclic (CH_2CH_2O) which resulted in a cleavage of C-C bond with a reaction barrier of 1.29 eV. This reaction barrier was much lower compared with that required for C-C bond cleavage in AAL (3.82 eV). The authors proposed an optimum pathway for the cleavage of C-C

bond on PtRhSnO$_2$: *CH$_3$CH$_2$OH →*CH$_3$CHO + H*→ *CH$_2$CH$_2$O + 2H* → *CH$_2$ + *CH$_2$O + 2H*. *In situ* IRRAS experiments and DFT calculations revealed that each of constituents (Pt, Rh, and SnO$_2$) in the ternary PtRhSnO$_2$/C catalysts played an important but different role in complete oxidation of ethanol at room temperature. The synergy effect of three constituents yielded efficiency and high selectivity to CO$_2$ for EOR. Pt in the ternary catalysts presented a lower activity relative to pure Pt, due to the electron transfer from Rh to Pt. It weakly interacted with ethanol and other dissociated oxygenates and hydrocarbons, and was only active for dehydrogenation. The interaction between Pt and Rh leaded to more unoccupied d-states and made it strongly bound to CH$_2$CH$_2$O. Therefore, the role of Rh was to form and adsorb the key intermediate CH$_2$CH$_2$O which entailed the cleavage of C-C bond at a reasonable rate. As for SnO$_2$ in the ternary catalysts, its role was to form strong interaction with water which could not only supply abundant OH species to effectively oxidize the CO$_{ads}$ generated on Rh active sites but also could prevent the Pt and Rh sites from reacting with H$_2$O and make them available for the oxidation of ethanol. On the basis of this work, this group subsequently investigated the effect of atomic ratio of Pt:Rh:Sn on the catalytic performance of the PtRhSnO$_2$/C electrocatalysts. With the optimal composition (Pt:Rh:Sn = 3:1:4), the synergy effect of the three components led to the highest activity for ethanol oxidation characterized by the most negative onset potential, the highest oxidation current and the capability to break the C–C bond in ethanol at room temperature.

2.5 Problematics of the electro-catalyst for EOR

Over the past decades, many advances have been made in increasing the performance of DEFCs [5, 7, 131]. Nevertheless, there are still some critical problems concerning the electro-catalysts to address, in particular difficulties from the development of anode catalysts, which are summarized as follows:

(i)   The high cost of electro-catalysts. Platinum is scarce and expensive noble metal and the high loading of Pt in MEA is a critical obstacle limiting the commercialization of DEFCs [151];

(ii)   Sluggish reaction kinetics at the anode;

(iii)   The difficulties associated with ethanol complete oxidation to CO$_2$ and the C-C bond breaking [1, 4, 22]. The partial oxidation of ethanol not only lowers the efficiency of entire fuel cell but also deteriorate the durability of catalysts due to the numerous poisoning intermediates;

(iv)   The low durability of catalysts is another significant issue for the practical application of DEFCs. During long-term operation of DEFCs, electrochemical corrosion of support materials (e.g. Vulcan XC-72) leads to aggregation, dissolution, and isolation of catalysts, in turn resulting in the performance degradation of the entire DEFC [10].

2.5 The objectives of the thesis

Based on the problematics presented above and the relevant literature review on Pt-based catalysts for PEM-based DEFCs, our primary goal is to develop nanostructured free-standing Pt-FMOs electrode with higher catalytic activity and durability for DEFCs applications. The free-standing electrodes with two types of architectures are constructed by combining Pt and FMO in different fashions on the substrate.

Towards the main goal, we followed the subsequent sub-objectives:

1. The catalyst layer of two architectures constructed by FMO and Pt are fabricated by using the PLD-based technique, namely layer-by-layer architecture and co-deposited architecture. The first architecture is fabricated by depositing Pt layer onto a layer of FMO. The second architecture is the co-deposited structure of Pt and FMO obtained by ablating both targets of Pt and FMO simultaneously. Different FMOs including CeO_2, SnO_2, MnO_2, and TiO_2 have been integrated into these two types of architecture.

2. With regard to each architecture, the optimized growth condition for each kind of FMOs is systematically studied by varying the gas background pressure in PLD deposition chamber.

3. The microstructures, physical properties and electrochemical performance towards EOR of the catalyst layer developed in sub-objective 1 and 2 are systematically characterized. In addition, the correlation of the structure and electrochemical performance for each kind of catalyst are studied and discussed in order to guide us develop a superior performed catalyst.

2.6 Organization of the thesis

This doctoral thesis is composed of 5 parts and organized as follows:

Chapter 1 introduces the background and motivations of this work.

Chapter 2 starts with the literature review of the study in Pt-based catalysts for PEM-based DEFCs over the past decades. Subsequently, the remaining key problems in the development of Pt-based catalysts are pointed out. At the end, the objectives and organization of the thesis are introduced.

Chapter 3 is devoted to the methodology of this thesis, including the introduction of the materials and the synthesis methods have been used, details of synthesis processes of various FMO-based catalysts, and then the detailed description of various physicochemical and electrochemical characterization techniques that have been employed.

Chapter 4 includes all the 4 articles written throughout the thesis. A summary precedes each publication in order to highlight the motivations of that work.

Chapter 5 presents the main conclusions obtained from this work and finally proposes the prospects of this work.

REFERENCES

[1] E. Antolini. J. Power Sources, 170 (2007) 1-12.

[2] Y. Nie, L. Li, Z. Wei. Chem. Soc. Rev., 44 (2015) 2168-2201.

[3] A. Chen, P. Holt-Hindle. Chem. Rev., 110 (2010) 3767-3804.

[4] S. Song, P. Tsiakaras. Appl. Catal. B, 63 (2006) 187-193.

[5] M.Z.F. Kamarudin, S.K. Kamarudin, M.S. Masdar, W.R.W. Daud. Int. J. Hydrogen Energy, 38 (2013) 9438-9453.

[6] J. Friedl, U. Stimming. Electrochim. Acta, 101 (2013) 41-58.

[7] A. Brouzgou, A. Podias, P. Tsiakaras. J. Appl. Electrochem., 43 (2013) 119-136.

[8] A. Brouzgou, S.Q. Song, P. Tsiakaras. Appl. Catal. B, 127 (2012) 371-388.

[9] Y. Shao, J. Liu, Y. Wang, Y. Lin. J. Mater. Chem., 19 (2009) 46-59.

[10] Z. Zhang, J. Liu, J. Gu, L. Su, L. Cheng. Energy & Environmental Science, 7 (2014) 2535-2558.

[11] Y.-J. Wang, D.P. Wilkinson, J. Zhang. Chem. Rev., 111 (2011) 7625-7651.

[12] M.J. Prieto, G. Tremiliosi-Filho. Electrochem. Commun., 13 (2011) 527-529.

[13] F. Colmati, G. Tremiliosi-Filho, E.R. Gonzalez, A. Berna, E. Herrero, J.M. Feliu. Faraday Discuss., 140 (2009) 379-397.

[14] C. Lamy, A. Lima, V. LeRhun, F. Delime, C. Coutanceau, J. Léger. J. Power Sources, 105 (2002) 283-296.

[15] G.A. Camara, R.B. de Lima, T. Iwasita. Electrochem. Commun., 6 (2004) 812-815.

[16] C. Lamy, A. Lima, V. LeRhun, F. Delime, C. Coutanceau, J.M. Léger. J. Power Sources, 105 (2002) 283-296.

[17] N. Fujiwara, K.A. Friedrich, U. Stimming. J. Electroanal. Chem., 472 (1999) 120-125.

[18] F.H.B. Lima, E.R. Gonzalez. Electrochim. Acta, 53 (2008) 2963-2971.

[19] C. Lamy, E.M. Belgsir, J.M. Léger. J. Appl. Electrochem., 31 (2001) 799-809.

[20] L. Jiang, G. Sun, S. Sun, J. Liu, S. Tang, H. Li, B. Zhou, Q. Xin. Electrochim. Acta, 50 (2005) 5384-5389.

[21] J.M. Léger, S. Rousseau, C. Coutanceau, F. Hahn, C. Lamy. Electrochim. Acta, 50 (2005) 5118-5125.

[22] W. Zhou, Z. Zhou, S. Song, W. Li, G. Sun, P. Tsiakaras, Q. Xin. Appl. Catal. B, 46 (2003) 273-285.

[23] A. Tabet-Aoul, M. Mohamedi. J. Mater. Chem., 22 (2012) 2491-2497.

[24] P. Bommersbach, M. Chaker, M. Mohamedi, D. Guay. J. Phys. Chem. C, 112 (2008)

14672-14681.

[25] J. De Souza, S. Queiroz, K. Bergamaski, E. Gonzalez, F. Nart. J. Phys. Chem. B, 106 (2002) 9825-9830.

[26] W. Zhou, M. Li, L. Zhang, S.H. Chan. Electrochim. Acta, 123 (2014) 233-239.

[27] W. Hong, J. Wang, E. Wang. ACS Applied Materials & Interfaces, 6 (2014) 9481-9487.

[28] A.O. Neto, M. Giz, J. Perez, E. Ticianelli, E. Gonzalez. J. Electrochem. Soc., 149 (2002) A272-A279.

[29] M. Watanabe, S. Motoo. Journal of Electroanalytical Chemistry and Interfacial Electrochemistry, 60 (1975) 275-283.

[30] M. Watanabe, S. Motoo. Journal of Electroanalytical Chemistry and Interfacial Electrochemistry, 60 (1975) 267-273.

[31] N.M. Marković, H.A. Gasteiger, P.N. Ross, X. Jiang, I. Villegas, M.J. Weaver. Electrochim. Acta, 40 (1995) 91-98.

[32] S.L. Gojković, T.R. Vidaković, D.R. Đurović. Electrochim. Acta, 48 (2003) 3607-3614.

[33] J.K. Norskov, T. Bligaard, J. Rossmeisl, C.H. Christensen. Nat Chem, 1 (2009) 37-46.

[34] J.K. Nørskov, F. Abild-Pedersen, F. Studt, T. Bligaard. Proceedings of the National Academy of Sciences, 108 (2011) 937-943.

[35] U.B. Demirci. J. Power Sources, 173 (2007) 11-18.

[36] C. Lamy, S. Rousseau, E. Belgsir, C. Coutanceau, J. Léger. Electrochim. Acta, 49 (2004) 3901-3908.

[37] S. Song, W. Zhou, Z. Zhou, L. Jiang, G. Sun, Q. Xin, V. Leontidis, S. Kontou, P. Tsiakaras. Int. J. Hydrogen Energy, 30 (2005) 995-1001.

[38] C. Lamy, S. Rousseau, E.M. Belgsir, C. Coutanceau, J.M. Léger. Electrochim. Acta, 49 (2004) 3901-3908.

[39] F. Colmati, E. Antolini, E.R. Gonzalez. J. Power Sources, 157 (2006) 98-103.

[40] B. Coq, F. Figueras. Coord. Chem. Rev., 178-180 (1998) 1753-1783.

[41] S. Wasmus, A. Küver. J. Electroanal. Chem., 461 (1999) 14-31.

[42] E. Antolini, J.R.C. Salgado, E.R. Gonzalez. Appl. Catal. B, 63 (2006) 137-149.

[43] W. Zhou, S. Song, W. Li, Z. Zhou, G. Sun, Q. Xin, S. Douvartzides, P. Tsiakaras. J. Power Sources, 140 (2005) 50-58.

[44] J.H. Kim, S.M. Choi, S.H. Nam, M.H. Seo, S.H. Choi, W.B. Kim. Appl. Catal. B, 82 (2008) 89-102.

[45] V. Spinace Estevam, M. Linardi, A.O. Neto. Electrochem. Commun., 7 (2005) 365-369.

[46] J. Asgardi, J.C. Calderón, F. Alcaide, A. Querejeta, L. Calvillo, M.J. Lázaro, G. García, E.

Pastor. Appl. Catal. B, 168–169 (2015) 33-41.

[47] F. Vigier, C. Coutanceau, A. Perrard, E. Belgsir, C. Lamy. J. Appl. Electrochem., 34 (2004) 439-446.

[48] L. Colmenares, H. Wang, Z. Jusys, L. Jiang, S. Yan, G.Q. Sun, R.J. Behm. Electrochim. Acta, 52 (2006) 221-233.

[49] M. Zhu, G. Sun, Q. Xin. Electrochim. Acta, 54 (2009) 1511-1518.

[50] D.R.M. Godoi, J. Perez, H.M. Villullas. J. Power Sources, 195 (2010) 3394-3401.

[51] R.M. Antoniassi, A. Oliveira Neto, M. Linardi, E.V. Spinacé. Int. J. Hydrogen Energy, 38 (2013) 12069-12077.

[52] F. Colmati, E. Antolini, E.R. Gonalez. J. Electrochem. Soc., 154 (2007) B39-B47.

[53] G.N. Vayssilov, Y. Lykhach, A. Migani, T. Staudt, G.P. Petrova, N. Tsud, T. Skála, A. Bruix, F. Illas, K.C. Prince, V.r. Matolı´n, K.M. Neyman, J. Libuda. Nat. Mater., 10 (2011) 310-315.

[54] S. Basri, S.K. Kamarudin, W.R.W. Daud, Z. Yaakub. Int. J. Hydrogen Energy, 35 (2010) 7957-7970.

[55] C. Sun, H. Li, L. Chen. Energy & Environmental Science, 5 (2012) 8475-8505.

[56] Q. Fu, H. Saltsburg, M. Flytzani-Stephanopoulos. Science, 301 (2003) 935-938.

[57] W. Huang, Y. Gao. Catalysis Science & Technology, 4 (2014) 3772-3784.

[58] T. Montini, M. Melchionna, M. Monai, P. Fornasiero. Chem. Rev., 116 (2016) 5987-6041.

[59] J. Paier, C. Penschke, J. Sauer. Chem. Rev., 113 (2013) 3949-3985.

[60] L. Fan, C. Wang, M. Chen, B. Zhu. J. Power Sources, 234 (2013) 154-174.

[61] W.C. Chueh, Y. Hao, W. Jung, S.M. Haile. Nat. Mater., 11 (2012) 155-161.

[62] P. Furler, J.R. Scheffe, A. Steinfeld. Energy & Environmental Science, 5 (2012) 6098-6103.

[63] J.R. Scheffe, M. Welte, A. Steinfeld. Ind. Eng. Chem. Res., 53 (2014) 2175-2182.

[64] Y. Xu, X. Zhou, O.T. Sorensen. Sensors and Actuators B: Chemical, 65 (2000) 2-4.

[65] P. Jasinski, T. Suzuki, H.U. Anderson. Sensors and Actuators B: Chemical, 95 (2003) 73-77.

[66] X. Feng, D.C. Sayle, Z.L. Wang, M.S. Paras, B. Santora, A.C. Sutorik, T.X. Sayle, Y. Yang, Y. Ding, X. Wang. Science, 312 (2006) 1504-1508.

[67] Q. He, S. Mukerjee, R. Zeis, S. Parres-Esclapez, M.J. Illán-Gómez, A. Bueno-López. Appl. Catal. A, 381 (2010) 54-65.

[68] Z. Sun, X. Wang, Z. Liu, H. Zhang, P. Yu, L. Mao. Langmuir, 26 (2010) 12383-12389.

[69] D.R. Ou, T. Mori, H. Togasaki, M. Takahashi, F. Ye, J. Drennan. Langmuir, 27 (2011) 3859-3866.

[70] D.R. Ou, T. Mori, K. Fugane, H. Togasaki, F. Ye, J. Drennan. J. Phys. Chem. C, 115 (2011)

19239-19245.

[71] L. Yu, J. Xi. Int. J. Hydrogen Energy, 37 (2012) 15938-15947.

[72] A. Neto, L. Farias, R. Dias, M. Brandalise, M. Linardi, E. Spinacé. Electrochem. Commun., 10 (2008) 1315-1317.

[73] A. Neto, M. Linardi, D. Anjos, G. Tremiliosi-Filho, E. Spinacé. J. Appl. Electrochem., 39 (2009) 1153-1156.

[74] M. Batzill, U. Diebold. Prog. Surf. Sci., 79 (2005) 47-154.

[75] B.-Y. Kim, J.S. Cho, J.-W. Yoon, C.W. Na, C.-S. Lee, J.H. Ahn, Y.C. Kang, J.-H. Lee. Sensors and Actuators B: Chemical, 234 (2016) 353-360.

[76] L. Wang, Y. Wang, K. Yu, S. Wang, Y. Zhang, C. Wei. Sensors and Actuators B: Chemical, 232 (2016) 91-101.

[77] W. Li, C. Shen, G. Wu, Y. Ma, Z. Gao, X. Xia, G. Du. J. Phys. Chem. C, 115 (2011) 21258-21263.

[78] J. Lin, Z. Peng, C. Xiang, G. Ruan, Z. Yan, D. Natelson, J.M. Tour. ACS Nano, 7 (2013) 6001-6006.

[79] S. Sladkevich, J. Gun, P.V. Prikhodchenko, V. Gutkin, A.A. Mikhaylov, V.M. Novotortsev, J.X. Zhu, D. Yang, H.H. Hng, Y.Y. Tay, Z. Tsakadze, O. Lev. Nanotechnology, 23 (2012) 485601.

[80] C. Du, M. Chen, X. Cao, G. Yin, P. Shi. Electrochem. Commun., 11 (2009) 496-498.

[81] S.C. Zignani, V. Baglio, D. Sebastián, S. Siracusano, A.S. Aricò. Electrochim. Acta, 191 (2016) 183-191.

[82] S. Sago, A.B. Suryamas, G.M. Anilkumar, T. Ogi, K. Okuyama. Mater. Lett., 105 (2013) 202-205.

[83] E. Ciapina, S. Santos, E. Gonzalez. J. Solid State Electrochem., 17 (2013) 1831-1842.

[84] S.H. Ryan, H. Drew, C. Zhongwei. Nanotechnology, 21 (2010) 165705.

[85] H.L. Pang, J.P. Lu, J.H. Chen, C.T. Huang, B. Liu, X.H. Zhang. Electrochim. Acta, 54 (2009) 2610-2615.

[86] L. Jiang, L. Colmenares, Z. Jusys, G.Q. Sun, R.J. Behm. Electrochim. Acta, 53 (2007) 377-389.

[87] J. Mann, N. Yao, A.B. Bocarsly. Langmuir, 22 (2006) 10432-10436.

[88] P.J.D. Lindan. Chem. Phys. Lett., 328 (2000) 325-329.

[89] W.-P. Zhou, S. Axnanda, M.G. White, R.R. Adzic, J. Hrbek. J. Phys. Chem. C, 115 (2011) 16467-16473.

[90] H. Zhang, C. Hu, X. He, L. Hong, G. Du, Y. Zhang. J. Power Sources, 196 (2011) 4499-

4505.

[91] L. Jiang, G. Sun, Z. Zhou, S. Sun, Q. Wang, S. Yan, H. Li, J. Tian, J. Guo, B. Zhou, Q. Xin. J. Phys. Chem. B, 109 (2005) 8774-8778.

[92] D. Reyes-Coronado, G. Rodríguez-Gattorno, M.E. Espinosa-Pesqueira, C. Cab, R.d. Coss, G. Oskam. Nanotechnology, 19 (2008) 145605.

[93] U. Diebold. Surf. Sci. Rep., 48 (2003) 53-229.

[94] D.A.H. Hanaor, C.C. Sorrell. J. Mater. Sci., 46 (2011) 855-874.

[95] L. Pauling, J.H. Sturdivant. Zeitschrift für Kristallographie-Crystalline Materials, 68 (1928) 239-256.

[96] D.O. Scanlon, C.W. Dunnill, J. Buckeridge, S.A. Shevlin, A.J. Logsdail, S.M. Woodley, C.R.A. Catlow, M.J. Powell, R.G. Palgrave, I.P. Parkin, G.W. Watson, T.W. Keal, P. Sherwood, A. Walsh, A.A. Sokol. Nat. Mater., 12 (2013) 798-801.

[97] P. Xiao, X. Guo, D.-J. Guo, H.-Q. Song, J. Sun, Z. Lv, Y. Liu, X.-P. Qiu, W.-T. Zhu, L.-Q. Chen, U. Stimming. Electrochim. Acta, 58 (2011) 541-550.

[98] T. Berger, D. Monllor‐Satoca, M. Jankulovska, T. Lana‐Villarreal, R. Gomez. ChemPhysChem, 13 (2012) 2824-2875.

[99] M.E. Kurtoglu, T. Longenbach, Y. Gogotsi. International Journal of Applied Glass Science, 2 (2011) 108-116.

[100] K.-W. Park, S.-B. Han, J.-M. Lee. Electrochem. Commun., 9 (2007) 1578-1581.

[101] M.G. Hosseini, M.M. Momeni. Electrochim. Acta, 70 (2012) 1-9.

[102] X. Liu, J. Chen, G. Liu, L. Zhang, H. Zhang, B. Yi. J. Power Sources, 195 (2010) 4098-4103.

[103] S. Siracusano, A. Stassi, E. Modica, V. Baglio, A.S. Aricò. Int. J. Hydrogen Energy, 38 (2013) 11600-11608.

[104] J. Shim, C.-R. Lee, H.-K. Lee, J.-S. Lee, E.J. Cairns. J. Power Sources, 102 (2001) 172-177.

[105] Y. Fu, Z. Wei, S. Chen, L. Li, Y. Feng, Y. Wang, X. Ma, M. Liao, P. Shen, S. Jiang. J. Power Sources, 189 (2009) 982-987.

[106] L. Yu, J. Xi. Electrochim. Acta, 67 (2012) 166-171.

[107] K. Drew, G. Girishkumar, K. Vinodgopal, P.V. Kamat. J. Phys. Chem. B, 109 (2005) 11851-11857.

[108] H. Hua, C. Hu, Z. Zhao, H. Liu, X. Xie, Y. Xi. Electrochim. Acta, 105 (2013) 130-136.

[109] B. Hasa, E. Kalamaras, E.I. Papaioannou, L. Sygellou, A. Katsaounis. Int. J. Hydrogen Energy, 38 (2013) 15395-15404.

[110] M. Toupin, T. Brousse, D. Bélanger. Chem. Mater., 16 (2004) 3184-3190.

[111] C. Cheng, Y. Huang, N. Wang, T. Jiang, S. Hu, B. Zheng, H. Yuan, D. Xiao. ACS Appl Mater Interfaces, 7 (2015) 9526-9533.

[112] P. Simon, Y. Gogotsi. Nat. Mater., 7 (2008) 845-854.

[113] G. Yu, L. Hu, M. Vosgueritchian, H. Wang, X. Xie, J.R. McDonough, X. Cui, Y. Cui, Z. Bao. Nano Lett., 11 (2011) 2905-2911.

[114] A.L.M. Reddy, M.M. Shaijumon, S.R. Gowda, P.M. Ajayan. Nano Lett., 9 (2009) 1002-1006.

[115] D. Liu, B.B. Garcia, Q. Zhang, Q. Guo, Y. Zhang, S. Sepehri, G. Cao. Adv. Funct. Mater., 19 (2009) 1015-1023.

[116] A. Débart, A.J. Paterson, J. Bao, P.G. Bruce. Angew. Chem., 120 (2008) 4597-4600.

[117] C. Zhou, H. Wang, F. Peng, J. Liang, H. Yu, J. Yang. Langmuir, 25 (2009) 7711-7717.

[118] H. Huang, Q. Chen, M. He, X. Sun, X. Wang. J. Power Sources, 239 (2013) 189-195.

[119] H. Huang, H. Chen, D. Sun, X. Wang. J. Power Sources, 204 (2012) 46-52.

[120] S.K. Meher, G.R. Rao. J. Phys. Chem. C, 117 (2013) 4888-4900.

[121] G.-Y. Zhao, H.-L. Li. Appl. Surf. Sci., 254 (2008) 3232-3235.

[122] C. Zhou, F. Peng, H. Wang, H. Yu, C. Peng, J. Yang. Electrochem. Commun., 12 (2010) 1210-1213.

[123] M. El-Deab, L. Kibler, D. Kolb. Electrochem. Commun., 11 (2009) 776-778.

[124] C. Sun, Y. Zhang, S. Song, D. Xue. J. Appl. Crystallogr., 46 (2013) 1128-1135.

[125] K. Chen, C. Sun, D. Xue. Phys. Chem. Chem. Phys., 17 (2015) 732-750.

[126] H. Chen, Y. Wang, Y.-K. Lv. RSC Advances, 6 (2016) 54032-54040.

[127] S. Liang, F. Teng, G. Bulgan, R. Zong, Y. Zhu. J. Phys. Chem. C, 112 (2008) 5307-5315.

[128] M.-W. Xu, G.-Y. Gao, W.-J. Zhou, K.-F. Zhang, H.-L. Li. J. Power Sources, 175 (2008) 217-220.

[129] J. Cai, Y. Huang, B. Huang, S. Zheng, Y. Guo. Int. J. Hydrogen Energy, 39 (2014) 798-807.

[130] Y. Wang, M. Mohamedi. ChemElectroChem, 3 (2016) 1-8.

[131] Y. Wang, S. Zou, W.-B. Cai. Catalysts, 5 (2015) 1507-1534.

[132] I. Kim, O.H. Han, S. Chae, Y. Paik, S.H. Kwon, K.S. Lee, Y.E. Sung, H. Kim. Angewandte Chemie International Edition, 50 (2011) 2270-2274.

[133] T. Iwasita, E. Pastor. Electrochim. Acta, 39 (1994) 531-537.

[134] Q. Wang, G.Q. Sun, L.H. Jiang, Q. Xin, S.G. Sun, Y.X. Jiang, S.P. Chen, Z. Jusys, R.J. Behm. Phys. Chem. Chem. Phys., 9 (2007) 2686-2696.

[135] H. Wang, Z. Jusys, R.J. Behm. J. Power Sources, 154 (2006) 351-359.

[136] S. Rousseau, C. Coutanceau, C. Lamy, J.-M. L´eger. J. Power Sources, 158 (2006) 18-24.

[137] H. Hitmi, E.M. Belgsir, J.M. Léger, C. Lamy, R.O. Lezna. Electrochim. Acta, 39 (1994) 407-415.

[138] L. Huang, E.G. Sorte, S.G. Sun, Y.Y.J. Tong. Chem. Commun., 51 (2015) 8086-8088.

[139] S.C.S. Lai, S.E.F. Kleyn, V. Rosca, M.T.M. Koper. J. Phys. Chem. C, 112 (2008) 19080-19087.

[140] A. Ferre-Vilaplana, C. Buso-Rogero, J.M. Feliu, E. Herrero. J. Phys. Chem. C, 120 (2016) 11590-11597.

[141] A. Kowal, M. Li, M. Shao, K. Sasaki, M.B. Vukmirovic, J. Zhang, N.S. Marinkovic, P. Liu, A.I. Frenkel, R.R. Adzic. Nat. Mater., 8 (2009) 325-330.

[142] H.A. Asiri, A.B. Anderson. J. Electrochem. Soc., 162 (2015) F115-F122.

[143] Y. Choi, P. Liu. Catal. Today, 165 (2011) 64-70.

[144] G.A. Camara, T. Iwasita. J. Electroanal. Chem., 578 (2005) 315-321.

[145] H. Wang, Z. Jusys, R.J. Behm. J. Phys. Chem. B, 108 (2004) 19413-19424.

[146] W. Zhu, J. Ke, S.-B. Wang, J. Ren, H.-H. Wang, Z.-Y. Zhou, R. Si, Y.-W. Zhang, C.-H. Yan. ACS Catal., 5 (2015) 1995-2008.

[147] E. Méndez, J.L. Rodríguez, M.C. Arévalo, E. Pastor. Langmuir, 18 (2002) 763-772.

[148] M. Li, A. Kowal, K. Sasaki, N. Marinkovic, D. Su, E. Korach, P. Liu, R.R. Adzic. Electrochim. Acta, 55 (2010) 4331-4338.

[149] D.A. Cantane, W.F. Ambrosio, M. Chatenet, F.H.B. Lima. J. Electroanal. Chem., 681 (2012) 56-65.

[150] J.P.I. de Souza, S.L. Queiroz, K. Bergamaski, E.R. Gonzalez, F.C. Nart. J. Phys. Chem. B, 106 (2002) 9825-9830.

[151] X. Teng. Materials and Processes for Energy: Communicating Current Research and Technological Developments, Formatex Research Center, (2013) 473-484.

CHAPTER 3 METHODOLOGY

In this chapter, the methodology of my work is presented, showing how the project is accomplished in a rational order. First, I elaborate on the key steps of preparation of binderless electrodes comprising Pt and different functional metal oxides (FMOs: CeO_2, SnO_2, TiO_2, and MnO_2), the synthesis methods employed for the catalyst support (CNTs) and nanostructured Pt-FMO catalysts and the main parameters affecting materials synthesis, and finally the optimal synthesis conditions for those materials are addressed. Second, our work is dedicated to the characterization of as-synthesized materials before any application. The characterization of physicochemical properties is initially conducted, allowing the optimization of the different materials in order to achieve the planned nanostructures with higher efficiency and minimum cost. Finally, the third part of this chapter is devoted to electrochemical characterizations of the electrodes. In this part, we have studied the electrochemical behavior of the electrodes in sulfuric acid, followed by the evaluation of their electro-catalytic and durability performances towards both EOR and ORR, accompanied with post-mortem analyses of the surface morphology. Furthermore, the electrochemical properties of the various electrodes are correlated with structural properties previously established in the second part.

3.1 Material synthesis

Three dimensional (3D) binderless electrodes with two types of architectures are constructed by combining Pt and FMO in different fashions on the substrate. These electrodes are prepared by a combination of chemical vapor deposition and pulsed laser deposition techniques.

The 3D binderless electrodes basically comprise 3 components:

Substrate: untreated carbon paper (CP, Toray) is chosen as the substrate/current collector of the catalyst layer, which is made of a dense array of carbon microfibers with a diameter of 7-10 μm (as shown in Figure 3.1). The CP is the type of gas diffusion layer (GDL) often integrated as part of MEA in fuel cell systems, owing to its porous nature, high electrical conductivity, and good corrosion-resistance.

Catalyst Support: multi-walled Carbon nanotubes (CNTs) are employed as catalyst supports owing to their high electronic conductivity, high specific-surface-area and their resistance to oxidation/corrosion under the harsh fuel cell operating conditions. CNTs (shown in Figure 3.1)

in this doctoral project are synthesized by chemical vapor deposition and the detailed preparation conditions will be presented in the chemical vapor deposition section.
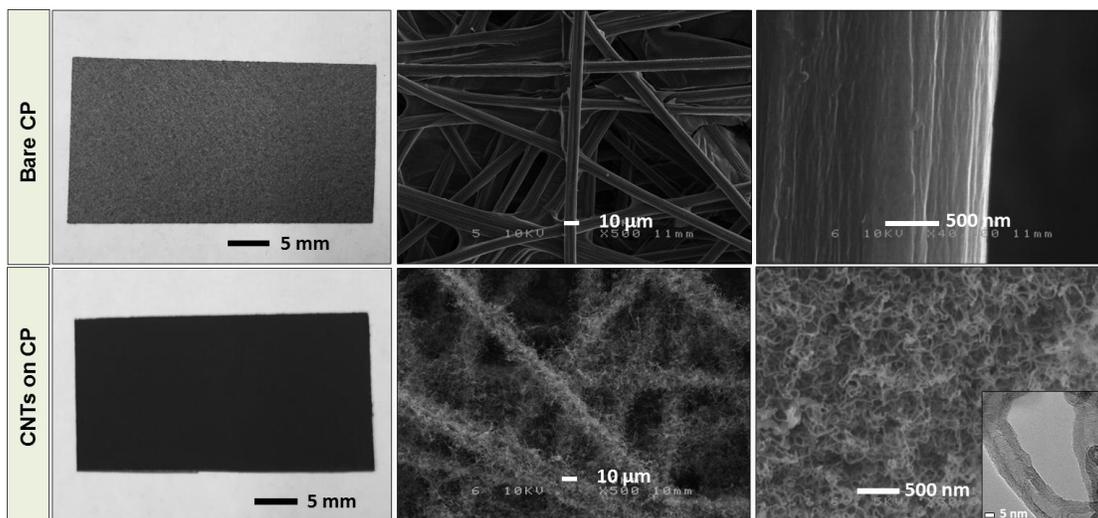
Figure 3.1 The photos and SEM images with low and high magnifications of bare CP (upper row) and CNTs grown on CP (bottom row).

Catalysts: two architectures were considered and are presented in Figure 3.2. The first architecture is called layer onto layer structure which is made of scaled nanostructured films of FMO and Pt. Pt layer is deposited onto a layer of metal oxide and both layers are obtained by single beam pulsed laser deposition (PLD). The second architecture is the co-deposited structure of Pt and FMO obtained by ablating both targets of Pt and FMO simultaneously via the cross-beam PLD setup.
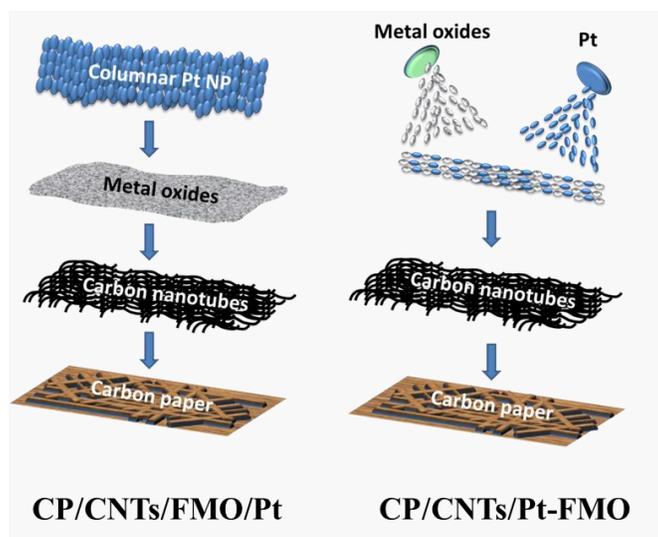
Figure 3.2 The representation of two catalyst layer architectures containing Pt and FMO: (left) Layer onto layer structure, (right) Co-deposition structure.

46

3.1.1 Chemical vapor deposition

Carbon nanotubes (CNTs) are seamless tubular, honeycomb arrangement of carbon atoms, exhibiting extraordinary mechanical and electronic properties and superior thermal conductivity. Sumio Iijima's paper in nature reported for the first time the growth of MWCNTs by arc discharge evaporation method, followed by detailed analysis of microstructure (wall thickness, diameter, and length) and crystal structure by high-resolution electron microscope [1]. Since then, a global interest in CNTs has been sparked [2-5].
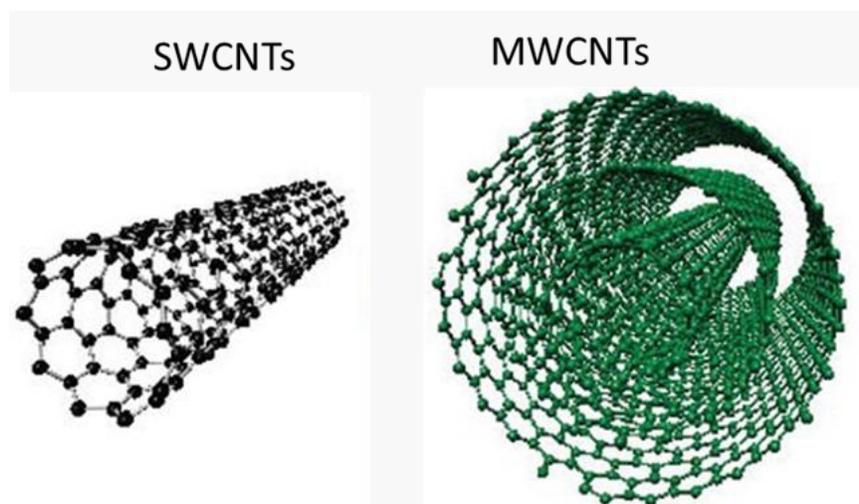
Figure 3.3 Schematic diagrams of SWCNTs and MWCNTs [6].

The CNTs can be broadly classified into two categories: single-walled carbon nanotubes (SWCNTs) and MWCNTs, are schematically presented in Figure 3.3 [5-7]. In our study, we are only concerned with the synthesis of MWCNTs which is used as the support of catalysts for DEFCs due to their superior electronic conductivity and high specific surface area [8]. An individual MWCNT contains a set of hollow tubes formed by concentric graphene layers with a constant interlayer separation of 0.34 nm. MWCNTs have been proved to be a promising supporting material for noble catalysts towards fuel cell reactions, due to their unique structures and excellent electrical properties. M. Carmo and E.R. Gonzalez et al. showed that MWCNTs supported PtRu catalysts yielded power densities higher than that of the Vulcan XC-72 carbon-supported catalysts in the direct methanol fuel cell performance test [9]. Prabhuram et al. have reported an enhancement of 35-39% in power density by MWCNT-supported PtRu catalyst compared with Vulcan XC-72 carbon-supported catalyst, despites that both catalysts contained similar PtRu loading, particle size, dispersion and electrochemical surface area [10]. In addition,

it was found that MWCNTs/Pt displayed higher durability than that of carbon black-supported Pt catalysts under the accelerate durability test [11].

3.1.1.1 CNT synthesis via CVD

CVD is a well-established method for CNTs synthesis by thermal decomposition of hydrocarbons (methane, ethane, acetylene, and ethylene etc.) in the presence of metal catalysts (such as nickel, iron, cobalt or a combination of those such as cobalt/molybdenum or cobalt/iron) [5, 12, 13]. Compared with other available techniques such as arc-discharge, laser ablation, CVD is a simpler and more economic method based on easy scale-up and limited equipment required [14]. In addition, CVD enables to grow CNTs in various forms such as powder, thin/thick films on varieties of substrates, straight or coiled, aligned or entangled, by decomposing hydrocarbon precursors in the presence of catalysts.
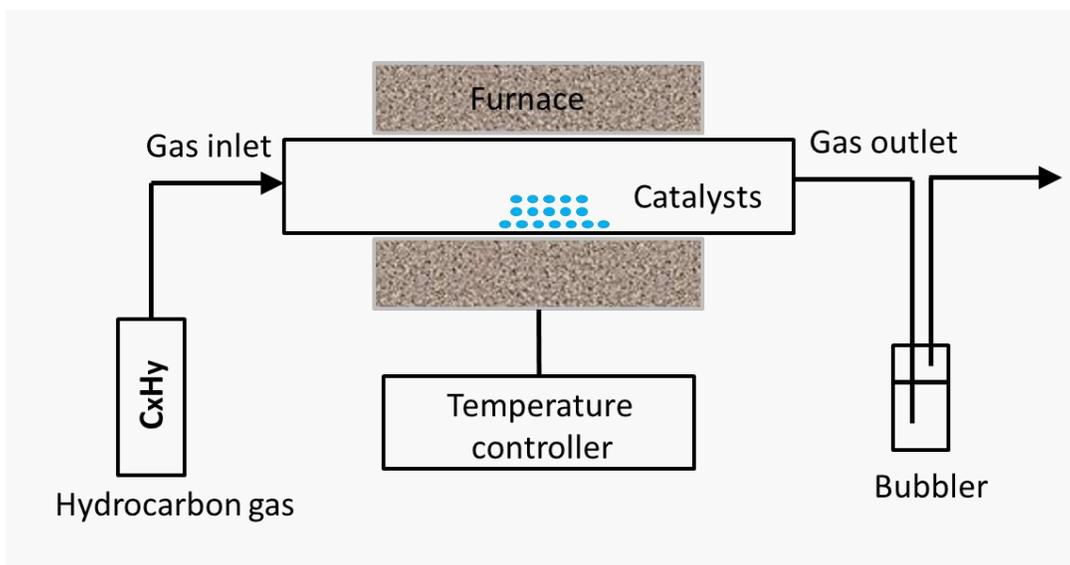
Figure 3.4 Schematic diagram of the CVD reactor for CNTs growth [13].

The experimental set-up for CNTs growth by CVD is shown schematically in Figure 3.4. The process involves passing a hydrocarbon vapor through a tubular reaction in which the hydrocarbon gets decomposed by catalyst material at high temperature. The hydrocarbon and catalyst can be any form: solid, liquid or gas, which can be placed inside the reactor or be fed from outside. The floating catalyst method is often used where metal nanoparticles are liberated by the pyrolysis of the catalyst vapor at a specific temperature. Alternatively, substrates coated with catalysts can be directly placed in the reaction tube and decomposition reaction is initiated when a suitable temperature is reached for CNTs growth. In term of hydrocarbon, if a liquid state (e.g. ethanol, benzene) is used the liquid is heated in a flask and the vapor is carried by purged

inert gases (e.g. Ar) to the reaction zone. In the case of a solid hydrocarbon (e.g. ferrocene, naphthalene, camphor, etc.) which is placed in the low-temperature zone of the reaction tube and the volatile materials readily turn from solid to vapor and subsequently get to the high-temperature reaction zone. Gaseous hydrocarbons (e.g. methane, acetylene, and ethylene etc.) are most often and easiest used in CVD process which can be directly introduced into the reaction zone by carrying gases [13].

3.1.1.2 The mechanism of growth of carbon nanotubes

In the literature, different theories have been proposed to explain the growth of CNTs, but they are often contradictory and none of them were universally accepted [13, 15-19]. The divergence of the proposed mechanisms is attributed to the variety of factors (such as the catalyst, the carbon precursor, the reaction temperature, vapor pressure, and so on) determining the growth regime. Whatever the debate, those ideas lead to two complementary theories for the growth of CNTs: Tip-Growth model and Base-Growth model [18], illustrated in Figure 3.5 [13]. The determining factor of these two theories is the relative adhesion between the catalyst and the substrate [20].
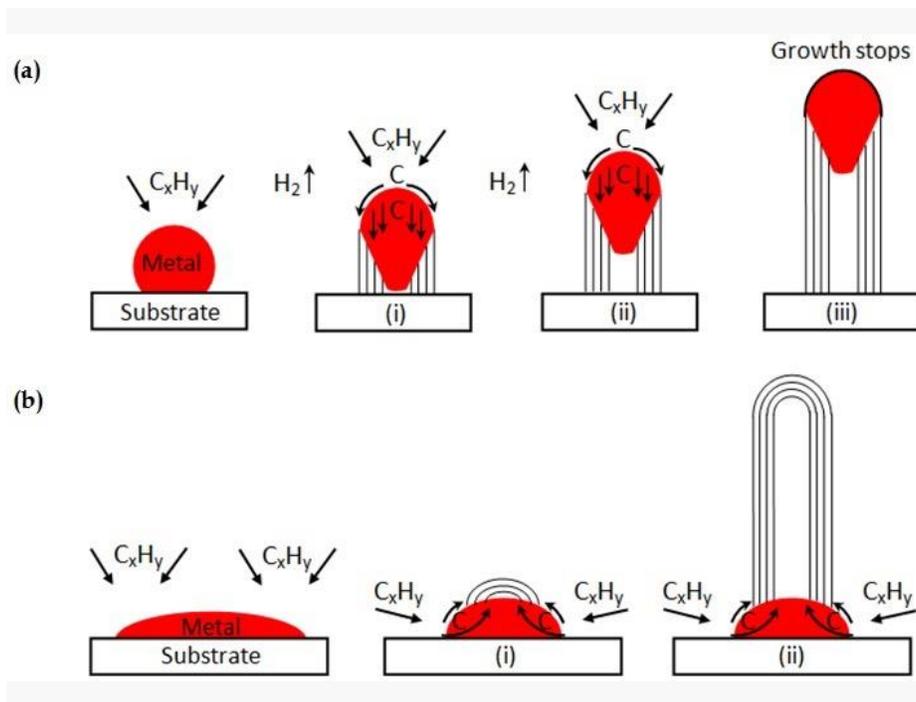
Figure 3.5 CNTs growth mechanism: (a) tip-growth model (b) base-growth model [13].

When the substrate-catalyst adhesion is weak and an acute contact angle exists between metal and substrate, the hydrocarbon first adsorbs on the surface of the catalyst particle

49

whereupon its dissociation occurs, the diffusion of carbon goes down through the metal, and CNTs precipitate out across the metal bottom, pushing the entire catalyst particle off the substrate. The growth of CNTs continues as long as the top surface of catalyst is exposed to hydrocarbon. As soon as the top surface is fully covered by excess carbon, the growth of CNTs stops due to the cease of the catalytic activity of the catalysts. This is known as "tip-growth model" (as shown in Figure 3.5 (a)).

When the substrate-catalyst adhesion is relatively strong and the contact angle between metal and substrate is obtuse. The initial stage for hydrocarbon decomposition, carbon diffusion and participation on the top surface of catalyst resembles that involved in tip-growth process. While the CNT precipitation fails to push the catalyst particle up. The carbon precipitation is compelled to emerge on the metal's apex and crystallizes out as a hemispherical dome, then extends up in the form of a seamless graphic cylinder. The deposition of hydrocarbon occurs on the lower peripheral surface of the catalyst, and as dissolved carbon diffuses upward, contrary to the diffusing down process in tip-growth model. During the formation of nanotubes, the original catalyst particles remain fixed to the substrate, so this is called "base-growth model" (as shown in Figure 3.5 (b)).

3.1.1.3 The experimental conditions for CNTs growth

Through the thesis, the substrate used for CNTs support is untreated carbon papers (CP, Toray). For CNTs growth, a 5-nm-thick Ni layer was firstly deposited by PLD onto one side of the CP substrate. This Ni layer was deposited at room temperature by ablating a polycrystalline Ni target (99.95%, Kurt J. Lesker Co.) under vacuum by means of a pulsed KrF excimer laser (wavelength = 248 nm, pulse duration ≈ 17 ns, repetition rate = 30 Hz). The laser fluence was set at 4 J cm^{-2}, and the target-to-substrate distance was fixed at 5 cm. In order to obtain a uniform ablation over the target surface and avoid the drilling of target, the Ni target was continuously rotated. The following PLD part gives a detailed description of the PLD setup. The setup of CVD used in our lab for CNTs growth is illustrated in Figure 3.6. As to the growth process, the Ni-coated-CP substrate was first put into a horizontal quartz tube, which is inserted in a furnace afterward. The furnace was programed heated to growth temperature of 700 $^{\circ}$C in 30 min under a hydrogen flow of 70 cm^3 min^{-1} (standard cubic centimeters per minute, sccm). During this step, the Ni film is broken into spherical Ni nanoparticles covering uniformly the carbon fibers. Subsequent to the Ni nanoparticles formation, the growth of CNTs was initiated by simultaneously introducing acetylene (carbon source), argon (gas carrier) and hydrogen at flow rates of 20, 140

and 100 sccm, respectively. After a synthesis time of 35 min, the flows of acetylene and argon were cut off and the furnace was cooled down to room temperature under a flow of 60 sccm H_2.
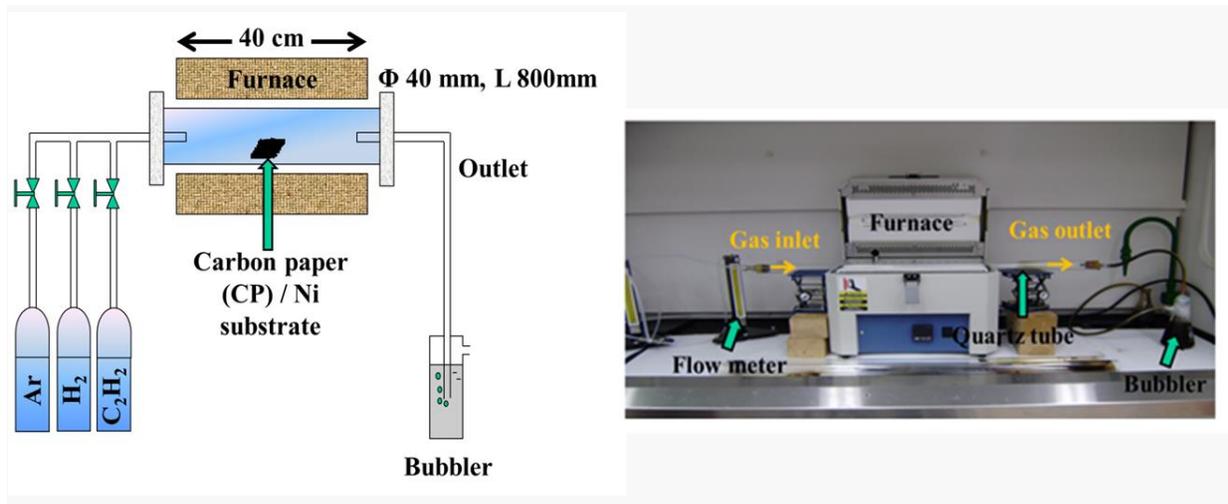
Figure 3.6 Schematic diagram (left) and photo (right) of CVD setup for CNTs growth.

3.1.2 Pulsed laser deposition

Pulsed laser deposition is a physical deposition process, which shares some common characteristics with molecular beam epitaxy and sputter depositions. This technique has emerged in the last decade as a versatile deposition method for the growth of thin films from almost all condensed-matter targets, including metals, insulators, semiconductors, polymers even biological materials, with tunable thickness, crystallinity, morphology and composition to accomplish tailored properties [21].

3.1.2.1 Single beam PLD

In typical PLD, shown schematically in Figure 3.7 (a), a high-power pulsed laser beam is focused onto a target of the material to be deposited. The material is vaporized from the target in a highly forward-directed plasma plume when the energy density surpasses the ablation threshold of the material. The resulting plume expands and propagates at a high velocity to the substrate before depositing on it.
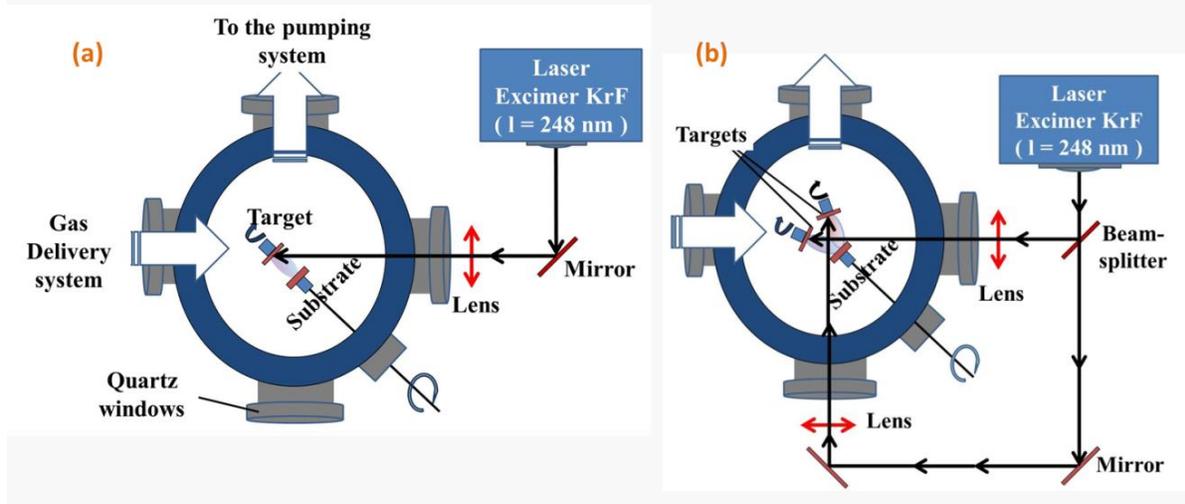
Figure 3.7 Schematic illustration of (a) PLD and (b) CBPLD setup.

The entire process of PLD can be generally divided into three stages [21].

1) Laser-material interaction and plasma plume formation

When the laser pulse is adsorbed by the surface of the target, the electromagnetic energy is instantaneous converted into electronic excitation in forms of plasmons, unbound electrons or excitons in the case of insulator, and then to thermal, chemical and mechanical energy leading to the evaporation, ablation, plasma creation and even exfoliation. A plasma plume is developed on the surface of target, which consists of energetic species including neutral atoms, molecules, ions, electrons, clusters, even particulates etc. The ablation rate (the number of ablated atoms per square centimeter per second) is determined by several factors such as the nature of the target material, wavelength and duration of laser and laser fluence, F (F = laser energy per pulse / focal spot area, in J cm^{-2}). To create a plasma plume with adequate ablation rate, the laser fluence across the focal area should exceed the threshold F of the material, which is dependent on the laser wavelength, duration and the intrinsic properties of material [22]. To ensure that deposition on a substrate proceed from a homogeneous gas plume, the chosen value of the laser fluence needs to provide a desired ablation rate but avoid generating micron-sized particulates or damaging target, such as the formation of cracks, flakes. In the literature, KrF excimer laser (λ =248 nm, pulse duration 10-30 ns) and Nd:YAG laser (λ =266 nm, pulse duration 7 ns) are most often used pulse laser in PLD configurations, the on-target fluence are chosen in the range between 2 to 8 J cm^{-2} for most materials [23-33].

2) Plasma expansion

In this stage the ejected species expand and propagate in the form of plasma plume along the direction perpendicular to target surface. If the ablation is performed under vacuum or low gas pressure, the plume is very narrow and forward directed. While in an ambient gas with higher pressure, a shock wave front arises from collisions between the expanding plasma and the surrounding gas molecules, which propagates with gradually decreasing velocity towards a substrate. The spatial distribution of the laser-induced plume is quite non-uniform due to its highly-directed nature. The flux distribution of the plume is symmetric with respect to the surface normal of the target and can be described by a $cos^n(\theta)$ function, where n varies from 2 to more than 20 and θ represents the angle to the surface normal. To ensure homogeneity of deposition film, substrate has to be rotated in a raster manner. In addition, the background gas pressure and gas molar mass in the PLD chamber play important roles on the spatial and temporal distributions of ejected species in the propagation process and significantly influence the microstructure, chemistry and properties of deposited films. Background gases mainly serve two purposes. First, the gas can actively participate in the chemistry of film growth as reactive species (e.g., O_2, N_2) during the collisions between the plasma and the background gas species. For example, O_2 is needed to compensate for the loss of lighter element of O ensuring stoichiometric transfer from target to substrate, when the film of metal oxides is fabricated. Second, gases (e.g. He, Ar) are introduced to tune the kinetic energies (KE) of the ablated species landing onto the substrate. Gas molecules confine the plasma in a smaller volume by increasing the number of collisions between the plasma and the gas molecules; in turn lower the KE of propagating species to an extent determined by gas pressure/mass.

In comparison with expansion into a vacuum, the interaction of the plasma plume with the ambient gas is a more complex process which includes deceleration and thermalization of energetic species, recombination, interpenetration, formation of shock waves, clusters formation in the plasma plume, and so forth. Many studies have been devoted to understand the dynamics of the plasma expansion, in order to interpret the variations of structure and morphology with the deposition parameters such as, the background gas pressure/mass, the target-to-substrate distance. Time-of-flight (TOF) emission spectroscopy has been extensively employed to investigate the dynamics of plume expansion and propagation processes. Irissou et al. has studied the structural and morphological variations of gold thin films with the background gases (He, N_2, Ar and O_2), gas pressure and target-to-substrate distances by monitoring the velocity of the neutral gold species at a specific distance with TOF [32, 34]. They have found that the target-to-substrate distance and the gas pressure are interdependent deposition parameters; both of them affect the number of collisions of ablated species with the surrounding gas molecules and

in turn give rise to lower velocity of neutral Au species as they are increased. While for a fixed gas pressure and target-to-substrate distance, a remarkable deceleration effect is observed when the inert gas with higher molar mass is employed. All films exhibit a transition from highly oriented, dense film to polycrystalline, porous assembly, coupled with a decrease of crystallite size as the kinetic energy of ejected species decreases, irrespective of the nature of the background gas. Bailini et al. have found the same trend in the depositions of tungsten and tungsten oxide materials, by using the non-dimensional ratio (L) of the target-to-substrate distance to the time integrated visible plume length which couples the effect of inert gas pressure and target-to-substrate distance. The non-dimensional ratio permits to qualitatively select the film growth regime of tungsten and tungsten oxide materials: compact structure (L<1), nanostructured (L~1), then to foam-like (L>1) [24].

Unique to the PLD process, the cluster nucleation in the propagating plume is enabled in a high pressure atmosphere due to the supersaturation of ablated species in a confined region, which leads to cluster-assembled depositions with different morphologies such as densely packed columnar structure, tree-like hierarchical architectures with large internal surface areas and open channels, and so forth [35]. It needs to note that the clusters (few nm) forming in the plume are different from the droplets and particles (0.1 μm to 10 μm) which are much bigger and are ejected from the ablation stage. The structural and morphological variations are dependent on the deposition conditions which affect the plume expansion dynamics (e.g. gas pressure/mass) and films growth mechanisms (e.g. substrate roughness, temperature) [30, 33, 36, 37].

Compared with the PLD performed in the gaseous phase, the propagation of plasma plume in a liquid medium is analogous to that occurs in a high gas pressure atmosphere, where strong confinement of vapor plume by the liquid exists. Pulsed Laser ablation in liquid (PLAL) is promising as a rapid and simple approach for the preparation of noble metal nanoparticles for catalysis, biological sensing applications [38-40].

3) Nucleation and growth of the film on the substrate surface

In the third stage, the plasma plume impinges on the surface of substrate where the nucleation and growth of films proceed. The nucleation rate and growth kinetics of film are mainly dependent on the kinetic energy (KE) and density of arrival species on the substrate, the nature of substrate (e.g. temperature, chemistry, roughness and crystallographic orientation). The dependency between the film microstructure and these deposition parameters can be well interpreted with the structural zone model proposed by Movchan and Demchishin in 1969 for the thick films growth with thermal evaporation method [41]. In thermal evaporation, the reduced

temperature (Tr = Ts/Tm), where Ts is the substrate temperature and Tm is the melting temperature of the deposited material, was related to three microstructural zones: 1) zone-I (Tr < 0.3): shadowing and low adatom mobility yield a porous columnar structure 2) zone- II (0.3 < Tr < 0.5): surface diffusion control give rise to a polycrystalline dense columnar structure and 3) zone-III (Tr > 0.5) bulk diffusion control results in a dense microstructure of enhancement of crystallization and grain size. In each case the actual threshold values for the separation of different zones, are strongly determined by the intrinsic properties of deposited materials. This structural model was extended by Thornton to sputter processes, which is also applied to PLD synthesis [42-45]. In PLD, as discussed in the plasma plume expansion part, the interdependent factors of background gas pressure/mass and substrate-to-target distance play an important role in determining the microstructure, complementary to the effect of the substrate temperature. They influence the KE of the species impinging on the substrate and thus their mobility. In the structural mode for PLD, a transition zone T between zone 1 and zone 2, where a fibrous structure is formed with fewer voids and defects. Infortuna et al have well described the dependence of microstructure on temperature and pressure with a map of microstructures which is compiled as a function of substrate pressure and background gas pressure [43]. Moreover, Passoni et al. have reported that the substrate rotation enhances the shadowing effects due to the continuous changes of the deposition angle of each point on the substrate [37]. Additionally, the incident angles of ejected species get widen as the increasing of background gas pressure, enhancing the oblique flux component impinging on the substrate, which favors void formation by shadowing [45]. This growth mechanism is analogous to that of glancing angle deposition but without the need for high tilt angles and sophisticated substrate motion control. On the contrary, a flux of highly energetic species enables atomic and/or molecular diffusion and reorganization at the substrate surface, and a dense and highly oriented film made of large nanocrystallites is favored.

For the cluster assembly occurring at high gas pressure, deposition regimes including cluster deposition–diffusion–aggregation, cluster melting and coalescence and cluster implantation were observed, depending on background gas pressure and target-to-substrate distance which influence the kinetic energy of the ablated species [46].

3.1.2.2 Cross-beam laser deposition (CBPLD)

CBPLD shown in Figure 3.7 (b) can be considered as a twinned PLD where two targets are brought so close to each other that the emerging ablation plumes by synchronized laser ablation are able to interact and simultaneously deposit on the substrate [47-49]. It enables to produce multi-elements nanostructured materials including alloys, metal-oxides composites etc.,

with different morphology, composition and so forth relevant properties. As conventional PLD, the deposition parameters for the CBPLD are the same, such as background gas pressure/mass, substrate temperature. Due to the variations in the intrinsic properties of two targets, laser fluence (energy density) and the laser spots have to be adjusted in each case to "balance" the plasma fluxes [50]. This asymmetric mode of CBPLD operation is mostly used for co-deposition of different materials with continuously variable ratios [47].

3.1.1.3 The experimental conditions for PLD and CBPLD-synthesized catalysts

In this project, PLD and CBPLD are carried out at room temperature in a stainless steel chamber which can be evacuated to a pressure of 4×10^{-5} Torr with a turbo pump. A pulsed KrF excimer laser (λ= 248 nm, pulse width= 17 ns, and repetition rate = 50 Hz) was used for all the ablation experiments. Pure Pt, CeO_2, SnO_2, TiO_2 and MnO_2 targets in diameter of 1 inch were used, which are purchased from Kurt J. Lesker Co.

Two architectures are constructed and investigated.

(1) Layer-onto-layer architecture CP/CNTs/FMO/Pt

One colleague in our group has initiated this work by constructing the Layer-onto-layer architectured CP/CNTs/CeO_2/Pt and CP/CNTs/SnO_2/Pt catalysts [51, 52]. Following those works, the same architectures were constructed by using two other oxides MnO_2 and TiO_2 and the resulting catalysts are represented as CP/CNTs/MnO_2/Pt and CP/TiO_2/Pt. Conventional PLD is used for the electrode preparation of the Layer-onto-layer architecture electrodes [51, 52]. The substrate (Untreated CP or CP/CNTs) was facing the target with fixed distance of 5 cm, and the laser beam was incident at an angle of 45° to the surface of target. The target and substrate was continuously rotated and translated to obtain a uniform ablation over the whole target and uniform coating on the substrate. For CP/CNTs/MnO_2/Pt electrodes, the MnO_2 layer is deposited using F of 2.5 J cm^{-2} and 20000 laser pulses either under vacuum, in the presence of Helium gas (0.5 Torr or 2 Torr of He) or oxygen gas (10 mTorr of O_2) background pressures. As for CP/TiO_2/Pt electrodes, the TiO_2 layer is deposited using F of 4 J cm^{-2} and 20000 laser pulses with the same gas background variations. The Pt layers for both MnO_2 and TiO_2 supported electrodes were deposited under the same condition that is F of 4 J cm^{-2}, 20000 laser shots and 2 Torr of He gas background.

(2) Co-deposits of Pt-FMO binary catalysts by CBPLD

Table 3.1 The deposition conditions for co-depositions of Pt-FMO.

Substrate	Primary support	Catalyst layer				Background pressure
		Material	F_{Pt} (J cm^{-2})	F_{FMO} (J cm^{-2})	Number of laser shots	
CP	CNTs	Pt-CeO$_2$	4	4	50,000	UV*
						0.5 T*
						2 T
		Pt-SnO$_2$	4	4	50,000	UV
						0.5 T
						2 T
		Pt-MnO$_2$	4	4	20,000	UV
						0.5 T
						2 T
CP	-	Pt-TiO$_2$	4	2.5	20,000	UV
						0.5 T
						2 T

* UV and T stand for under vacuum and Torr, respectively.

Four kinds of Pt-FMO binary catalysts (Pt-CeO$_2$, Pt-SnO$_2$, Pt-TiO$_2$ and Pt-MnO$_2$) with varied morphologies were prepared by CBPLD. For all CBPLD-synthesized samples, the substrate-to-target distance was 5 cm and targets were continuously rotated and translated during entire deposition processes.

(3) Preparation of ternary catalysts composed of Pt, CeO$_2$ and SnO$_2$ by CBPLD

Based on the work on co-deposits of Pt-CeO$_2$ and Pt-SnO$_2$, It was found that both Pt-CeO$_2$ grown under 0.5T He displayed higher catalytic performance toward ethanol oxidation, which guided us to fabricate ternary catalysts composed of Pt, CeO$_2$ and SnO$_2$ aiming to combine the advantages of two types of co-deposits for ethanol oxidation. Ternary catalysts were prepared with different combinations of these three components. For all deposits, laser fluence was fixed at 4 J cm^{-2} and 0.5 T of He gas background was used. As for the deposition procedure, secondary support CeO$_2$ (or SnO$_2$) is deposited on the substrate (CP/CNTs) with 5000 (or 10000) laser shots, followed by a codeposition of Pt-SnO$_2$ (or Pt-CeO$_2$) on top. The detailed conditions are listed in Table 3.2.

Table 3.2 The deposition conditions for ternary catalysts.

Substrate CP	Primary support (CNTs)	Secondary support		Catalyst layer	
		Material	Number of laser shots	Material	Number of laser shots
		CeO$_2$	5,000	Pt-SnO$_2$	50000
			10,000	Pt-SnO$_2$	
		SnO$_2$	5,000	Pt-CeO$_2$	
			10,000	Pt-CeO$_2$	

3.2 Structural characterizations of electrode materials

This part deals with various physical techniques employed for morphological and microstructural characterization of the electrode materials prepared in this project. The principal methods of characterization include scanning electron microscopy (SEM), Transmission Electron Microscopy (TEM), X-Ray Diffraction (XRD), X-Ray Photoelectron Spectroscopy (XPS), and Atomic Force Microscopy (AFM). Additionally, Neutron Activation Analysis (NAA) was employed for determining the mass loading ($\mu g\ cm^{-2}$) of Pt.

3.2.1 Scanning electron microscopy

In numbers of scientific and industry-related field, scanning electron microscopy is a powerful magnification technique that delivers high-resolution, sharp, black and white 3D images with information about the topography, morphology and composition on samples' surface. It functions in a similar fashion to optical microscope, but focus beams of electrons instead of visible light, to magnify an object. Compared with conventional optical microscope, scanning electron microscope provides images with higher resolution and greater depth of field, due to the smaller de Broglie wavelength of electrons and smaller aperture size in the final lens and longer working distance, respectively.

To create an SEM image, the incident electron beam is scanned in a raster pattern across the sample's surface. A variety of signals are generated by the interactions of the incident electron beam with atoms at or near the surface of the sample (shown in Figure 3.8), including backscattered electrons (due to elastic scattering), secondary electrons with low energy (due to inelastic scattering), diffracted backscattered electrons, characteristic X-rays, visible light, specimen current, transmitted electrons and heat. A variety of detectors are used to attract different types of scattered electrons, and secondary electron detector is predominantly used for SEM imaging. It varies with the topography of the sample surface: edges are bright, recesses are dark. The ratio of the image display size to the sample area scanned by the electron beam gives the magnification. The characteristic X-rays are used for elemental analysis.
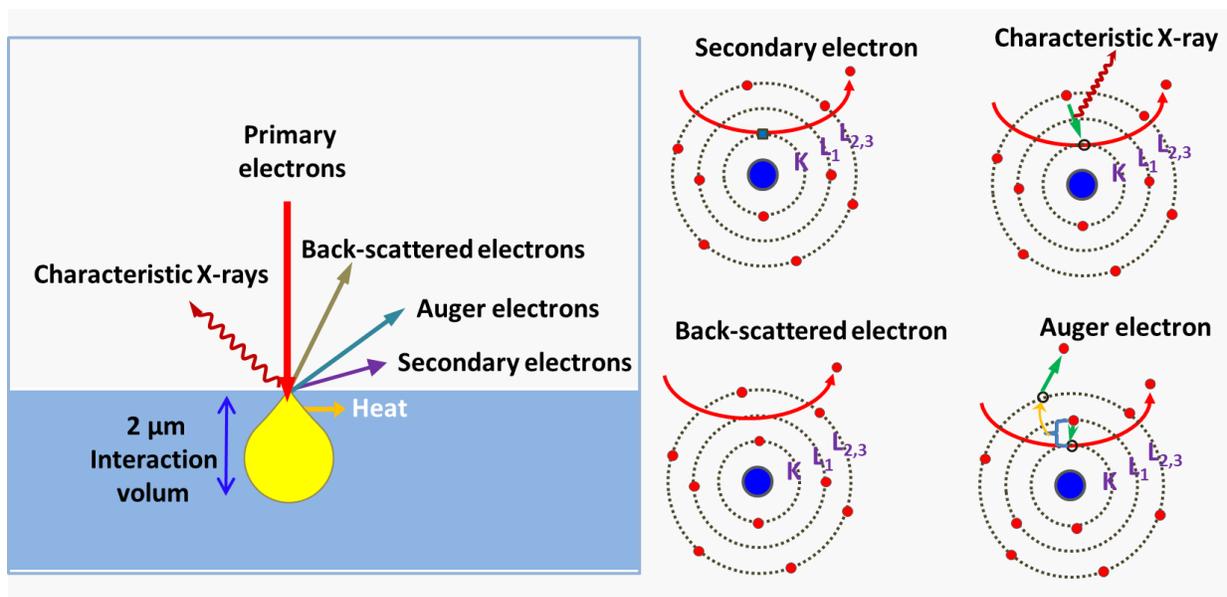
Figure 3.8 Signals generated from the interaction between SEM electron beam and specimen under study.

The essential components of an SEM including electron source (i.e., tungsten filament), electromagnetic and/or electrostatic lenses, vacuum chamber, sample chamber and stage, detectors for different types of signals of interest and data output devices.

In this thesis, two SEM facilities, JEOL-JSM-6300F (INRS) and JEOL-JSM-7401F (located in the cleanroom of INRS-EMT), have been used to examine the surface morphology of the prepared samples.

3.2.2 Transmission electron microscopy

Transmission electron microscopy is an advanced technique to provide morphologic, compositional and crystallographic information on samples from the interactions taking place between samples (less than 500 nm in thickness) and energetic electrons. Specifically, an electron beam accelerated with high voltage (~ 200 KV) passes through an ultra-thin (less than 500 nm in thickness) specimen, instead of scanning across the surface of the samples the surface information by in SEM. As shown in Figure 3.9, the high-energy electrons with very small wavelength generate a variety of secondary signals, such as transmitted electrons, characteristic X-rays, secondary electrons, Auger electrons and so on. These secondary signals can be used to generate an image and simultaneously give information about local structure (by imaging of defects such as dislocations), average structure (using diffraction to identify crystal class and lattice parameter) and chemical composition.
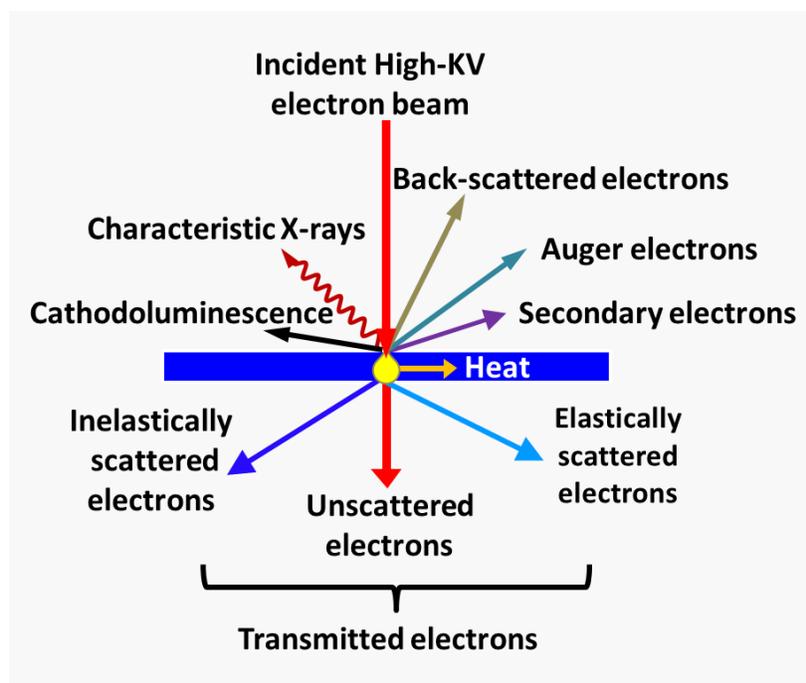
Figure 3.9 Diagram illustration of the interaction of highly energetic electrons with matter

In the thesis, TEM is used to observe the morphology and size of as-prepared catalysts on the substrate. Crystal structure information of materials was identified with SAED. High-resolution (HR)-TEM and Selected area electron diffraction patterns (SAED) were obtained with JEOL-JEM-2100F (École Polytechnique de Montréal, Montréal, Canada) operating at 200 kV. Particle size distributions were determined by measuring more than 100 individual particles in TEM images.

3.2.3 X-ray Diffraction Analysis (XRD)

X-ray diffraction is a powerful, rapid and widely available technique in material science, mainly for phase identification of crystalline material ("fingerprint") and determining unit cell dimensions within crystals, for distinguishing between the crystalline form and amorphous form and for quantification of the percent crystallinity of a sample.
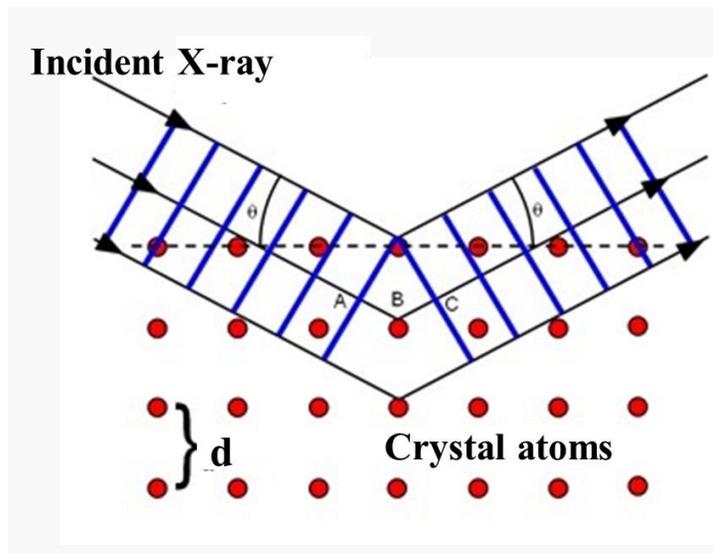
Figure 3.10 Diffraction of X-ray by parallel planes of atoms in a crystalline material.

XRD analysis is accomplished by constructive interference of X-rays and the crystalline sample. Typically, a cathode ray tube generates X-rays which are filtered to produce monochromatic radiation and then collimated to a single direction before impinging onto the sample. The interaction of incident X-rays and a set of lattice planes with an equal interplanar distance (d-spacing) produces constructive interference when conditions satisfy Bragg's Law (as shown in Figure 3.10).

$$n\lambda = 2d \ sin \theta \qquad (3.1)$$

where λ is the wavelength of incident X-ray, n is an integer representing the order of reflection, *d* is the spacing between adjacent planes in the lattice, *θ* is the angle of incidence/reflection to the planes, *n* is any integer.

By scanning the sample through a *2θ* angle range, a characteristic diffraction pattern can be acquired. A diffractogram is accordingly plotted, which is represented as intensity vs. *2θ*. A Series of peak is shown in the diffractogram, which occur where the X-ray are diffracted by crystal planes with specific orientation according to Bragg's law. The crystal planes in cubic systems are described using three integers called miller indices *h, k, l* and (*hkl*) denotes a set of planes.

The characteristic x-ray diffraction patterns are commonly used to identify or "fingerprint" crystalline structure exists in the material being studied. By comparison with standard reference patterns and measurements, both peak position and relative intensities must fit to identify a particular phase. The standard references patterns are from the Powder diffraction file (PDF)

which is maintained by JCPDS (Joint Committee for Powder Diffraction Standards). Furthermore, the crystallite size and lattice parameters can be estimated.

The crystallite size can be estimated with the Scherrer formula as follows.

$$L = \frac{0.89 \, \lambda}{B(2\theta) \times cos \, \theta} \tag{3.2}$$

where *B (2θ)* is FWHM in radians of the investigated peak; λ is wavelength of X-ray in meters; *θ* is Bragg angle in radians and *L* is particle size in meters.

The lattice parameter (constant) can be calculated from derived Bragg's equation which is related to the miller indexes of lattice plane and crystal systems. Take a Face-centered cubic (FCC) crystal as an example, the lattice parameter a is calculated with the following equation.

$$a = \frac{\lambda \times \sqrt{h^2 + k^2 + l^2}}{2sin \, \theta} \tag{3.3}$$

XRD analyses in this thesis were performed using a Bruker D8 Advance diffractometer equipped with a Cu Kα source (λ = 0.15406 nm) operating at 40 kV and 40 mA. All diffractograms were acquired in the $\theta - 2\theta$ scan mode with an angular step size (*2θ*) of 0.04° and an acquisition time of 4 s per step. Eva V14 software was applied to determine the diffraction angles of the diffraction peaks under study and their corresponding full width at half maximum (FWHM) values, which are used to estimate the crystallite size and lattice parameters.

3.2.4 Micro-Raman spectroscopy

Raman spectroscopy is a vibrational spectroscopy, much like infrared spectroscopy. It is a highly selective and versatile technique, which provides a simple, fast and non-destructive, both qualitative and quantitative analysis for both organic and inorganic materials in the forms of solids, liquids and gases. To date, Raman spectroscopy has become an established and a practical tool for chemical analysis and characterization applicable to various chemical species. For instance, it is probably the most important tool being employed to research, develop and control the quality of carbon-based materials, including structural identification, thickness/diameter, defects determination for CNTs/graphene, examination of the structure composition of amorphous carbon, and etc. [53]. Furthermore, it is also effective for the analysis in catalysis, photovoltaics, semiconductors and 2D materials (such as MoS_2, WSe_2).
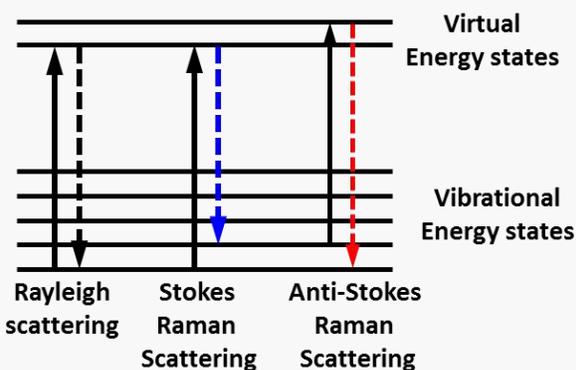
Figure 3.11 Energy level diagram for Raman scattering (left) and the photo of Micro-Raman spectroscopy from Renishaw (right).

Raman scattering arises from a change in the polarizability of the molecule due to an interaction of photos with molecules. When a laser impinges upon a molecule, photons are absorbed by the material and scattered. There are mainly three types of scattered photos in the scattering process, as shown in Figure 3.11. The majority of resulting scattered photons is due to elastic scattering called Rayleigh and these photos have the same frequency as incident ones. A small fraction of resulting photos are from inelastic scattering termed Raman scattering, which either possess higher frequency (designated as Anti-stokes Raman scattering) or lower frequency (Stokes Raman scattering) than incident photos.

Raman spectroscopy is conducted on a Raman system mainly composed of a laser as excitation source, a microscope for the sampling apparatus and a spectrometer for the detector. Specifically, a sample is illuminated with a monochromatic light (a laser in the visible, near infrared or near UV range). Electromagnetic radiation from the illuminated region passes through lens, monochromator, filters and finally directs onto the detector.

A plot of intensity of Raman scattered light as a functions of Raman shift (in units of wavenumbers, cm^{-1}) is a Raman spectrum. Raman shift is the frequency difference of the incident radiation and Raman radiation, which is irrespective of the frequency of the incident radiation. That means that the same Raman shifts of the molecule can be obtained by using the laser with wavelength of either 514.5 nm or 785 nm. Raman bands in the spectrum are related to a specific rotational, vibrational or other low-frequency mode of chemicals, which gives insight into the chemical bonds and symmetry of molecules in the system. Micro-Raman spectroscopy comprises of a specially designed Raman spectrometer integrated with an optical microscope, which enables

63

researchers to acquire Raman spectra of microscopic samples. Phase and structural analysis of CNTs substrate and certain metal oxides in this thesis were characterized by Micro-Raman spectroscopy (Renishaw shown in Figure 3.11) using a 514.5 nm laser radiation of an Ar^+ laser with a circular polarization. The laser beam was focused onto the sample to a spot size of 1 µm in diameter (Renishaw Imaging Microscope Wire™).

3.2.5 X-ray photoelectron spectroscopy

XPS is also known as electron spectroscopy for chemical analysis (ESCA), is a surface analysis technique which can give information about the elemental composition, empirical formula, chemical state and electronic state within a material. Its typical analysis depth is 1 to 10 nm.

In principle, XPS is based on the photoelectric effect. Figure 3.12 illustrates the schematic diagram of the photoemission process involved in XPS analysis. Briefly, when the surface of sample is illuminated by an X-ray, the energy of X-ray photos is completely absorbed by a core electron. If the photo energy is large enough, the core electron will escape from the atom, emit out of the surface and reach the electron energy analyzer. The emitted electron with a certain kinetic energy is referred to as the photoelectron. The Binding energy of emitted electrons from the photoemission process can be determined by the following equation:

$$E_B = h\nu - E_K - \Phi \tag{3.4}$$

where E_B is the binding energy of the core electron, $h\nu$ is the energy of incident X-ray photos, E_K is the kinetic energy of the photoelectron measured by the instrument and Φ is the work function dependent on both the material and spectrometer.
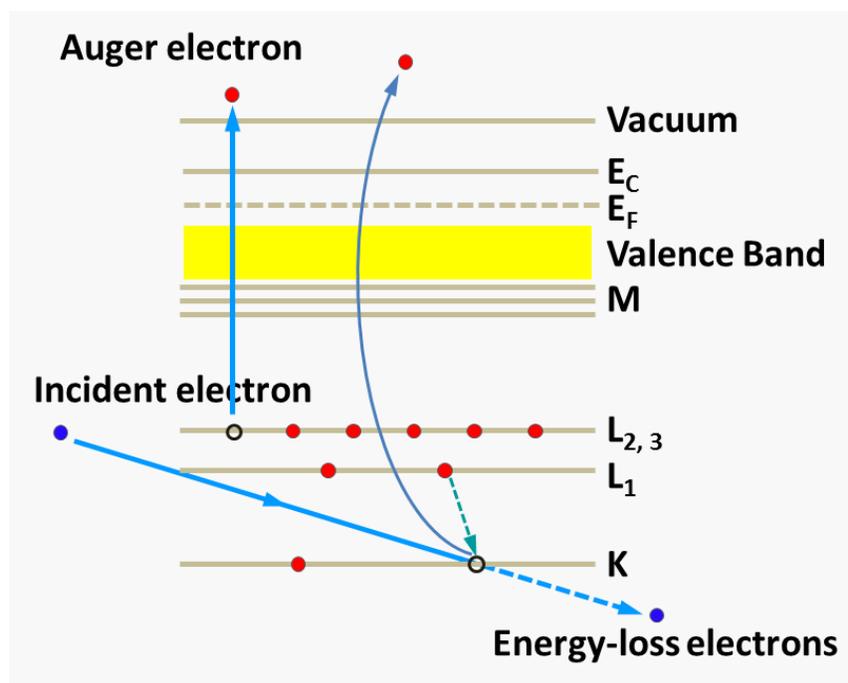
Figure 3.12 Schematic diagram of the photoemission process in XPS.

A XPS spectrum is a plot of intensity of photoelectrons as a function of binding energy (in unit of eV). The intensity of photoelectrons is dependent on the amount of element within the XPS sampling volume. The binding energy is related to several factors including: (1) the element from which the electron is ejected; (2) the orbital (e.g. 1s, 2s, 2p) from which the electron is emitted and (3) the chemical environment of the detected atom from which the electron is emitted. In practice, two types of XPS spectra are acquired during a XPS test, survey spectrum and high-resolution spectra for the elements in question. Survey spectrum is firstly obtained for most XPS analyses, which is a broad, low energy resolution scan. The acquisition takes less time and the survey spectrum provides an overview to all the elements presented in a sample. Each element has a characteristic set of peaks at corresponding BE values. The BE values are experimentally determined and the BE table of common chemicals are established in various XPS handbooks and websites. These characteristic BE values for given elements allow the qualitative analysis, such as the determination of unknown elemental compositions within a sample. Subsequently, high-resolution XPS spectra are recorded by just sweeping the energy ranges of desired peaks at higher resolutions. They are commonly used for the elemental identification and the determination of chemical states and elemental composition of chemical species on material surface, because of their higher signal/noise ratio leading to higher quantitative accuracy.

65

Herein, XPS was used to identify the chemical state and determine the atomic concentration of chemical species in our samples. The measurements were performed using a VG Escalab 220i-XL. Based on the conductivity of our samples, two types of Al sources ($h\nu$ =1486.6 eV) are employed, one is an Al K$\alpha_{1,2}$ monochromatic source for materials with higher conductivity and the other is an Al polychromatic twin-anode source for material with relative lower conductivity. For the test with the Al Kα monochromatic source, the anode was operated at 10 kV and 20 mA. All samples were analyzed with a spot size of 250×1000 µm located approximately in the center of the sample. For the test with the twin-anode source, the anode was operated at 15 kV. The pass energy of the analyzer was fixed at 100 eV for survey spectra and at 20eV for high-resolution multiplex scan spectra with both X-ray sources. Quantification of the elements was carried out with Casa XPS software (Casa Software Ltd.).

3.2.6 Atomic-force microscopy

Atomic-force microscopy is a type of Scanning Probe Microscopy, derived from the scanning tunnelling microscope (STM) which could well resolve the atomic surface structure of conductors but not of insulators. And AFM is originally designed as a complementary tool to STM for imaging surfaces of nonconductive samples. AFM works in a fashion resembling STM, an atomically sharp tip is raster scanned across a sample surface using a feedback loop to adjust parameters (e.g. tip-sample distance, tip-sample force and so on) to generate the topographic image of the sample surface. Unlike STM, atomic forces are used to map the tip-sample interaction in AFM, instead of using the quantum mechanics.

There are four critical components typically included in AFM as shown in Figure 3.13:

a) Sharp tip held on an end of a spring-like cantilever as a probe, which is brought into proximity of sample surface and interact with atoms on the surface. The atomic force between the tip and sample is exploited by AFM to image the sample topography. The dimension and feature of the tip directly determine the resolution and quality of topographic images.

b) Scanner which is normally made from piezoelectric materials and is responsible for moving the tip or sample very precisely in x, y and z axes.

c) Laser beam deflection system is used to monitor the height variations of the tip as it passes over a sample. As the height of tip varies along with the real sample topography, there are slight changes in direction of laser beams reflected by the back of the cantilever. The direction

changes of reflected beams are tracked by a position-sensitive photodiode (PSPD), and thus the height variations of the tip are recorded.

d) Feedback system is used to control the height of the tip above the surface with a constant tip-sample separation based on the input parameters.

During the topography acquisition, the signal from the PSPD passes through a feedback system, and into the z-movement part of the scanner, in order to maintain the probe-sample distance at a set value.
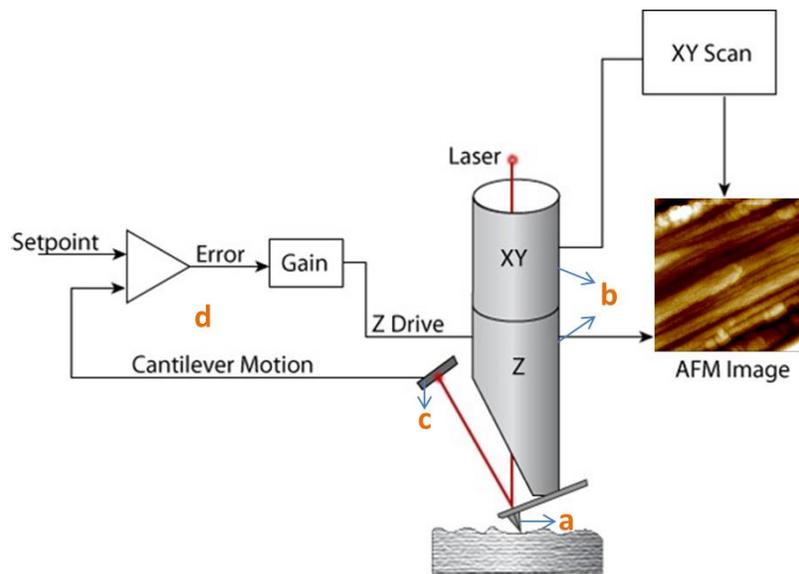
Figure 3.13 Schematic diagram of AFM with (a) cantilever tip (b) scanner (c) laser beam deflection system and (d) feedback system.

According to the nature of tip motion, AFM operation modes are generally divided into static mode (also called contact mode) and dynamic mode which subdivided into non-contact mode and tapping (intermittent contact) mode. Nowadays, tapping mode is the most frequently used AFM mode when operating in ambient conditions, due to less damage being brought to the sample surface and the probe.

In the thesis, the surface topography (roughness) was characterized by atomic force microscopy (AFM) using a Nanoscope III microscope from Digital Instruments Veeco Metrology Group. All measurements were operated in a tapping (intermittent contact) mode. Both the data collection and analyses were carried out on NanoScope™ system integrating the hardware for manipulation and software for analysis.

3.2.7 Neutron activation analysis

Neutron activation analysis is a type of non-destructive chemical analysis which allows discretely sampling of elements in a vast amount of materials and is often used for measuring the concentration or mass of elements in a sample either in the state of solid or liquid [54-56]. In principle, the sample is irradiated with neutrons and radioactive isotopes of elements in the bulk are formed which emit detectable gamma-rays (as shown in Figure 3.14). Since the radioactive emissions and radioactive decay paths for each element are unique and well known, it is possible to determine the concentrations and mass of the elements within it by studying the emission spectra of the radioactive sample with respect to the emission spectra of standard reference material of interest [55, 56].

In our work, the Pt loading is determined with NAA technique on all our samples (pure Pt and Pt-FMO catalysts) using a SLOWPOKE nuclear reactor (École Polytechnique de Montréal, Montréal, Canada). For the Pt deposits with 20000 times of laser shot, the mass loading of Pt with NAA is 48 µg cm^{-2}. The Pt and Pt-FMO deposits with 50000 times of laser shot, the mass loading of Pt with NAA is 120 µg cm^{-2}.
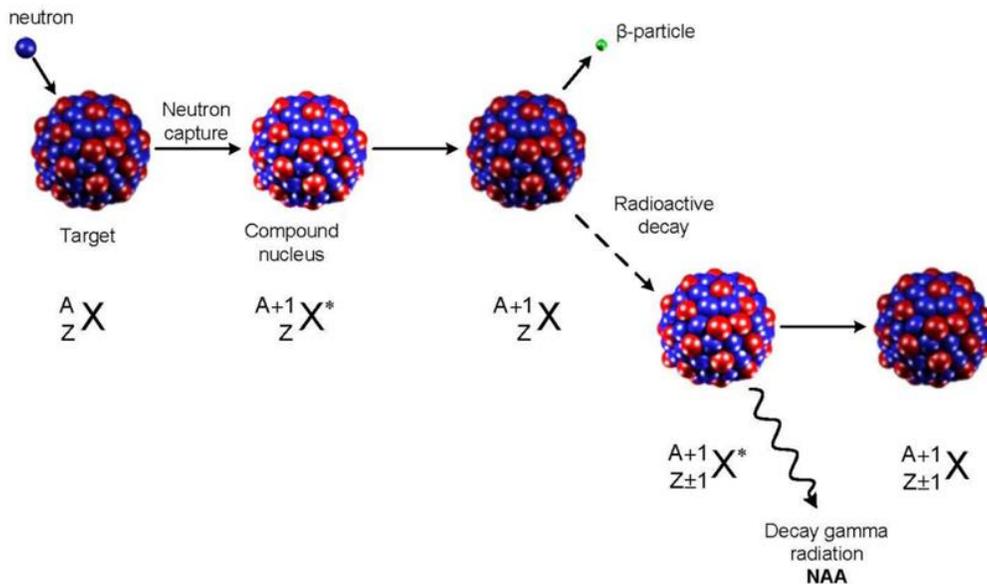
Figure 3.14 Schematic diagram representing the process of neutron capture by a target nucleus followed by the emission of gamma-rays [54].

3.3 Electrochemical characterization

In the effort to explore cost-effective, active and stable catalysts for fuel cell applications, the electrochemical catalytic performance of the catalysts is of primary interest and mainly concerned properties. Physical characterization techniques (e.g. spectroscopic methods), by contrast, are aimed to understand the physicochemical properties and their effects on the electrochemical performance of the catalysts under investigation, eventually give us a guidance in the design of new and breakthrough electrocatalysts for fuel cell applications.

Different electrochemical characterization techniques such as cyclic voltammetry (potentiodynamic) and chronoamperometry (potentiostatic) are employed in this project to evaluate the electrocatalytic performance of the catalysts. In the following part, there is a brief introduction to terms, concepts, principles, and basic electrochemical techniques involved in the project.

3.3.1 Electrochemical fundamental concepts

3.3.1.1 Electrochemical Reactions and Cells

Electrochemical reaction refers to the chemical reactions occurring at the interface between an electronic conductor (Electrode) and an ionic conductor (Electrolyte), associated with the passage of electric current and the production of electrical energy. It is a heterogeneous charge-transfer process at the electrode/electrolyte interface instead of a homogeneous one involved in many chemical reactions. In an electrochemical system, a single interface cannot be experimentally studied, so an electronically closed loop is required for a measurable current to flow. This entire loop comprises electrochemical cell and external wiring and circuitry.

An electrochemical cell generally consists of at least two electrodes in contact with one electrolyte phase. The basis for an electrochemical cell is a redox reaction which can be broken down into two independent half-reactions, a reduction half-reaction and an oxidation half-reaction taking place on two individual electrode/electrolyte interfaces, respectively.

3.3.1.2 Electrode

Electrode mostly refers to the electronically conducting materials, such as metals, graphite, and semiconductors. The electrode can be classified in many ways. The electrode at which the oxidation reaction occurs is called anode and the electrode at which reduction takes place is

called cathode. In an electrochemical cell, the electrode of interest is called **working electrode (WE)** in voltammetry or **indicator electrode** in potentiometry. For fuel cell applications, the entity of the WE is electrocatalysts where the oxidation of fuel (e.g. H_2 or ethanol) or the reduction of oxidant occur, the potential of which and the current passing through which is controlled and monitored, respectively. Another electrode in the cell passes all the current needed to balance the charge added or removed by the working electrode, which is called **counter electrode (CE)** (also known as auxiliary electrode). There is no specific material requirement for CE as long as it does not affect reactions occurring at the WE. In most electrochemical studies, the CE is generally an inert conductor such as Pt or graphite. In the modern electrochemical cell, a third electrode, termed **reference electrode (RE)** is often employed, which is non-polarizable and provides a stable and reproducible potential over time and with changing temperature. The standard hydrogen electrode (SHE), or normal hydrogen electrode (NHE) with arbitrarily assigned potential of zero, is the internationally accepted reference electrode. From an experimental standpoint, potentials of working electrodes are often measured and quoted with respect to some commercially available reference electrodes other than the NHE, such as Saturated Calomel (SCE), Silver/Silver Chloride (Ag/AgCl), Mercury/Mercury Oxide (Hg/HgO), etc. The choice of the reference electrode is dictated by the experimental conditions, such as the testing temperature, the composition and nature of the electrolyte, as well as the current applied, and more.

The configuration of WE, CE and RE is called three-electrode setup as shown in Figure 3.15 (a), which is the most commonly employed setup for the electrochemical characterizations of a variety of materials applied in catalysis, electrochemical capacitors, and lithium batteries, etc. In measurements, the three-electrode setup is connected to a PC-controlled potentiostat. In essence, potentiostat is used to control the potential difference between WE and RE and measures the current flowing through the working electrode. Basically, two circuits are consisted: a polarizing circuit that applies the potential to the cell, and a measuring circuit that records the cell current. The polarizing circuit is between WE and RE in which no current flows. This can exclude the ohmic drop from electrolyte resistance, and thus allows the potential of the WE to be precisely controlled relative to the RE. The measuring circuit is between the WE and CE in which the current flows through the WE/electrolyte interface, electrolyte and CE/electrolyte interface and is monitored.
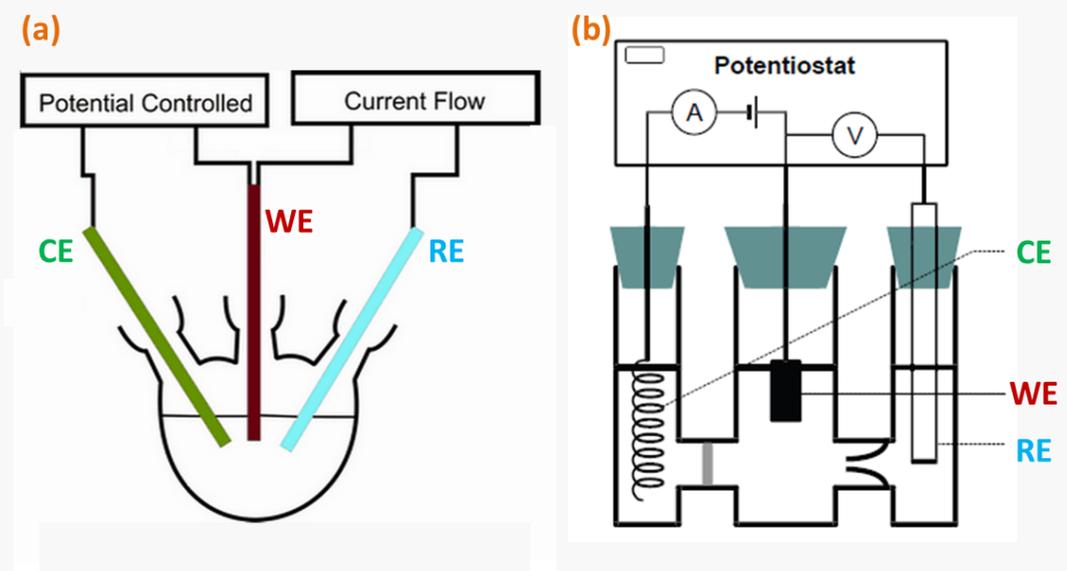
Figure 3.15 Diagrams of (a) three-electrode setup and (b) three-compartment cell.

To avoid the interfering from the reaction on the counter electrode, the measurement is generally conducted using a typical three-compartment cell (as shown in Figure 3.15 (b)). The intermediate compartment is for WE, separated from another two compartments respectively for RE and CE, together with two openings for gas inlet and outlet permitting the electrolyte deaeration or gas stripping tests.

3.3.1.3 Electrolyte

Electrolyte is an integral component of an electrochemical cell. It is responsible for the charge transfer and acts as medium for electroactive species of interest, which can be classified into liquid and solid electrolytes. Liquid electrolytes include aqueous solution and nonaqueous solution and molten salts. Solid electrolyte is usually referred to as the solid polymer electrolyte, such as Nafion, Polytetrafluoroethylene (PTFE). Liquid electrolyte is basically composed of solvent and supporting electrolyte (or called inert electrolyte). An excess of supporting electrolyte is used to minimize solution resistance, eliminate the electromigration effects and maintain a constant ionic strength. Supporting electrolyte can be a mineral acid (e.g. hydrochloric acid, sulfuric acid), an inorganic salt (potassium chloride or nitrate), or a buffer (such as acetate, phosphate, or citrate). The choice of the supporting electrolytes primarily depends on its solubility in the solvent employed, its electrical conductivity, electrochemical activity, and chemical reactivity. Briefly, it should not react with electroactive species of interest, products, and solvent, and doesn't undergo specific adsorption on electrode and electrochemical reactions within the investigation

potential range. In many instances, the electrolyte solution should be deaerated by pursing inert gases (e.g. N_2 or Ar) prior to electrochemical measurements.

3.3.1.4 Variables in Electrochemical Characterizations

A study of electrochemical behavior is accomplished by holding certain variables (e.g. scan rate, stationary electrode, or quiescent solution) of an electrochemical cell constant and monitoring how other variables (e.g. current) vary with changes in the controlled variables (e.g. potential).

The primary variables related to the electrochemical reactions are the **potential** of the working electrode, the **current (density)** flowing through the working electrode/electrolyte interface and the **charge** transferring across the interface, along with the **mass-transport** rate of the reactant/product at the surface of the working electrode.

3.3.1.5 Potential

In electrochemistry, electrode potential refers to the interfacial potential difference between an electrode and its electrolyte, for example $E_{H^+/H_{2(Pt)}}$. However, it is physically impossible to empirically obtain the potential difference at a single interface. Instead, a galvanic cell is established, which is made up of two half-cell reactions at the electrode of interest and a standard reference electrode. The overall potential of the galvanic cell can be measured easily by a high impedance voltmeter. Because the potential of reference electrode is known, it is easy to determine the standard potential of the half reaction involved at the electrode of interest, according to the Nernst equation.

For systems at equilibrium, the electrode potential and the concentration of the participants are governed by Nernst equation. The two forms of the equations for full galvanic cell and half-cell are below [57]:

$$E_{cell} = E_{cell}{}^0 + \frac{RT}{nF} \ln Q_r \; (Overall\; cell\; potential\; for\; aA + bB \;\leftrightarrow cC + dD) \qquad (3.5)$$

$$E_{red} = E_{red}{}^0 + \frac{RT}{nF} \ln \frac{a_{ox}(0,t)}{a_{red}(0,t)} \quad \binom{Half\; cell\; reduction\; potential\; for}{Ox + ne^- \rightarrow Red} \qquad (3.6)$$

where

E_{cell} is the cell potential at the temperature under investigation (V);

$E_{cell}{}^0$ is the standard cell potential (V);

E_{red} is the half-cell reduction potential at the temperature under investigation (V);

$E_{red}{}^0$ is the standard half-cell reduction potential (V);

R is the universal gas constant (8.31 J K^{-1} mol^{-1});

T is the temperature (K);

n is the number of moles of electrons transferred in the cell reaction or half-reaction ;

F is the Faraday constant, the magnitude of electric charge per mole of electrons (96485 C mol^{-1});

a is the chemical activity for the relevant species, where a_{ox} is the oxidizing agent and a_{red} is the reducing agent;

Q_r is the reaction quotient ($Q_r = \frac{[A]^a[B]^b}{[C]^c[D]^d}$).

In electrochemical tests, electrode potential is always expressed with respect to a reference electrode (e.g. SHE), instead of an absolute value. For potentiostatic (e.g. CV, chronoamperometry) methods, the electrode potential is controlled to derive an electron transfer reaction and the current response is recorded. The applied potential on the working electrode can be viewed as "electron pressure", which forces the electroactive species to lose or gain electrons at the electrode/electrolyte interface and the concentration gradient are formed between the surface and the bulk solution, leading to the flowing of faradaic current. If the kinetics of electron transfer is rapid, the concentrations of O and R at the electrode surface can be assumed to be at equilibrium with the electrode potential, as governed by the Nernst equation for the half-reaction.

3.3.1.6 Current

Current reflects the rate at which charge transfer across the electrode/electrolyte interface. In a three electrode cell, the current from redox reactions at the working electrode and the auxiliary electrodes is called faradaic current. Dependent on the electron flow direction, the faradic current can be divided into anodic current and cathodic current. An anodic current is the flow of electrons into a working electrode from a second phase (usually an electroactive species in electrolyte) as a result of the oxidation. Conversely, cathodic current is the current in which electrons flowing from the working electrode to a species in solution.

An electrochemical reaction on the electrode/electrolyte surface involve a series processes, such as mass transfer, electrons transfer, chemical reactions preceding or following the electron transfer and other surface reactions (adsorption, desorption, and so on). The magnitude of the current is limited by the rate of the most sluggish process called rate determining step (rate-limiting step). The simplest reactions involve only heterogeneous electron transfer, mass transfer of a reactant to the electrode, and mass transfer of the product to the bulk solution. The rate constant for electron transfer depend upon the potential applied on the working electrode. If a high overpotential is applied to the WE, the electrode process is mass-transfer controlled and the mass-transfer limited current can be studied. In another case, some specific WE can be employed, such as roasting disk electrode (RDE) which can eliminate the mass transport effect, the reaction kinetics can be investigated.

3.3.1.7 Mass-transport rate

In electrocatalysis, the current is as a function of the rate of mass transfer of reactant to the surface of electrode. The mass transport to the electrode/electrolyte interface composed of three modes of mass transfer, is governed by Nernst-planck equation [57].

$$J_i(x) = -D_i \frac{\partial C_i(x)}{\partial x} - \frac{z_i F}{RT} D_i C_i \frac{\partial \emptyset(x)}{\partial x} - C_i \vartheta(x) \qquad (3.7)$$

where the three modes of mass transfer are as follows:

(1) Migration: is the movement of a charged species driven by the electric potential;

(2) Diffusion: is controlled by the concentration gradient of a chemical species;

(3) Convection: is caused by density gradient or forced convection (stirring or electrode rotating).

Several important techniques relies exclusively on mass-transport-limited conditions in the absent of the other two modes of mass transport. This is accomplished by utilizing excessive supporting electrolyte and a quiescent solution. Accordingly, the resulting current is called diffusion-limited-current, which is generated at higher overpotential where electron-transfer rate is fast and the diffusion rate of reactant is the rate-determining step.

3.3.2 Electrochemical techniques

3.3.2.1 Cyclic voltammetry

CV is a valuable tool to study the mechanisms and rates of oxidation and reduction processes, which enables a rapid characterization of electrochemical reactions occurring at the interface between the electrode and the electrolyte solution. It is not only capable of providing qualitative information about electrode reaction mechanisms and kinetics, but also can determine several quantitative properties of charge transfer reactions. Thus, CV is often initially conducted to survey the reactivity of new electrochemical materials.

In cyclic voltammetry (CV), the potential of working electrode is linearly swept back and forth between two potential limits with a constant rate, and the current response that flows between the working electrode and the auxiliary electrode is recorded accordingly. The current versus potential plot is termed cyclic voltammogram the shape of which is basically constrained by several parameters, including potential scan rate, the potential range. The potential scan rate can be controlled in a wide range and most studies are conducted between 1 mV s^{-1} to 1000 mV s^{-1}. The potential range is generally the values at which the decomposition of the electrolyte solution starts. In most cases, the chosen potential region just needs to contain an oxidation or reduction process of interest. In the case of aqueous solution, the limits are the onset potential for hydrogen and oxygen evolution.

A typical potential-time plot applied in CV and the resulting cyclic votammogram on a simple electrode process are shown in Figure 3.16. During CV measurement, the system begins from the initial potential (A) at which no redox reaction takes place. At a critical potential (B) in the positive-going scan, the electroactive species begin to be oxidized and an anodic current starts to flow. With potential goes higher, the anodic current rises as the reaction kinetics increases. Eventually, a characteristic diffusion-controlled peak appears since at some point the diffusion layer of R has grown sufficiently above the electrode so that the flux of reactant toward the electrode is not fast enough to satisfy that required by the Nernst equation. When the potential goes higher beyond this point, the current starts to decay until the potential san is reversed (D). During the backward potential scan (from D to I), a current generated by the reduction reaction at the electrode, will start to flow at a critical point and then reach a cathodic current peak.
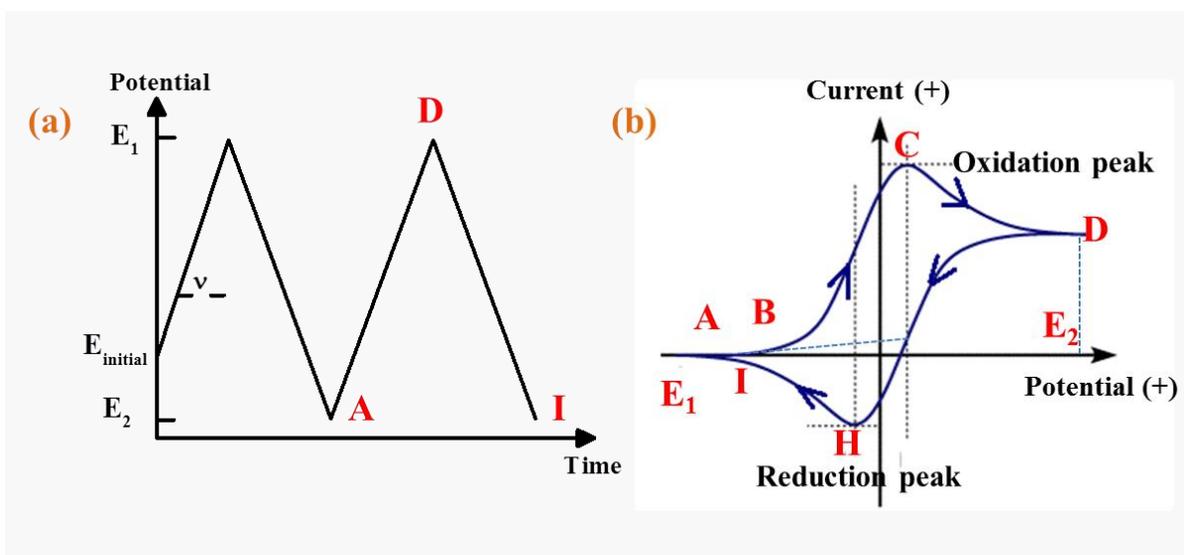
Figure 3.16 (a) Potential-time wave applied for CV and (b) the resulting i-E curve.

If the reaction is thermodynamically reversible or kinetically fast enough, the peak current in CV is governed by the Randles-Sevcik equation [57]:

$$i_p = (2.69 \times 10^5)n^{3/2}ACD^{1/2}\vartheta^{1/2} = KC \tag{3.8}$$

where i_p is the peak current (in A), n is the number of electrons, A is the area of the working electrode (in cm^2), D is the diffusion coefficient (in cm^2 s^{-1}), ϑ is the scan rate (in V s^{-1}), and C is the bulk concentration of the electroactive species (in mol cm^{-3}). For a reversible system, the anodic ($i_{p,a}$) and cathodic ($i_{p,c}$) peak currents are equal, and the ratio $i_{p,a}/i_{p,c}$ is 1.

3.3.2.2 Linear sweep voltammetry

Linear sweep voltammetry (LSV) is another type of voltammetry technique which is operated in a similar manner to CV and can be simply regarded as a half of the CV. In LSV measurements, the potential applied to WE is linearly swept from E_1 to E_2 with a constant rate instead of being cycled between these two potentials. CV in most cases is applicable to where LSV is employed. In certain circumstances, only oxidation or reduction on the electrode is interested such as the oxygen reduction reaction test on Pt catalysts, or the reaction is irreversible, LSV is commonly carried out instead of CV because CV cannot give more information than LSV.

3.3.2.3 Chronoamperometry
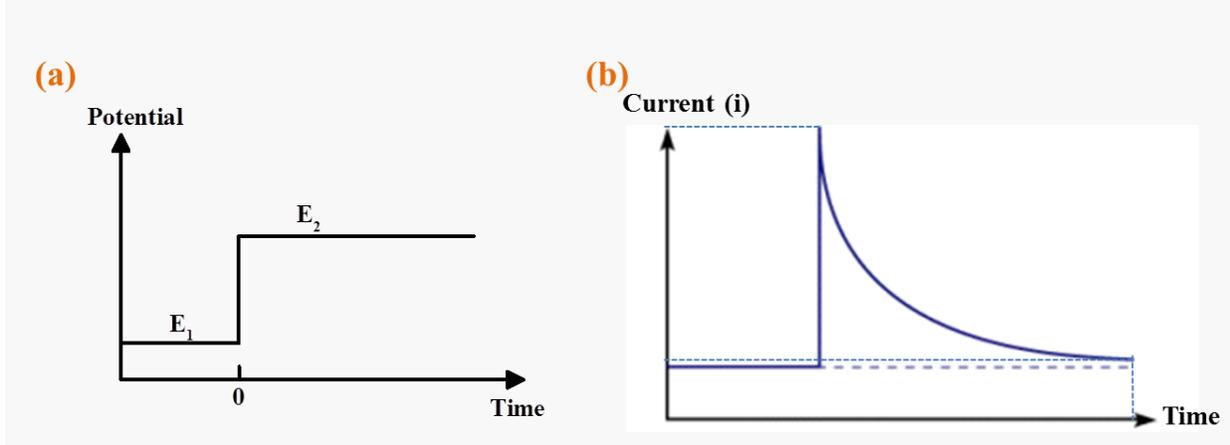
Figure 3.17 (a) Typical waveform of CA and (b) current–time response.

Instead of CV or LSV, chronoamperometry shown in Figure 3.17 (a) is accomplished by stepping instantaneously the potential from a potential at which no faradaic reaction occurs (e.g. the open circuit potential (OCP)) to a potential at which the reaction rate is controlled by mass transport rate (mass-transfer-limited region). The resulting current is measured versus time, as shown in Figure 3.17 (b). It is can be observed that the current rises instantaneously after the change in voltage and then begins to decay as a function time. Initially, the current is very large, being primarily limited by the ohmic resistance of the electrolyte and part of the current is consumed for (dis)charging the electrochemical double layer established adjacent to the surface of the WE. Due to the high overvoltage applied on the electrode, the reactants in vicinity of the surface get rapidly consumed. Because a stationary electrode and unstirred solution is used, the mass transfer from the bulk solution to surface of electrode is solely controlled by diffusion. As time progresses, the diffusion layer get expanded over time due to the depletion of reactant, and thus the concentration gradient decrease leading to the decay in the current. The diffusion-limited current-time dependence at a planar electrode is governed by the Cottrell equation [57]:

$$i_{D\,(t)} = \frac{nF\sqrt{D}\,C_0 A}{\sqrt{\pi}\sqrt{t}} = K_{cot}\,t^{-1/2} \tag{3.9}$$

where n, F, D, C, and t are the number of electrons, Faraday's constant, the diffusion coefficient, the concentration, and time, respectively.

3.3.3 Experimental Procedures for the electrochemical measurement

In this thesis, all the electrochemical tests are conducted in a three-compartment cell with a potentiostat/galvanostat (PGSTAT) Autolab from EcoChemie at room temperature. PLD and CBPLD-synthesized Pt-based catalysts were used as WE, a Pt coil was used as the CE and an Ag/AgCl, 3 M KCl was used as the RE. To minimize the ohmic drop, the reference electrode was separated from the analyte solution by a Luggin capillary that is placed very close to the WE. Throughout the thesis, the potential values are with respect to Ag/AgCl, 3 M KCl electrode. Prior to each electrochemical test, dissolved oxygen was removed from the electrolyte solution by bubbling argon for at least 30 min. Initially, the electrode surface is brought into a reproducible state by repetitive potential cycling in 0.5 M H_2SO_4. This procedure is also referred to as electrochemical cleaning and catalysts activation process [58]: While the upper potential limit needs to be lower if the catalysts are composed of leachable metals. This process also serves another two purposes. First, the features of Pt electrode are able to be examined in the blank electrolyte, and quantities (e.g. the real surface area) associated with the number of active sites can be acquired with this step. Second, the resulting cyclic voltammogram also acts as a reference to the behaviors of catalysts in the presence of electroactive species of interest (e.g. Ethanol, O_2).

Then, the electrocatalytic activity towards EOR is evaluated by means of CV, in a mixture of 1 M C_2H_5OH + 0.5 M H_2SO_4 deaerated solutions for ethanol oxidation reactions and in a solution of 0.5 M H_2SO_4 saturated by O_2 for oxygen reduction reactions, respectively. Afterwards, the catalysts for EOR undergo a durability test with a long term chronoamperometric test under a fix potential.

The detailed chemical reactions occurring during each step are elaborated in the following individual parts.

3.3.3.1 Features of Pt electrode in Acidic electrolyte

Figure 3.18 shows a typical voltammetry profile of polycrystalline Pt in the absence of electroactive species, which exhibits the characteristic "butterfly" shape due to the molecular hydrogen re-oxidation/evolution, the atomic hydrogen adsorption/desorption ($H_{ads/des}$), the double layer charging/discharging, and the Pt oxides formation/reduction processes [59-61]. The $H_{ads/des}$ region occurs at potentials between -0.165 to ca. 0.19 V, where a monolayer of atomic hydrogen

is under-potentially deposited onto the surface of Pt in the positive potential sweep via the following reaction:

$$Pt + H^+ + e^- \leftrightarrow Pt - H_{ads} \tag{3.10}$$

This reaction is a reversible process and thus a H_{ads} desorption process just occurs on the subsequent negative sweep. This $H_{ads/des}$ region is commonly composed of multiple peaks originated from different crystalline facets of polycrystalline Pt. The well-resolution of the $H_{ads/des}$ peaks in both the cathodic and the anodic sweeps indicates a better cleanliness of the exposed Pt surfaces.

In a lower potential range (ca. -0.165 V~0.2 V), hydrogen evolution occurs on the negative scan:

$$2Pt - H_{ads} \leftrightarrow 2Pt + H_2 \tag{3.11}$$

The counterpart anodic peak is due to re-oxidation of molecular H_2 evolved from the negative scan.
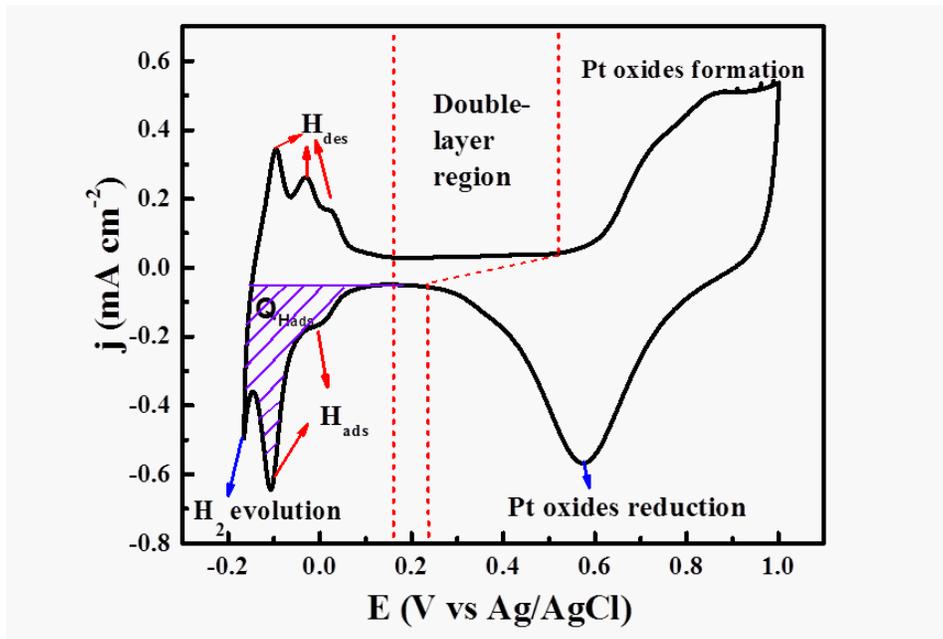
Figure 3.18 Cyclic voltammogram of polycrystalline Pt electrode in 0.5 M H₂SO₄-Ar purged solution with a scan rate of 50 mV s⁻¹.

The area under the anodic or the cathodic H_{upd} peaks can be employed to determine the real electroactive surface area (*ESA*) of Pt and some Pt-based (e.g. alloys or Pt-FMO) catalysts. However, the peaks due to H_2 evolution/reoxidation overlap with the $H_{ads/des}$ region, inhibiting an

79

accurate determination of the *ESA*. In most cases, the negative potential limit is chosen just at the onset potential of the H_2 evolution.

The Pt oxides formation/reduction reactions occur at higher potentials ranging from ca. 0.57 V to 1.2 V, exhibiting the common hysteresis character attributed to their sluggish kinetics [62]. In the positive-going sweep direction, Pt sites successively undergo two processes [63, 64]:

$$Pt + H_2O \leftrightarrow Pt^{\delta+} - O_{chem}^{\delta-} + 2H_{aq}^+ + 2e^- \qquad (3.12)$$

$$Pt^{\delta+} - O_{chem}^{\delta-} \rightarrow Pt^{2+} - O^{2-} \qquad (3.13)$$
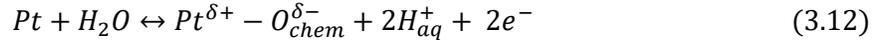
The intermediate region between H_{ads}/H_{des} region and the region for Pt oxides formation/reduction is the region where no faradic reactions take place except the double layer charging and discharging processes on the electrode. It is worth noting that the charging and discharging currents flow over the entire positive and negative sweep, respectively. As a result, the contribution from double-layer current must be subtracted prior to the quantitative analysis with other two regions.

3.3.3.2 The determination of surface area of electrode and roughness factor

For nanostructured catalysts, the real *ESA*, (in cm^2) of the catalysts is more concerned with respect to their geometric surface area (A_g, in cm^2). A_g is determined by assumption that the surface of electrode or the catalyst substrate is truly flat, while *ESA* gives the real surface area accessible to electrochemical reactions. The ratio between *ESA* and A_g, which is termed roughness factor (*RF*) reflecting the porosity or other natures associated to the accessibility of electroactive species to the active sites on catalyst.

$H_{ads}/_{des}$ region is often exploited to estimate *ESA* and/or the area specific activity (*ASA*, g m^{-2}) of Pt-based catalysts. In this work these two values are solely calculated from the charge associated with the H_{ads} process ($Q_{H_{ads}}$, in C), which is given by the following integration equation:

$$Q_{H_{ads}} = \frac{\int i \, dE}{\vartheta} \qquad (3.14)$$

where i (in A) is the transient current generated at the potential E (in V) in the H_{ads} region, and ϑ is the scan rate (V s^{-1}).

ESA is estimated as follows:

$$ESA = \frac{Q_{H_{ads}}}{0.21} \tag{3.15}$$

0.21 mC cm^{-2} is the charge to form a monolayer of hydrogen on Pt, which is estimated by assuming 1.3×10^{15} Pt atoms per cm^2 on polycrystalline Pt surfaces [65, 66].

ASA can be estimated based on the following equation:

$$ASA = \frac{Q_{H_{ads}}}{Pt\ loading \times 0.21 \times A_g} \tag{3.16}$$

3.3.3.3 Ethanol oxidation reaction

Cyclic voltammetry swept within the range of 0 V ~ 1.0 V at different scan rates of 5, 10, 20, 50, 100 and 200 mV s^{-1}, were carried out to qualitatively study catalysts activity toward ethanol oxidation. The activity of a catalyst can be valued by two important parameters: onset potential (E_{onset}, defined as the potential at which the anodic current starts to flow) and anodic peak current density (j_p). More active electrocatalysts will lead to an onset potential at a lower overpotential and a higher peak current at a relatively low potential.
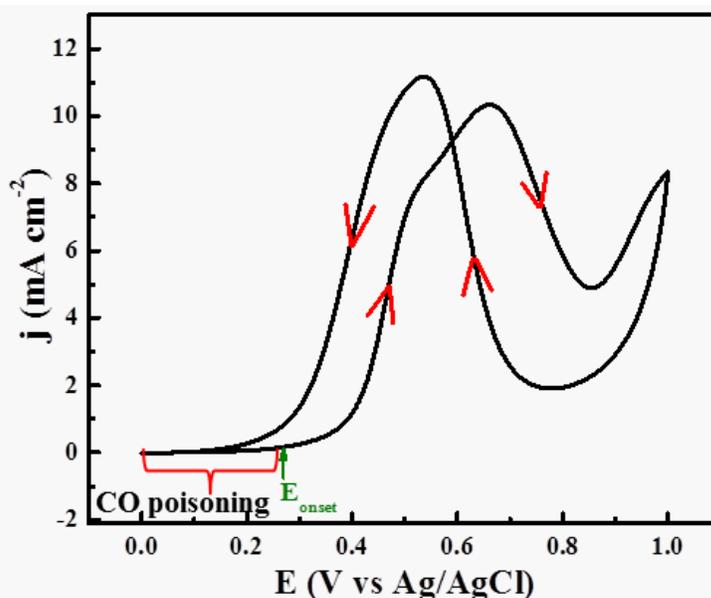
Figure 3.19 Cyclic voltammogram of CNTs/Pt electrode in 0.5 M H$_2$SO$_4$ + 1.0 M CH$_3$CH$_2$OH solution solution with a scan rate of 5 mV s^{-1}.

Figure 3.19 shows the voltammetric response of CNTs/Pt electrode, displaying typical ethanol oxidation waves in agreement with the literature [67, 68]. Briefly, the ethanol oxidation is

almost completely hindered by adsorbed poisoning intermediates (e.g. CO_{ads} and hydrocarbon residues) when the applied potential is below 0.28 V. Above the onset potential of 0.28 V, the intermediates start to be oxidized at an appreciable rate, leading to an ill-resolved double peak in the positive scan. At higher potentials, the reaction is first inhibited by Pt oxides formation and then increases again at ca. 0.9V due to the generation of Pt-OH which helps the removal of CO poisoning species. In the negative scan, after the reduction of Pt oxide, the anodic peak at ca. 0.52 V is due to the oxidation of remaining residues at the surface [67, 69].

To compare a series of catalysts with the same Pt loading, the peak currents normalized to A_g and to Pt mass loading are used. These parameters are extracted from CV curves recorded with a slow scan rate of 5 mV s^{-1} (quasi-steady state).

3.3.3.4 Durability test
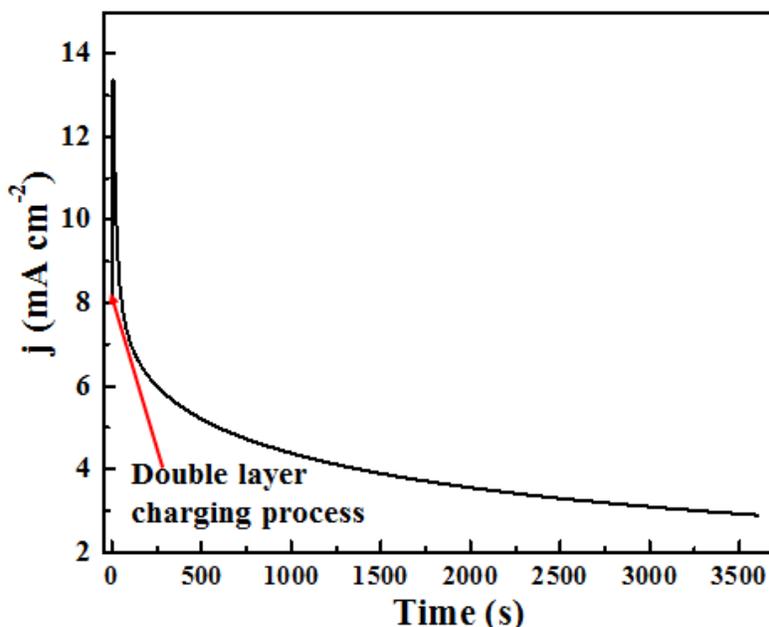
Figure 3.20 Chronoamperometric curve of CNTs/Pt electrode in 0.5 M H₂SO₄ + 1.0 M CH₃CH₂OH solution at an applied potential of 0.6 V.

A highly durable catalyst is crucial for the commercialization of fuel cells. For the catalysts towards EOR, chronoamperometric data were collected by stepping the potential from OCP to 0.6 V for a period of 3600 s, in contact with 0.5 M H₂SO₄ + 1.0 M ethanol solution at 25 °C. Figure 3.20 shows the *i-t* response of CNTs/Pt electrode. Initially, the charging process of the double-layer is accomplished in the first few seconds accompanied by the generation of a high charging current. Subsequently, there is a significant decay in current density which is due to the rapid

82

increase of the surface coverage by poisoning species such as CO$_{ads}$ [70, 71]. Finally, a quasi-steady state is reached up is attained to 1 h. A promising electrocatalyst should maintain a high steady state current density with time.

3.3.3.5 Oxygen reduction

The primary objective of this work is to explore the potential application of the PLD-synthesized FMO-Pt catalysts as cathodes for ORR. Due to the Micro-porous feature of as-prepared electrodes by using CP as the substrate, it is difficult to performance Rotating Disk Electrode (RDE) measurements of ORR on these electrodes. The electrochemical tests are carried out in the same 3-compartment cell as EOR tests in a quiescent electrolyte, which enables us to rapidly screen new catalysts for ORR.
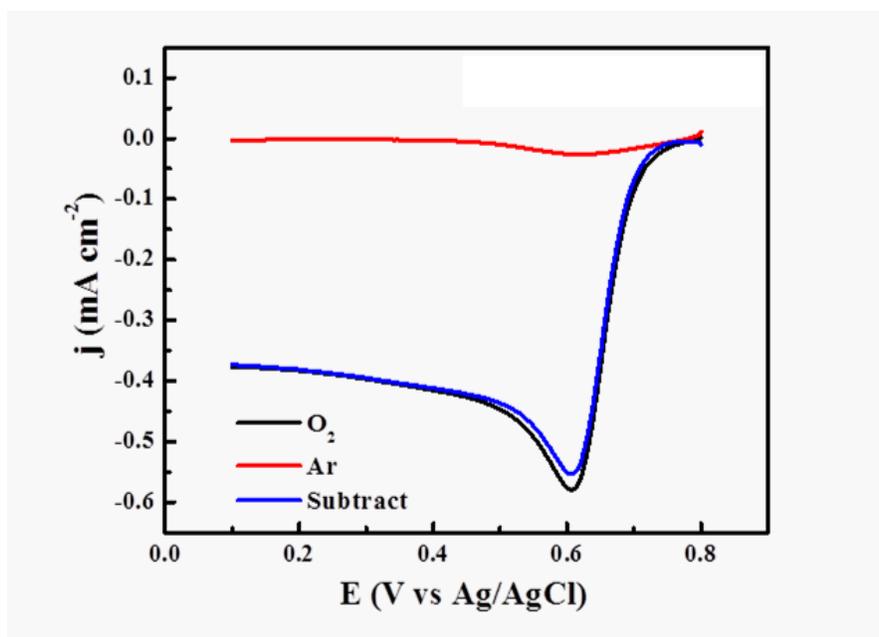
Figure 3.21 Electroactivity towards oxygen reduction reaction in 0.5 M H$_2$SO$_4$-oxygen saturated solution with a potential scan rate of 5 mV s^{-1}.

Upon completion of the electrochemical cleaning process in H$_2$SO$_4$ solution, the background current is measured with LSV scanned from 0.8 V to 0.1 V at scan rate of 5 mV s^{-1} which is mainly owing to contributions of capacitive current and faradic current from the reduction of Pt oxides. Afterward, the electrolyte is saturated with O$_2$ gas for at least 30 min. Then measurements are performed by linear potential scanning from 0.8 to 0.2 V at a scan rate of 5 mV s^{-1}. To assess the ORR performance of various electrodes, the LSVs were corrected from the residue (background) current recorded in deaerated H$_2$SO$_4$ solution (as shown in Figure 3.21). Two important parameters are extracted from the corrected LSV curves, namely, peak current

density and onset potential [72]. Regarding the onset potential, there are two ways to define it. It can be referred to as the potential at which the current starts to emerge. Alternatively, E_{onset} is often defined as the overpotential required achieving a certain current density [73].

For a series of catalysts with the same Pt mass loading, the catalyst displaying higher peak current density at lower potential and higher onset potential is regarded as a better catalytic activity for ORR.

REFERENCES

[1] S. Iijima. Nature, 354 (1991) 56-58.

[2] R.H. Baughman, A.A. Zakhidov, W.A. de Heer. Science, 297 (2002) 787-792.

[3] S. Iijima, T. Ichihashi. Nature, 363 (1993) 603-605.

[4] D. Tasis, N. Tagmatarchis, A. Bianco, M. Prato. Chem. Rev., 106 (2006) 1105-1136.

[5] E.T. Thostenson, Z. Ren, T.-W. Chou. Composites Science and Technology, 61 (2001) 1899-1912.

[6] A.J. Zarbin. Quim. Nova, 30 (2007) 1469.

[7] P.M. Ajayan. Chem. Rev., 99 (1999) 1787-1800.

[8] L. Dai, D.W. Chang, J.B. Baek, W. Lu. Small, 8 (2012) 1130-1166.

[9] M. Carmo, V.A. Paganin, J.M. Rosolen, E.R. Gonzalez. J. Power Sources, 142 (2005) 169-176.

[10] J. Prabhuram, T.S. Zhao, Z.K. Tang, R. Chen, Z.X. Liang. J. Phys. Chem. B, 110 (2006) 5245-5252.

[11] Y. Shao, G. Yin, Y. Gao. J. Power Sources, 171 (2007) 558-566.

[12] K.S. Ibrahim. Carbon letters, 14 (2013) 131-144.

[13] M. Kumar, Y. Ando. J. Nanosci. Nanotechnol., 10 (2010) 3739-3758.

[14] W.Z. Li, S.S. Xie, L.X. Qian, B.H. Chang, B.S. Zou, W.Y. Zhou, R.A. Zhao, G. Wang. Science, 274 (1996) 1701-1703.

[15] C.P. Deck, K. Vecchio. Carbon, 43 (2005) 2608-2617.

[16] S. Amelinckx, X. Zhang, D. Bernaerts, X. Zhang, V. Ivanov, J. Nagy. Opt. Commun, 2664 (1994) 977.

[17] S. Hofmann, R. Sharma, C. Ducati, G. Du, C. Mattevi, C. Cepek, M. Cantoro, S. Pisana, A. Parvez, F. Cervantes-Sodi, A.C. Ferrari, R. Dunin-Borkowski, S. Lizzit, L. Petaccia, A. Goldoni, J. Robertson. Nano Lett., 7 (2007) 602-608.

[18] M. Lin, J.P. Ying Tan, C. Boothroyd, K.P. Loh, E.S. Tok, Y.-L. Foo. Nano Lett., 6 (2006) 449-452.

[19] Y. Saito. Carbon, 33 (1995) 979-988.

[20] S. In Kwang, Y. Wan Jun, C. You Suk, C. Gyu Seok, K. Dojin. Nanotechnology, 15 (2004) S590.

[21] Pulsed laser deposition of thin films: applications-led growth of functional materials, John Wiley & Sons, 2007.

[22] A. Giardini Guidoni, C. Flamini, F. Varsano, M. Ricci, R. Teghil, V. Marotta, T.M. Di Palma.

Appl. Surf. Sci., 154–155 (2000) 467-472.

[23] D.H. Lowndes, D.B. Geohegan, A.A. Puretzky, D.P. Norton, C.M. Rouleau. Science, 273 (1996) 898-903.

[24] A. Bailini, F. Di Fonzo, M. Fusi, C.S. Casari, A.L. Bassi, V. Russo, A. Baserga, C.E. Bottani. Appl. Surf. Sci., 253 (2007) 8130-8135.

[25] Z. Chen, D. Pan, B. Zhao, G. Ding, Z. Jiao, M. Wu, C.-H. Shek, L.C.M. Wu, J.K.L. Lai. ACS Nano, 4 (2010) 1202-1208.

[26] G. Divitini, O. Stenzel, A. Ghadirzadeh, S. Guarnera, V. Russo, C.S. Casari, A.L. Bassi, A. Petrozza, F. Di Fonzo, V. Schmidt, C. Ducati. Adv. Funct. Mater., 24 (2014) 3043-3050.

[27] C.S. Casari, S. Foglio, M. Passoni, F. Siviero, C.E. Bottani, A. Li Bassi. Phys. Rev. B, 84 (2011).

[28] R. Ghosh, Y. Hara, L. Alibabaei, K. Hanson, S. Rangan, R. Bartynski, T.J. Meyer, R. Lopez. ACS Applied Materials & Interfaces, 4 (2012) 4566-4570.

[29] A. Pereira, F. Laplante, M. Chaker, D. Guay. Adv. Funct. Mater., 17 (2007) 443-450.

[30] F. Di Fonzo, D. Tonini, A. Li Bassi, C.S. Casari, M.G. Beghi, C.E. Bottani, D. Gastaldi, P. Vena, R. Contro. Applied Physics A, 93 (2008) 765-769.

[31] C. Hamel, S. Garbarino, É. Irissou, F. Laplante, M. Chaker, D. Guay. Int. J. Hydrogen Energy, 35 (2010) 8486-8493.

[32] E. Irissou, B. Le Drogoff, M. Chaker, M. Trudeau, D. Guay. J. Mater. Res., 19 (2004) 950-958.

[33] F.D. Fonzo, C.S. Casari, V. Russo, M.F. Brunella, A.L. Bassi, C.E. Bottani. Nanotechnology, 20 (2009) 015604.

[34] E. Irissou, B. Le Drogoff, M. Chaker, D. Guay. Appl. Phys. Lett., 80 (2002) 1716-1718.

[35] J.H. Noh, J.H. Park, H.S. Han, D.H. Kim, B.S. Han, S. Lee, J.Y. Kim, H.S. Jung, K.S. Hong. J. Phys. Chem. C, 116 (2012) 8102-8110.

[36] F. Sauvage, F. Di Fonzo, A. Li Bassi, C.S. Casari, V. Russo, G. Divitini, C. Ducati, C.E. Bottani, P. Comte, M. Graetzel. Nano Lett., 10 (2010) 2562-2567.

[37] L. Passoni, F. Ghods, P. Docampo, A. Abrusci, J. Martí-Rujas, M. Ghidelli, G. Divitini, C. Ducati, M. Binda, S. Guarnera, A. Li Bassi, C.S. Casari, H.J. Snaith, A. Petrozza, F. Di Fonzo. ACS Nano, 7 (2013) 10023-10031.

[38] J. Zhang, D.N. Oko, S. Garbarino, R. Imbeault, M. Chaker, A.C. Tavares, D. Guay, D. Ma. J. Phys. Chem. C, 116 (2012) 13413-13420.

[39] S. Petersen, S. Barcikowski. Adv. Funct. Mater., 19 (2009) 1167-1172.

[40] W.T. Nichols, T. Sasaki, N. Koshizaki. J. Appl. Phys., 100 (2006) 114912.

[41] B. Movchan, A. Demchishin. Fiz. Metal. Metalloved, 28 (1969) 653-660.

[42] J.A. Thornton. Journal of Vacuum Science & Technology A, 4 (1986) 3059-3065.

[43] A. Infortuna, A.S. Harvey, L.J. Gauckler. Adv. Funct. Mater., 18 (2008) 127-135.

[44] C. Thompson. Annual Review of Materials Science, 30 (2000) 159-190.

[45] S. Mukherjee, D. Gall. Thin Solid Films, 527 (2013) 158-163.

[46] D. Cattaneo, S. Foglio, C.S. Casari, A. Li Bassi, M. Passoni, C.E. Bottani. Surf. Sci., 601 (2007) 1892-1897.

[47] A. Tselev, A. Gorbunov, W. Pompe. Rev. Sci. Instrum., 72 (2001) 2665-2672.

[48] P. Bommersbach, M. Mohamedi, D. Guay. ECS Trans., 6 (2008) 217-223.

[49] R. Imbeault, D. Reyter, S. Garbarino, L. Roué, D. Guay. J. Phys. Chem. C, 116 (2012) 5262-5269.

[50] E. Irissou, F. Vidal, T. Johnston, M. Chaker, D. Guay, A.N. Ryabinin. J. Appl. Phys., 99 (2006) 034904.

[51] A. Tabet-Aoul, M. Mohamedi. Phys. Chem. Chem. Phys., 14 (2012) 4463-4474.

[52] A. Tabet-Aoul, F. Saidani, D. Rochefort, M. Mohamedi. Int. J. Electrochem. Sci, 6 (2011) 6385-6397.

[53] M.S. Dresselhaus, G. Dresselhaus, R. Saito, A. Jorio. Phys. Rep., 409 (2005) 47-99.

[54] Concepts, Instrumentation and Techniques of Neutron Activation Analysis, INTECH Open Access Publisher, 2013.

[55] R.R. Greenberg, P. Bode, E.A. De Nadai Fernandes. Spectrochimica Acta Part B: Atomic Spectroscopy, 66 (2011) 193-241.

[56] R. Zeisler, R.R. Greenberg. Journal of Radioanalytical Chemistry, 75 (1982) 27-37.

[57] Electrochemical methods: fundamentals and applications, Wiley New York, 1980.

[58] Y. Garsany, O.A. Baturina, K.E. Swider-Lyons, S.S. Kocha. Anal. Chem., 82 (2010) 6321-6328.

[59] K. Kinoshita, D.R. Ferrier, P. Stonehart. Electrochim. Acta, 23 (1978) 45-54.

[60] H. Angerstein-Kozlowska, B.E. Conway, W.B.A. Sharp. Journal of Electroanalytical Chemistry and Interfacial Electrochemistry, 43 (1973) 9-36.

[61] D.A.J. Rand, R. Woods. Journal of Electroanalytical Chemistry and Interfacial Electrochemistry, 35 (1972) 209-218.

[62] D. Gilroy, B. Conway. Can. J. Chem., 46 (1968) 875-890.

[63] G. Jerkiewicz, G. Vatankhah, J. Lessard, M.P. Soriaga, Y.-S. Park. Electrochim. Acta, 49 (2004) 1451-1459.

[64] M. Alsabet, M. Grden, G. Jerkiewicz. J. Electroanal. Chem., 589 (2006) 120-127.

[65] A. Pozio, M. De Francesco, A. Cemmi, F. Cardellini, L. Giorgi. J. Power Sources, 105 (2002) 13-19.

[66] T. Schmidt, H. Gasteiger, G. Stäb, P. Urban, D. Kolb, R. Behm. J. Electrochem. Soc., 145 (1998) 2354-2358.

[67] H. Wang, Z. Jusys, R.J. Behm. J. Power Sources, 154 (2006) 351-359.

[68] G.A. Camara, T. Iwasita. J. Electroanal. Chem., 578 (2005) 315-321.

[69] T. Iwasita, E. Pastor. Electrochim. Acta, 39 (1994) 531-537.

[70] X. Zhang, H. Zhu, Z. Guo, Y. Wei, F. Wang. J. Power Sources, 196 (2011) 3048-3053.

[71] J. Asgardi, J.C. Calderón, F. Alcaide, A. Querejeta, L. Calvillo, M.J. Lázaro, G. García, E. Pastor. Appl. Catal. B, 168–169 (2015) 33-41.

[72] M.N. Banis, S. Sun, X. Meng, Y. Zhang, Z. Wang, R. Li, M. Cai, T.-K. Sham, X. Sun. J. Phys. Chem. C, 117 (2013) 15457-15467.

[73] M.S. Faber, S. Jin. Energy & Environmental Science, 7 (2014) 3519-3542.

CHAPTER 4 PUBLICATIONS

The section is composed of four publications on the basis of the objectives of the doctoral project. Briefly, in two different manners (Co-deposition or LOL) four different FMOs were combined with Pt catalysts for DEFCs applications.

Article 1 presents the results of CeO_2-based catalysts towards ethanol oxidation. Pt-CeO_2 nanostructured thin films of different morphologies were prepared by means of CBPLD under different background gas pressures. According to the XRD, XPS, Micro-Raman and TEM analyses, the interactions of Pt with CeO_2 were found to vary with synthesis gas pressure, ultimately leading to different catalytic behavior. Furthermore, we have demonstrated the differences in structural properties of catalysts comprised of Pt and CeO_2 but with different architectures (Co-deposition and LOL). It was found that when CeO_2 material is beneath or when it is mixed with Pt, the interactions between Pt with CeO_2 are not similar, leading inevitably to different electrocatalytic performances. Given proper tailoring synthesis conditions, CBPLD-developed Pt-CeO_2 thin films are remarkably stable and provide electrochemical performance much greater than the layer onto layer CeO_2/Pt architecture.

Article 2 shows the results of SnO_2-based catalysts towards ethanol oxidation. Co-deposited Pt-SnO_2 thin films were prepared by using CBPLD under three different conditions. The physic-chemical properties of synthesized nanocomposites were characterized with SEM, XRD, XPS, Micro-Raman and TEM. It is observed that the interaction of SnO_2 with Pt modifies the electronic structure of the latter inducing the formation of ionized Pt^{2+} and Pt^{4+} while Sn revealed mixed Sn^{4+} and Sn^{2+} cations. An optimum electrocatalytic performance towards EOR is obtained with a Pt-SnO_2 grown under 0.5 Torr of He atmosphere. Versus a CNT/Pt electrode, this CNT/Pt-SnO_2 electrode (i) oxidizes ethanol at much lower potentials (86 mV negative), and (ii) displays a superior specific mass activity of 1.6 times and 2.2 times by cyclic voltammetry and long-term stability, respectively. Such performance is ascribed to a combination of: (i) SnO_2 has abundant hydroxyls on the surface and decrease the CO poisoning based on a bifunctional mechanism; (ii) modification of the electronic structure of Pt (electronic effect) and (iii) a semi-porous surface morphology favorable for the mass transfer of ethanol molecules.

Article 3 shows the results of MnO_2-based catalysts towards ethanol oxidation. The (Pt-MnO_2) nanocomposites with different surface morphology are directly grown for the first time at room temperature through CBPLD method and their electroactivity in sulfuric acid and towards

ethanol electrooxidation are examined. It is demonstrated that the electrochemical activity of the CNT/(Pt–MnO$_2$) nanocomposites outperforms the benchmark CNT/Pt material. The superior catalytic performance of the Pt-MnO$_2$ electrocatalyst towards ethanol oxidation is attributed to the presence of MnO$_2$, which promotes the electrocatalytic oxidation of ethanol by accelerating the dehydrogenation process, provides hydroxyl to oxidize the adsorbed intermediates (CO-like species) on Pt surface and by that increases Pt utilization through the synergistic effect between Pt and MnO$_2$.

Article 4 presents the results of TiO$_2$-based catalysts with LOL structure towards oxygen reduction reaction. Via pulsed laser deposition, various morphologies of TiO$_2$ thin films are synthesized at room temperature onto conductive microfibrous CP substrate. All synthesized TiO$_2$ films were characterized with SEM, XRD, XPS, Micro-Raman. Ultimately, their electrocatalytic supporting properties to Pt are investigated in H$_2$SO$_4$ and O$_2$-saturated H$_2$SO$_4$ solution. It is found that regardless of the film morphology, all the synthesized TiO$_2$ films dramatically increase the electroactive surface area of Pt and enhance its electroactivity towards oxygen reduction reaction as compared with bare Pt electrode.

ARTICLE 1

Cross-Beam Pulsed Laser Fabrication of Free-Standing Nanostructured Carbon Nanotubes-Pt-Ceria Anode with Unprecedented Electroactivity and Durability for Ethanol Oxidation

Fabrication par ablation laser à flux croisés d'anode de nanotubes de carbone-Pt-cérine nanostructurée et autosupportée avec une électroactivité et une durabilité sans précédent pour l'oxydation de l'éthanol

Authors

Youling Wang, Amel Tabet-Aoul, Maxime Gougis, Mohamed Mohamedi

Énergie, Matériaux et Télécommunications (EMT), Institut National de la Recherche Scientifique (INRS), Université d'Avant-garde, 1650 Boulevard Lionel Boulet, Varennes, Québec, J3X 1S2, Canada.

Contribution

I performed all the experimental synthesis, the electro-chemical measurements, and all characterizations (XRD, SEM and XPS) except the TEM and NAA measurements that have been done by technicians. I also realized the data analysis and interpretation of results. I participated in the writing with the help of other authors.

Résumé traduit

En raison des propriétés intrinsèques, comme une grande capacité pour stocker et libérer d'oxygène avec peu de distorsion du réseau, oxygène de maille qui a un rôle clé dans l'élimination de l'effet de l'empoisonnement au CO, non-toxicité, l'abondance, à faible coût et à faible traitement de la température, le CeO_2 apparaît comme une classe unique de matériau d'électrode pour piles à combustible à électrolyte polymère basse température, telles que des piles à combustible à l'éthanol direct (DEFCs). Cependant, l'exploitation maximale de ses propriétés fonctionnelles, est strictement dépendante de la disponibilité des voies de synthèse optimisées qui permettent la conception sur mesure, architecturing et la manipulation de CeO_2 de manière

précise quand il est combiné avec d'autres matériaux fonctionnels. Ici, nous utilisons l'ablation laser à flux croisés (CBPLD) pour synthétiser diverses noveles films de Pt-CeO$_2$ nanostructuré et autoportantes sur des nanotubes de carbone comme anodes pour la réaction d'oxydation de l'éthanol. Une autre signification de ce travail est qu'il établit l'importance de la conception de l'architecture de la couche de catalyseur. En effet, nous démontrons ici que lorsque le matériau CeO$_2$ est au-dessous ou quand il est mélangé avec Pt, les interactions entre Pt avec CeO$_2$ ne sont pas similaires menant inévitablement à performances électrocatalytiques différentes. Données les conditions propres de synthèse, les films de Pt-CeO$_2$ développées par CBPLD sont remarquablement stables et offrent des performances électrochimiques largement superieures à l'architecture couche sur couche CeO$_2$/Pt. Ces résultats, en plus du dépôt planaire du catalyseur Pt-CeO$_2$ peuvent ouvrir une nouvelle avenue pour les micro DEFCS pour les systèmes électroniques portables de faibles puissances.

Mots clés

Dépôt par ablation laser à flux croisés; Nanocatalyseurs de platine-cérine; Nanotubes de carbone, Éthanol; Amélioration de l'électroactivité et de la durabilité; Structure autosupportée du catalyseur

Abstract

Owing to its inherent properties such as great capacity to store and release oxygen with little distortion of the lattice, lattice oxygen that has a key role in removing the CO poisoning effect, non-toxicity, abundance, low cost and low temperature processing, CeO$_2$ is emerging as a unique class of electrode material for low temperature polymer electrolyte fuel cells such as direct ethanol fuel cells (DEFCs). However, the maximal exploitation of its functional properties is strictly reliant on the availability of optimized synthesis routes that allow tailor-designing, architecturing and manipulation of CeO$_2$ in a precise manner when it is combined with other functional materials. Here we use the cross-beam pulsed laser deposition (CBPLD) technique to synthesize various new free-standing (binderless) Pt-CeO$_2$ nanostructured thin films onto carbon nanotubes as anodes for ethanol oxidation reaction. Further significance of this work is that it establishes the importance in the design of the catalyst layer architecture. Indeed, we demonstrate here that when CeO$_2$ material is beneath or when it is mixed with Pt, the interactions between Pt with CeO$_2$ are not similar leading inevitably to different electrocatalytic performances. Given proper tailoring synthesis conditions, CBPLD-developed Pt-CeO$_2$ thin films are remarkably stable and provide electrochemical performance much greater than the layer onto layer CeO$_2$/Pt architecture. These

findings in addition to the planar deposition of Pt-CeO$_2$ catalyst may open new avenue for commercial micro DEFCs to power portable electronic systems.

Graphical abstract
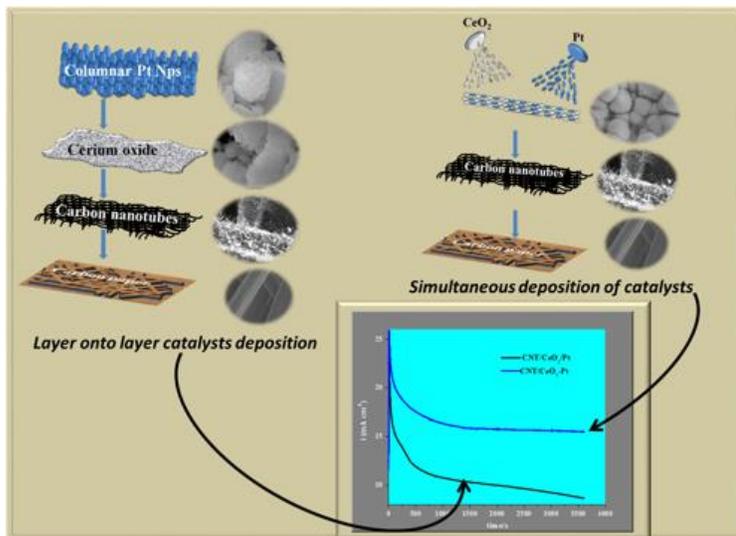
Key words

Cross-beam pulsed laser deposition; Platinum-ceria nanocatalysts; Carbon nanotubes, ethanol; Electroactivity and durability enhancement; Free-standing catalyst structure

1. Introduction

Several metal oxides are cheap, abundant and green. Owing to particular native properties and functions of their own, some functional metal oxide (FMO) are emerging as a unique class of electrode materials for a wide spectrum of applications in energy conversion devices such as fuel cells, photoelectrochemical cells [1, 2] and energy storage devices, like rechargeable batteries and supercapacitors [3]. Depending on the energy type system, FMO can act as a supporting matrix to improve catalyst dispersion and its stability against sintering and particles aggregation; be itself the electroactive material; or promotes certain electrocatalytic reactions. The future of energy conversion and storage technologies is strictly dependent on the readiness of improved production methods that permit tailor-designing, architecturing and handling of FMOs in a specific way to enhance particular functional properties principally when they are combined with other functional materials.

We have interest in developing FMO-based catalysts for green-based fuel cells principally low temperatures DEFCs. Ethanol is particularly interesting as a green, nontoxic fuel with high theoretical energy density and can be generated from biomass, which could make DEFCs advantageous low greenhouse gas emission power sources. Platinum is found to be the most active catalyst towards electrooxidation of ethanol. However, at Pt catalyst, the complete oxidation of ethanol to CO_2 is not achieved, because of CO poisoning and because the breaking of the C-C bond is not easily achieved at low temperature, which has a detrimental effect on the fuel cell efficiency [4]. It is now clear that a good electrocatalyst must activate C-H, C-O, and C-C bonds where Pt cannot realize these multiple functions alone. Solutions were then sought by combining Pt with one or two additional metals, such as Ru, Re, Rh or Sn among others [5]. These studies revealed somehow an enhancement of ethanol oxidation compared to pure Pt. Nevertheless, the complete oxidation of ethanol to CO_2 at low potentials was not accomplished, instead generating only acetic acid and acetaldehyde.

Cerium dioxide or ceria (CeO_2) is one of the cheapest and most abundant rare earth oxides and represents one of the most actively investigated FMO in materials applications [6-12]. Indeed, its inherent properties such as great capacity to store and release oxygen with little distortion of the lattice [13], as the cerium atom reversibly undergoes oxidation/reduction processes from Ce^{4+} to Ce^{3+}, lattice oxygen that has a key role in removing the CO poisoning effect, non-toxicity and low temperature processing make CeO_2 of great interest for energy conversion systems such as solid oxide fuel cells (SOFC) [14-16], and methanol fuel cells [17].

The chemistry of CeO_2 combined with Pt in ethanol solution is scarce. But the few published studies have shown that CeO_2 can promote the oxidation of ethanol at Pt catalyst [18-23]. Nevertheless, the textural properties of the CeO_2 seem dependent on the processing routes of Pt-CeO_2 composite electrodes often leading to different results. Consequently, several hypotheses have been suggested concerning the function of CeO_2 vis-à-vis the electrooxidation of ethanol. Indeed, CeO_2's role has been argued to be restricted to enhancing Pt nanoparticles dispersion, or to provide oxygen atoms at potentials lower than that achieved by Pt (bi-functional effect), or to modify the electronic structure of Pt and lessens the potential of ethanol adsorption of Pt (the electronic effect); or both the bi-functional and electronic effects. We believe that these discrepancies in interpretation associated to the function of CeO_2 are mainly due to the methods of synthesis of Pt-CeO_2 composites and to the architecturing of the electrode structure itself.

Several methods have been employed to prepare Pt-CeO_2 composites including combined method of impregnation and hot ammonium carbonate precipitation [24]; Pt-doped

94

CeO$_2$ thin film catalysts prepared by magnetron sputtering [25]; Pt/CeO$_2$ nanofibers synthesized through an electrospinning method followed by calcination [26]; layer onto layer Pt/CeO$_2$ prepared by pulsed laser deposition [27]; ultrasound-assisted method to fabricate Pt–CeO$_2$ hybrids [28]; microwave-assisted polyol process [29]; solution combustion route [30, 31]; and wet impregnation method [32].

We report for the first time adapting and optimizing the CBPLD method to synthesize at room temperature Pt-CeO$_2$ thin films of various surface morphologies onto carbon nanotubes (CNTs). An asymmetric CBPLD geometry makes it possible to mix materials of different targets (here CeO$_2$ and Pt) directly in the laser plasma with good control over film composition. For further details regarding the general characteristic of CBPLD, the reader is directed towards the review of Tselev et al [33]. Herein, CNTs, which act as the catalyst support are fabricated by chemical vapor deposition (CVD) onto an electrically conductive carbon paper substrate, CP (the current collector, CC), which is the type of gas diffusion layer used in fuel cell devices. Such materials are comprehensively characterized with scanning electron microscopy (SEM), X-ray diffraction (XRD), X-ray photoelectron spectroscopy (XPS), microRaman spectroscopy, and transmission electron microscopy (TEM) techniques and new insights into the interaction of CeO$_2$ with Pt materials are reported. Afterwards, we study the electroactivity and durability with post-mortem surface morphology of CeO$_2$-Pt co-deposits as well as catalytic promoting properties of CeO$_2$ to Pt towards the ethanol oxidation reaction (EOR).

A second crucial issue that has not been addressed in the literature concerns the proper way in which CeO$_2$ must be inserted within the whole catalyst layer in order to fully benefit from its promoting properties in electrocatalysis of fuel cells reactions. There are two ways of including CeO$_2$ into the catalyst layer, the first one is to intercalate it between the catalyst support and Pt, i.e., the layer onto layer architecture [27]; and the second way is to simultaneously deposit Pt and CeO$_2$ onto the catalyst support. Now, does CeO$_2$ have the same effect on the electrocatalytic performance regardless of its position in the catalyst layer? Such question is undertaken here and response is provided that helps a proper architecturing of advanced functional Pt and CeO$_2$ energy materials.

95

2. Experimental Section

2.1. Materials

Ni (99.99%), Pt (99.99%) and CeO_2 (99.99%) targets used for the PLD and CBPLD were purchased from Kurt J. Lesker Co. Untreated carbon paper (CP, Toray) was purchased from Electrochem. The CP is the type of gas diffusion layer used in fuel cell devices (Figure S1). Sulfuric acid (H_2SO_4, 96%) and ethanol (100% purity) were purchased from Agros Organics and Commercial Alcohols inc., respectively. The reactants were used as received without further purification.

2.2. Syntheses

CNTs were grown at 700ºC by CVD using Ni as catalyst deposited by PLD onto CP substrate, acetylene (carbon source), hydrogen and argon (gas carrier) gases at flow rates of 30, 140 and 100 sccm, respectively. Full details regarding the CNTs synthesis can be found elsewhere [34, 35].

Pt-CeO_2 composites were prepared by CBPLD (dual beam) by simultaneously depositing Pt and CeO_2. All the deposits were made at room temperature by means of a pulsed KrF excimer laser (λ= 248 nm, pulse width= 17 ns, and repetition rate= 50 Hz) using a laser fluence of 4 J cm^{-2}. Pt-CeO_2 composites were deposited under different conditions of background gas pressure in order to obtain different surface morphologies. Prior to each deposition, the chamber was evacuated with a turbo pump (4×10^{-5} Torr). In all cases, the substrate-to-target distance was fixed at 5 cm. In order to obtain a uniform ablation over the target surface, the target was continuously rotated and translated. Each (Pt-CeO_2) catalyst was deposited with 50000 laser pulses giving a Pt loading of 120 µg cm^{-2} (measured by neutron activation analysis, NAA). Three catalysts are considered in this work, namely: (Pt-CeO_2)$_{UV}$, (Pt-CeO_2)$_{0.5T}$, and (Pt-CeO_2)$_{2T}$, where the subscripts UV and T stand for under vaccum and Torr, respectively.

2.3. Material Characterization

The surface morphology of the as-prepared samples was characterized using SEM (JEOL, JSM 7401F apparatus) and TEM and high-resolution (HR)-TEM (JEOL-JEM-2100F operating at 200 kV).

The crystalline structure of all samples was determined by XRD using a Bruker D8 Advance diffractometer equipped with a Cu Kα source. The diffractometer was operated at 40 kV and 40 mA. All diffractograms were acquired in the Grazing Incidence Diffraction (GID) scan mode with an incident angle of 2°, 2θ angular step size of 0.05° and acquisition time of 5 seconds per step.

XPS measurements were performed using a VG Escalab 220i-XL equipped with an Al Kα source (1486.6 eV). The anode was operated at 10 kV and 20 mA. The pass energy of the analyzer was fixed at 20 eV. All samples were analyzed with a spot size of 250 × 1000 μm located approximately in the center of the sample. A survey spectrum ranging from 0 to 1350 eV was first acquired, and then higher resolution multiplex scan spectra (Pt 4f, Ce 3d, O 1s, and C1s core levels) were obtained. Quantification of the elements was carried out with CasaXPS software (Casa Software Ltd.) by fitting the core level spectra after a Shirley background removal. The metallic components of the Pt 4f region were fitted using a Gaussian/Lorentzian asymmetrically modified line shape, and a Gaussian/Lorentzian line shape was used to fit the other components. The C 1s core level peak at 284.6 eV, resulting from hydrocarbon contaminants at the surface, was used as an internal reference. All spectra have been recalibrated with respect to the C 1s core level peak of adventitious carbon contamination.

2.4. Electrochemical Characterization

The electrochemical properties of all samples were evaluated by cyclic voltammetry (CV) and chronoamperometry (CA) in a three compartment electrochemical cell at room temperature. A Pt coil was used as the counter electrode and an Ag/AgCl, 3 M NaCl was used as the reference electrode. The reference electrode was separated from the analyte solution by a Luggin capillary that is very close to the working electrode to minimize the ohmic drop. Data acquisition was conducted with a potentiostat/galvanostat Autolab from EcoChemie. CV measurements were carried out in 0.5 M H_2SO_4 and in a mixture of 1 M C_2H_5OH + 0.5 M H_2SO_4 deaerated solutions. CA was employed for durability evaluation of the catalysts in 1 M C_2H_5OH + 0.5 M H_2SO_4. Prior to the electrochemical measurements in ethanol, the surface of the working electrode was cleaned electrochemically by potential cycling in 0.5 M H_2SO_4. Before each test, dissolved oxygen was removed from the solution by bubbling argon for 30 min. Both the geometric area of the electrode and its Pt loading were used to rationalize the activity of electrocatalyst.

3. Results and Discussion
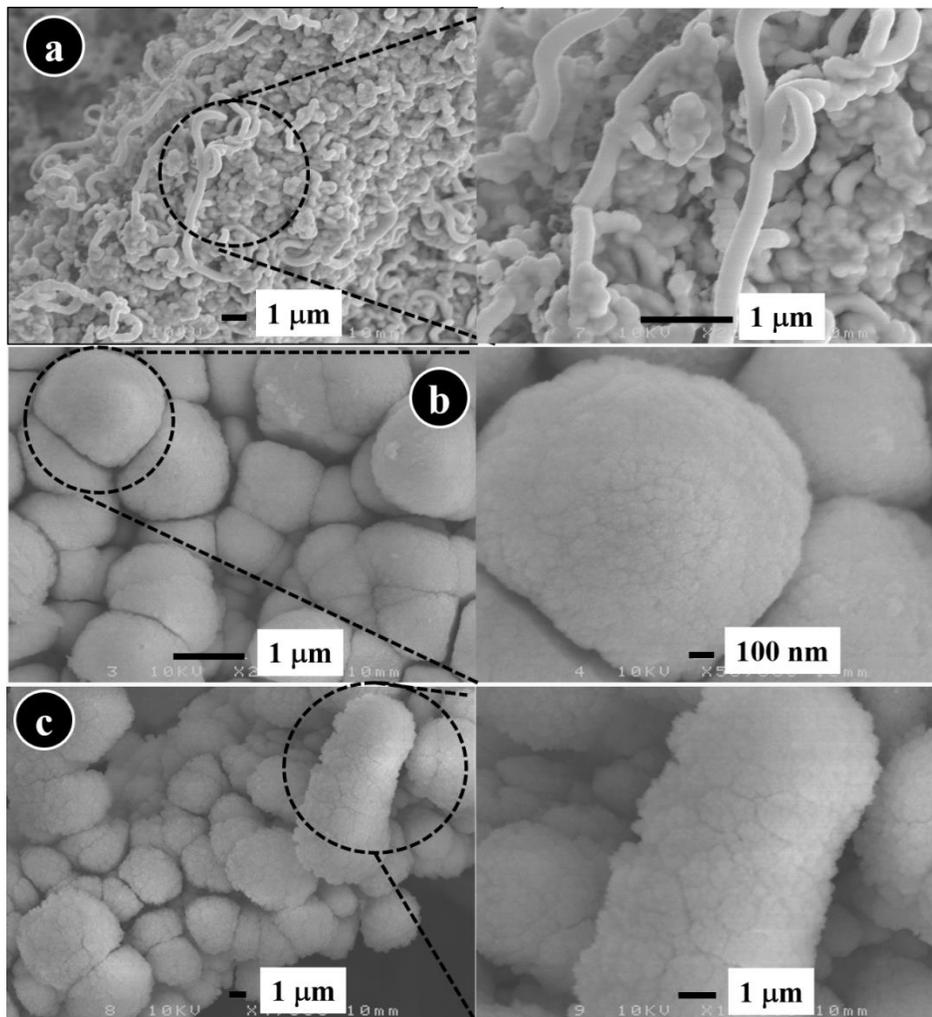
3.1. Characterization

Figure 1. SEM micrographs with increasing magnification of CBPLD-synthesized (Pt-CeO$_2$) films onto CNTs catalyst support. (a) (Pt-CeO$_2$)$_{UV}$ film; (b) (Pt-CeO$_2$)$_{0.5T}$ film; and (c) (Pt-CeO$_2$)$_{2T}$ film.

Figure 1 shows SEM images with increasing magnifications of CBPLD synthesized Pt-CeO$_2$ onto CNTs. Considerable differences in the surface morphology are observed between the various deposits. Figure 1a shows that CNTs are homogeneously coated with a (Pt-CeO$_2$)$_{UV}$ film that is smooth and of closed structure. On the other hand, Pt-CeO$_2$ films deposited under He atmosphere display porous structures. The (Pt-CeO$_2$)$_{0.5T}$ particles gather into highly compacted large grains in a fashion reminiscent of a calotte (Figure 1b), whereas (Pt-CeO$_2$)$_{2T}$ particles assemble into cauliflower or broccoli-like arrangements (Figure 1c). SEM images at higher

magnification shows that the surface topography of $(Pt-CeO_2)_{2T}$ is more porous but looks scaly and brittle.

The XRD profiles of the $(Pt-CeO_2)$ samples show the presence of diffraction peaks (111), (200), (220), and (311) corresponding to the fcc fluorite structure of CeO_2 (JCPDS file 13-1002) (Figure S2). The Pt(111) reflection was observed at the $(Pt-CeO_2)_{UV}$ but no detectable Pt at the $(Pt-CeO_2)_{0.5T}$ and $(Pt-CeO_2)_{2T}$ samples. However, the existence of Pt particles was verified by using energy dispersion spectroscopy (EDS) under transmission electron microscope (Figure S3).

The PLD involves complex physical processes of laser-material interaction during the impact of the high-power pulsed radiation on a solid target [36, 37]. Briefly, the morphological differences observed between the deposited $Pt-CeO_2$ films are principally due to the decrease of the kinetic energy of the deposited species which varies with the atmosphere in the deposition chamber. The variation of the kinetic energy of the plasma species induces a modification of the surface mobility of the deposited species. In vacuum, the absence of collisions between the expanding plasma and the surrounding gas molecules leads to a situation where the kinetic energy of the plasma species is the highest. Greater surface mobility of the deposited species transforms into denser films and surface reorganization that lead to minimization of the energy, which is the case observed here for $(Pt-CeO)_{UV}$ (Figure 1a). On the contrary, the presence of an atmosphere in the deposition chamber will decrease the kinetic energy of the plasma species. Owing to that fact, the expanding plasma will interact more strongly with the molecules of the gas. As the pressure in the deposition chamber is increased, the likelihood for the plasma species to lose part of their kinetic energy through a contact (collision) with the gas molecules will be also increased, thus lowering the kinetic energy of the plasma species. This decrease of the kinetic energy of the plasma species induces a modification of the surface mobility of the deposited species leading to a porous film (Figure 1b and Figure 1c). More details regarding the influence of the atmosphere chamber on the physical processes of laser-material interaction can be found elsewhere [33, 36-38].

The high-resolution Pt 4f and Ce 3d core level XPS spectra of the $CNT/(Pt-CeO_2)$ thin films are shown in Figure 2a and Figure 2b, respectively. For referencing, the Pt 4f core level spectrum of pure PLD-deposited Pt onto CNTs is also reported in Figure 2a. The Pt 4f spectrum of pure Pt shows a doublet containing a low energy band (Pt $4f_{7/2}$) and a high energy band (Pt $4f_{5/2}$) at 71.30 and 74.58 eV, respectively. The 3.28 eV binding energy (*BE*) difference between the Pt $4f_{7/2}$ and Pt $4f_{5/2}$ is consistent with Pt being in a metallic state [39]. No other chemical states of Pt were identified and satisfactory fitting of each core level peak was obtained using only one

component with an asymmetric profile. On the other hand, the XPS spectra of the co-deposited CNT/(Pt-CeO$_2$) films reveal that Pt is present in more than one oxidation states. To identify the different chemical states of Pt, the spectra could be fitted by three overlapping curves, labeled Pt^0, Pt^{2+}, and Pt^{4+}. Pt-CeO$_2$ composite exhibiting ionized platinum have been observed by some researchers [25, 40, 41], and this is the first time it is observed for (Pt-CeO$_2$) films prepared by CBPLD technique. The position and relative amount of Pt species were estimated from the relative intensities of these three peaks, and the results are summarized in Table 1. The position of Pt^{2+} and Pt^{4+} are in accordance with these reported in the literature [42-44]. From Table 1, it can be noted that (Pt-CeO$_2$)$_{UV}$ contains significant amount of Pt^0 of 63 at%. The amount of Pt^0 significantly decreased to less than 7 at% for samples deposited under He atmosphere. Furthermore, the Pt^{2+}/Pt^{4+} ratio increased with the increase of the background pressure. The Ce 3d core level XPS spectra of the (Pt-CeO$_2$) films reported in Figure 2b consist of three 3d$_{5/2}$–3d$_{3/2}$ doublets characteristic of Ce^{4+} (CeO$_2$) and two doublets of Ce^{3+} [45, 46]. Table 1 shows the Ce^{3+}/Ce^{4+} ratio obtained by calculating sums of areas of the Ce 3d doublets. The (Pt-CeO$_2$)$_{2T}$ displayed the highest Ce^{3+}/Ce^{4+} ratio, while (Pt-CeO$_2$)$_{0.5T}$ and (Pt-CeO$_2$)$_{UV}$ showed ratios close to each other.

Table 1 XPS parameters extracted from Figure 2a and Figure 2b.

Sample	Pt^0		Pt^{2+}		Pt^{4+}		Pt^{2+}/Pt^{4+}	Ce^{3+}/Ce^{4+}
	BE (eV)	at%	BE (eV)	at%	BE (eV)	at%		
Pt	71.30	100	-	-	-	-	-	
(Pt-CeO$_2$)$_{UV}$	71.12	62.97	72.63	31.45	74.12	5.58	5.64	0.64
(Pt-CeO$_2$)$_{0.5T}$	70.84	6.32	72.30	85.96	73.84	7.03	12.23	0.61
(Pt-CeO$_2$)$_{2T}$	71.67	4.71	73.17	91.06	74.67	4.23	21.52	1.02

The results of Figure 2a and Figure 2b show that CeO$_2$ was reduced during its simultaneous deposition with Pt. These observations are similar to Pt doped CeO$_2$ layers deposited by (rf) magnetron sputtering on CNTs [41, 47, 48]. The authors assumed this behavior to a relative increase of oxygen vacancies, which are present at the cerium oxide crystallite surface. They supposed that Pt^{4+} (PtO$_2$) species correspond to Pt cations substituting Ce cations in the CeO$_2$ lattice, and that Pt^{2+} are formed by Pt atoms located at the crystallite surface. The authors further observed an increase in the Pt^{2+}/Pt^{4+} ratio with Pt content which could be hypothetically explained by higher segregation of platinum to the grain boundary region with increasing dose of Pt doping. Despite that in our work, the amount of Pt was the same for all the (Pt-CeO$_2$) samples, we do however observe an increase in the Pt^{2+}/Pt^{4+} with the increase of the background pressure (Table 1). Such trend is observed for the first time and will be a subject of study in the future.
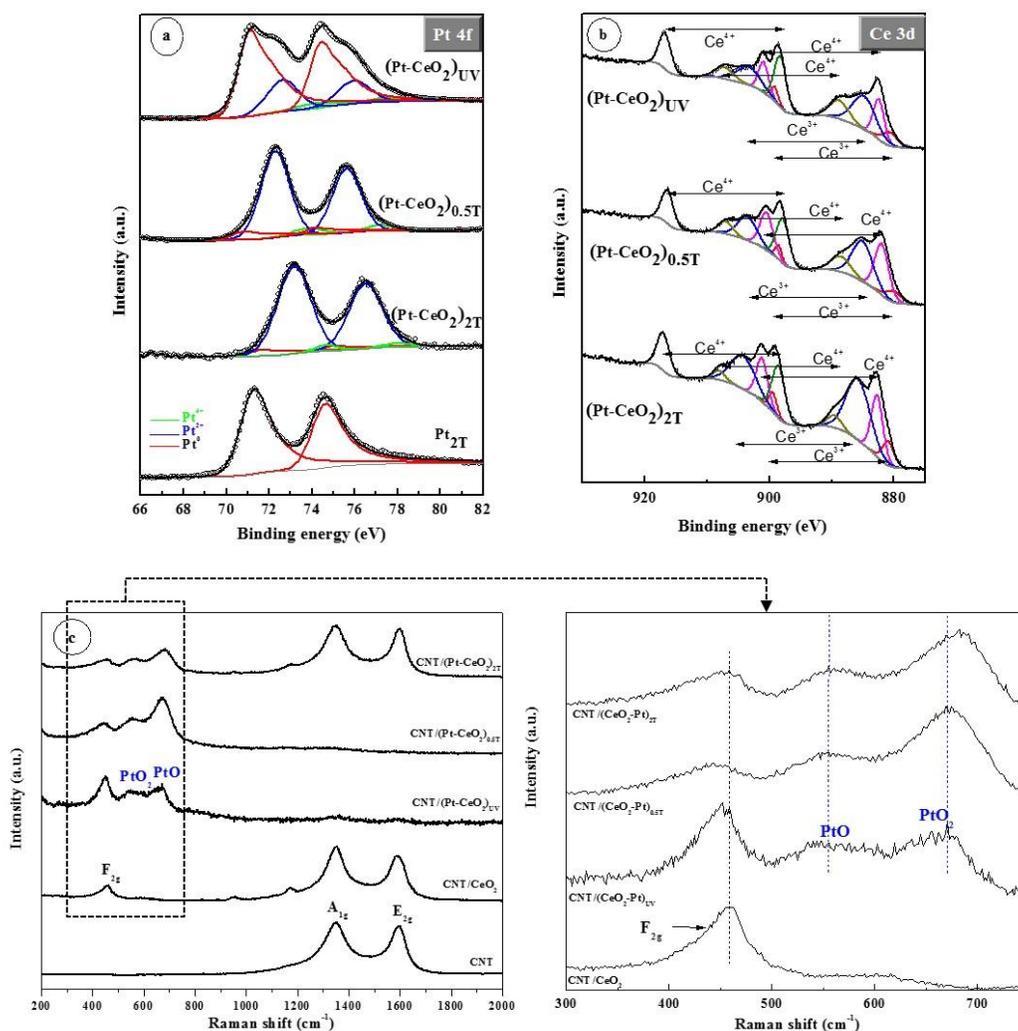
Figure 2. Spectroscopy analyses of CBPLD-synthesized (Pt-CeO$_2$) films. High-resolution XPS spectra of (a) Pt 4f core level (the spectrum of pure Pt is shown for referencing) and (b) Ce 3d core level. (c) Raman spectra. The Raman spectra of bare CNTs and CNT/CeO$_2$ materials are shown for referencing.

The Raman spectra of the pristine CNTs, CNT/CeO$_2$, and CNT/(Pt-CeO$_2$) samples are presented in Figure 2c. The spectrum of pristine CNTs exhibits two main characteristic bands, the first order G mode (E$_{2g}$ symmetry) at ~1596 cm^{-1} ascribed to a regular sp^2 graphitic network, and the D mode (A$_{1g}$ symmetry) at ~1348 cm^{-1}, which reflects the disorder and defects in the carbon lattice [49]. In addition to the D and G bands characteristics of the CNTs, the spectrum of the CNT/CeO$_2$ layers displays bands within 200~1170 cm^{-1} range. The band located at ~458.5 cm^{-1} is ascribed to triply degenerate Raman active F$_{2g}$ mode [50]. Only the oxygen atoms move in this mode, which is therefore very sensitive to the oxygen sublattice disorder resulting from processing and/or grain-size-induced non-stoichiometry.

Table 2. Raman parameters of CeO$_2$ extracted from Figure 2c.

Sample	F$_{2g}$ (cm^{-1})	FWHM (cm^{-1})	Grain size (nm)
CNT/CeO$_2$	458.5	45.0	3.6
CNT/(Pt-CeO$_2$)$_{UV}$	452.6	35.8	4.8
CNT/(Pt-CeO$_2$)$_{0.5T}$	446.0	44.5	3.6
CNT/(Pt-CeO$_2$)$_{2T}$	456.4	61.5	2.4

Mixing Pt to ceria definitely produces a dramatic change in the Raman response and clearly reflects interactions between CeO$_2$ and Pt. The position of the F$_{2g}$ band and its corresponding full width half maximum (FWHM) for all the samples are resumed in Table 2. For a bulk CeO$_2$, the F$_{2g}$ mode is located at ~465.4 cm^{-1} with a FWHM of 9.5 cm^{-1} [51, 52]. As can be seen from Table 2, all CeO$_2$-based samples synthesized under our conditions displayed a red shift and broadening of the FWHM compared to bulk CeO$_2$. Some authors have reported red shift and broadening of the phonons in ceria materials, which was differently interpreted. It was ascribed for example to the formation of nanocrystalline phase for the film [53], or to poorer crystalline quality for the film, or to the softening of the Raman F$_{2g}$ mode in nanocrystalline ceria (457 cm^{-1} versus 464.3 cm^{-1} in polycrystalline sample) as a consequence of phonon confinement effects [54]. Other researchers simultaneously considered phonon confinement, stress, size distribution and non-stoichiometry as possible causes for grain size induced variations of ceria Raman spectra [50]. The Raman line broadening of CeO$_2$ has been described by the dependence of the half-width, Γ, on the inverse of grain size, d_g, which follows a linear behavior [55-57].

$$\Gamma\ (cm^{-1}) = 10 + \ (124.7/d_g) \tag{1}$$

As can be seen from Table 2, the Raman line broadens with decreasing grain size. Using the above relation, we found the crystal size of the CeO$_2$ in the (Pt-CeO$_2$) samples to be 4.8, 3.6, and 2.4 nm for the (Pt-CeO$_2$)$_{UV}$, (Pt-CeO$_2$)$_{0.5T}$ and (Pt-CeO$_2$)$_{2T,}$ respectively (Table 2). Figure S4 shows that these data follow a linear behavior, which is in good correlation with that reported for nanoscrystalline CeO$_2$ powder specimens [51].

In addition to the F$_{2g}$ mode, the three CNT/(Pt-CeO$_2$) samples showed two new Raman bands at ~547.3 and ~678.3 cm^{-1} (Figure 2c). The 678.3 cm^{-1} vibration is consistent with the vibration of crystalline PtO, whereas the 547.3 cm^{-1} vibration is consistent with the vibration of crystalline PtO$_2$ [58, 59]. In Figure 2c is also reported the Raman spectrum of CNT/CeO$_2$/Pt layer onto layer architecture, which does not show the presence of Pt-oxide. The results from Raman are a clear demonstration of oxidation of Pt in the co-deposited samples. Consequently, it can be

concluded that the Pt^{4+} (PtO_2 species) appearing in the XPS correspond to Pt^{4+} substituting Ce^{4+} cations in the CeO_2 lattice, which corroborates the assumption of Fiala et al [47].
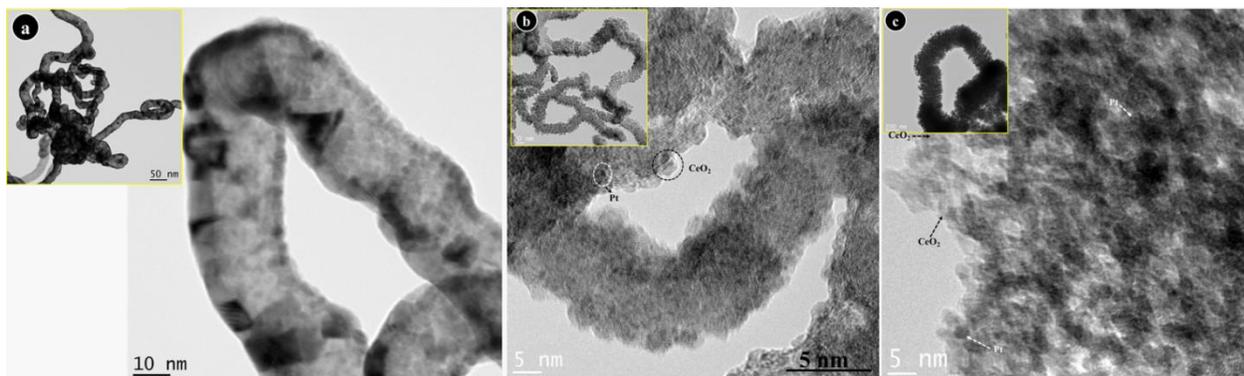
Figure 3 Upper left panels are TEM and main panels are HR-TEM micrographs of CBPLD-synthesized (Pt-CeO₂) films onto CNTs catalyst support. (a) (Pt-CeO₂)_UV film; (b) (Pt-CeO₂)_0.5T film; and (c) (Pt-CeO₂)_2T film.

Figure 3 shows TEM and HR-TEM images of the different CBPLD-synthesized (Pt-CeO_2) films onto CNTs. In all cases, it can be seen that CNTs are well-coated with Pt-CeO_2 films. In addition, the images confirm the marked difference in the morphology of the different deposits, i.e., a highly closed structure of the $(Pt$-$CeO_2)_{UV}$ film and the porous structure for the $(Pt$-$CeO_2)_{0.5T}$ and $(Pt$-$CeO_2)_{2T}$ films. The crystallographic orientation by means of selected area electron diffraction (SAED) patterns of the $CNT/(Pt$-$CeO_2)_{UV}$ film reveal both the presence of polycrystalline Pt and CeO_2 (Figure S5a). On the other hand, the SAED patterns of both $CNT/(Pt$-$CeO_2)_{0.5T}$ (Figure S5b) and $CNT/(Pt$-$CeO_2)_{2T}$ (Figure S5c) show the presence of CeO_2, Ce_2O_3 and PtO but no Pt. These observations are in line with those obtained with XRD, XPS and Raman analyses.

3.2. Electroactivity
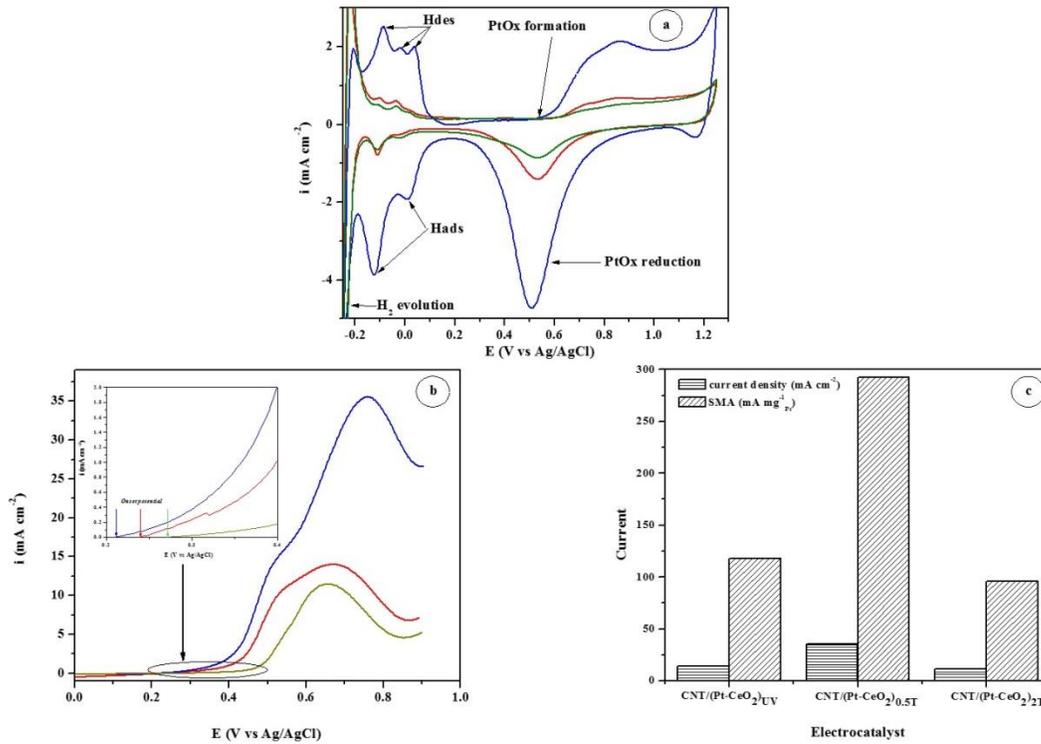
Figure 4. Electroactivity of CBPLD-synthesized (Pt-CeO$_2$) films onto CNTs catalyst support. (a) Cyclic voltammetry in 0.5 M H$_2$SO$_4$-argon purged solution with a potential scan rate of 50 mV s^{-1}. (b) Linear scan voltammetry in 0.5 M H$_2$SO$_4$ + 1 M C$_2$H$_5$OH argon purged solution with a potential scan rate of 5 mV s^{-1}. (c) Current peak density and *SMA* values extracted from Figure 4b. (Pt-CeO$_2$)$_{UV}$ (red line), (Pt-CeO$_2$)$_{0.5T}$ (blue line) and (Pt-CeO$_2$)$_{2T}$ (green line).

Figure 4a presents CVs with potential scan rate of 50 mV s^{-1} at the CNT/(Pt-CeO$_2$) electrodes in 0.5 M H$_2$SO$_4$ deaerated solution. The CVs include the very well-known hydrogen adsorption (H$_{ads}$) and desorption (H$_{des}$) peaks in the potential region of ca. -0.2 to 0.1 V vs. Ag/AgCl [60, 61]. The Pt oxide formation occurs within 0.50~0.6 V range where as its counterpart reduction peak potential takes place between 0.50 and 0.55 V vs. Ag/AgCl (as depicted in Figure 4a). Although similar electrochemical features are observed, their resolution depended markedly on the morphology of the different (Pt-CeO$_2$) samples. First, the characteristic peaks in the H$_{ads}$/H$_{des}$ region at (Pt-CeO$_2$)$_{0.5T}$ sample are distinctively sharper, which clearly indicates the higher number and better cleanliness of the exposed Pt surfaces in the (Pt-CeO$_2$)$_{0.5T}$ sample [62]. Second, the greater symmetric peak shapes in the H$_{ads}$/H$_{des}$ region of (Pt-CeO$_2$)$_{0.5T}$ sample are also suggestive of a highly reversible hydrogen adsorption/desorption process as compared with that of (Pt-CeO$_2$)$_{UV}$ and (Pt-CeO$_2$)$_{2T}$ samples [63]. Finally, the CV profile of (Pt-CeO$_2$)$_{0.5T}$ sample displays a

higher capacitive current after the Pt oxide formation, which indicates that this material possesses higher surface area.

In addition, from Figure 4a, it is seen that the voltammetric current responses of the samples in the H_{ads}/H_{des} region are different. Since the Pt loading in all the samples is the same, the variation in the current response is attributed to the difference in the number of electroactive sites in the samples for hydrogen adsorption/desorption. Basically, this is characterized as the real electroactive surface area (*ESA*) of the samples, which can be determined as follows:

$$ESA = Q_H/Q_{ref} \tag{2}$$

Q_H is obtained by integrating the charge in the hydrogen adsorption region of the CVs shown in Figure 4a, corrected for the double-layer current by back extrapolation of the current from the double layer region. Q_{ref} is a conversion factor of 210 C cm^{-2}, generally accepted for polycrystalline Pt electrodes [64]. The *ESA* of Pt nanocrystals in (Pt-CeO$_2$)$_{UV}$, (Pt-CeO$_2$)$_{0.5T}$, and (Pt-CeO$_2$)$_{2T}$ samples was estimated to be 5.61, 16.80, and 2.77 cm^2 respectively. The electrochemical activity of the Pt-CeO$_2$ catalysts can be further assessed with the area specific activity (*ASA*) (normalized by the Pt catalyst loading to generate mass activity) as follows:

$$ASA = Q_H/(Q_{ref} \times Pt\ loading \times A_g) \tag{3}$$

where A_g represents the geometric electrode area.

Note that the *ESA* provides an intrinsic electrocatalytic value of a catalyst, whereas *ASA* is an essential parameter concerning the practical application, i.e., the economic value of the catalyst, which basically is the activity normalized to cost. The *ASA* of Pt in (Pt-CeO$_2$)$_{UV}$, (Pt-CeO$_2$)$_{0.5T}$, and (Pt-CeO$_2$)$_{2T}$ samples was estimated to be 8.81, 38.2, and 6.46 m^2 g^{-1}, respectively. These results show that, despite of similar Pt loading in each sample, the (Pt-CeO$_2$)$_{0.5T}$ electrode displayed much higher *ESA* and *ASA* values.

Afterwards, the electrocatalytic activity of the Pt-CeO$_2$ samples was investigated towards ethanol electrooxidation. Figure 4b shows linear scan voltammograms (LSVs) recorded in 0.5 M H$_2$SO$_4$+ 1 M C$_2$H$_5$OH solution with slow scan rate of 5 mV s^{-1} (quasi-steady state). The LSVs at all the electrodes displayed well defined characteristic ethanol oxidation waves in agreement with the literature [65, 66]. The insert of Figure 4b shows that (Pt-CeO$_2$)$_{0.5T}$ catalyst oxidizes ethanol at potentials lower than those delivered by (Pt-CeO$_2$)$_{UV}$ and (Pt-CeO$_2$)$_{2T}$ electrodes. Figure 5c compares peak current densities, i_p (mA cm^{-2}), and the specific mass activity, *SMA* (peak current

divided by the Pt loading) extracted from LSVs of Figure 4b. It can be observed that $(Pt\text{-}CeO_2)_{0.5T}$ electrode displayed the highest i_p and *SMA* of 35.10 mA cm^{-2} and 292.5 mA mg$_{Pt}^{-1}$, respectively. Such values are particularly significant since they are obtained at scan rates as low as 5 mV s^{-1}.
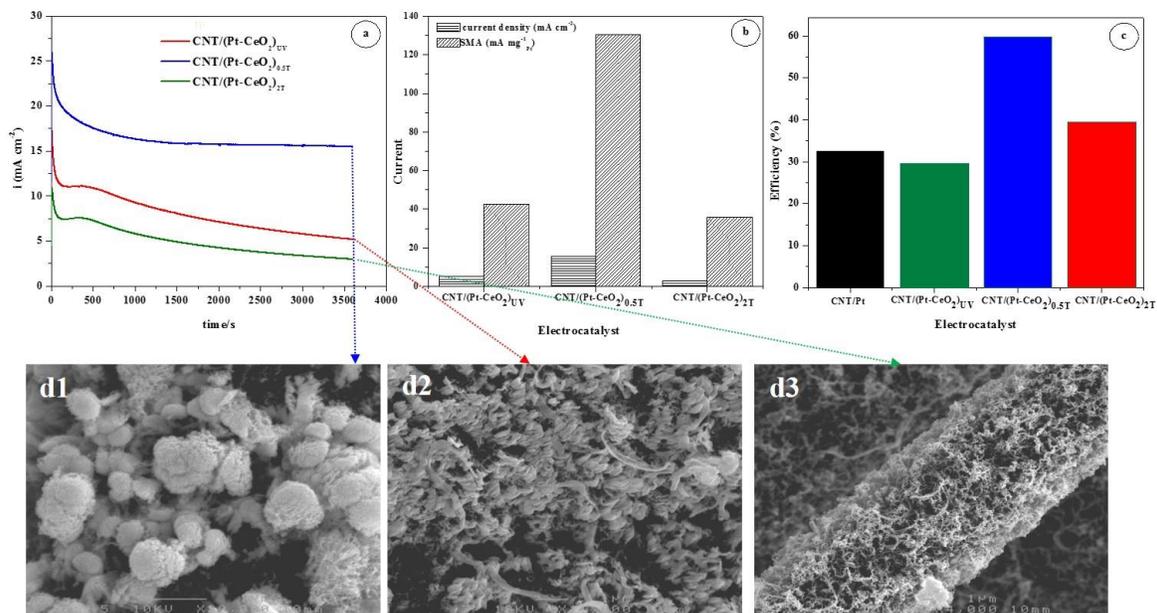
3.3. Durability

Figure 5 (a) Durability in 0.5 M H$_2$SO$_4$+ 1 M C$_2$H$_5$OH argon purged solution of CBPLD-synthesized (Pt-CeO$_2$) films onto CNTs catalyst support. (b) Steady-state density and *SMA* values extracted from Figure 5a. (c) Efficiency (the efficiency of CNT/Pt catalyst is shown for referencing). Bottom are SEM images taken after durability measurements shown in Figure 5a.

From a practical point of view, the durability of a catalyst during long-time operation is crucial. Long-term chronoamperometric tests were carried out by stepping the potential from the open circuit potential to 0.6 vs Ag/AgCl in 0.5 M H$_2$SO$_4$+1 M C$_2$H$_5$OH. The current values were recorded for 1 hour, and the resulting current density-time (*i-t*) curves are shown in Figure 5a. All *i-t* responses displayed an initial fast decay due to the rapid increase of the surface coverage by intermediate species, such as adsorbed CO during ethanol oxidation reaction. However, there is a marked difference in the durability between the three (Pt-CeO$_2$) catalysts. The current continued to decrease slowly at the $(Pt\text{-}CeO_2)_{UV}$ and $(Pt\text{-}CeO_2)_{2T}$ catalysts until reaching a quasi-steady state upon 1 hour operation. On the other hand, the current rapidly attained a perfectly steady-state at the $(Pt\text{-}CeO_2)_{0.5T}$ catalyst. Figure 5b resumes the steady-state current densities (i_{ss}) altogether with the *SMA* (steady-state current divided by the Pt loading) which shows that (Pt-

CeO$_2$)$_{0.5T}$ catalyst delivered a large *SMA* of 130 mA mg$_{Pt}^{-1}$ three times greater than (Pt-CeO$_2$)$_{UV}$ and (Pt-CeO$_2$)$_{2T}$ electrodes.

The durability can be further quantified by plotting the stability efficiency calculated as *i*$_{ss}$ from Figure 5a divided by the initial current density (*t* = 0). Figure 5c, confirms that the (Pt-CeO$_2$)$_{0.5T}$ electrode outperforms the other electrodes by retaining about 60% of its initial activity demonstrating by that a high tolerance to CO poisoning.

Post-mortem analysis by SEM of the surface morphology after durability measurements are shown in Figure 5d1-d3. The CNT/(Pt-CeO$_2$)$_{UV}$ surface became flaky which is in fact the Pt-CeO$_2$ catalyst that has detached from the beneath CNTs (Figure 5d2). Worse was the stability of the (Pt-CeO$_2$)$_{2T}$ catalyst, which has completely disconnected from the CNTs (Figure 5d3) and has fallen in the electrolyte. On the other hand, the (Pt-CeO$_2$)$_{0.5T}$ catalyst (Figure 5d1) has not undergone any major change The obtained *ESA*, *ASA* and results of Fig. 4 and Fig. 5 indicate that the electrochemical performance is not significantly different between the (Pt-CeO$_2$)$_{UV}$ and the (Pt-CeO$_2$)$_{2T}$ electrodes. Nevertheless, the (Pt-CeO$_2$)$_{0.5T}$ far exceeds the latter two in terms of electroactivity and durability.

The formation of ionized species Pt$^{2+,4+}$ has been observed for Pt-doped cerium oxide films prepared by rf sputtering on a Si wafer, and on multiwall carbon nanotubes (MWCNTs) [48]. The Pt^{2+}/Pt^{4+} ratio depended on the deposition angle and increased in the case of the film deposition on the MWCNTs. Besides the effect of the substrate, the authors further observed an increase of Pt^{2+}/Pt^{4+} ratio with Pt content onto MWCNTs substrate, which was explained by higher segregation of platinum to the CeO$_2$ grain boundary region. When used as an anode material in hydrogen-fed polymer membrane fuel cell (PMFC), Pt–CeO$_2$ films deposited on carbon nanotubes (CNTs) exhibits very high specific power [41]. The activity of this material is explained by high activity of embedded Pt$^{2+,4+}$ cations toward H$_2$ dissociation and formation of protonic hydrogen.

In our work with the CBPLD technique, the substrate (CNTs), the Pt loading, the laser fluence, and the substrate-to-target distance were fixed. It was only the background atmosphere that was changed and we do however observe an increase of the Pt^{2+}/Pt^{4+} ratio with the background gas pressure (Table 1). Such phenomenon is observed for the first time with CBPLD method and is very complex to explain for the time being.

Nevertheless, in our work, the electrochemical performance cannot be connected to the presence of high concentration of Pt^{2+} since the (Pt-CeO$_2$)$_{2T}$ showed the least electroactivity. For

instance, we can only link the electrochemical performance to the morphology of the (Pt-CeO$_2$) deposits. The (Pt-CeO$_2$)$_{UV}$ film is of closed structure (Fig. 1a and Fig. 3a), which is not suitable for a better accessibility of the electrolyte. The morphology of the (Pt-CeO$_2$)$_{UV}$ looks porous but mechanically fragile (Fig. 1c and Fig. 2d3). On the other hand, the (Pt-CeO$_2$)$_{0.5T}$ particles arrangement into uniform and compact calottes-like shapes (Figure 1b) with higher *ESA* and surface roughness factor (*ESA* divided by the geometric area of the electrode) of about 46 compared to around 11 for (Pt-CeO$_2$)$_{UV}$ and (Pt-CeO$_2$)$_{2T}$ electrodes, explain the high electrochemical performance and durability of the (Pt-CeO$_2$)$_{0.5T}$ anode catalyst. This is due to the highly dispersed Pt crystallites, which expose a larger number of active sites for surface reactions. This is evident from the hydrogen adsorption/desorption during CV measurements (Fig. 4a), which shows a higher *ESA* of Pt crystallites dispersed on the (Pt-CeO$_2$)$_{0.5T}$ sample as compared with (Pt-CeO$_2$)$_{UV}$ and (Pt-CeO$_2$)$_{2T}$ samples.

3.4. The catalyst layer architecture: Co-deposited Pt-CeO$_2$ versus layer onto layer deposited CeO$_2$/Pt

As mentioned at the end of the introduction part, we will address here the approach on whether or not CeO$_2$ adds the same functionality to the Pt catalyst when it is arranged differently in the catalytic layer. Figure 6a shows a rough representation of two architectures of the catalyst layer in which CeO$_2$ is incorporated differently. The first architecture is the one developed in this work that is CC/CNT/(Pt-CeO$_2$), whereas in the second one, CeO$_2$ is intercalated between CNTs and Pt (CC/CNT/CeO$_2$/Pt). In the CC/CNT/CeO$_2$/Pt architecture, CeO$_2$ and Pt were also deposited by PLD and we have already reported their synthesis, characterization and electroactivity towards ethanol electrooxidation [27]. XPS analysis of the CC/CNT/CeO$_2$/Pt structures did not show a change in the electronic structure of Pt deposited onto the CeO$_2$ layer. The only effect observed from the interaction between CeO$_2$ and Pt was the reduction in the particle size of Pt by CeO$_2$ [27].

Figure 6b compares LSVs at CC/CNT/Pt, CC/CNT/CeO$_2$/Pt and CC/CNT/(Pt-CeO$_2$)$_{0.5T}$ electrodes in ethanol containing solution. The onset potential for ethanol electrooxidation reaction is of 0.27 V vs Ag/AgCl at CC/CNT/Pt electrode, whereas at both CC/CNT/CeO$_2$/Pt and CNT/(CeO$_2$-Pt)$_{0.5T}$ is 0.20 V vs Ag/AgCl (Figure 6c). On the other hand, a marked difference is observed in the current peak densities delivered by the electrodes. The LSVs show that the current peak density at the CC/CNT/(Pt-CeO$_2$)$_{0.5T}$ electrode is 35.65 mA cm^{-2} vs 26.45 mA cm^{-2} at the CC/CNT/CeO$_2$/Pt electrode. The durability performance of the CC/CNT/CeO$_2$/Pt-

architecture is very bad as can be seen in Figure 6d, the current declined rapidly and approached zero upon 1 hour of testing, which indicates bad tolerance to CO-poisoning.
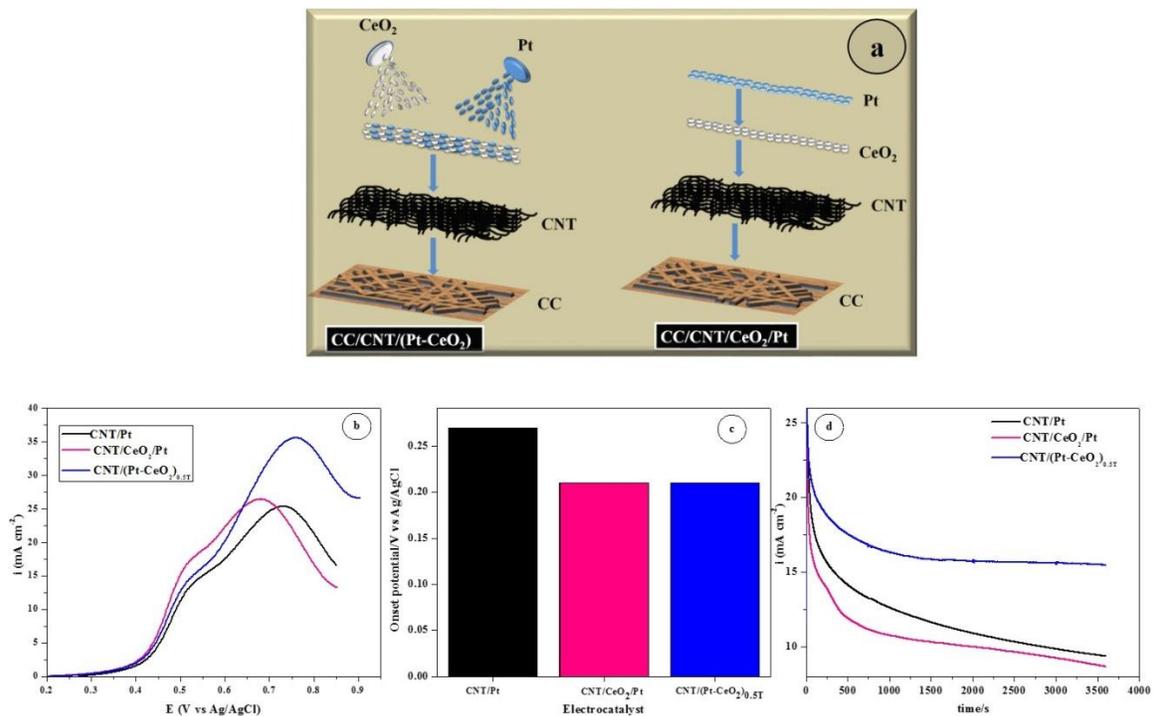
Figure 6. (a) Rough representation of two catalyst layer architectures in which CeO₂ is positioned differently: (left) mixed (Pt-CeO₂) onto CNTs vs (right) layer onto layer (CNT/CeO₂/Pt). (b) Linear scan voltammetry in 0.5 M H₂SO₄+ 1 M C₂H₅OH argon-purged solution with a potential scan rate of 5 mV s⁻¹. (c) Onset potential of ethanol oxidation reaction. (d) Durability in 0.5 M H₂SO₄+ 1 M C₂H₅OH argon purged solution. The results of CNT/Pt catalyst layer are shown for referencing.

In light of these observations, we can argue that CeO_2 brings a beneficial effect to Pt towards the electrooxidation of ethanol. However the extent of such favorable influence clearly depends on the position of CeO_2 within the whole catalyst layer. When intercalated between the catalyst support (CNTs in this case) and the Pt catalyst, CeO_2 is prone to adsorption of OH species at potentials lower than those achieved by pure Pt. However with such catalyst layer structure, the number of OH_{ads} is not sufficient for removal of adjacent CO_{ads} on Pt as observed with durability results (Fig. 6d, pink line). On the other hand, CeO_2 when deposited simultaneously with Pt modifies the electronic structure of Pt (electronic effect) and is prone to adsorption of higher number of OH adsorbed species at lower potentials (bi-functional effect) [67, 68], which provides significant CO-poisoning tolerance to Pt during the ethanol electrooxidation reaction and by that high durability (Fig. 6d, blue line). However, in addition to the electronic effect and bi-functional effect, the surface morphology is another decisive parameter. Indeed, within the three co-

deposited (Pt-CeO_2) samples, the unique morphology of the (Pt-CeO_2)$_{0.5T}$ sample (Fig. 1b) seems to offer a more pronounced oxygen mobility of OH_{ads} on the surface of the CeO_2. This, in effect boosts the conversion of adsorbed CO to free CO_2 on the (Pt-CeO_2)$_{0.5T}$ sample.

4. Conclusions

The CBPLD technique is employed and optimized for the first time to simultaneously deposit nanostructured thin films of Pt-CeO_2 catalysts onto CNTs directly grown on anode gas diffusion layer that is employed for the fuel cell catalyst fabrication. The thin film microstructure was investigated as function of CBPLD deposition parameters such as the ambient gas pressure giving rise to different microstructures with different electrocatalytic properties.

From SEM, TEM, XRD, XPS and Raman analyses, it was observed that the extent of the interaction between Pt and CeO_2 was influenced by the PLD-background gas pressure condition during deposition. The films deposited under He gas atmosphere exhibit high concentration of Pt^{2+}, whereas film deposited under vacuum displays high concentration of Pt^0. Ce reveals mixed Ce^{4+} and Ce^{3+} cations. The grain size of CeO_2 in the (Pt-CeO_2) samples was also influenced by the PLD-background gas pressure. The physical phenomena responsible for such trends are very complex but very interesting from the fundamental point of view and thus deserve further studies.

Among the synthesized samples, the CNT/Pt-CeO_2 composite made under 0.5 Torr of helium displayed an unprecedented catalyst activity, high tolerance to CO poisoning judging from chronoamperometric curves, and robust durability towards EOR, compared to pure Pt or to the layer onto layer CNT/CeO_2/Pt architecture. Such remarkable performance of Pt-CeO_2 catalyst towards EOR has never been reported to the best of our knowledge. In addition, the free-standing (binderless) catalyst layer structure, the planar deposition of Pt-CeO_2 catalyst with its ultra-low loading of Pt (120 g cm^{-2}) make this anode architecture more appealing for commercial micro DEFCs to power portable electronic systems.

Further significance of this work is that it demonstrates the importance in the design of the catalyst layer architecture principally when it comes to fully benefit from the promoting catalytic properties of CeO_2 in particular. Indeed, we prove here that when CeO_2 material is beneath or when it is mixed with Pt, the interactions between Pt with CeO_2 are not similar leading inevitably to different electrocatalytic performances. Given proper tailoring synthesis conditions, mixed Pt-CeO_2 composites are remarkably stable and provide electrochemical performance greater than

the layer onto layer CeO_2/Pt architecture. Such findings have general implications for other types of fuel cells and catalysis.

Acknowledgments

References

[1] K. Singh, J. Nowotny, V. Thangadurai. Chem. Soc. Rev., 42 (2013) 1961-1972.

[2] N. Nuraje, R. Asmatulu, S. Kudaibergenov. Current Inorganic Chemistry, 2 (2012) 124-146.

[3] Y. Ren, Z. Ma, P.G. Bruce. Chem. Soc. Rev., 41 (2012) 4909-4927.

[4] F. Vigier, C. Coutanceau, F. Hahn, E.M. Belgsir, C. Lamy. J. Electroanal. Chem., 563 (2004) 81-89.

[5] M.Z.F. Kamarudin, S.K. Kamarudin, M.S. Masdar, W.R.W. Daud. Int. J. Hydrogen Energy, 38 (2013) 9438-9453.

[6] S. Carrettin, P. Concepción, A. Corma, J.M. López Nieto, V.F. Puntes. Angewandte Chemie International Edition, 43 (2004) 2538-2540.

[7] J. Wang, J. Xi, Y. Bai, Y. Shen, J. Sun, L. Chen, W. Zhu, X. Qiu. J. Power Sources, 164 (2007) 555-560.

[8] F. Khatkhatay, A. Chen, J.H. Lee, W. Zhang, H. Abdel-Raziq, H. Wang. ACS Applied Materials & Interfaces, 5 (2013) 12541-12547.

[9] O. Parlak, M.M. Demir. ACS Applied Materials & Interfaces, 3 (2011) 4306-4314.

[10] A. Pinna, C. Figus, B. Lasio, M. Piccinini, L. Malfatti, P. Innocenzi. ACS Applied Materials & Interfaces, 4 (2012) 3916-3922.

[11] T. Taniguchi, Y. Sonoda, M. Echikawa, Y. Watanabe, K. Hatakeyama, S. Ida, M. Koinuma, Y. Matsumoto. ACS Applied Materials & Interfaces, 4 (2012) 1010-1015.

[12] A. Younis, D. Chu, I. Mihail, S. Li. ACS Applied Materials & Interfaces, 5 (2013) 9429-9434.

[13] C.T. Campbell, C.H.F. Peden. Science, 309 (2005) 713-714.

[14] E. Fabbri, D. Pergolesi, E. Traversa. Chem. Soc. Rev., 39 (2010) 4355-4369.

[15] Z.-P. Li, M. Toshiyuki, G.J. Auchterlonie, J. Zou, D. John. ACS Applied Materials & Interfaces, 3 (2011) 2772-2778.

[16] Y. Chen, Y. Zhang, J. Baker, P. Majumdar, Z. Yang, M. Han, F. Chen. ACS Applied Materials & Interfaces, 6 (2014) 5130-5136.

[17] D.R. Ou, T. Mori, H. Togasaki, M. Takahashi, F. Ye, J. Drennan. Langmuir, 27 (2011) 3859-3866.

[18] J. Anderson, A. Karakoti, D.J. Díaz, S. Seal. J. Phys. Chem. C, 114 (2010) 4595-4602.

[19] C. Xu, P.K. Shen. Chem. Commun., 10.1039/B408589B (2004) 2238-2239.

[20] D. Díaz, N. Greenletch, A. Solanki, A. Karakoti, S. Seal. Catal. Lett., 119 (2007) 319-326.

[21] C. Xu, P.K. Shen. J. Power Sources, 142 (2005) 27-29.

[22] Q. He, S. Mukerjee, B. Shyam, D. Ramaker, S. Parres-Esclapez, M.J. Illán-Gómez, A. Bueno-López. J. Power Sources, 193 (2009) 408-415.

[23] A. Neto, M. Linardi, D. Anjos, G. Tremiliosi-Filho, E. Spinacé. J. Appl. Electrochem., 39 (2009) 1153-1156.

[24] K. Fugane, T. Mori, D.R. Ou, A. Suzuki, H. Yoshikawa, T. Masuda, K. Uosaki, Y. Yamashita, S. Ueda, K. Kobayashi, N. Okazaki, I. Matolinova, V. Matolin. Electrochim. Acta, 56 (2011) 3874-3883.

[25] V. Matolín, I. Matolínová, M. Václavů, I. Khalakhan, M. Vorokhta, R. Fiala, I. Piš, Z. Sofer, J. Poltierová-Vejpravová, T. Mori, V. Potin, H. Yoshikawa, S. Ueda, K. Kobayashi. Langmuir, 26 (2010) 12824-12831.

[26] H. Tang, H. Sun, D. Chen, X. Jiao. Mater. Lett., 77 (2012) 7-9.

[27] A. Tabet-Aoul, M. Mohamedi. Phys. Chem. Chem. Phys., 14 (2012) 4463-4474.

[28] X. Wang, D. Liu, S. Song, H. Zhang. Chem. Commun., 48 (2012) 10207-10209.

[29] S.K. Meher, G.R. Rao. ACS Catal., 2 (2012) 2795-2809.

[30] S. Sharma, M. Hegde. J. Chem. Phys., 130 (2009) 114706.

[31] P. Bera, A. Gayen, M.S. Hegde, N.P. Lalla, L. Spadaro, F. Frusteri, F. Arena. J. Phys. Chem. B, 107 (2003) 6122-6130.

[32] M.A. Scibioh, S.-K. Kim, E.A. Cho, T.-H. Lim, S.-A. Hong, H.Y. Ha. Appl. Catal. B, 84 (2008) 773-782.

[33] A. Tselev, A. Gorbunov, W. Pompe. Rev. Sci. Instrum., 72 (2001) 2665-2672.

[34] Z. Hamoudi, M.A.E. Khakani, M. Mohamedi. J. Electrochem. Soc., 159 (2012) B331-B339.

[35] A. Tabet-Aoul, M. Mohamedi. J. Mater. Chem., 22 (2012) 2491-2497.

[36] D.B. Chrisey, G.K. Hubler. Pulsed Laser Deposition of Thin Film, John Wiley & Sons, Inc., New York, 1994.

[37] A. Pereira, F. Laplante, M. Chaker, D. Guay. Adv. Funct. Mater., 17 (2007) 443-450.

[38] R. Dolbec, E. Irissou, M. Chaker, D. Guay, F. Rosei, M.A. El Khakani. Phys. Rev. B, 70

(2004) 201406.

[39] Handbook of X-ray Photoelectronic Spectroscopy, Perkin-Elmer Corp, Eden Prairie, MN, 1979.

[40] V. Matolín, M. Cabala, I. Matolínová, M. Škoda, M. Václavů, K.C. Prince, T. Skála, T. Mori, H. Yoshikawa, Y. Yamashita, S. Ueda, K. Kobayashi. Fuel Cells, 10 (2010) 139-144.

[41] M. Václavů, I. Matolínová, J. Mysliveček, R. Fiala, V. Matolín. J. Electrochem. Soc., 156 (2009) B938-B942.

[42] P. Bera, K.R. Priolkar, A. Gayen, P.R. Sarode, M.S. Hegde, S. Emura, R. Kumashiro, V. Jayaram, G.N. Subbanna. Chem. Mater., 15 (2003) 2049-2060.

[43] X.L. Tang, B.C. Zhang, Y. Li, Y. Xu, Q. Xin, W.J. Shen. J. Mol. Catal. A: Chem., 235 (2005) 122-129.

[44] L. Österlund, S. Kielbassa, C. Werdinius, B. Kasemo. J. Catal., 215 (2003) 94-107.

[45] V. Matolín, M. Cabala, V. Cháb, I. Matolínová, K.C. Prince, M. Škoda, F. Šutara, T. Skála, K. Veltruská. Surf. Interface Anal., 40 (2008) 225-230.

[46] I. Alvarez-Clemares, G. Mata-Osoro, A. Fernández, S. Lopez-Esteban, C. Pecharromán, J. Palomares, R. Torrecillas, J.S. Moya. Adv. Eng. Mater., 12 (2010) 1154-1160.

[47] R. Fiala, I. Khalakhan, I. Matolínová, Václavu, M., M. Vorokhta, Z. Sofer, S. Huber, V. Potin, V. Matolín. J. Nanosci. Nanotechnol., 11 (2011) 5062-5067.

[48] V. Matolín, I. Khalakhan, I. Matolínová, M. Václavů, K. Veltruská, M. Vorokhta. Surf. Interface Anal., 42 (2010) 882-885.

[49] M.S. Dresselhaus, G. Dresselhaus, R. Saito, A. Jorio. Phys. Rep., 409 (2005) 47-99.

[50] J. Spanier, R. Robinson, F. Zhang, S.-W. Chan, I. Herman. Phys. Rev. B, 64 (2001) 245407.

[51] W. Weber, K. Hass, J. McBride. Phys. Rev. B, 48 (1993) 178-185.

[52] I. Estrela-Lopis, G. Romero, E. Rojas, S. Moya, E. Donath (2011) Nanoparticle uptake and their co-localization with cell compartments–a confocal Raman microscopy study at single cell level. J. Phys.: Conf. Ser. IOP Publishing, p 012017.

[53] Y. Zhang, P.D. Edmondson, T. Varga, S. Moll, F. Namavar, C. Lan, W.J. Weber. Phys. Chem. Chem. Phys., 13 (2011) 11946-11950.

[54] S. Aškrabić, R. Kostić, Z. Dohčević-Mitrović, Z.V. Popović. J. Phys.: Conf. Ser., 92 (2007) 012042.

[55] S. Maensiri, C. Masingboon, P. Laokul, W. Jareonboon, V. Promarak, P.L. Anderson, S. Seraphin. Cryst. Growth Des., 7 (2007) 950-955.

[56] I. Kosacki, V. Petrovsky, H.U. Anderson, P. Colomban. J. Am. Ceram. Soc., 85 (2002)

2646-2650.

[57] I. Kosacki, T. Suzuki, H.U. Anderson, P. Colomban. Solid State Ionics, 149 (2002) 99-105.

[58] J.R. McBride, G.W. Graham, C.R. Peters, W.H. Weber. J. Appl. Phys., 69 (1991) 1596-1604.

[59] W. Lin, A.A. Herzing, C.J. Kiely, I.E. Wachs. J. Phys. Chem. C, 112 (2008) 5942-5951.

[60] K. Kinoshita, D.R. Ferrier, P. Stonehart. Electrochim. Acta, 23 (1978) 45-54.

[61] T.J. Schmidt, H.A. Gasteiger, G.D. Stäb, P.M. Urban, D.M. Kolb, R.J. Behm. J. Electrochem. Soc., 145 (1998) 2354-2358.

[62] Q.-S. Chen, F.J. Vidal-Iglesias, J. Solla-Gullon, S.-G. Sun, J.M. Feliu. Chemical Science, 3 (2012) 136-147.

[63] W. Sheng, H.A. Gasteiger, Y. Shao-Horn. J. Electrochem. Soc., 157 (2010) B1529-B1536.

[64] A. Pozio, M. De Francesco, A. Cemmi, F. Cardellini, L. Giorgi. J. Power Sources, 105 (2002) 13-19.

[65] H. Wang, Z. Jusys, R.J. Behm. J. Power Sources, 154 (2006) 351-359.

[66] T. Iwasita, E. Pastor. Electrochim. Acta, 39 (1994) 531-537.

[67] S. Mukerjee, R.C. Urian. Electrochim. Acta, 47 (2002) 3219-3231.

[68] A. Cuesta. ChemPhysChem, 12 (2011) 2375-2385.

Supplementary Data
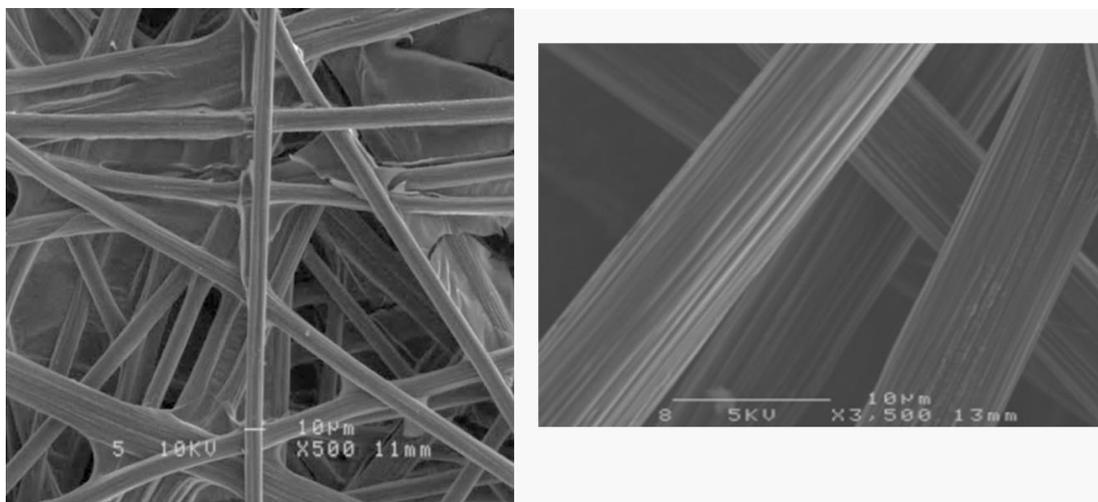
Figure S1: The carbon paper substrate used in this work is an untreated carbon paper (CP, Toray) made of 3D network of carbon fibers each having a diameter ranging between 7 and 10 μm. This type of CP is well known in the area of fuel cells as the gas diffusion layer in Membrane Electrode Assembly (MEA) and it is highly porous with good electrical conductivity and thus can also act as the current collector in the structures developed in this work.
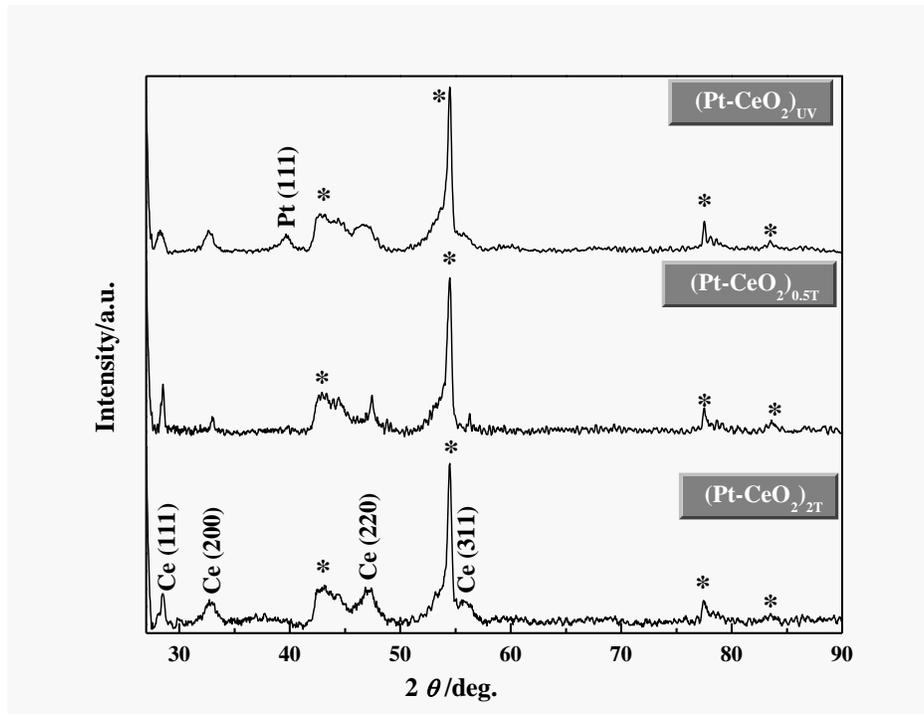
Figure S2: XRD patterns of (Pt-CeO$_2$) samples synthesized under different background gas atmospheres. (*) are patterns related to carbon.
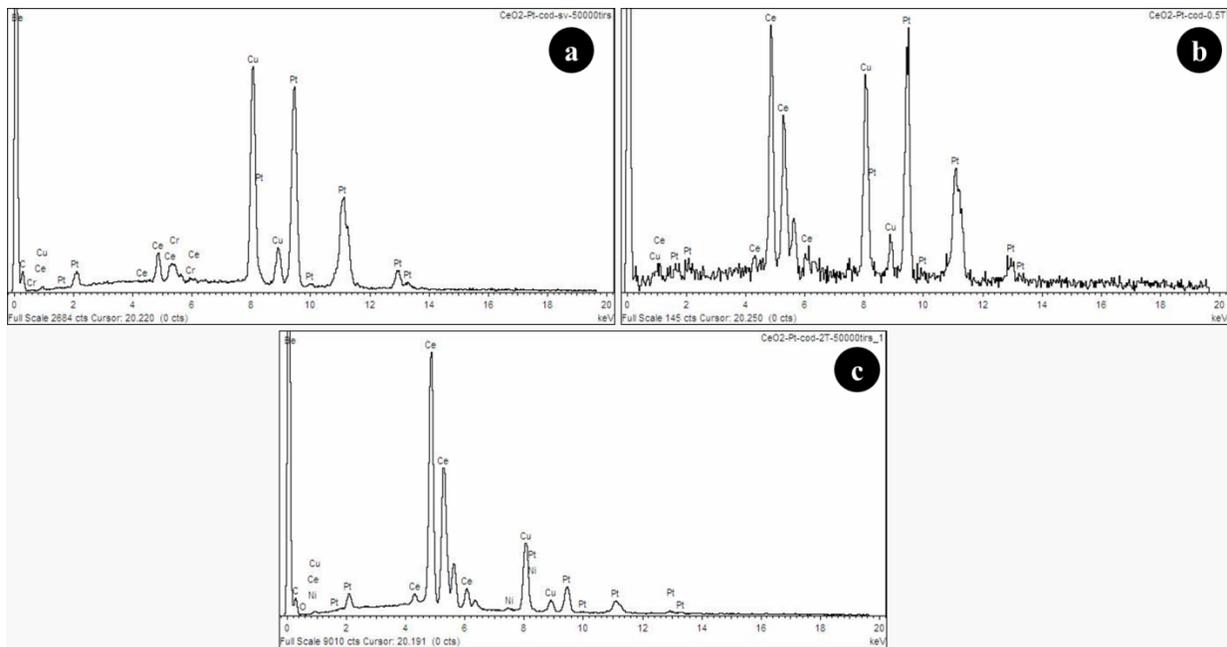
Figure S3: Energy dispersion spectroscopy (EDS) under transmission electron microscope of CNT/(Pt-CeO₂) samples: (a) CNT/(Pt-CeO₂)$_{UV}$, (b) CNT/(Pt-CeO₂)$_{0.5T}$, and (c) CNT/(Pt-CeO₂)$_{2T}$.
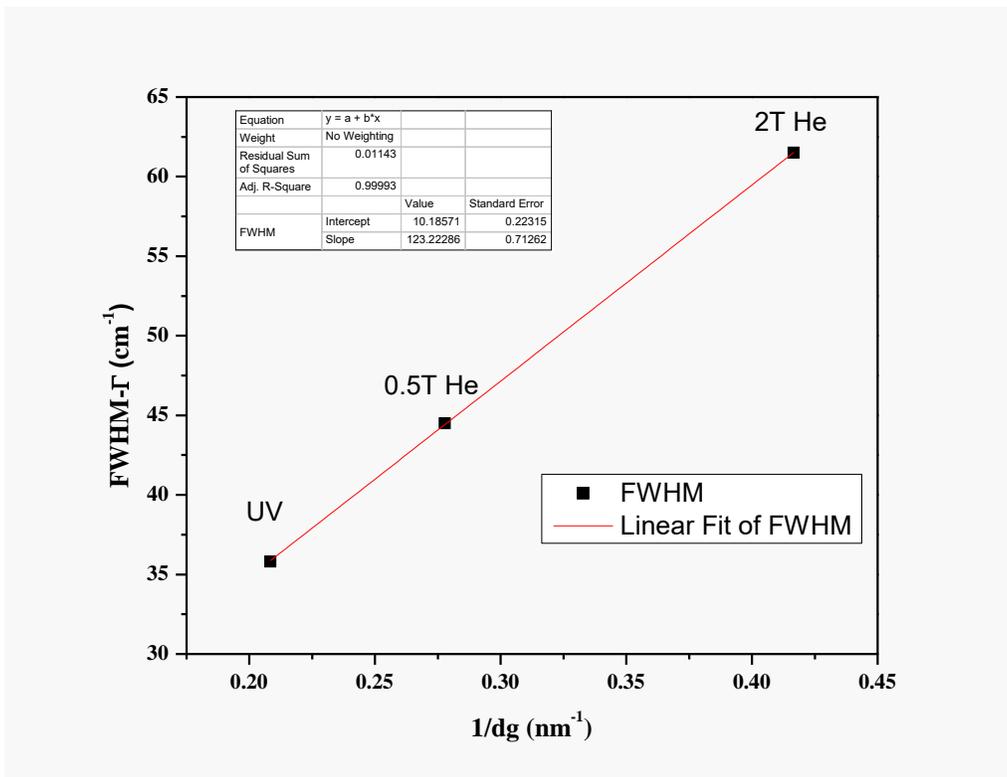
Figure S4: Variation of the half-width, Γ, corresponding to the Raman line of CeO₂ on the inverse of grain size, dg.
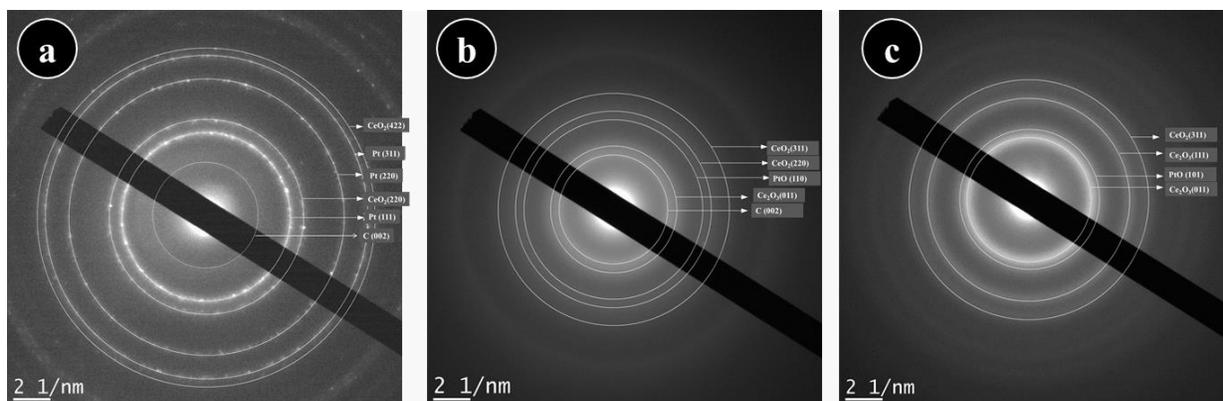
Figure S5: SAED patterns of CNT/(Pt-CeO$_2$) samples: (a) CNT/(Pt-CeO$_2$)$_{UV}$, (b) CNT/(Pt-CeO$_2$)$_{0.5T}$, and (c) CNT/(Pt-CeO$_2$)$_{2T}$.

ARTICLE 2

Room temperature synthesis of mixed platinum and tin oxide nanocomposite catalyst with enhanced mass activity and durability for ethanol electrooxidation in an acidic medium

Synthèse à température ambiante d'un catalyseur nanocomposite de platine et d'oxyde d'étain avec des améliorations de l'activité de masse et de la durabilité pour l'électrooxydation de l'éthanol dans un milieu acide

Authors

Youling Wang, Amel Tabet-Aoul, Mohamed Mohamedi

Énergie, Matériaux et Télécommunications (EMT), Institut National de la Recherche Scientifique (INRS), Université d'Avant-garde, 1650 Boulevard Lionel Boulet, Varennes, Québec, J3X 1S2, Canada.

Contribution

I performed all the experimental synthesis, the electro-chemical measurements, and all characterizations (XRD, SEM and XPS) except the TEM and NAA measurements which have been done by technicians. I also realized the data analysis and interpretation of results. I participated in the writing of the article with the help of other co-authors.

Publication

Résumé traduit

Les oxydes métalliques de transition-Pt apparaissent comme une nouvelle classe d'électrodes pour des réactions d'oxydation de l'alcool. Nous préparons des nanocomposites Pt-SnO_2 à température ambiante de différentes morphologies de surface par ablation laser à flux croisés sur des substrats de nanotubes de carbone pour réaliser une amélioration de la réaction d'oxydation de l'éthanol (EOR). Les nanocomposites synthétisés sont caractérisés par microscopie électronique à balayage (MEB), spectroscopie photoélectronique de rayons X (SPX), diffraction des rayons X (DRX), spectroscopie Raman, et microscopie électronique en

transmission (MET). Il est observé que l'interaction du SnO_2 avec le Pt modifie la structure électronique de celui-ci induisant la formation d'ions Pt^{2+} et Pt^{4+} alors que le Sn est sous forme de cations mixtes de Sn^{4+} et Sn^{2+}. Une performance électrocatalytique optimale envers l'EOR est obtenue avec une structure Pt-SnO_2 synthétisée sous 0.5 Torr d'hélium. Comparée à l'électrode de CNT/Pt, cette électrode de CNT/Pt-SnO_2 (i) oxyde l'éthanol à des potentiels plus bas (86 mV négatif), et (ii) montre une activité de masse spécifique supérieure de 1.6 fois et 2.2 fois par voltamétrie cyclique et une stabilité à long terme, respectivement. Une telle performance est attribuée à une combinaison de: (i) l'abondance d'hydroxyles sur la surface du SnO_2 et la diminution de l'empoisonnement au CO sur la base du mécanisme bifonctionnel; (ii) la modification de la structure électronique de Pt (effet électronique) et (iii) une morphologie semi-poreuse de la surface favorable pour le transfert de masse des molécules d'éthanol.

Mots clés

Substrat de nanotubes de carbone; Dépôt par ablation laser à flux croisés; Amélioration de l'electroactivité et de la durabilité; Éthanol; Dioxyde d'étain-platine nanostructuré.

Abstract

Pt-transition metal oxides are emerging as new class of electrodes for alcohol oxidation reactions. We prepare at room temperature Pt-SnO_2 nanocomposites of various surface morphologies onto carbon nanotubes for enhanced ethanol oxidation reaction (EOR) by cross-beam pulsed laser deposition technique. Synthesized nanocomposites are characterized by scanning electron microscopy (SEM), X-ray photoelectron spectroscopy (XPS), XRD, Raman spectroscopy, and transmission electron microscopy (TEM). It is observed that the interaction of SnO_2 with Pt modifies the electronic structure of the latter inducing the formation of ionized Pt^{2+} and Pt^{4+} while Sn revealed mixed Sn^{4+} and Sn^{2+} cations. An optimum electrocatalytic performance towards EOR is obtained with a Pt-SnO_2 grown under 0.5 Torr of He atmosphere. Versus a CNT/Pt electrode, this CNT/Pt-SnO_2 electrode (i) oxidizes ethanol at much lower potentials (86 mV negative), and (ii) displays a superior specific mass activity of 1.6 times and 2.2 times by cyclic voltammetry and long-term stability, respectively. Such performance is ascribed to a combination of: (i) SnO_2 has abundant hydroxyls on the surface and decrease the CO poisoning based on a bifunctional mechanism; (ii) modification of the electronic structure of Pt (electronic effect) and (iii) a semi-porous surface morphology favorable for the mass transfer of ethanol molecules.

Key words

Carbon nanotubes substrate; Cross-beam pulsed laser deposition; Electroactivity and durability enhancement; Ethanol; Nanostructured tin dioxide-platinum.

1. Introduction

Direct ethanol fuel cells (DEFCs) are promising electrochemical power sources in portable and transportation applications because of their high energy densities, low operating temperatures and ease of transportation and storage. Add to that, ethanol a green, safe fuel and can be produced from biomass could make DEFCs advantageous for low greenhouse gas emission power sources. However, as far as DEFC catalysts are concerned, cost, performance and durability are some issues to solve before their widespread commercialization can be realized.

Platinum electrocatalyst is mainly responsible for the question of cost because it is expensive and its supply is limited due to its low content in the Earth's crust. As for performance, the catalytic activity towards ethanol oxidation reaction (EOR) is still insufficient to obtain the required efficiency. This is because, at Pt, the whole oxidation of ethanol to CO_2 is not attained due to CO poisoning at low voltages and the breaking of the C-C bond not easily achieved at low temperatures, which has a negative effect on the fuel cell efficiency [1]. Therefore, preparation of fine nanoparticles catalysts, combination with transition metals, and high dispersion of Pt particles on a support with a high specific surface area, have been attempted to diminish Pt usage and thus cost, and enhance its performance in DEFCs. Pt has been for example combined with one or two additional metals, such as Ru, Re, Rh, Sn among others [2], and recently Ir [3]. Although these combinations produced somehow an improvement of ethanol oxidation, the full oxidation of ethanol to CO_2 at low potentials was not achieved, instead generating only acetic acid and acetaldehyde. Very recently, PtPd [4] and non Pt-based catalysts Au@Pt core–shell [5], Rh–Sn [6], Pd and M catalysts (M: Ru, Sn, Ir, Cu, Rh, Ag) [7-11], have shown promising performance towards EOR in alkaline media.

The other crucial issue is the long-term durability of electrocatalysts. During long-term operation of PEFCs, the aggregation of metal nanoparticles and the electrochemical corrosion of supports (commonly carbon black) lead to the deterioration of catalysts and by that to the degradation of overall fuel cell efficiency.[12] The aggregation of metal nanoparticles can be prevented or limited by selecting a support which must not only be stable under the operating conditions and in strongly acidic/alkaline media but also which strongly interacts with the metal catalyst. For example, carbon nanotubes (CNTs) instead of carbon black have been used as a

support for noble metal nanocatalysts to improve the stability and resistance to corrosion of the catalysts [13].

Several transition metal oxides (TMOs) are inexpensive, abundant and environmentally benign. Because of particular native properties and functions of their own, some TMOs are emerging as a new class of electrode materials for a large range of applications such as energy conversion devices like polymer electrolyte fuel cells (PEFCs) [14], photoelectrochemical cells [15-16] and energy storage systems, including rechargeable batteries and electrochemical capacitors [17].

Among TMOs, the catalytic function of SnO_2 is attracting the interest of researchers. SnO_2 is an n-type semiconductor with higher electronic conductivity. It possesses good corrosion resistance in acidic media and thus is projected to be stable under the working conditions of PEFCs. In addition, SnO_2 has abundant hydroxyls on the surface, which can potentially weaken CO poisoning at low potentials according to the bifunctional mechanism [14]. Ke and Waki prepared $Pt/SnO_2/MWCNTs$ composites by first assembling SnO_2 nanoparticles on MWCNTs with a method of hydrolysis-oxidation of $SnCl_2$ in water at room temperature, then loading Pt onto the obtained $SnO_2/MWCNTs$ with a colloidal method, and finally reducing in a hydrogen atmosphere at 150°C [18]. The authors found that tin oxide promotes the methanol oxidation reaction (MOR) on Pt through providing extra adsorption sites for OH_{ad}/H_2O_{ad} or enhancing the affinity of Pt to OH_{ad}/H_2O_{ad}. Jiang et al. employed size-controllable SnO_2 nanoparticles, produced by heating ethylene glycol solutions containing $SnCl_2$, to prepare a carbon-supported $Pt–SnO_2$ catalyst [19-20]. The catalyst exhibited higher performance for the EOR compared with that of Pt/C, and this performance was ascribed to the presence of both adequately large Pt ensembles for ethanol dehydrogenation and C–C bond splitting and of tin oxide for OH generation. Silva et al. showed that electron beam irradiation prepared $Pt–SnO_2/C$ with Pt:Sn atomic ratios of 50:50 displayed good performance for the EOR in acidic media [21]. Hulin Zhang et al, prepared SnO_2 nanoscrystals with different morphologies by the hydrothermal method, and were used as supports for Pt nanocatalysts towards oxidation of methanol/ethanol [22]. The Pt/SnO_2 flower-shaped catalyst showed higher electrocatalytic activity and better long-term cycle stability compared with Pt/C/Graphite electrode. Higuchi et al prepared highly dispersed Pt and SnO_2 double nanoparticles containing different Pt/Sn ratios on carbon black by the modified Bönnemann method. The $Pt/SnO_2(3:1)/CB$ electrode showed the highest specific activity and lowest overpotential for EOR, and was superior to a Pt/CB electrode [23].

In continuation of our efforts to develop new catalysts based on metal oxides that enable or provide enhanced catalytic performance towards ethanol oxidation reaction, we report the synthesis of Pt-SnO_2 nanocomposites onto carbon nanotubes (CNTs) substrate. Such nanocomposites are for the first time grown at room temperature by an asymmetric cross beam pulsed laser deposition (CBPLD) geometry, which permits to mix SnO_2 and Pt directly in the laser plasma. In addition, it is also known that the morphology of metal oxides has a marked influence on their physical properties and electrochemical performance [14]. Thus, in this work, the gas atmosphere in the deposition chamber was also varied in order to produce various morphologies of the Pt-SnO_2 nanocomposites. For further details regarding the general characteristic of CBPLD, the reader is directed towards the review of Tselev et al [24]. Herein, CNTs, which act as the electron conductivity enhancers are grown by chemical vapor deposition (CVD) onto an electrically conductive carbon paper substrate. Such synthesized CNT/(Pt-SnO_2) materials are comprehensively characterized with SEM, XRD, XPS, micro Raman spectroscopy, and TEM (HR-TEM) techniques. A second objective of this work is to study the electroactivity and durability with post-mortem analysis of the surface morphology of the laser grown SnO_2-Pt nanocomposites, as well as catalytic promoting properties of SnO_2 to Pt towards EOR.

2. Experimental Section

2.1. Materials

Ni (99.99%), Pt (99.99%) and SnO_2 (99.99%) targets used for the PLD and CBPLD were purchased from Kurt J. Lesker Co. Untreated carbon paper (CP, Toray) was purchased from Electrochem. Sulfuric acid (96% purity) and ethanol (100% purity) were purchased from Agros Organics and Commercial Alcohols Inc., respectively.

2.2. Syntheses

CNTs were grown at 700ºC by chemical vapor deposition (CVD) using Ni as catalyst deposited by PLD onto CP substrate, acetylene (carbon source), hydrogen and argon (gas carrier) gases at flow rates of 30, 140 and 100 sccm, respectively. Full details regarding the synthesis of CNTS can be found elsewhere [25-26].

Pt-SnO_2 composites were prepared by CBPLD (dual beam) by simultaneously depositing Pt and SnO_2. All the deposits were made at room temperature by means of a pulsed KrF excimer

laser (λ= 248 nm, pulse width= 17 ns, and repetition rate = 50 Hz) using a laser fluence of 4 J cm^{-2}. Pt-SnO$_2$ composites were deposited under different background gas pressure in order to obtain different surface morphologies. Prior to each deposition, the chamber was evacuated with a turbo pump (4×10^{-5} Torr). Helium was then introduced in the deposited chamber. In this study, samples were prepared either under vacuum (4×10^{-5} Torr) or in the presence of He at a fixed background pressure (0.5 Torr or 2 Torr). In all cases, the substrate-to-target distance was fixed at 5 cm. In order to obtain a uniform ablation over the target surface, the target was continuously rotated and translated. Each (Pt-SnO$_2$) catalyst was deposited with 50000 laser pulses giving a Pt loading of 120 g cm^{-2} (measured by neutron activation analysis, NAA [27-28]. Three catalysts are considered in this work, namely: (Pt-SnO$_2$)$_{UV}$, (Pt-SnO$_2$)$_{0.5T}$, and (Pt-SnO$_2$)$_{2T}$, where the subscripts UV and T stand for under vacuum and Torr, respectively

2.3. Material Characterization

The surface morphology of the as-prepared samples was characterized using SEM (JEOL, JSM 7401F apparatus) and TEM and high-resolution (HR)-TEM (JEOL-JEM-2100F operating at 200 kV).

The crystalline structure of all samples was determined by XRD using a Bruker D8 Advance diffractometer equipped with a Cu Kα source. The diffractometer was operated at 40 kV and 40 mA. All diffractograms were acquired in the Grazing Incidence Diffraction (GID) scan mode with an incident angle of 2°, 2θ angular step size of 0.05° and acquisition time of 5 seconds per step.

XPS measurements were performed using a VG Escalab 220i-XL equipped with an Al Kα source (1486.6 eV). The anode was operated at 10 kV and 20 mA. The pass energy of the analyzer was fixed at 20 eV. All samples were analyzed with a spot size of 250 × 1000 μm located approximately in the center of the sample. A survey spectrum ranging from 0 to 1350 eV was first acquired, and then higher resolution multiplex scan spectra (Pt 4f, Sn 3d, O 1s, and C1s core levels) were obtained. Quantification of the elements was carried out with CasaXPS software (Casa Software Ltd.) by fitting the core level spectra after a Shirley background removal. The metallic components of the Pt 4f and Sn 3d regions were fitted using a Gaussian/Lorentzian asymmetrically modified line shape, and a Gaussian/Lorentzian line shape was used to fit the other components. The C 1s core level peak at 284.6 eV, resulting from hydrocarbon

contaminants at the surface, was used as an internal reference. All spectra have been recalibrated with respect to the C 1s core level peak of adventitious carbon contamination.

2.4. Electrochemical Characterization

The electrochemical properties of all samples were evaluated by cyclic voltammetry (CV) and chronoamperometry (CA) in a three compartment electrochemical cell at room temperature. A Pt coil was used as the counter electrode and an Ag/AgCl, 3 M NaCl was used as the reference electrode. The reference electrode was separated from the analyte solution by a Luggin capillary that is very close to the working electrode to minimize the ohmic drop. Data acquisition was conducted with a potentiostat/galvanostat Autolab from EcoChemie.

Prior to the electrochemical measurements in ethanol, the surface of the working electrode was cleaned and activated electrochemically in 0.5 M H_2SO_4 deaerated solution by potential multi-cycling at 50 mV s^{-1} until a stable CV was obtained. During that process, the cathodic limit was fixed to -0.25 V few millivolts before H_2 evolution reaction, whereas the anodic limit was set to 0.5 V to avoid the leaching of tin that may occur at more positive potential [26]. As expected, the resulting CVs (not shown) did not display, the H_{ads}/H_{des} features known for polycrystalline Pt owing to interaction or alloying between Pt and Sn [29]. Afterwards, CV and CA were employed for durability evaluation of the catalysts in 1 M C_2H_5OH + 0.5 M H_2SO_4. Before each test, dissolved oxygen was removed from the solution by bubbling argon for 30 min. Both the geometric area of the electrode and its Pt loading were used to rationalize the activity of electrocatalysts.

3. Results and Discussion

3.1. Characterization

The morphology of all prepared samples was examined by SEM (Fig. 1). A very smooth film and of closed structure was observed for Pt-SnO$_2$ grown under vacuum (Fig. 1a). The images of the Pt-SnO$_2$ synthesized under 0.5 Torr of He show that the product retains the shape of the CNTs and consists of small nanoparticles (Fig. 1b). On the other hand, the nanoparticles aggregated heavily for Pt-SnO$_2$ produced under 2 Torr of He (Fig. 1c).
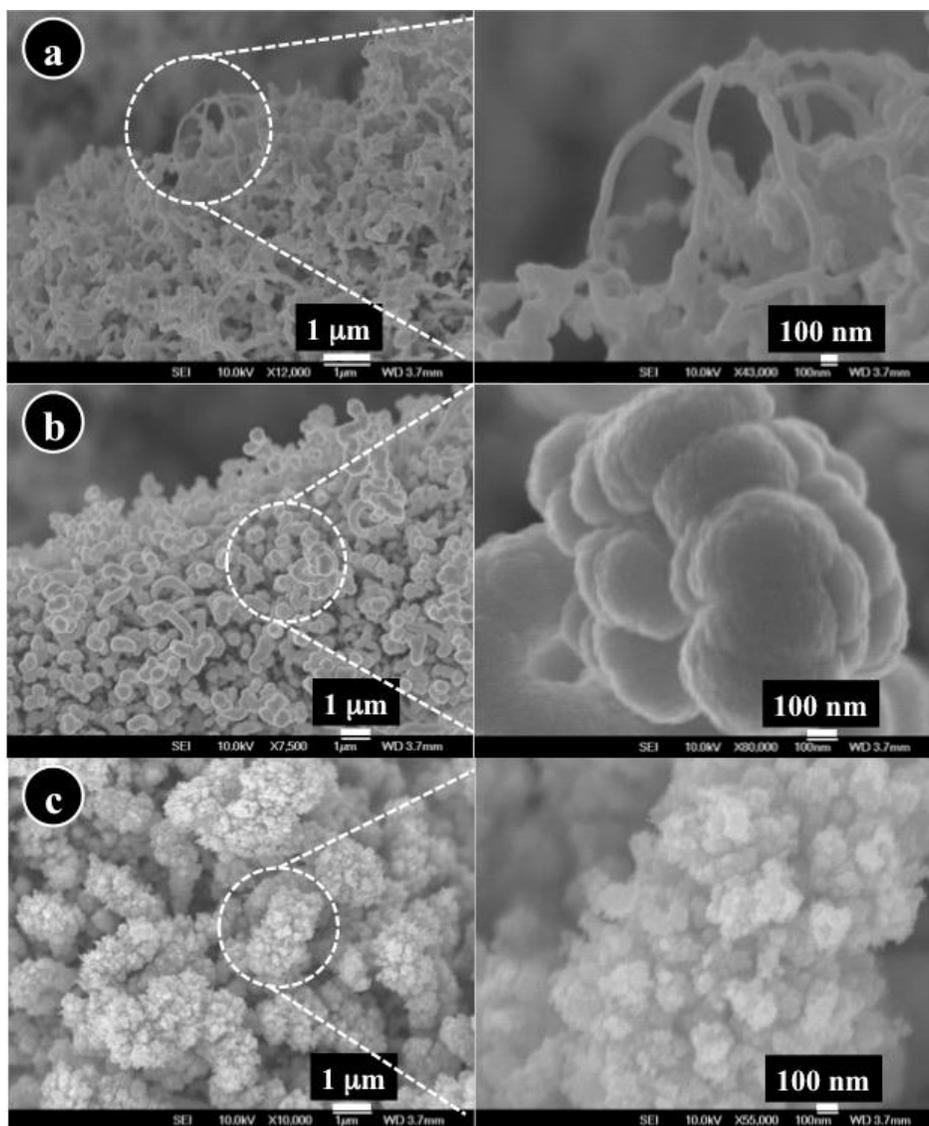
Figure 1. SEM micrographs with increasing magnification of CBPLD-synthesized (Pt-SnO$_2$) nanocomposites onto CNTs catalyst support. (a) CNT/(Pt-SnO$_2$)$_{UV}$, (b) CNT/(Pt-SnO$_2$)$_{0.5T}$, and (c) CNT/(Pt-SnO$_2$)$_{2T}$.

The XRD profiles of the CNT/(Pt-SnO$_2$) samples are presented in Figure S1 (*Supplementary material*). The profile of the CNT/(Pt-SnO$_2$)$_{UV}$ shows the presence of diffraction peaks Pt(111), Pt(200), Pt(220), SnO$_2$ (101) and strong peaks of the CNTs support. On the other hand, weak SnO$_2$ peak was detected at CNT/(Pt-SnO$_2$)$_{0.5T}$ and CNT/(Pt-SnO$_2$)$_{2T}$. However, the existence of Sn was verified using energy dispersion spectroscopy (EDS) under transmission electron microscope (Figure S2). The Scherrer analysis of the primary 111 peaks for Pt revealed a lattice parameter within 3.933 and 3.940 Å higher than that of pure CNT/Pt (3.923 Å), which indicates that Sn is dissolved in the fcc phase of Pt and that a true solid solution is formed [30-31].

The Raman spectra of the SnO_2 target (as a reference) and SnO_2 in the (Pt-SnO_2) composites are shown in Fig. 2. The spectrum of the SnO_2 target shows a pronounced band at 631 cm^{-1}, corresponding to A_{1g} mode, and three bands at 773, 458 and 119 cm^{-1} corresponding to B_{2g}, E_g and B_{1g} modes, respectively; this being in accordance with rutile bulk SnO_2 [32-33]. In addition to the fundamental Raman peaks of rutile SnO_2, two other Raman peaks at about 241 and 284 cm^{-1} are also observed. According to the literature, these two Raman peaks correspond to IR-active E_u (2) TO and E_u (2) LO (TO is the mode of the transverse optical (TO) phonons, LO is the mode of the longitudinal optical (LO) phonons), respectively [34-35]. In comparison, only a broad band in the 400 to 800 cm^{-1} region is observed in the spectra for SnO_2 in the (Pt-SnO_2) composites. This broad band appears to center near 621 cm^{-1}. The broadening may at first sight be attributed to a decrease in grain size due to the synthesis conditions of the CBPLD. However the broadening is too significant and cannot be explained solely by the size effect. We have thus conducted Raman analysis on CNT/SnO_2 sample. SnO_2 was synthetized onto CNTs using PLD with 20000 laser pulses under 2 Torr of He and its corresponding spectrum is shown in Figure S3. The spectrum displays the E_g (448 cm^{-1}), A_{1g} (631 cm^{-1}) and the B_{2g} (775 cm^{-1}) modes. Although the position of the two latter modes can be fairly established, their features such as the full width at half maximum (FWHM) are difficult to estimate due to their overlapping with the D mode (A_{1g} symmetry) related the disorder and defects in the carbon lattice of the CNTs substrate. On the other hand, the E_g mode is well resolved and thus can be examined. First, it is obvious that E_g mode is shifted most, and second its FWHM is 104 cm^{-1} significantly broader than the FWHM of the corresponding mode of the SnO_2 target (31.7 cm^{-1}). Diéguez et al. showed that when the nanoparticle size is decreased, the bands associated with the classical modes of SnO_2 shift to lower wave numbers and broaden [34]. Similar observations regarding the broadening of the E_g mode were also reported by Sun et al. for SnO_2 nanobelts [33]. We can thus confirm that the reduction in the grain size of SnO_2 is one of the factors responsible for the broadening in the Raman spectra of the (Pt-SnO_2) nanocomposites. The other factor believed to be responsible for the broadening of the Raman band is the presence of PtO and PtO_2 compounds. A parallel can be made with Raman spectra of (Pt-CeO_2) nanocomposites grown by CBPLD reported in our previous publication [36]. The Raman spectra of the (Pt-CeO_2) samples revealed band at ~547.3 and ~678.3 cm^{-1} corresponding to the vibrations of crystalline PtO_2 and PtO, respectively. It is therefore likely that PtO_x bands are also present in the Raman spectra of (Pt-SnO_2) overlapping those of SnO_2 within the 400-800 cm^{-1} range. Further information on this subject is provided by XPS in the following.
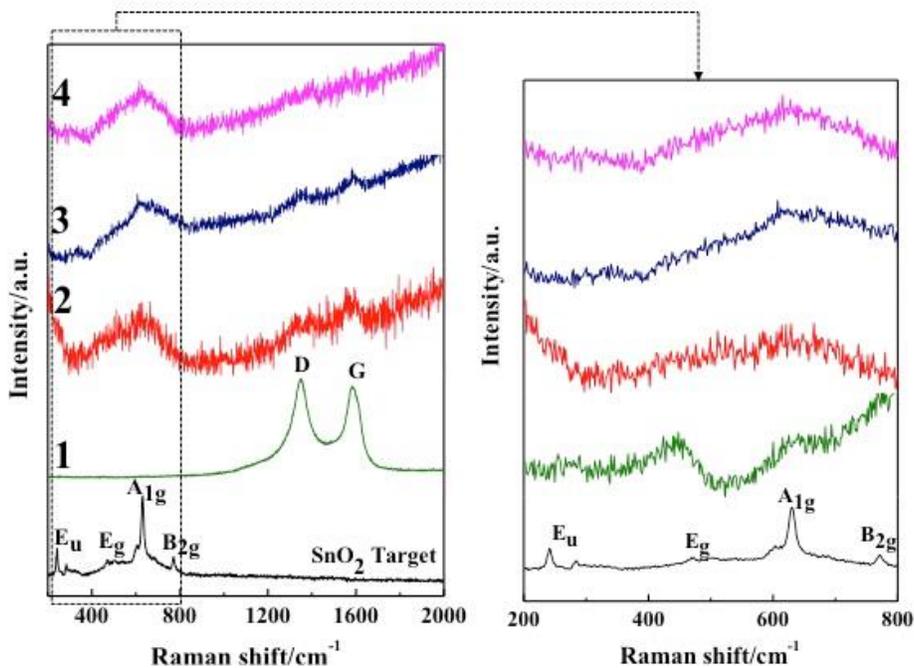
Figure 2. Raman spectra of (1) CNTs substrate, (2) CNT/(Pt-SnO₂)_UV, (3) CNT/(Pt-SnO₂)_{0.5T} film, and (4) CNT/(Pt-SnO₂)_{2T} nanocomposites. The Raman spectrum of the SnO₂ target is shown for referencing.

XPS measurements were performed to determine the chemical composition of surface elements and their oxidation states. The surveys scan spectra showed that Sn, Pt, O, and C are the only elements existing on the surface of all the CNT/(Pt-SnO$_2$) samples (Figure S4). The Pt 4f core-level spectrum of pure Pt deposited by PLD onto CNTs reported in our previous publication showed a doublet containing a low energy band (Pt 4f$_{7/2}$) and a high-energy band (Pt 4f$_{5/2}$) at 71.30 and 74.58 eV, respectively [36]. On the other hand, the XPS spectra of the co-deposited (Pt-SnO$_2$) reveal that Pt is present in more than one oxidation states, which could be identified as Pt^0, Pt^{2+}, and Pt^{4+} (Fig. 3). The position and relative amount of Pt species estimated from the relative intensities of these three peaks are summarized in Table 1. The position of Pt^{2+} and Pt^{4+} are in accordance with these reported in the literature [37-38]. From Table 1, it can be noted that (Pt-SnO$_2$)$_{UV}$ contains significant amount of Pt^0 of about 95 at%. The amount of Pt^0 significantly decreased to less than 50 at% for (Pt-SnO$_2$) samples deposited under He atmosphere. It was only the background atmosphere that was changed during the deposition process, however, we observed that the Pt^{2+}/Pt^{4+} ratio increased when the background atmosphere was changed from vacuum to 0.5 Torr of He and further augmented under 2 Torr of He (Table 1). Such phenomenon is observed for the first time with CBPLD method and is very complex to explain for the time being.

127
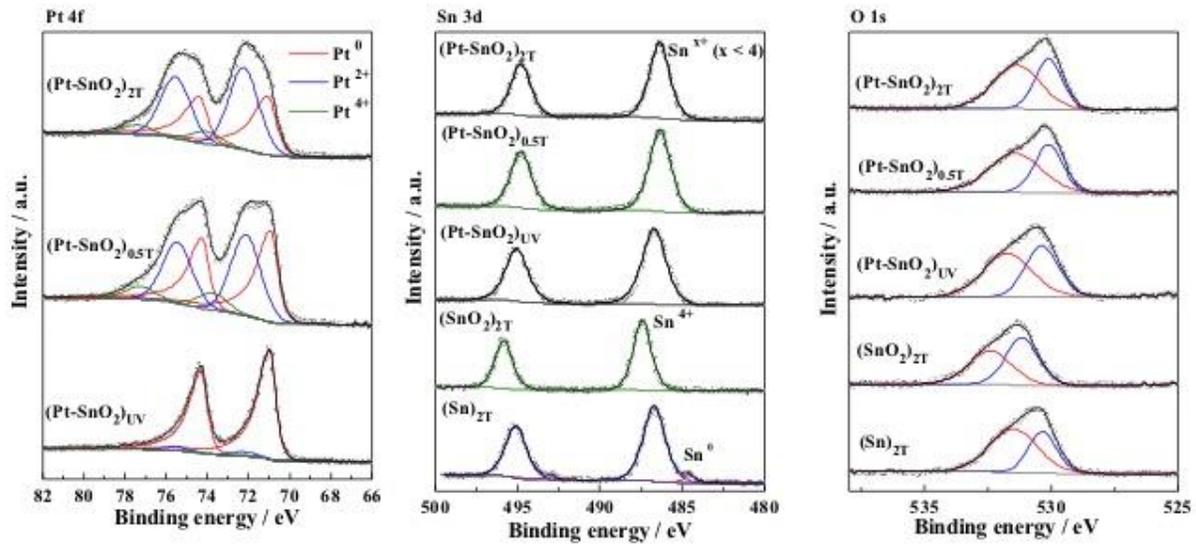
Figure 3. High-resolution XPS spectra (as indicated in the figures) of Pt 4f core level, Sn 3d core level and O 1s core-level.

Table 1 XPS parameters extracted from the core-level spectrum of Pt 4f (Fig. 3)

Sample	Pt^0		Pt^{2+}		Pt^4		Pt^{2+}/Pt^{4+}
	BE (eV)	at%	BE (eV)	at%	BE (eV)	at%	
CNT/SnO_2	-	-	-	-	-	-	-
$CNT/ (Pt-SnO_2)_{UV}$	70.97	95.14	72.17	3.98	73.79	0.89	4.46
$CNT/ (Pt-SnO_2)_{0.5T}$	70.90	47.03	72.13	57.39	73.75	9.27	6.19
$CNT/ (Pt-SnO_2)_{2T}$	71.05	40.24	72.22	51.84	74.05	7.93	6.54

Figure 3 shows the XPS spectra of the Sn 3d region in the ($Pt-SnO_2$) samples. Chemical identification of SnO and SnO_2 by XPS has been proven difficult because of the very small difference in the binding energy of Sn^{2+} and Sn^{4+} species. To discriminate as correctly as possible between the different oxidation states of Sn in our ($Pt-SnO_2$) samples, we have also synthesized by PLD, Sn and SnO_2 on CNTs substrate and their corresponding Sn 3d regions are also reported Fig. 3. The Sn 3d core-level in CNT/Sn could be deconvoluted correctly into two components, whereas only one component provided satisfactory resolution for Sn 3d in the CNT/SnO_2 and $CNT/(Pt-SnO_2)$ samples. From these fittings, the extracted binding energies with their ascription to the different oxidation states of Sn are reported in Table 2. It can be seen that Sn and SnO_2 interact differently with CNTs and Pt. Such behaviors are observed for the first time and have not been reported in the literature. Bazargan et al. acquired XPS spectra of SnO_2 and SnO powders, which exhibited Sn $3d_{5/2}$ binding energies of 487.0 and 486.6 eV, respectively [39]. The authors also observed metallic Sn^0 with a lower binding energy at 485.0 eV. Accordingly, the higher binding energy component (486.7~486.8 eV) is due to the presence of Sn^{4+}. On the other hand,

128

the lower binding energies at 486.3 eV does not agree with either SnO or SnO_2 and is likely related to a built-up as a mixture of Sn^{2+} and Sn^{4+}. We must emphasize that since no oxygen gas was used during deposition of pure Sn onto CNTs, the presence of SnO_2 on its surface occurred as a result of exposure to air.

Table 2 XPS parameters extracted from the core-level spectrum of Sn 3d (Fig. 3).

	Sn^0	Sn^{4+}	Sn^{2+}	Sn^{2+}/Sn^{4+}	O 1s	
CNT/Sn	484.5	486.6	-	-	530.4	531.7
CNT/SnO_2	-	486.8	-	-	530.6	532.1
CNT/(Pt-SnO_2)$_{UV}$	-	486.7	-	-	530.3	531.7
CNT/(Pt-SnO_2)$_{0.5T}$	-	-	-	486.3	530.1	531.4
CNT/(Pt-SnO_2)$_{2T}$	-	-	-	486.3	530.1	531.3

In Figure 3, the XPS O1s lines of as-deposited CNT/(Pt-SnO_2) along with that of CNT/Sn and CNT/SnO_2 are presented. A simple visual shape analysis of XPS O1s peak shows that it is wide, asymmetrical, and exhibits an evident shoulder at the high binding energy side of the spectrum. The main parameters used in the applied fitting procedure as well as the obtained best fitting parameters are also summarized in Table 2. The component at 531.3~532.1 eV is attributed to the surface lattice oxygen and the one located at 530.1~530.6 is ascribed to the bulk lattice oxygen [40].
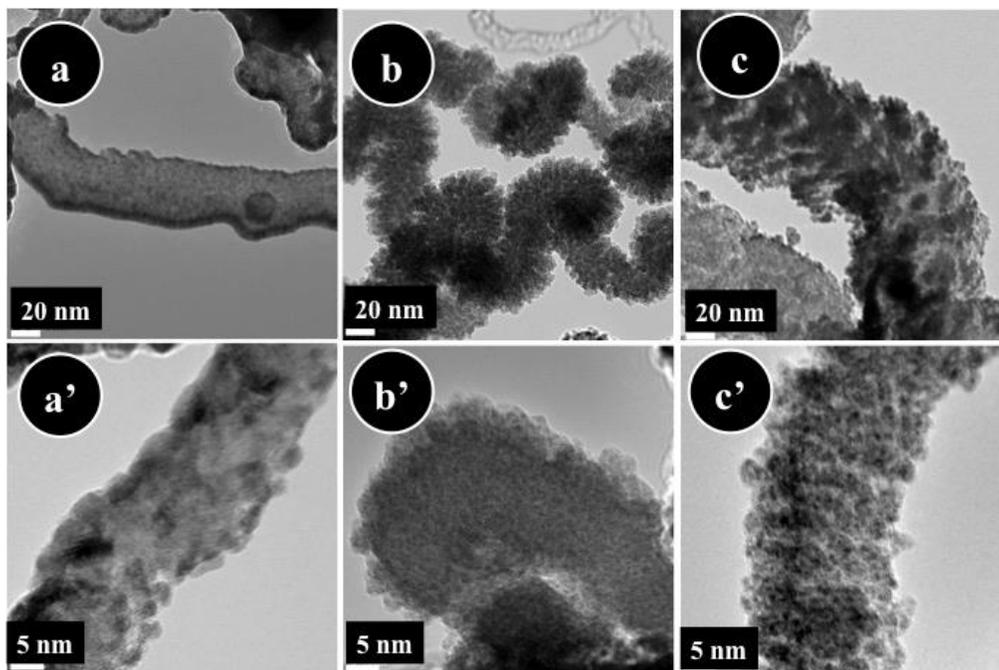
Figure 4. TEM and HR-TEM micrographs of CBPLD-synthesized (Pt-SnO_2) nanocomposites onto CNTs catalyst support: (a, a') CNT/(Pt-SnO_2)$_{UV}$, (b, b') CNT/(Pt-SnO_2)$_{0.5T}$, and (c, c') CNT/(Pt-SnO_2)$_{2T}$.

Figure 4 shows TEM and HR-TEM images of the different CBPLD-synthesized (Pt-SnO$_2$) films onto CNTs. In all cases, it can be seen that CNTs are well coated with Pt-SnO$_2$. In addition, the images confirm the marked difference in the morphology of the different deposits, i.e., a highly closed structure of the (Pt-SnO$_2$)$_{UV}$ film and the semi-porous and highly porous structure for the (Pt-SnO$_2$)$_{0.5T}$ and (Pt-SnO$_2$)$_{2T}$ films, respectively.

3.2. Electroactivity in ethanol solution
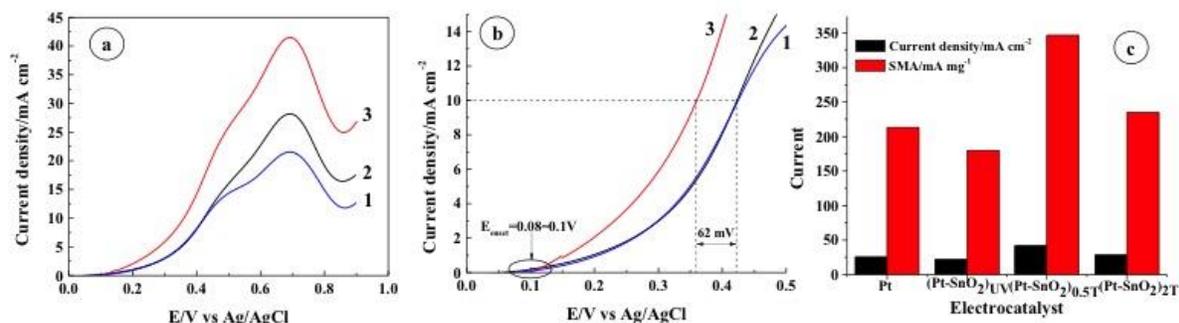
Figure 5. Electroactivity of CNT/(Pt-SnO$_2$) nanocomposites. (a) Linear scan voltammograms of ethanol electrooxidation in 0.5 M H$_2$SO$_4$ + 1 M C$_2$H$_5$OH argon purged solution with a potential scan rate of 5 mV s^{-1}. (b) Onset potential of ethanol electrooxidation, (c) Current peak density and *SMA* values extracted from Fig. 5a. (1) CNT/(Pt-SnO$_2$)$_{UV}$, (2) CNT/(Pt-SnO$_2$)$_{2T}$, and (3) CNT/(Pt-SnO$_2$)$_{0.5T}$.

The electrocatalytic activity of the CNT/(Pt-SnO$_2$) samples was investigated towards ethanol electrooxidation reaction. Fig. 5a shows linear scan voltammograms (LSVs) recorded in 0.5 M H$_2$SO$_4$ + 1 M C$_2$H$_5$OH solution with slow scan rate of 5 mV s^{-1} (quasi-steady state). The LSVs at all the electrodes displayed typical ethanol oxidation waves in agreement with the literature [41-42]. The peak position is almost similar for the three samples, i.e., 0.7 V vs Ag/AgCl. There is also no significant difference in the onset potential E_{onset} (the onset is defined as the potential value at which the anodic current starts to flow, as depicted in Fig. 5b), which is located within 0.08 and 0.1 V vs Ag/AgCl. Nevertheless, the electrocatalytic performance can be better studied by establishing an arbitrary criterion such as comparing the corresponding potential at a given current density. Thus, at a chosen current density of 10 mA cm^{-2}, the (Pt-SnO$_2$)$_{0.5T}$ catalyst oxidizes ethanol at potentials much negative (62 mV negative) than those delivered by (Pt-SnO$_2$)$_{UV}$ and (Pt-SnO$_2$)$_{2T}$ electrodes (Fig. 5b). In addition, at the same current density of 10 mA cm^{-2}, the potential is 86 mV negative than at Pt electrode [36]. This demonstrates that (Pt-SnO$_2$)$_{0.5T}$ promotes the oxidation of CO at low potentials. Next, Fig. 5c compares peak current densities (mA cm^{-2}), and the specific mass activity, *SMA* (peak current divided by the Pt loading)

extracted from LSVs of Fig. 5a. For reference, the performance of CNT/Pt is also reported in Fig. 5c. It can be observed that $(Pt-SnO_2)_{0.5T}$ electrode displayed the highest current densities and *SMA* of 41.6 mA cm^{-2} and 346.7 mA mg$_{Pt}^{-1}$, respectively. Such values are particularly significant since they are obtained at scan rates as low as 5 mV s^{-1}.

3.3. Durability

Afterwards, the durability of the catalyst was investigated by long-term chronoamperometry tests carried out by stepping the potential from the open circuit potential to 0.6 vs Ag/AgCl in 0.5 M H_2SO_4+1 M C_2H_5OH solution and recording the current for 1 hour. The resulting current density-time curves are shown in Fig. 6a. All *i-t* responses show that the current density rapidly decreased during the first few seconds and then reached a steady state upon 1 hour. The initial fast decrease of the current density is due to the rapid increase of the surface coverage by intermediate species, such as adsorbed CO during ethanol oxidation reaction. However, there is a marked difference in the durability between the three $(Pt-SnO_2)$ catalysts, as the current density is different for each sample at a given time. Fig. 6b resumes the steady-state current densities altogether with the *SMA* (steady-state current divided by the Pt loading), which shows that $(Pt-SnO_2)_{0.5T}$ catalyst delivered the largest *SMA* of 170.2 mA mg$_{Pt}^{-1}$ three times greater than $(Pt-SnO_2)_{UV}$ and $(Pt-SnO_2)_{2T}$ electrodes.
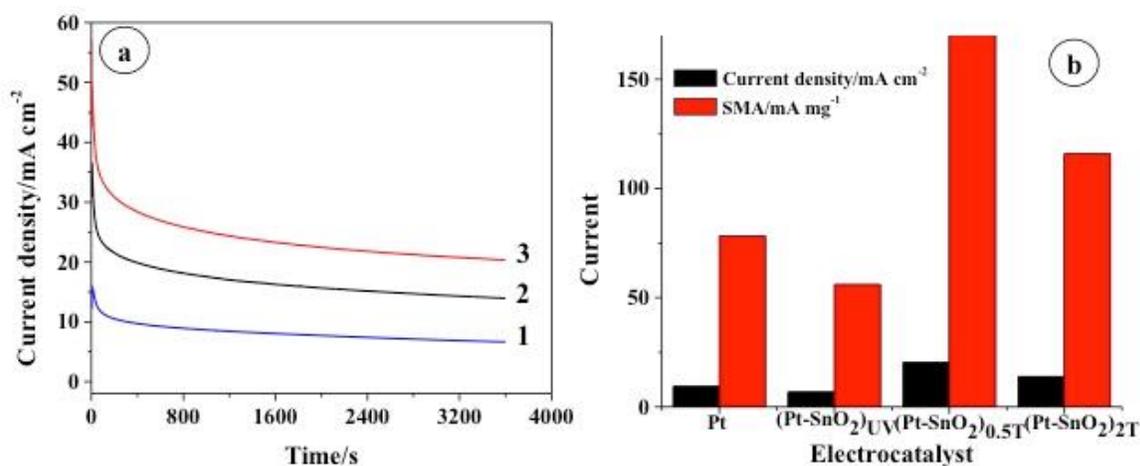
Figure 6. (a) Durability results in 0.5 M H_2SO_4+1 M C_2H_5OH argon purged solution. (b) Steady-state current density and *SMA* values extracted from Fig. 6a. (1) CNT/(Pt-SnO₂)ᵤᵥ, (2) CNT/(Pt-SnO₂)₂ₜ, and (3) CNT/(Pt-SnO₂)₀.₅ₜ.

131

Post-mortem analyses by SEM of the surface morphology after durability measurements are shown in Figure S5. The $(Pt-SnO_2)_{UV}$ and $(Pt-SnO_2)_{0.5T}$ surface morphologies have undergone no major changes after the durability studies. On the other hand, the $(Pt-SnO_2)_{2T}$ catalyst has completely detached from the CNTs and has fallen in the electrolyte.

As compared to porous Pt (Fig. 5c and Fig. 6b), the enhanced performance obtained with $(Pt-SnO_2)_{0.5T}$ and $(Pt-SnO_2)_{2T}$ catalysts may be due to the fact that more OH provided by tin oxide at low potential promote the oxidative removal of strongly bounded intermediates (such as CO) than with Pt catalyst. Yet, the $(Pt-SnO_2)_{UV}$ was not better than Pt catalyst (Fig. 5c and Fig. 6b) because the former catalyst is of closed structure (Fig. 1a and Fig. 4a), a structure that is not suitable for a better accessibility of the electrolyte. With regard to durability, $(Pt-SnO_2)_{2T}$ looked highly porous but structurally fragile (Fig. 1c and Fig. 4c), which explains its weak mechanical tenure after durability measurements. On the other hand, the $(Pt-SnO_2)_{0.5T}$ particles arrangement into uniform and compact semi-porous shapes (Fig. 1b and Fig. 4b) point out to an optimum surface morphology for both electrochemical and durability performances.

For instance, the electrochemical performance can be explained by the fact that, SnO_2 when deposited simultaneously with Pt modifies the electronic structure of Pt (electronic effect) and is prone to adsorption of higher number of OH adsorbed species at lower potentials (bi-functional effect), which provides significant CO-poisoning tolerance to Pt during the ethanol electrooxidation as shown in equations (1) and (2) [43]:

$$SnO_2 + H_2O \rightarrow SnO_2-OH_{ad} + H^+ + e^- \tag{1}$$

$$Pt-CO_{ad} + SnO_2-OH_{ad} \rightarrow Pt + SnO_2 + CO_2 + H^+ + e^- \tag{2}$$
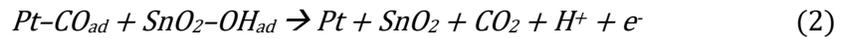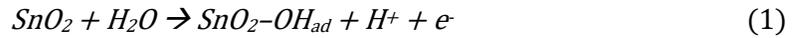
However, the electrochemical performance is also conditioned by the surface morphology of the catalyst. Indeed, within the three co-deposited $(Pt-SnO_2)$ samples, the unique morphology of the $(Pt-SnO_2)_{0.5T}$ sample seems to offer a more pronounced oxygen mobility of OH_{ads} on the surface of the SnO_2, which has the effect of boosting the conversion of adsorbed CO to free CO_2 on the $(Pt-SnO_2)_{0.5T}$ sample.

4. Conclusions

The CBPLD technique is employed to simultaneously deposit nanocomposites thin films of Pt-SnO$_2$ onto CNTs substrate. The thin film surface morphology was varied by changing the ambient gas pressure in the deposition chamber.

From SEM, TEM, XRD, XPS and Raman analyses, it was observed that the extent of the interaction between Pt and SnO$_2$ was influenced by the background gas pressure condition during deposition. The films deposited under He gas atmosphere exhibit high concentration of Pt^{2+}, whereas film deposited under vacuum displays high concentration of Pt^0, while Sn reveals mixed Sn^{4+} and Sn^{2+} cations.

Within the synthesized samples, the CNT/Pt-SnO$_2$ nanocomposite made under 0.5 Torr displayed a specific mass activity 1.6 times (voltammetric studies) and 2.2 times (durability studies) greater than CNT/Pt electrode catalyst. Finally and more importantly, this (Pt-SnO$_2$)$_{0.5T}$ catalyst oxidized ethanol at potentials much lower compared to the CNT/Pt electrode. Such enhanced electrocatalytic performance is obtained through a combination of several factors: (i) SnO$_2$ has abundant hydroxyls on the surface and decrease the CO poisoning based on a bifunctional mechanism; (ii) strong interactions with Pt nanoparticles, which modifies the electronic structure of Pt nanocatalyst (electronic effect); and (iii) a surface morphology favorable for the mass transfer of ethanol molecules. Based on the excellent electrochemical performance, the binder-free catalyst layer structure and the planar deposition of Pt-SnO$_2$ catalyst in addition to an ultra-low loading of Pt (120 g cm^{-2}) make this anode architecture attractive for micro-DEFCs to power portable electronic systems.

Acknowledgments

References

[1] F. Vigier, C. Coutanceau, F. Hahn, E. M. Belgsir and C. Lamy, J. Electroanal. Chem., 563, 81 (2004).

[2] M. Z. F. Kamarudin, S. K. Kamarudin, M. S. Masdar and W. R. W. Daud, Int. J. Hydrogen

Energy, 38, 9438 (2013).

[3] Y.-W. Lee, E.-T. Hwang, D.-H. Kwak and K.-W. Park, Catal. Sci. Technol., 6, 569 (2016).

[4] Jakub Seweryn, Adam Lewera, J. Power Sources, 205, 264 (2012).

[5] P. Gnanaprakasam, S. E. Jeena and T. Selvaraju, J. Mater. Chem. A, 3, 18010 (2015).

[6] Minjeh Ahn, In Young Cha, Joong Kee Lee, Sung Jong Yoo and Yung-Eun Sung, J. Mater. Chem. A, 3, 17130 (2015).

[7] Liang Ma, Hui He, Andrew Hsu, Rongrong Chen, J. Power Sources, 241, 696 (2013).

[8] Eun Ja Lim, Youngmin Kim, Sung Mook Choi, Seonhwa Lee, Yuseong Noh and Won Bae Kim, J. Mater. Chem. A, 3, 5491 (2015).

[9] Xiao Zhao, Jian Zhang, Liangjun Wang, Zhaolin Liu and Wei Chen, J. Mater. Chem. A, 2, 20933 (2014).

[10] Shuiyun Shen and Tianshou Zhao, J. Mater. Chem. A, 1, 906 (2013).

[11] Cheng Peng, Yongli Hu, Mingrui Liu, Yixiong Zheng, J. Power Sources, 278, 69 (2015).

[12] V. Tripkovic, F. Abild-Pedersen, F. Studt, I. Cerri, T. Nagami, T. Bligaard and J. Rossmeisl, Chem Cat Chem, 4, 228 (2012).

[13] Jiwei Ma, Aurélien Habrioux, and Nicolas Alonso-Vante, ChemElectroChem, 1, 37 (2014).

[14] Z. Zhang, J. Liu, J. Gu, L. Su and L. Cheng, Energy Environ. Sci., 7, 2535 (2014).

[15] K. Singh, J. Nowotny and V. Thangadurai, Chem. Soc. Rev., 42, 1961 (2013).

[16] N. Nuraje, R. Asmatulu and S. Kudaibergenov, Curr. Inorg. Chem., 2, 124 (2012).

[17] Y. Ren, Z. Ma and P. G. Bruce, Chem. Soc. Rev., 41, 4909 (2012).

[18] K. Ke and K. Waki, J. Electrochem. Soc., 154, A207 (2007).

[19] L. Jiang, G. Sun, Z. Zhou, S. Sun, Q. Wang, S. Yan, H. Li, J. Tian, J. Guo, B. Zhou and Q. Xin, J. Phys. Chem. B, 109, 8774 (2005).

[20] L. Jiang, L. Colmenares, Z. Jusys, G. Q. Sun and R. J. Behm, Electrochim. Acta, 53, 377 (2007).

[21] J. C. M. Silva, R. F. B. De Souza, L. S. Parreira, E. T. Neto, M. L. Calegaro and M. C. Santos, Appl. Catal. B, 99, 265 (2010).

[22] H. Zhang, C. Hu, X. He, L. Hong, G. Du, Y. Zhang, J. Power Sources, 196, 4499 (2011).

[23] E. Higuchi, K. Miyata, T. Takase, H. Inoue, J Power Sources, 196, 1730 (2011).

[24] A. Tselev, A. Gorbunov and W. Pompe, Rev. Sci. Instrum., 72, 2665 (2001).

[25] Z. Hamoudi, M. A. E. Khakani and M. Mohamedi, J. Electrochem. Soc., 159, B331(2012).

[26] A. Tabet-Aoul and M. Mohamedi, J. Mater. Chem., 22, 2491 (2012).

[27] R. R. Greenberg, P. Bode and E. A. De Nadai Fernandes, Spectrochimica Acta Part B: Atomic Spectroscopy, 66, 193 (2011).

[28] R. Zeisler and R. R. Greenberg, J. Radioanal. Chem., 75, 27 (1982).

[29] D.-H. Lim, D.-H. Choi, W.-D. Lee and H.-I. Lee, Appl. Catal. B, 89, 484 (2009).

[30] S. C. Zignani, E. R. Gonzalez, V. Baglio, S. Siracusano, A. S. Aricò, Int. J. Electrochem. Sci., 7, 3155 (2012).

[31] Luhua Jiang, Gongquan Sun, Zhenhua Zhou, Weijiang Zhou, Qin Xin, Catalysis Today, 93–95, 665 (2004).

[32] W. Wang, C. Xu, G. Wang, Y. Liu and C. Zheng, J. Appl. Phys., 92, 2740 (2002).

[33] S. H. Sun, G. W. Meng, G. X. Zhang, T. Gao, B. Y. Geng, L. D. Zhang and J. Zuo, Chem. Phys. Lett., 376, 103 (2003).

[34] A. Diéguez, A. Romano-Rodríguez, A. Vilà and J. R. Morante, J. Appl. Phys., 90, 1550 (2001).

[35] Y. Liu, C. Zheng, W. Wang, C. Yin and G. Wang, Adv. Mater., 13, 1883 (2001).

[36] Y. Wang, A. Tabet-Aoul, M. Gougis and M. Mohamedi, J. Power Sources, 273, 904 (2015).

[37] P. Bera, K. R. Priolkar, A. Gayen, P. R. Sarode, M. S. Hegde, S. Emura, R. Kumashiro, V. Jayaram and G. N. Subbanna, Chem. Mater., 15, 2049 (2003).

[38] X. L. Tang, B. C. Zhang, Y. Li, Y. Xu, Q. Xin and W. J. Shen, J. Mol. Catal. A: Chem., 235, 122 (2005).

[39] S. Bazargan, N. F. Heinig, D. Pradhan and K. T. Leung, Cryst. Growth Des., 11, 247 (2011).

[40] J. Szuber, G. Czempik, R. Larciprete, D. Koziej and B. Adamowicz, Thin Solid Films, 391, 198 (2001).

[41] H. Wang, Z. Jusys and R. J. Behm, J. Power Sources, 154, 351 (2006).

[42] T. Iwasita and E. Pastor, Electrochim. Acta, 39, 531 (1994).

[43] F. Ye, J. Li, T. Wang, Y. Liu, H. Wei, J. Li and X. Wang, J. Phys. Chem. C, 112, 12894 (2008).

Supplementary Data
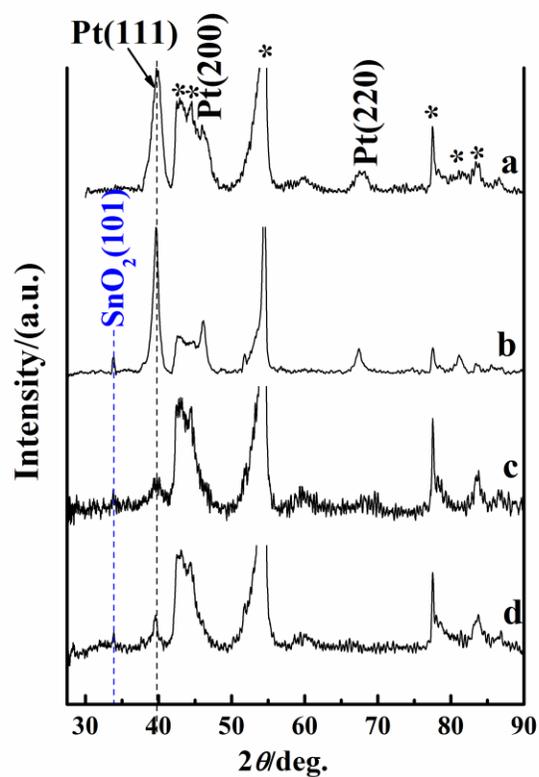
Figure S1 XRD profiles of PLD-deposited Pt and CBPLD-deposited (Pt-SnO$_2$) nanocomposites onto carbon nanotubes substrate. (a) CNT/Pt, (b) CNT/(Pt-SnO$_2$)$_{UV}$, (b) CNT/(Pt-SnO$_2$)$_{0.5T}$, and (c) CNT/(Pt-SnO$_2$)$_{2T}$ nanocomposites. (*) patterns related to carbon.
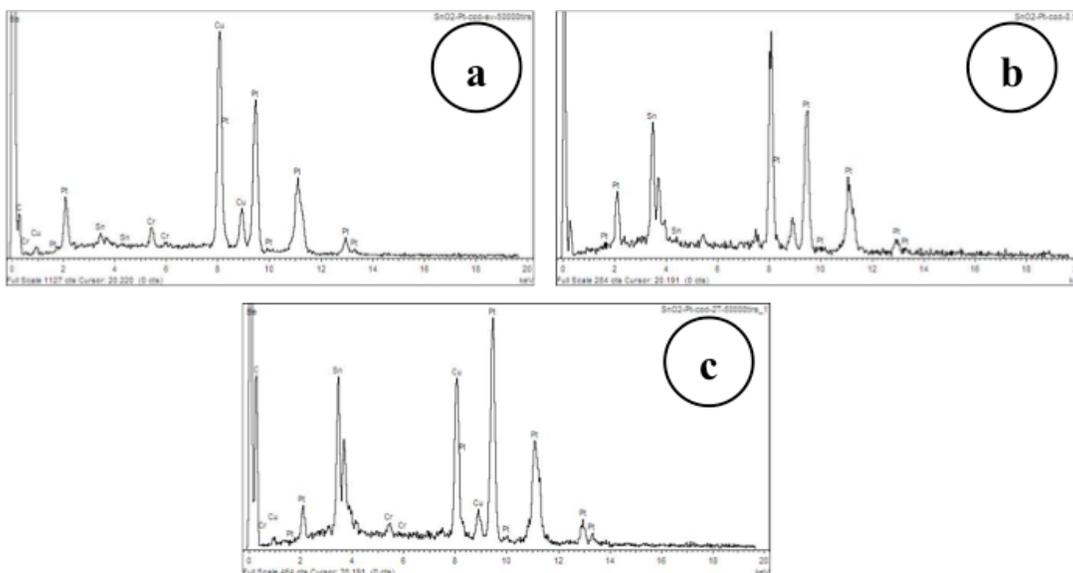
Figure S2 Energy dispersion spectroscopy (EDS) graphs under transmission electron microscope of CBPLD-synthesized (Pt-SnO₂) films onto CNTs catalyst support. (a) CNT/(Pt-SnO₂)ᵤᵥ, (b) CNT/(Pt-SnO₂)₀.₅ₜ, and (c) CNT/(Pt-SnO₂)₂ₜ nanocomposites.
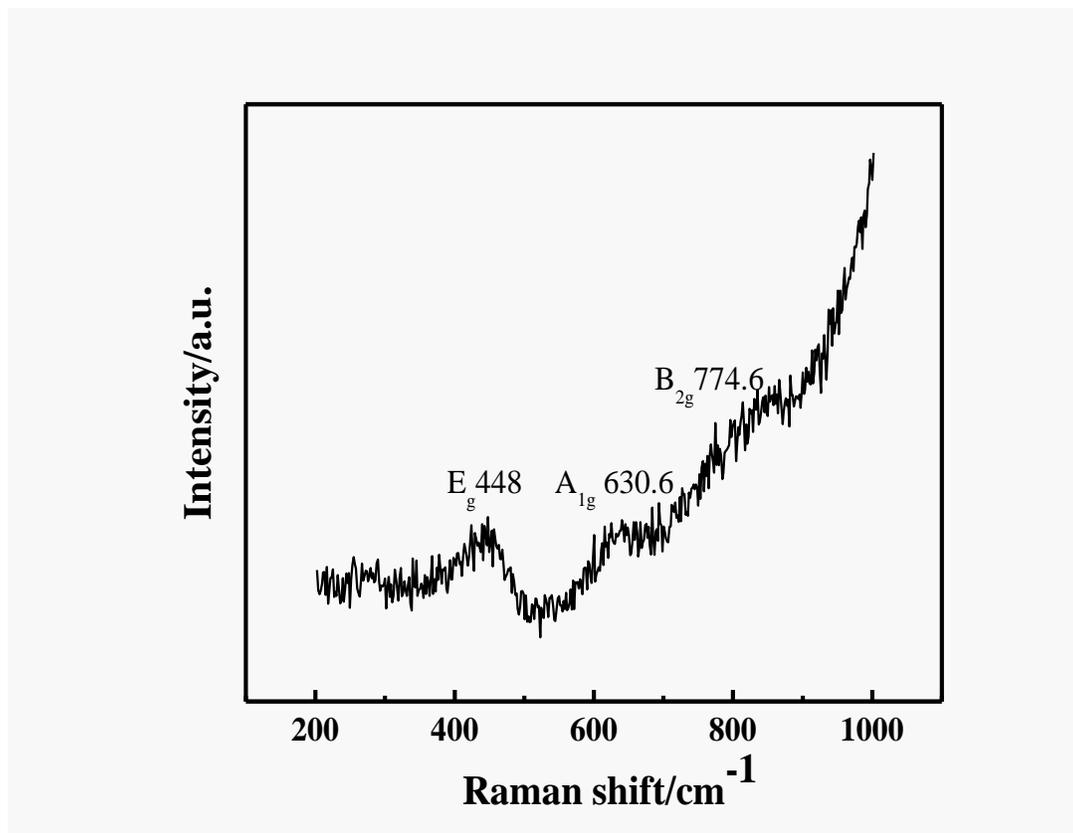
Figure S3 Raman spectrum of CNT/SnO₂ sample. SnO₂ was synthetized onto CNTs using pulsed laser deposition with 20000 laser pulses under 2 Torr of He.
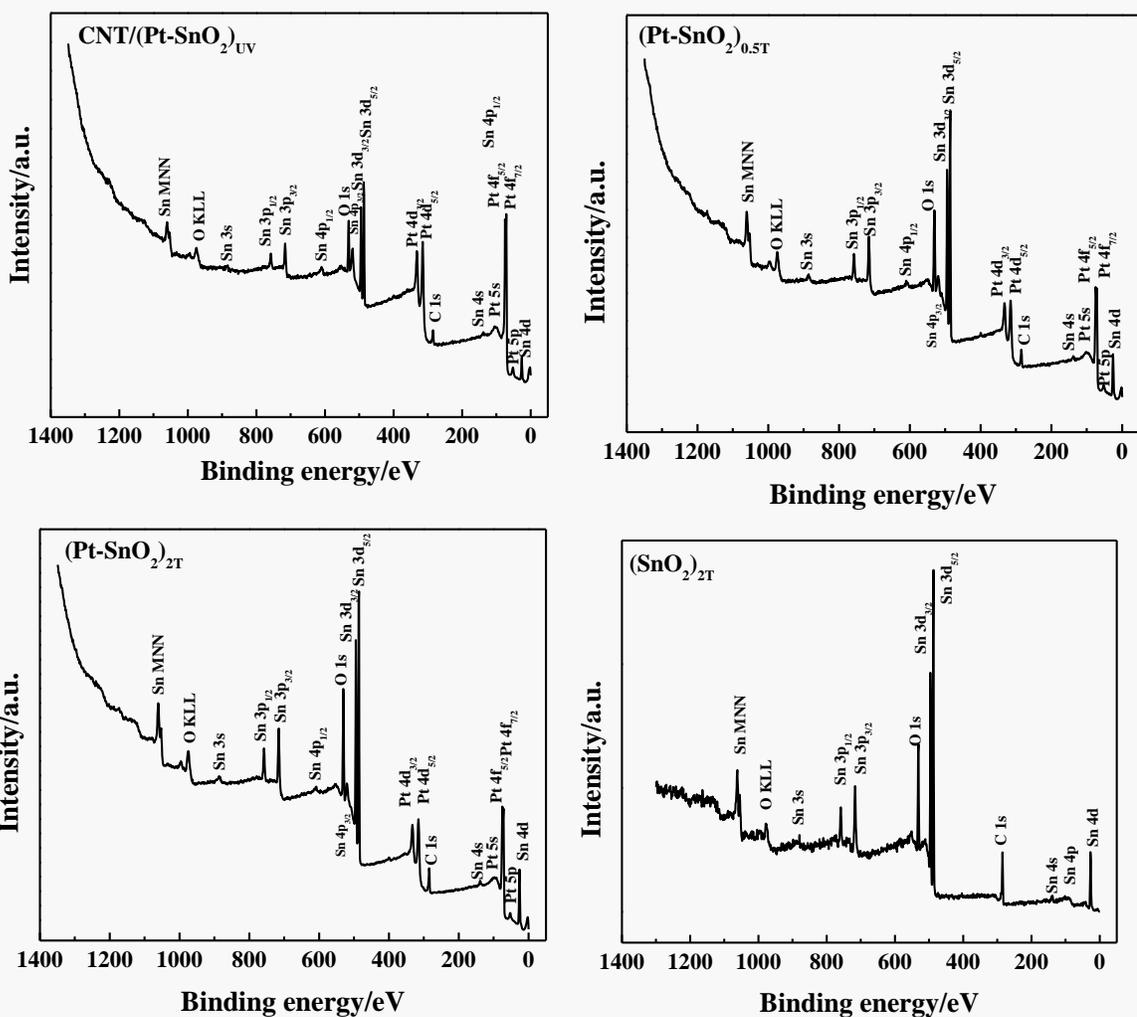
Figure S4 XPS survey scans as indicated in the figures of CNT/(Pt-SnO$_2$)$_{UV}$; CNT/(Pt-SnO$_2$)$_{0.5T}$; CNT/(Pt-SnO$_2$)$_{2T}$ and CNT/(SnO$_2$) samples.

138
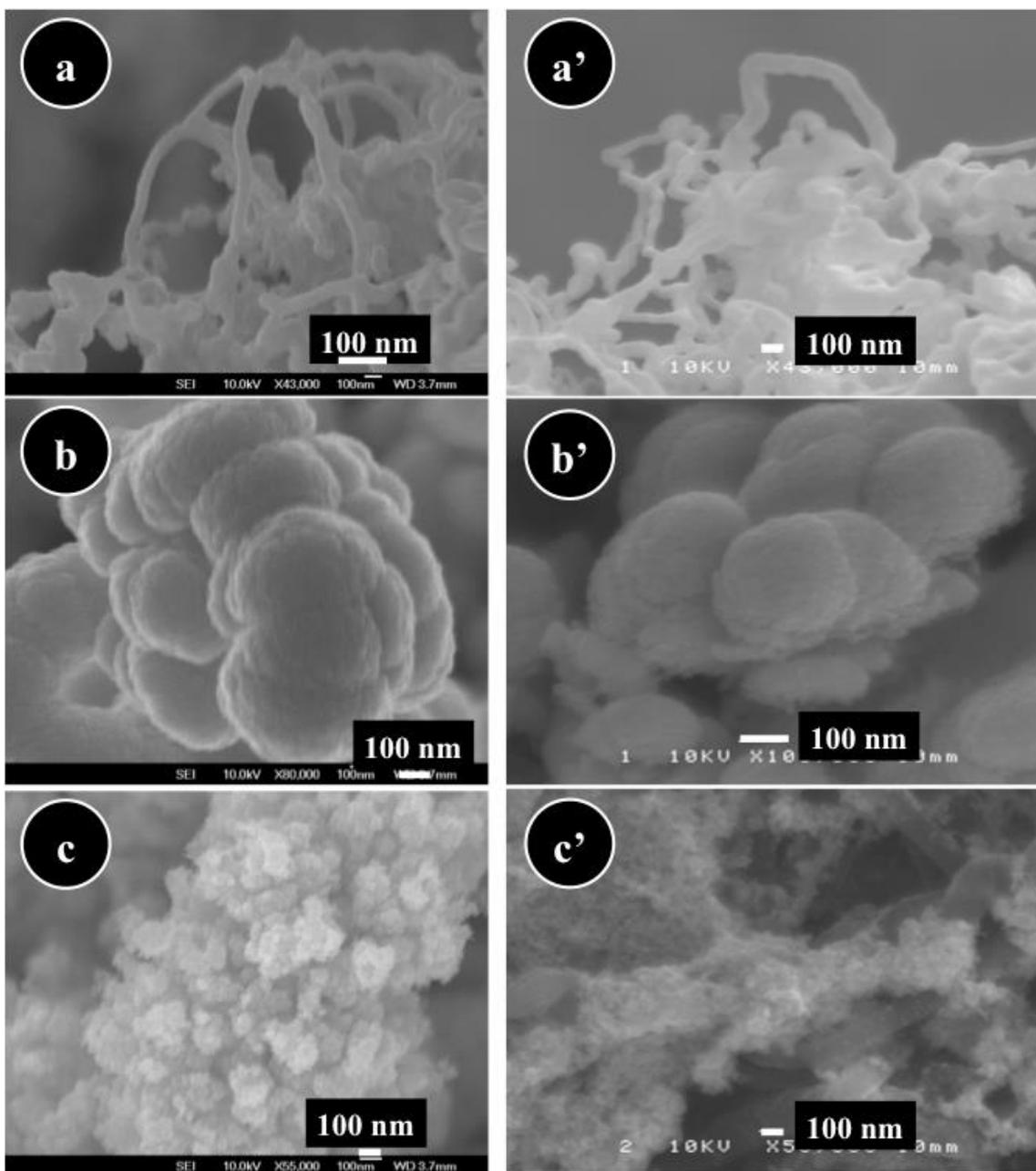
Figure S5 SEM analysis of: as-prepared nanocomposites: (a) CNT/(Pt-SnO$_2$)$_{UV}$, **(b)** CNT/(Pt-SnO$_2$)$_{0.5T}$, **and (c)** CNT/(Pt-SnO$_2$)$_{2T}$ **and their (a'), (b') and (c') are their respective morphologies after durability measurements.**

ARTICLE 3

Synthesis, Characterization and Electrochemical Activity of Laser Co-Deposited Pt-MnO$_2$ decorated carbon nanotubes nanocomposites

Synthèse, caractérisation et activité électrochimique des nanocomposites de nanotubes carbone décorés par Pt-MnO$_2$ co-déposés avec l'ablation laser

Authors

Youling Wang, Mohamed Mohamedi

Énergie, Matériaux et Télécommunications (EMT), Institut National de la Recherche Scientifique (INRS), Université d'Avant-garde, 1650 Boulevard Lionel Boulet, Varennes, Québec, J3X 1S2, Canada.

Contribution

I performed all the experimental synthesis, the electro-chemical measurements, and all characterizations (XRD, SEM and XPS) except the TEM and NAA measurements which have been done by technicians. I also realized the data analysis and interpretation of results. I participated in the writing of the article with the help of other co-authors.

Publication

Résumé traduit

Une couche de catalyseur ternaire sans liant de CNT (nanotubes de carbone)/(Pt-MnO$_2$) est présentée. Des nanocomposites de (Pt-MnO$_2$) de différentes morphologies de surface sont déposées directement pour la première fois à la température ambiante sur des CNTs par ablation laser à flux croisés et leurs électroactivités dans l'acide sulfurique et envers l'électrooxydation de l'éthanol sont examinées. Il est démontré que l'activité électrochimique du CNT/(Pt-MnO$_2$) surpasse le matériau de référence CNT/Pt. La performance catalytique supérieure de l'électrocatalyseur Pt-MnO$_2$ à l'oxydation de l'éthanol est attribuée à la présence de MnO$_2$, qui favorise l'oxydation électrocatalytique de l'éthanol en accélérant le processus de déshydrogénation, fournit des espèces hydroxyles pour oxyder les intermédiaires adsorbés

ARTICLE 4

Laser synthesis of hierarchically organized nanostructured TiO$_2$ films on microfibrous carbon paper substrate: characterization and electrocatalyst supporting properties

Synthèse par laser de films de TiO$_2$ nanostructurées et organisées hiérarchiquement sur substrat de papier carbone microfibreux: caractérisation et propriétés de support électrocatalytique

Authors

Youling Wang, Amel Tabet-Aoul, Mohamed Mohamedi

Énergie, Matériaux et Télécommunications (EMT), Institut National de la Recherche Scientifique (INRS), Université d'Avant-garde, 1650 Boulevard Lionel Boulet, Varennes, Québec, J3X 1S2, Canada.

Contribution

I performed all the experimental synthesis, the electro-chemical measurements, and all characterizations (Micro-Raman, SEM, AFM and XPS) except NAA measurements which have been done by technicians. I also realized the data analysis and interpretation of results. I participated in the writing of the article with the help of other co-authors.

Publication

Résumé traduit

Le dioxyde de titane est bon marché, non-toxique, présente une résistance mécanique élevée, très stable dans des environnements acides et oxydants est étudié comme alternative au carbone en tant que support de catalyseur dans les piles à combustible à basse température. Ici, des films minces de TiO$_2$ avec diverses morphologies de surface sont synthétisés à température ambiante par dépôt par ablation laser sur un substrat microfibreux de papier carbone conducteur, qui est le type de substrat utilisé dans des dispositifs de stockage et de conversion d'énergie. Les films de TiO$_2$ déposées sous vide et en présence d'une faible pression d'oxygène sont très lisses et denses. Au contraire, les films de TiO$_2$ déposées en présence d'hélium sont des structures poreuses et alignées verticalement. Une augmentation de la pression d'hélium conduit à la

formation de nanostructures alignées verticalement ressemblant à des forêts. La spectroscopie micro-Raman révèle que les films sont amorphes et dont la phase cristalline est rutile. La spectroscopie de photoélectrons par rayons X montre que le Ti est dans un état complètement oxydé de Ti^{4+}. Les propriétés de support électrocatalytique au Pt sont étudiées dans H_2SO_4 et dans une solution de H_2SO_4 saturée en oxygène. On constate que, indépendamment de la morphologie du film, tous les films de TiO_2 synthétisées augmentent considérablement la surface électroactivé du Pt et améliorent son électroactivité envers la réaction de réduction d'oxygène par rapport au Pt non-supporté.

Mots clés

Abstract

Titanium dioxide is cheap, non-toxic, exhibits a high mechanical resistance, very stable in acidic and oxidative environments is being studied as alternative to carbon as catalyst support in low-temperature fuel cells. Herein, via pulsed laser deposition, various morphologies of TiO_2 thin films are synthesized at room temperature onto conductive microfibrous carbon paper substrate, which is the type of substrate, employed in energy storage and conversion devices. TiO_2 films deposited under vacuum and in the presence of mild pressure of oxygen are very smooth and dense. Instead, TiO_2 films deposited in the presence of helium atmosphere are of porous structures and vertically aligned. An increase in the helium pressure leads to the formation of forest-like vertically aligned nanostructures. Micro-Raman spectroscopy reveals that the films are amorphous and of rutile phase. X-ray photoelectron spectroscopy shows that Ti is in fully oxidized state of Ti^{4+}. The electrocatalytic supporting properties to Pt are investigated in H_2SO_4 and O_2-saturated H_2SO_4 solution. It is found that regardless of the film morphology, all the synthesized TiO_2 films dramatically increase the electroactive surface area of Pt and enhance its electroactivity towards oxygen reduction reaction as compared with bare Pt electrode.

Key words

1. Introduction

Proton exchange membrane (PEM) fuel cells continue to receive great attention as they are recognized as a promising future electrochemical power sources for mobile applications and eventually for transportation. Electrocatalysts (generally Pt-carbon) for PEM fuel cells must demonstrate a high specific surface activity towards the reduction of oxygen (cathode) and the catalytic oxidation of hydrogen/methanol, ethanol (anode). High electrocatalyst cost (exclusive use of Pt-based catalysts) and lack of stability of dispersed Pt nanoparticles are among some of the issues hampering the commercialization of PEMFCs. Therefore, numerous recent efforts have focused on the development of (i) novel nanostructures or composites with ultra-loaded Pt to lower the cost [1-2], and (ii) new nanostructured catalyst supports to replace activated carbons to improve catalyst dispersion and durability [3].

Electrocatalyst supports play a crucial role in determining the performance, durability and cost of PEMFC systems. A multitude of nanostructured materials including carbon nanostructures, metal oxides, conducting polymers and several hybrid conjugates have been systematically investigated over the past few decades to enhance the state of the art and also develop new PEMFC catalyst support. For further details related to recent development of catalyst supports, the reader is directed to the comprehensive review of Sharma and Pollet [4].

For instance, activated carbon (e.g. carbon black – Vulcan XC 72R) is the most widely used catalytic support. However, the development of more efficient supports is required to prevent detachment and/or aggregation of the Pt catalyst [5]. With regard to new catalyst support, the use of mesoporous carbon, a nanostructured porous material [6-7] or carbon nanotubes (CNTs) [8-9] have exhibited enhanced performance in PEM fuel cells.

Titanium dioxide is a widely employed semiconductor material with further potential applications in solar cells [10], biotechnology [11], photocatalysis [12], supercapacitors [13], lithium-ion batteries [14] and gas sensors [15]. Titanium dioxide is less costly, non-toxic, possesses a high mechanical resistance, more stable in acidic and oxidative environments is being studied as a replacement to carbon as catalyst support in low-temperature fuel cells. Despite these interesting properties, its low electronic conductivity has prevented so far any application. But progresses into enhancing the electronic conductivity of TiO_2 and its use in PEMFC seem to have been reached lately. For example, nanostructured TiO_2 electrodes display high stability when used in a PEM fuel cell as the cathode in acidic environments [16]. Drew et al. found that the use of nanostructured TiO_2 as a substrate improves the performance of Pt-Ru

catalysts for methanol oxidation [17]. Recently, Song et al. demonstrated that the use of TiO_2 nanotube supports for Pt/C enhances the catalytic activity and alleviates against electrode poisoning by CO during methanol oxidation [18-19]. Further information regarding titanium dioxide in fuel cell technology can be found in the review of Abdullah and Kamarudin [20].

For now, the carbon paper (CP) made of carbon fibers network remains an essential material as a substrate in energy storage and conversion devices. It is electrically conductive and its fiber network provides necessary support to anchor catalyst particles and facilitates collection and conduction of electrons. Controlled growth of TiO_2 films or aligned TiO_2 onto conducting microsized carbon fibres is challenging and the literature on this subject is very scarce. Only very recently, Jiang et al. hydrothermally synthesized TiO_2 nanorod arrays (NRs) on CP and converted the composite into TiO_2-C NRs by heat treatment at 900 °C under methane atmosphere. Afterwards, platinum nanoparticles were sputtered onto the TiO_2 NRs by physical vapor deposition to produce Pt-TiO_2-C [21]. Their as-prepared Pt-TiO_2-C exhibited high stability during accelerated durability tests when used as cathode in an H_2/O_2 fuel cell. Tao Yin et al. prepared *in situ* vertically oriented TiO_2 nanosheets (TiO_2-NSs) layer on the surface of a CP electrode via hydrothermal synthesis upon addition of a suitable amount of activated carbon powders in a reactor [22]. Their electrode demonstrated a performance superior to that of a bare CP electrode in a microbial fuel cell.

The prime objective of this work is to attempt to synthesize in one step and at room temperature nanostructured TiO_2 films directly onto a CP substrate using the pulsed laser deposition (PLD) method. The deposition conditions were varied so as to obtain different morphologies of the TiO_2 films. The second objective of this work is to study the catalytic supporting properties of these laser synthesized TiO_2 films towards platinum activity in H_2SO_4 and oxygen reduction reaction (ORR), two reactions of great importance to many electrochemical practical applications including fuel cells [23-25]. Because of its well-known behavior towards these two reactions, Pt is chosen here as a model catalyst for fundamental studies.

2. Experimental Section

2.1. Materials

TiO_2 (99.99%), Ti (99.99%) and Pt (99.99%) targets used for the PLD were purchased from Kurt J. Lesker Co., Canada. Cut pieces of Toray paper (Electrochem) were used as a carbon

fibers electrode and further coated with TiO_2 and Pt thin films. The carbon fiber network of the paper is the type of gas diffusion layer used in fuel cell devices, which is electrically conductive and can facilitate collection and conduction of electrons. Sulfuric acid (96% purity from Acros Organics) was used as received without further purification.

2.2. Syntheses

TiO_2 and Pt thin films were deposited by PLD at room temperature with a KrF excimer laser (λ= 248 nm, pulse width = 17 ns, and repetition rate = 50 Hz) and a laser fluence of 4 J cm^{-2}. The resulting plume was directed at a substrate held 5 cm above the target. In order to obtain a uniform ablation over the whole target surface, the target was continuously rotated and translated. Prior to deposition, the PLD chamber was evacuated with a turbo pump to a base pressure of 4×10^{-5} Torr.

In order to obtain various surface morphologies, TiO_2 films were deposited, under different background gas atmospheres, namely under vacuum, inert gas (helium), and oxygen. Thus a series of TiO_2 films with the same number of laser shots (20000 times) were prepared in vacuum, 0.5 Torr He, 2 Torr He, and a mild pressure of oxygen 10 mTorr. It has to be noted that TiO_2 film deposited under oxygen was conducted from the ablation of a pure Ti target. More details regarding the description of the PLD setup and its working principle can be found elsewhere [26]. In this paper the samples are denoted as $(TiO_2)_{UV}$, $(TiO_2)_{0.5THe}$, $(TiO_2)_{2THe}$ and $(TiO_2)_{10mTO2}$, where the subscripts UV and T stand for under vaccum and Torr, respectively.

2.3. Material Characterization

The surface morphology of the as-prepared TiO_2 films was characterized using scanning electron microscopy, SEM (JEOL, JSM 7401F apparatus) and by atomic force microscopy (AFM) using a Nanoscope III microscope from Digital Instrument.

Phase and structural analysis of the TiO_2 were characterized by micro-Raman spectroscopy (Renishaw) using a 514.5 nm (2.41 eV) laser radiation of an Ar+ laser with a circular polarization. The laser beam was focused onto the sample to a spot size of 1 μm in diameter (Renishaw Imaging Microscope WireTM).

The surface composition was studied by X-ray photoelectron spectroscopy, XPS via a VG Escalab 220i-XL equipped with an Al Kα source (1486.6 eV). The anode was operated at 10 kV

and 20 mA. The pass energy of the analyzer was fixed at 20 eV. All samples were analyzed with a spot size of 250 × 1000 µm located approximately in the center of the sample. A survey spectrum ranging from 0 to 1350 eV was first acquired, and then higher resolution multiplex scan spectra (Ti 2p, O 1s, and C 1s core levels) were obtained. Quantification of the elements was carried out with CasaXPS software (Casa Software Ltd.) by fitting the core level spectra after a Shirley background removal. The C 1s core level peak at 284.6 eV, resulting from hydrocarbon contaminants at the surface, was used as an internal reference. All spectra have been recalibrated with respect to the C 1s core level peak of adventitious carbon contamination.

2.4. Electrochemical Characterization

The electrochemical properties of all samples were evaluated by cyclic voltammetry (CV) in a three-compartment electrochemical cell at room temperature. A Pt coil was used as the counter electrode and an Ag/AgCl, 3 M KCl was used as the reference electrode. A Luggin capillary that is very close to the working electrode to minimize the ohmic drop separated the reference electrode from the analyte solution. Data acquisition was conducted with a potentiostat/galvanostat Autolab from EcoChemie. CV measurements were carried out in 0.5 M H_2SO_4 solution in the absence and presence of oxygen.

3. Results and Discussion

3.1. Film structure and morphology

Figure 1 presents the SEM images of the TiO_2 films synthesized by PLD onto CP substrate. Top views SEM images reveal that TiO_2 films deposited under vacuum (Fig. 1a) and 10 mT of O_2 (Fig. 1d) are dense and smooth. Introducing He led to a new deposition regime with increased roughness and segmentation of the film into clusters of particles. For example, the film deposited at 0.5 Torr of He, the surface roughness increased significantly, and micro-cracks can be seen at the surface (Fig. 1b). The cross-sectional view shows columnar ordered structures are the building blocks of the TiO_2 film. When the deposition pressure is increased to 2 Torr of He, the film revealed a more porous surface, and the cross-sectional view showed TiO_2 with forest-like structure (Fig. 1c). This morphological variation with the background pressure is principally due to the difference of the kinetic energy of the deposited species that varies with the atmosphere in the deposition chamber [26]. The increase of the porosity of the films by increasing the deposition

pressure can be explained by the fact that the kinetic energy of the pulsed particles decreases at higher pressure, and therefore the particles reaching the surface should have less energy, less mobility and therefore will give rise to more porous films. The thickness of the films was estimated by cross-section SEM images to be 190, 187, 2000, and 200 nm for $(TiO_2)_{UV}$, $(TiO_2)_{0.5THe}$, $(TiO_2)_{2THe}$, and $(TiO_2)_{10mTO2}$, respectively.
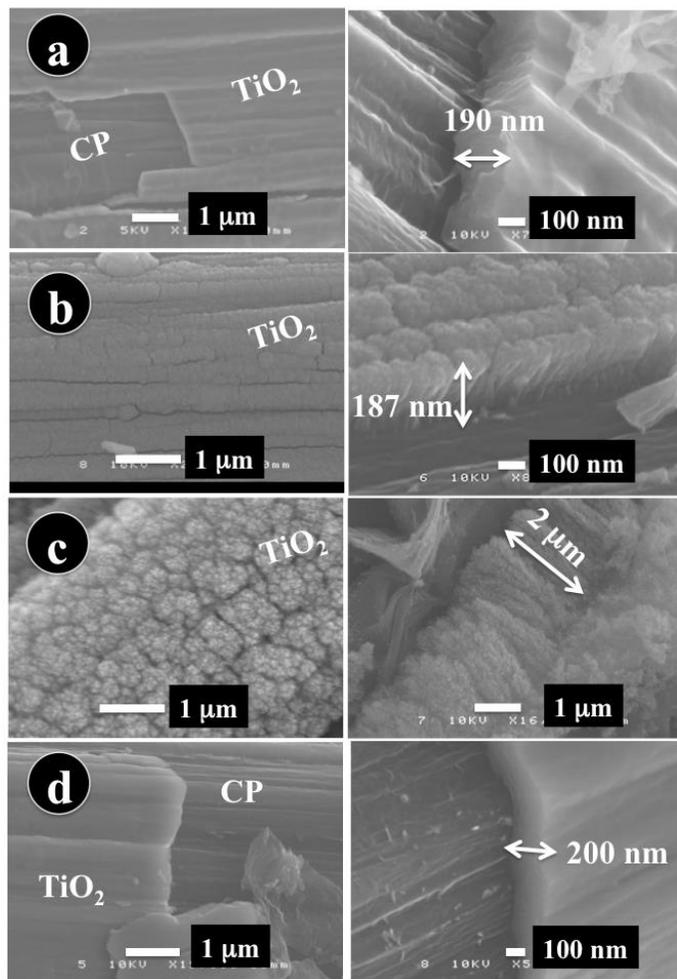
Fig. 1 Top view and corresponding cross-section SEM micrographs PLD-synthesized TiO₂ films onto carbon paper substrate. (a) $(TiO_2)_{UV}$; (b) $(TiO_2)_{0.5THe}$; (c) $(TiO_2)_{2THe}$ and (d) $(TiO_2)_{10mTO2}$.

Figure 2 shows AFM images of the TiO_2 films and the surface roughness measured across a carbon fiber was found to be around 12 nm and 15 nm for $(TiO_2)_{UV}$, and $(TiO_2)_{10mTO2}$, respectively. Deposits under He were found rougher with 19 nm and 87 nm obtained for $(TiO_2)_{0.5THe}$ and $(TiO_2)_{2THe}$, respectively.
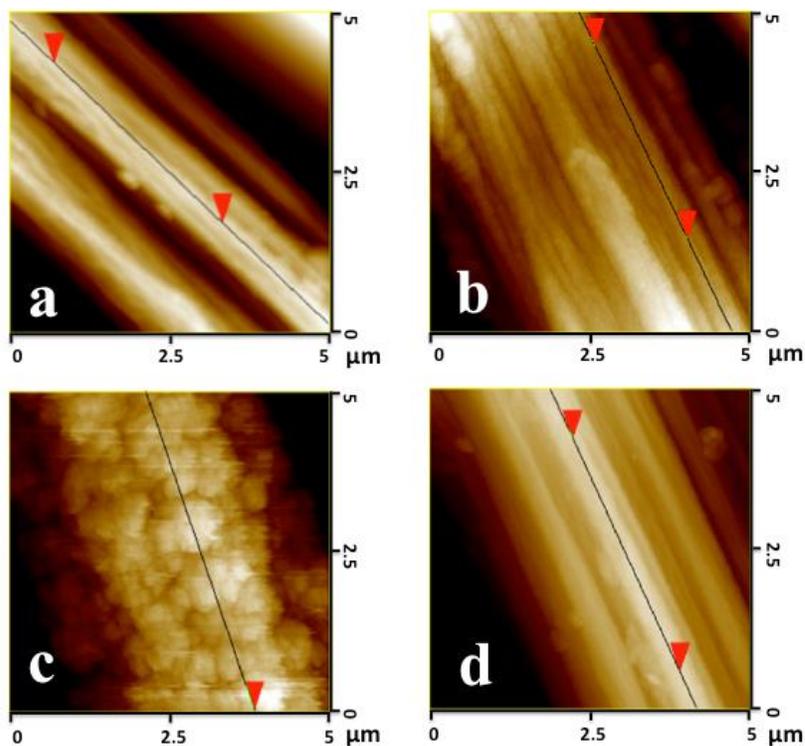
Fig. 2 AFM images of PLD-synthesized TiO$_2$ films onto carbon paper substrate. (a) (TiO$_2$)$_{UV}$; (b) (TiO$_2$)$_{0.5THe}$; (c) (TiO$_2$)$_{2THe}$ and (d) (TiO$_2$)$_{10mTO2}$.

The crystalline structure of the TiO$_2$ films was assessed with micro-Raman spectroscopy and results are reported in Fig. 3a. As a reference, the Raman spectrum of the TiO$_2$ target used for deposition is also reported in Fig. 3a. The TiO$_2$ target displays vibrational peaks at around 141 cm^{-1}, 236 cm^{-1}, 450 cm^{-1}, 610 cm^{-1} characteristics of rutile phase [27]. Only large bands around 450 and 610 cm^{-1} are observed for TiO$_2$ films deposited either under vaccum, helium or oxygen, which indicates that they are prevalently amorphous or disordered [28].

Figure 3b displays the high-resolution XPS Ti 2p core level of the TiO$_2$ films synthesized under different background atmospheres. The Ti 2p spectra show the binding energy of the Ti 2p$_{1/2}$ and Ti 2p$_{3/2}$ photoelectron peaks at around 464 eV and 458.3 eV, respectively, indicating that Ti was in fully oxidized state of Ti^{4+} at the surface of all the thin films [29-30]. The O 1s peak has a slightly asymmetric tail on the high-binding-energy side (Supplementary data, Fig. S1), which might be attributed to hydroxyl groups at the outermost surface as well as the adsorbed water resulting from moisture adsorption in air [31]. If we consider the relative areas corresponding to the main O 1s component (associated mainly to Ti^{4+}–O bonds) and the relative area corresponding to the main Ti 2p contribution, we find that the corresponding O/Ti atomic

ratio is 2.2, which is close, within the error of the experimental determination, to the expected stoichiometric ratio of 2.0.
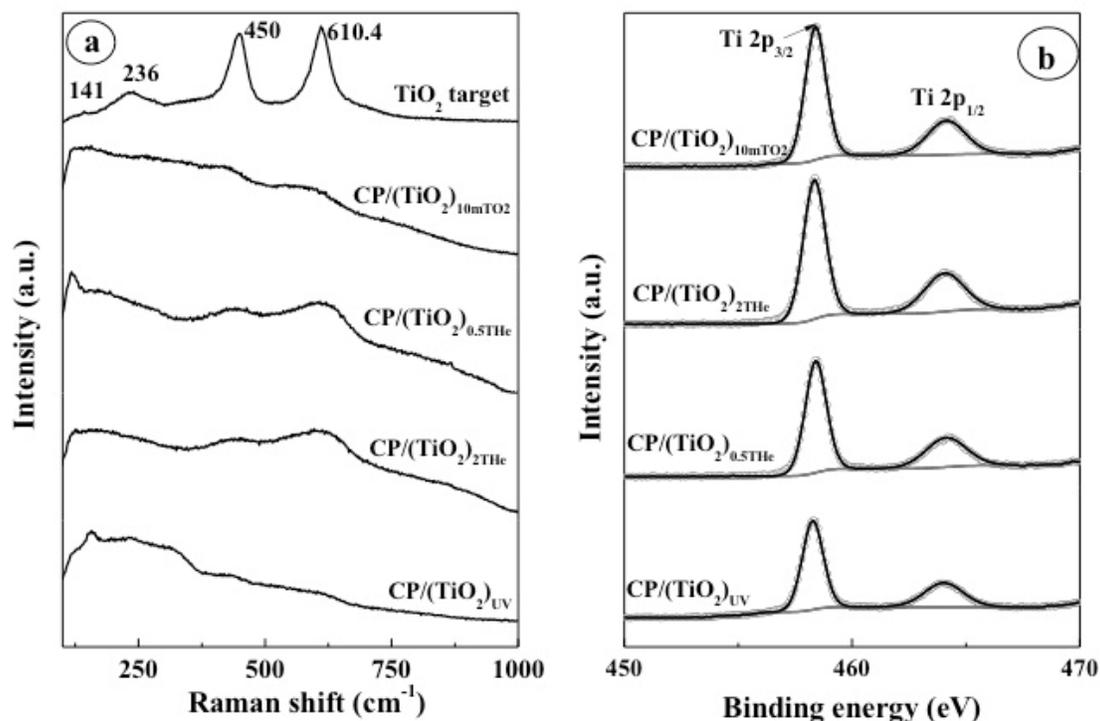
Fig. 3 Spectroscopy analyses of PLD-synthesized TiO$_2$ films. (a) Raman spectra. The Raman spectrum of the TiO$_2$ target is shown for referencing. (b) High-resolution XPS spectra of Ti 2p core level in CP/TiO$_2$ samples.

3.2. Electrochemical study

To explore the catalyst supporting properties of the laser synthesized TiO$_2$ films, Pt film onto each TiO$_2$ film was PLD-deposited under 2 Torr of He atmosphere with 20000 laser pulses (a loading of 48   g cm^{-2} measured by neutron activation analysis, NAA using a SLOWPOKE nuclear reactor). Figure 4a shows an example of Pt deposited onto TiO$_2$ film synthesized in presence of 10 mT of O$_2$. The cross-section image (Fig. 4b) clearly shows the carbon fiber coated with TiO$_2$ film beneath a Pt film with a thickness of about 80 nm. A benchmark electrode made of Pt deposited with similar conditions onto CP substrate was also fabricated (Fig. S2).
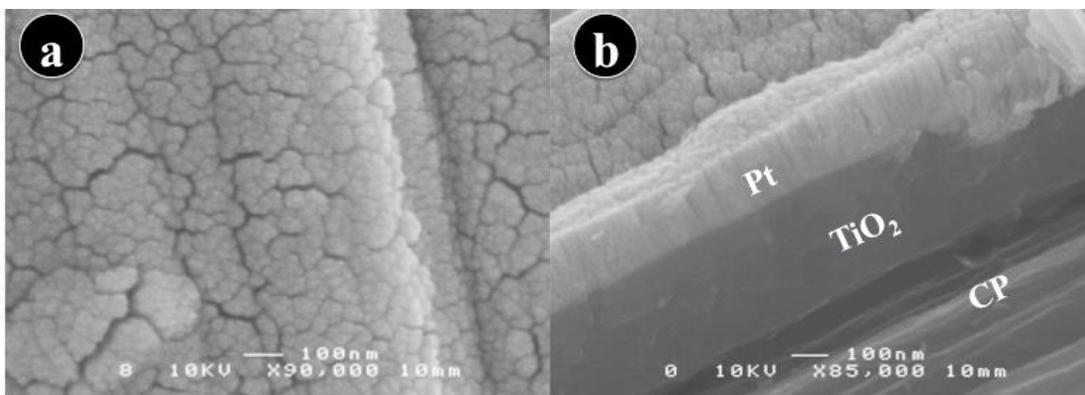
Fig. 4 Representative top view (a) and corresponding cross-section (b) SEM micrographs of Pt thin film deposited by PLD onto TiO_2 film itself deposited onto CP substrate.

The electroactivity study was first conducted in a deaerated 0.5 M H_2SO_4 electrolyte. Figure 5 shows comparative CVs recorded with 50 mV s^{-1} at $CP/TiO_2/Pt$ and bare CP/Pt electrode as a benchmark. It has to be reminded that all electrodes shown in Fig. 5 contain similar amount of Pt. The CV of bare CP/Pt reveals the characteristic features due to hydrogen adsorption/desorption, double layer charging, Pt oxide formation and Pt oxide reduction [32]. Similar features are observed at the $CP/TiO_2/Pt$ electrode indicating that the beneath TiO_2 film did not insulate the Pt nanoparticles and on the contrary the TiO_2 film improved the electroactivity of Pt. Indeed the current densities at the $CP/TiO_2/Pt$ electrodes are more much greater than those observed with the bare CP/Pt electrode. The measure of the effect of the TiO_2 film on the electrochemical activity of Pt can be established by estimating the electroactive surface area (*ESA*), which is determined by integrating the charge in the hydrogen adsorption region of the voltammograms corrected for the double-layer current, using a conversion factor of 210 μC cm^{-2} [33]. Accordingly, the *ESA* of Pt nanocrystals in CP/Pt, $CP/(TiO_2)_{UV}/Pt$, $CP/(TiO_2)_{0.5THe}/Pt$, $CP/(TiO_2)_{2THe}/Pt$, and $CP/(TiO_2)_{10mTO2}/Pt$ samples was estimated to be 3.3, 27.5, 15, 12.5, 29 m^2 g^{-1}. These results show that all $CP/TiO_2/Pt$ electrodes provided much higher *ESA*s than the bare CP/Pt electrode. On the other hand, despite a similar Pt loading in the different $CP/TiO_2/Pt$ electrodes, structures containing TiO_2 film deposited under vacuum and under oxygen atmosphere demonstrated by far the highest *ESA*s, which are more than 8 times greater than those of the bare CP/Pt electrode. The observations of Fig. 5 show that Pt supported with $(TiO_2)_{UV}$ and $(TiO_2)_{10mTO2}$ delivered close values of *ESA* due to the fact that both films possess thicknesses, surface roughness and morphologies very close to each other. Thus, it can be suggested that TiO_2 film having a smooth surface morphology offer a more effective utilization of the smaller size of Pt nanoparticles and their high dispersion loaded on the C/MnO_2 substrates.
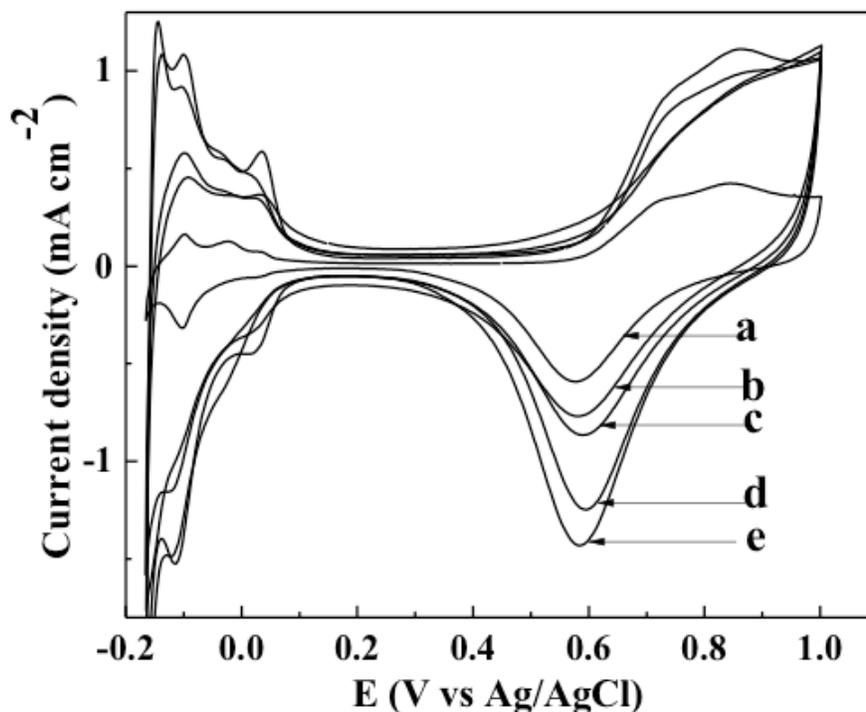
Fig. 5 Cyclic voltammetry in 0.5 M H_2SO_4-argon purged solution with a potential scan rate of 50 mV s^{-1}. (a) CP/Pt; (b) CP/(TiO$_2$)$_{2THe}$/Pt; (c) CP/(TiO$_2$)$_{0.5THe}$/Pt; (d) CP/(TiO$_2$)$_{UV}$/Pt; and (e) CP/(TiO$_2$)$_{10mTO2}$/Pt electrodes.

Afterwards, the 0.5 M H_2SO_4 solution was purged with oxygen for 30 min and oxygen electroreduction measurement started. Linear scan voltammograms (LSVs) were recorded before and after saturation of oxygen. The LSVs were corrected from any residual current observed before saturation with oxygen (Fig. S3). This residual current is mainly due to the current of the reduction of platinum oxide.

Representative LSVs recorded with 5 mV s^{-1} potential scan rate (quasi-steady state) at CP, CP/TiO$_2$, CP/Pt and CP/(TiO$_2$)$_{10mTO2}$/Pt electrodes in O$_2$-saturated 0.5 M H_2SO_4 solution are compared in Fig. 6a. As can be observed, the activities of CP, CP/TiO$_2$ electrodes are very low. On the other hand, a very large reduction waves are observed at the CP/Pt and CP/(TiO$_2$)$_{10mTO2}$/Pt electrodes. The effect of the TiO$_2$ surface morphology on the catalytic activity of Pt towards ORR is illustrated by the LSVs of Fig. 6b. The electrochemical performance in terms of current peak follows CP/(TiO$_2$)$_{10mTO2}$/Pt≈ CP/(TiO$_2$)$_{0.5THe}$/Pt> CP/(TiO$_2$)$_{UV}$/Pt>CP/(TiO$_2$)$_{2THe}$/Pt>CP/Pt.

The onset potential E_{onset} is another parameter that provides information about the kinetic of an electrochemical reaction. Nevertheless, E_{onset} is a concept that is often ill defined. It can be described as the potential value at which the current commences to develop for an electrochemical reaction. This approach is not usually accurate because of the difficulty of

167

identifying the E_{onset} on the CV curves. A second way is to establish some criterion, even if arbitrary for example estimate E_{onset} at a given current value for all the electrodes. Accordingly, a current value of -0.04 mA was selected and its corresponding E_{onset} was estimated (Fig. 6c). First, Fig. 6c shows that irrespective of the morphology, all TiO_2 supported electrodes displayed E_{onset} values more positive than the one displayed by the bare CP/Pt electrode. These observations demonstrate that TiO_2 films promoted faster kinetics of the ORR at Pt catalyst. Figure 6d reports E_{onset} (E_{onset} (TiO_2)/Pt–E_{onset} (Pt)) values extracted from Fig. 6c (indicated by arrows). A comparison among the TiO_2 morphologies shows that the $(TiO_2)_{0.5THe}$ is the support that most enhanced the kinetics at Pt, *i.e.* 50 mV more positive compared to bare Pt.
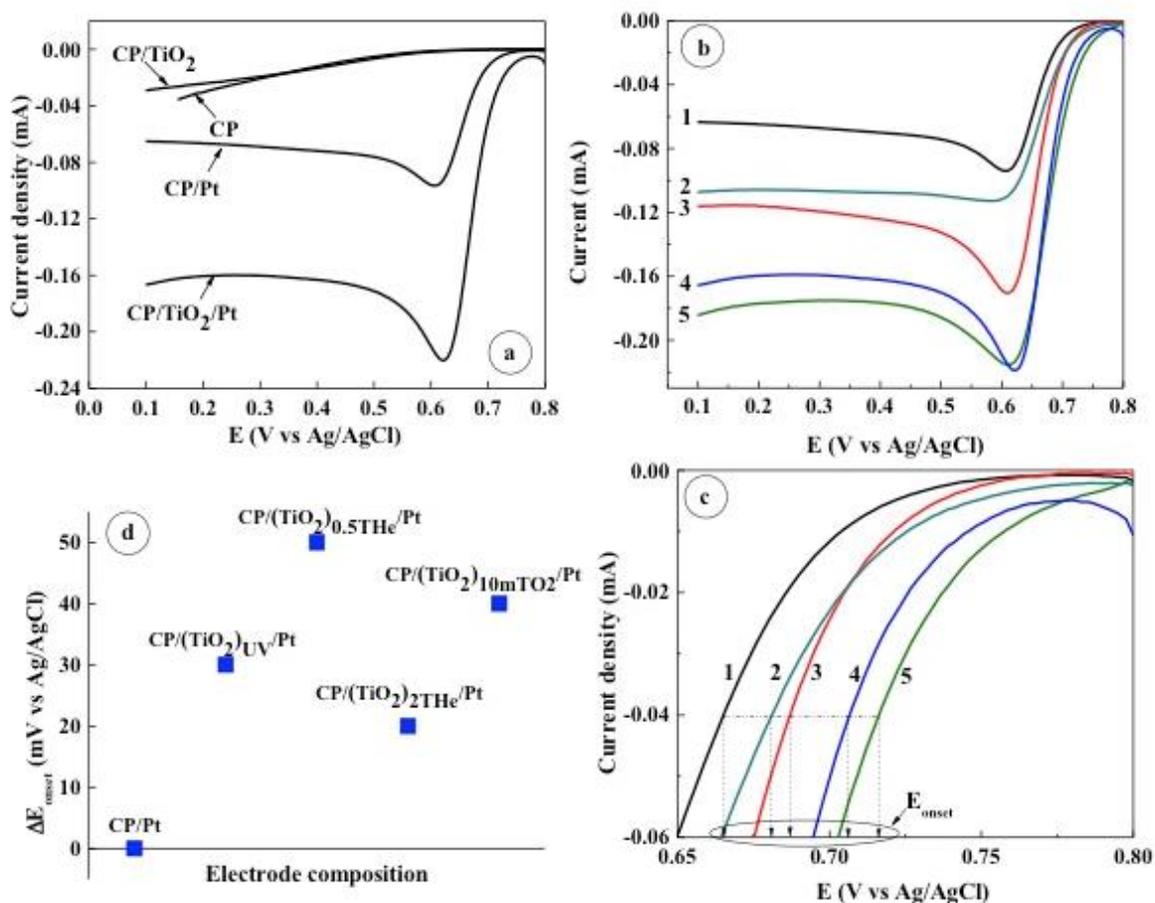
Fig. 6 Electroactivity towards oxygen reduction reaction in 0.5 M H_2SO_4-oxygen saturated solution. (a) Comparative LSVs of CP/Pt, CP/TiO_2, CP/Pt and CP/(TiO_2)/Pt electrodes. (b) LSVs of CP/(TiO_2)/Pt electrodes recorded with 5 mV s^{-1} potential scan rate. (c) Zoom out of Fig. 6b comparing E_{onset} delivered by the CP/Pt and the different CP/(TiO_2)/Pt electrodes at -0.04 mA. (1) CP/Pt; (2) CP/(TiO_2)$_{2THe}$/Pt; (3) CP/(TiO_2)$_{UV}$/Pt; (4) CP/(TiO_2)$_{10mTO2}$/Pt; and (5) CP/(TiO_2)$_{0.5THe}$/Pt. (d) ΔE_{onset} extracted from Fig. 6c.

It is therefore clear that whatever the morphology, all titanium oxide films synthesized here have greatly improved the electroactivity of platinum. These films are therefore an excellent catalyst support not only for Pt but may also be for Pt-alloys catalysts being investigated for ORR, methanol or ethanol electrooxidation reaction in fuel cells technology. Nevertheless, it remains to define the optimal morphology of the PLD synthesized TiO_2 films. This will require more experiences such as varying the thickness, pressure and probably consider the annealing effect on the electronic properties. Such experiments are underway and will be reported in due time.

4. Conclusions

The prime objective of this paper is to synthesize nanostructured TiO_2 films directly onto CP electrode substrate relevant to several electrochemical power sources devices. For the first time TiO_2 films were synthesized in one step on such substrate at room temperature and growth conditions were investigated conditions by using PLD technique. Films were deposited at different background pressures and gas environments, and all of them have been characterized for their microstructures and supporting catalyst properties. We found that TiO_2 films deposited under vacuum and in the presence of mild pressure of oxygen are very smooth and of a closed structure. On the other hand, TiO_2 films deposited in the presence of helium atmosphere are of porous and of columnar morphology. An increase in the helium pressure led to an increase of the film thickness growing into nanoforest-like vertically aligned structures.

Micro-Raman spectroscopy indicates that as-deposited TiO_2 films are amorphous and XPS analysis showed that Ti was in fully oxidized state of Ti^{4+} at the surface of all the synthesized films.

In H_2SO_4 medium and irrespective of the morphology, all the TiO_2 films demonstrated excellent catalyst supporting properties to Pt chosen as a model catalyst. Comparison of the response seen for the ORR suggests that Pt supported by laser synthesized TiO_2 films display enhanced catalytic activity as compared to bare Pt.

Our studies open a very simple and promising way to employ laser synthesized nanostructured TiO_2 films to enhance the Pt utilization and the activity of traditional Pt/C catalysts for other fuel cell reactions. We are currently working on optimizing film thickness, background gas pressure value (oxygen and helium) to tailor their properties towards alcohol fuel cells (methanol or ethanol oxidation).

Finally, single-step deposition of tunable density TiO$_2$ films with good adhesion to the inexpensive substrates, even plastics, kept at room temperature is possible by PLD in a variable background pressure, an interesting perspective both for photocatalytic and advanced photovoltaic applications, substituting the time consuming deposition of different layers and lengthy annealing steps.

Acknowledgments

References

[1] Mark K. Debe, Nature 486 (2012) 43–51.

[2] M. S. Çögenli, S. Mukerjee, A. Bayrakçeken Yurtcan, Fuel Cells 15 (2015) 288–297.

[3] G. G. Wallace, J. Chen, A. J. Mozer, M. Forsyth, D. R. MacFarlane, C. Wang, Materials Today 12 (2009) 20-27.

[4] S. Sharma, B. G. Pollet, J. Power Sources 208 (2012) 96–119.

[5] Y. Shao, G. Yin, Z. Wang, Y. Gao, J. Power Sources 167 (2007) 235-242.

[6] N. Nakagawa, Y. Suzuki, T. Watanabe, T. Takei and K. Kanamura, Electrochem. 75 (2007) 172–174.

[7] Y. Wang, L. Cheng, F. Li, H. Xiong, and Y. Xia, Chem. Mat. 19 (2007) 2095-2101.

[8] G. G. Wildgoose, C. E. Banks and R. G. Compton, Small 2 (2006) 182-193.

[9] M. S. Saha, A. Kundu, J. Power Sources 195 (2010) 6255-6261.

[10] H. Tao, W. Ke, J. Wang, Q. Liu, J. Wan, G. Yang, G. Fang, J. Power Sources 290 (2015) 144-152.

[11] K. S. Brammer, S. Oh, C. J. Frandsen and S. Jin, Biomaterials and Biotechnology Schemes Utilizing TiO_2 Nanotube Arrays, in: R. Pignatello (Ed.), Biomaterials Science and Engineering, InTech, Croatia, 2011, Chapter 9, pp. 193-210.

[12] K. Nakata, A. Fujishima, J. Photochem. Photobiol. C: Photochem. Rev. 13 (2012) 169–189.

[13] W. Zhong, S. Sang, Y. Liu, Q. Wu, K. Liu, H. Liu, J. Power Sources 294 (2015) 216-222.

[14] Y.-M. Lin, P. R. Abel, D. W. Flaherty, J. Wu, K. J. Stevenson, A. Heller, and C. B. Mullins, J. Phys. Chem. C 115 (2011) 2585–2591.

[15] J. Bai and B. Zhou, Chem. Rev. 114 (2014) 10131–10176.

[16] S. von Kraemer, K. Wikander, G. Lindbergh, A. Lundblad, Anders E. C. Palmqvist, J. Power Sources 180 (2008) 185-190.

[17] K. Drew, G. Girishkumar, K. Vinodgopal, P. V. Kamat, J. Phys. Chem. B 109 (2005) 11851-11857.

[18] H. Song, X. Qiu, X. Li, F. Li, W. Zhu, L. Chen, J. Power Sources 170 (2007) 50-54.

[19] H. Song, X. Qiu, D. Guo, F. Li, J. Power Sources 178 (2008) 97-102.

[20] N. Abdullah, S. K. Kamarudin, J. Power Sources 278 (2015) 109-118.

[21] S. Jiang, B. Yi, C. Zhang, S. Liu, H. Yu, Z. Shao, J. Power Sources 276 (2015) 80-88.

[22] T. Yin, Z. Lin, L. Su, C. Yuan, and D. Fu, ACS Appl. Mater. Interfaces 7 (2015) 400−408.

[23] A. N. Golikand and L. Irannejad, Electroanalysis 20 (2008) 1121-1127.

[24] D. C. Higgins, D. Meza, and Z. Chen, J. Phys. Chem. C 114 (2010) 21982-21988.

[25] Y. Bing, H. Liu, L. Zhang, D. Ghosh and J. Zhang, Chem. Soc. Rev. 39 (2010) 2184-2202.

[26] D. B. Chrisey, G. K. Hubler, Pulsed Laser Deposition of Thin Film, John Wiley & Sons, New York, 1994.

[27] M. Salari, K. Konstantinov and H. K. Liu, J. Mater. Chem. 21 (2011) 5128–5133.

[28] F. Di Fonzo, C. S. Casari, V. Russo, M. F. Brunella, A. Li Bassi and C. E. Bottani, Nanotechnology 20 (2009) 015604.

[29] J. F. Marco, A. Cuesta, M. Gracia, J. R. Gancedo, P. Panjan, D. Hanzel, Thin Solid Films 492 (2005)   158-165.

[30] P. M. Kumar, S. Badrinarayanan, M. Sastry, Thin Solid Films 358 (2000) 122-130.

[31] E. McCafferty, J. P. Wightman, Surf. Interface Anal. 26 (1998) 549–564.

[32] G. Jerkiewicz, Electrocatalysis 1 (2010) 179−199.

[33] A. Pozio, M. De Francesco, A. Cemmi, F. Cardellini, L. Giorgi, J. Power Sources 105 (2002) 13-19.

Supplementary Data
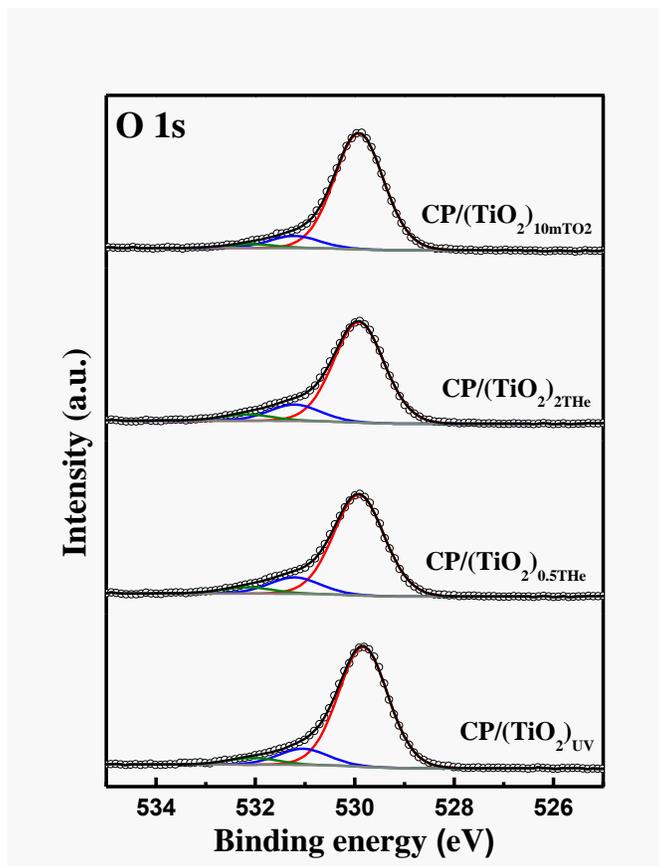
Figure S1: High-resolution XPS spectra of O 1s core level in the TiO₂ films synthesized with PLD.
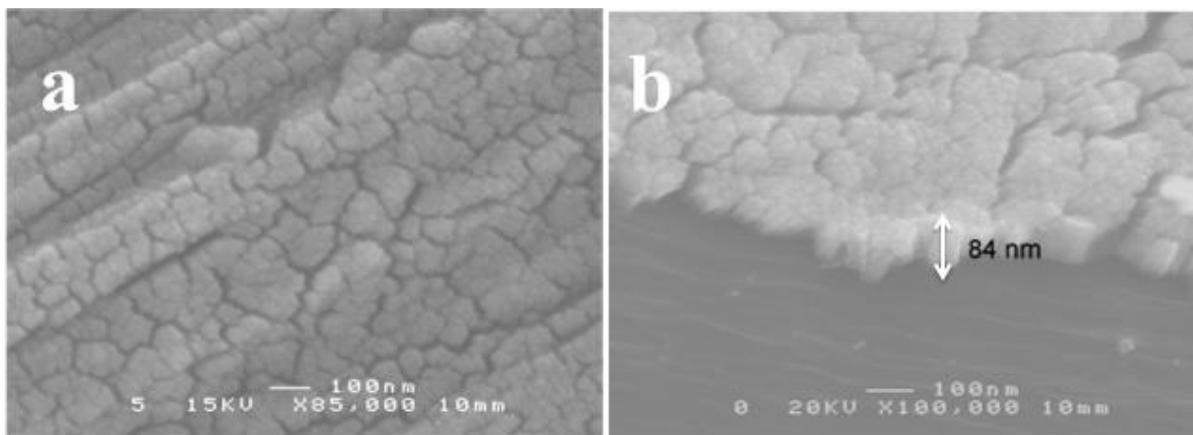
Figure S2: Top view (a) and corresponding cross-section (b) SEM micrographs PLD-synthesized Pt onto carbon paper substrate.
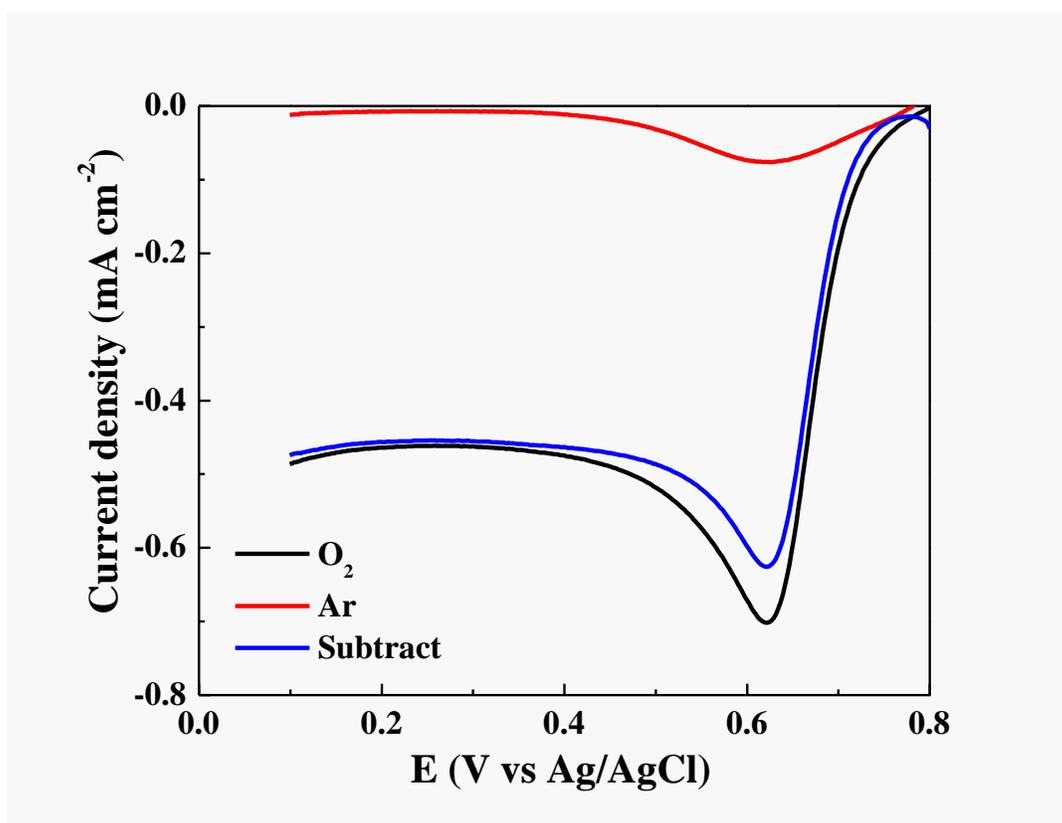
Figure S3: Correction of LSVs from the residual current present 0.5 M H$_2$SO$_4$ argon-saturated before saturation of the solution with oxygen. Potential scan rate of 5 mV s^{-1}.

CHAPTER 5 CONCLUSIONS AND PERSPECTIVES

5.1 Conclusions

In recent years, many efforts have been made to develop highly active, selective and durable Pt-based electrocatalysts for DEFCs. To meet the demands for DEFC electrocatalysts, a promising strategy is to combine Pt catalysts with nanostructured FMO to form platinum-FMO nanocomposites. Taking advantages of particular intrinsic properties and functions of FMOs, several nanostructured FMOs such as CeO_2, SnO_2, TiO_2, MnO_2... are emerging as a distinctive class of electrode materials in FC applications. FMOs could act as a supporting matrix to enhance the dispersion of noble catalysts (e.g. Pt) and the stability against sintering and particles aggregation, or act as co-catalysts of Pt to promote catalytic performance. The work presented in this thesis was devoted to the development of nanostructured Pt-FMO catalysts with high catalytic activity and durability for DEFCs, in particular for the electrocatalytic oxidation of ethanol. In order to gain insight of the role of FMO in catalytic behavior of Pt-based composites, FMO was incorporated into catalyst layer in two ways: the first one is to be intercalated between the layers of the catalyst support (or the substrate) and Pt catalysts, named LOL architecture; and the second way was to be simultaneously deposited with Pt onto catalyst support CNTs or substrate, named co-deposition architecture. Furthermore, owing to unique physiochemical nature for each kind of FMOs, the catalytic performance of Pt-FMO composite catalysts would largely depend on the FMO used. Herein, four kinds of FMO (CeO_2, SnO_2, MnO_2, and TiO_2) have been selected and systematically studied for developing the optimum catalyst. The general conclusion associated with the work described above is presented in this chapter.

First, MnO_2/Pt and TiO_2/Pt catalysts with the same architecture were investigated in this doctoral project based on the work of LOL nanostructured CeO_2/Pt and SnO_2/Pt which has been completed by my colleague. In order to further understand the role of FMO layer, the microstructures (size of the crystallites, structure, roughness, porosity, etc.) of the underlying oxide layer have been varied by changing the gas atmosphere during deposition, while the preparation conditions for Pt layer were maintained constant. All synthesized TiO_2 and MnO_2 films were found to be in amorphous form according to the XRD examinations. In agreement with the previous study, the morphologies of deposited films in PLD were largely dependent on the gas pressure during the deposition process. The morphology of deposited FMO films evolves from

dense and compact to porous finally to highly porous structure when the deposition pressure is varied from under vacuum to 0.5 Torr of He further to 2 Torr. This morphological variation with the background pressure is principally due to the difference of the kinetic energy of the deposited species which varies with the atmosphere in the deposition chamber. The details regarding the morphology variation as a function of background pressure can be found in the PLD section of chapter 3. In the case of Pt layer, the deposition conditions were kept constant. Interestingly, the morphology of Pt layer seems to mimic the morphology of the underlying FMO layer. When the underlying FMO layer is smooth, the surface of Pt layers is relatively flat composed of highly interconnected particles. On the other hand, when the underneath FMO is porous, Pt particles assemble into cauliflower-like arrangements.
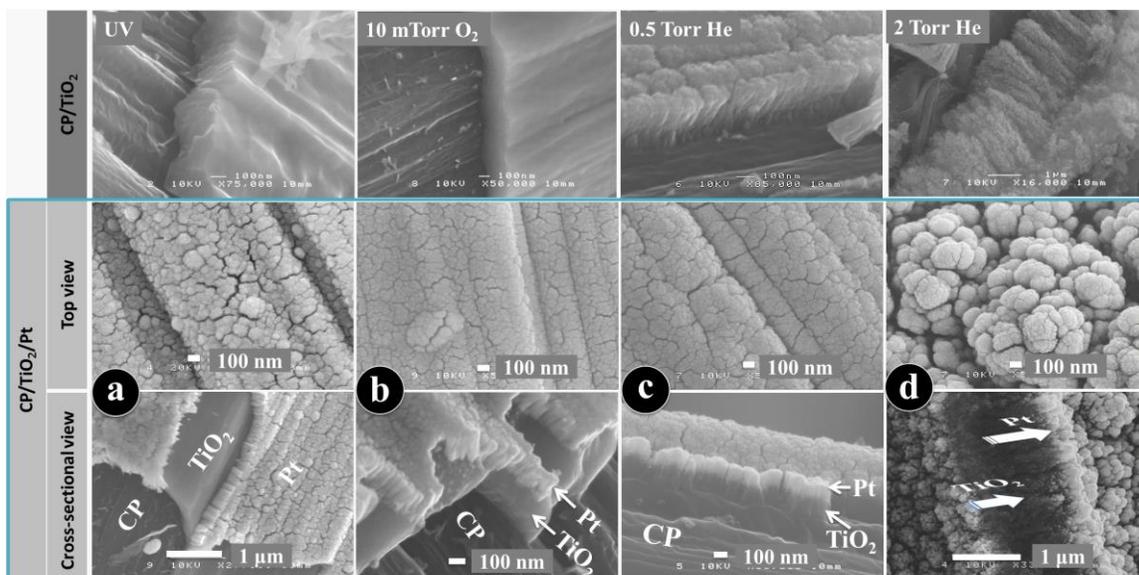
Figure 5.1 SEM micrographs of PLD-synthesized CP/(TiO$_2$) and CP/(TiO$_2$)/Pt samples. (a) CP/(TiO$_2$)$_{UV}$/Pt; (b) CP/(TiO$_2$)$_{10mTO2}$/Pt; (c) CP/(TiO$_2$)$_{0.5THe}$/Pt and (d) CP/(TiO$_2$)$_{2THe}$/Pt.

The morphology-dependent behavior of Pt layer on underlying FMO could be easily observed from the SEM images of CP/TiO$_2$/Pt samples. As seen in Figure 5.1, TiO$_2$ films evolve from dense and compact film to densely packed columns further to tree-like and fluffy structure when the deposition pressure is varied from under vacuum to 0.5 Torr of He further to 2 Torr. Accordingly, Pt films deposited on top change from columnar to cauliflower structure. The results suggest that the morphology (porosity) of the substrate will affect the morphology of deposited materials on it. This morphology difference is resulted from the deposition angle. In the case of a relatively flat substrate, the deposition angle is almost normal, whilst in the case of a rough substrate, a noticeable part of the film grows at grazing incidence, i.e. at glancing angle deposition

176

conditions (GLAD). Generally, GLAD deposition results in the formation of columnar and porous materials, whilst a normal incidence deposition (ND) leads to the formation of denser films. In consistent, the surface morphology of MnO_2 shows the same variation as that of TiO_2 as a function of gas pressure, and the morphology dependence of Pt on top of MnO_2 also shows the same evolution as that grown on TiO_2 film. Via XPS measurement, Pt was found to be predominantly in the metallic state. The CV and CA electrochemical studies have demonstrated that LOL structured MnO_2/Pt (or TiO_2/Pt) electrodes exhibited different EOR performance due to the morphological difference. Finally, the optimized preparation gas pressure for LOL-architectured MnO_2/Pt and TiO_2/Pt catalysts were found in terms of the electro-catalytic activity and durability for EOR.

After, four kinds of Pt-FMO co-deposited catalysts (Pt-CeO_2, Pt-SnO_2, Pt-TiO_2, and Pt-MnO_2) were prepared by CBPLD. We have systematically studied the variation in morphology, composition state of each kind of Pt-FMO co-deposited catalysts as a function of deposition background pressure. The optimized fabrication conditions for each kind of Pt-FMO co-deposits were obtained. The co-deposited Pt-FMO catalysts prepared under optimized condition displayed enhanced catalytic activities for ethanol oxidation relative to pure Pt catalysts. Specifically, optimized Pt-FMO nanocomposites are capable of catalyzing the oxidation of ethanol at a lower potential than Pt, and display higher specific mass activity in both voltammetric and durability studies.

Table 5.1 listed the electrochemical results for the optimized binary FMO-modified Pt catalyst. For comparison purpose, it also includes the results of PLD-synthesized Pt catalysts on CNTs and CP. Comparing two architectures of Pt-FMO catalysts; it was found that the position of FMO within the catalyst layer significantly affected the catalytic performance of the resulting catalyst towards ethanol oxidation. The co-deposited Pt-FMO catalysts exhibited a superior electrocatalytic performance towards ethanol oxidation relative to that with LOL architecture. Such enhanced electrocatalytic performance of Pt-FMO co-deposits is as results of a higher degree of interaction between Pt and FMOs. Co-deposition architecture could a give much higher degree of Pt-FMO (metal-support) contacts in three dimensions in comparison to two dimensional model of Pt onto FMO. FMO deposited simultaneously with Pt modifies the electronic structure of Pt (electronic effect) and is prone to adsorption of a higher number of OH adsorbed species at lower potentials (bi-functional effect), which is responsible for the enhanced catalytic activity and better durability. As for LOL architecture, FMO intercalated between the catalyst support and the Pt catalyst are beneficial for the reduction of the size of Pt NPs and the increase of Pt dispersion, but the layer structure could not provide sufficient OH_{ads} for removal of CO_{ads} on Pt and thus

exhibited inferior performance. Based on the excellent electrochemical performance, the binder-free catalyst layer structure and the planar deposition of Pt-FMO catalysts together with an ultra-low loading of Pt make this anode architecture attractive for micro-DEFCs to power portable electronic systems.

Table 5.1 The preliminary electrocatalytic results of optimized binary Pt-FMO catalysts towards ethanol oxidation.

Catalyst	Architecture	Onset potential (V vs Ag/AgCl)	Peak current (mA/mg$_{Pt}$) (CV @ 5 mV/s)	Steady-state current (mA/mg$_{Pt}$)
CP/Pt$_{2T}$	-	0.27	182.7	23.9
CNTs/Pt$_{2T}$	-	0.27	242.4	62.5
CNTs/CeO$_2$)$_{2T}$/Pt$_{2T}$	LOL	0.21	220	72.1
CNTs/(Pt-CeO$_2$)$_{0.5T}$	Co-deposition	0.21	292.5	130
CNTs/(SnO$_2$)$_{2T}$/Pt$_{2T}$	LOL	0.25	169.3	66.7
CNTs/(Pt-SnO$_2$)$_{0.5T}$	Co-deposition	0.10	345.7	169.7
CNTs/(MnO$_2$)$_{10mTO2}$/Pt$_{2T}$	LOL	0.13	249.4	61.7
CNTs/(Pt-MnO$_2$)$_{2T}$	Co-deposition	0.08	417.0	137.5
CP/(TiO$_2$)$_{0.5T}$/Pt$_{2T}$	LOL	0.22	98.7	33.3
CP/(Pt-TiO$_2$)$_{0.5T}$	Co-deposition	0.27	289.0	95.4

Regarding the superior catalytic activity of (Pt-SnO$_2$)$_{0.5T}$ and the excellent durability of (Pt-CeO$_2$)$_{0.5T}$, we believe that the effects of CeO$_2$ and SnO$_2$ on the reaction mechanism of ethanol oxidation are not the same. And thus ternary catalysts involving three substituents Pt, SnO$_2$ and CeO$_2$ have also been prepared in order to combine the excellent activity and durability, specifically, CNT/CeO$_2$ supported (Pt-SnO$_2$), CNT/SnO$_2$ supported (Pt-CeO$_2$) catalysts were synthesized. Considering the poor electronic conductivity of CeO$_2$ and SnO$_2$, the thickness of CeO$_2$ (or SnO$_2$) layer was varied from 5000 laser shots to 10000 laser shots, while the top co-deposit (Pt-SnO$_2$) (or (Pt-CeO$_2$)) remain deposited with optimized conditions that are 0.5T of He and 50000 pulses. Table 5.2 presents the preliminary electrochemical results of as-synthesized ternary catalysts towards ethanol oxidation. It is found that CNTs/(CeO$_2$)$_{5kp}$/(Pt-SnO$_2$) and CNTs/(SnO$_2$)$_{5kp}$/(Pt-CeO$_2$) delivered higher current density with respect to their counterparts with a thicker oxide layer. CNTs/(CeO$_2$)$_{5kp}$/(Pt-SnO$_2$) catalysts showed the highest catalytic activity and durability towards

EOR compared with other three ternary catalysts. Its catalytic current gets improved compared with $(Pt-CeO_2)_{0.5T}$, in particular at low potentials of practical interest, while its durability wasn't enhanced as expected. Therefore, further work needs to be carried out to get insights into the exact role of CeO_2 and SnO_2 in the process of ethanol oxidation when they are combined with Pt catalysts.

Such a systematic study will not only further advance our understanding of the role of FMO in the structural and electronic properties of Pt but also will shed light on its promotional effect with respect to ethanol electrooxidation which has not been established yet.

Table 5.2 The preliminary electrocatalytic results of ternary Pt-CeO$_2$-SnO$_2$ catalysts towards ethanol oxidation.

Catalyst	Onset potential (V vs Ag/AgCl)	Current density at 0.3 V (mA/mg$_{Pt}$) (CV @ 5 mV/s)	Peak current (mA/mg$_{Pt}$) (CV @ 5 mV/s)	Steady-state current (mA/mg$_{Pt}$)
CNTs/(CeO$_2$)$_{2T, 5kp}$/(Pt-SnO$_2$)$_{0.5T}$	0.12	30.2	300.8	166.6
CNTs/(CeO$_2$)$_{2T,10kp}$/(Pt-SnO$_2$)$_{0.5T}$	0.15	6.8	274.6	75
CNTs/(SnO$_2$)$_{2T, 5kp}$/(Pt-CeO$_2$)$_{0.5T}$	0.19	7.6	301.5	171
CNTs/(SnO$_2$)$_{2T, 10kp}$/(Pt-CeO$_2$)$_{0.5T}$	0.20	2.2	296.3	82
CNTs/(Pt-SnO$_2$)$_{0.5T}$	0.10	49	345.7	169.7
CNTs/(Pt-CeO$_2$)$_{0.5T}$	0.21	3.1	292.5	129.0

The cathode catalysts for ORR are facing the similar challenges as the anode catalysts in DEFCs, including the sluggish kinetics, poor durability due to the catalysts degradation and the incomplete reduction of O_2. FMO-modified Pt catalysts could be a promising candidate, due to the low cost and promoting effect of FMOs towards ORR. In addition to the synergetic effect of Pt-FMO interface, the spillover of oxygen-containing species to Pt was also demonstrated as the main factor that improves the electrocatalysis of ORR in Pt-FMO composites. In this thesis, the ORR performance of TiO_2 supported Pt has been studied. It was found that the synthesized TiO_2 films dramatically increase the electroactive surface area of Pt and enhance its electroactivity towards ORR with respect to bare Pt electrode. Due to the restriction in time, the ORR

investigation on other catalysts synthesized in this project has not been completed. However, it could be a good start for an intensive study of FMO-modified Pt catalysts for ORR.

5.2 Perspectives

There is still room to further optimize the structure of FMO-based Pt catalysts to get higher catalytic performance toward EOR by optimizing other synthesis parameters. As for superior co-deposited catalysts, during CBPLD process we can adjust the laser fluence on FMO but maintain the fluence on Pt target constant in order to vary the ratio of Pt and FMO, and thus obtain the optimized composition.

Other metal oxides could be further studied with the co-deposited structure, such as WO_x, RuO_x, and TaO_x in order to find the most suitable metal oxides for ethanol oxidation.

Rh has been well known to be the essential element for the breaking of C-C bond, which has been discussed in chapter 2. Therefore, Rh could be introduced to the binary Pt-FMO co-deposited and LOL catalysts, and the amount of Rh added could be further optimized. Furthermore, it would be necessary to explore the underlying mechanism of ethanol oxidation on the best performing ternary catalysts (Pt-Rh-FMO) by *in situ* DEMS and FTIRS.

In this project, all electrocatalytic tests were performed in 3-electrode cell. To realize the practical application, it is critically important to evaluate them in DEFCs in order to gain more information of the as-synthesized catalysts with PLD.

APPENDIX

A: Résumé de la Thèse

Introduction

L'énergie peut être reconnue comme l'un des piliers les plus importants de notre mode de vie moderne. Encore aujourd'hui, les sources dominantes de notre énergie consommée sont comblées en très grande majorité par les combustibles fossiles: charbon, pétrole et gaz naturel. Il est bien connu que les combustibles fossiles sont considérés comme des ressources non renouvelables, car elles demandent des millions d'années pour se constituer. Inévitablement, elles finiront par s'épuiser, ce qui est un fait incontesté et n'est qu'une question de temps en raison de leurs réserves limitées et la croissance rapide de la demande d'énergie. À part les problèmes d'appauvrissement des combustibles fossiles, leur combustion a causé une grande variété de problèmes environnementaux tels que le réchauffement climatique, les pollutions de l'air, les pluies acides, etc. Les conséquences de ces crises environnementales, en particulier du réchauffement climatique dû aux émissions excessives de CO_2, sont catastrophiques et vont finalement affecter toute la planète, y compris l'existence humaine. Pour répondre à la demande grandissante de l'énergie, à l'épuisement des combustibles fossiles et à la détérioration rapide de l'environnement, un changement dynamique se produit dans l'approvisionnement en énergie. Il se diversifie de plus en plus, ce qui permet de réduire notre dépendance excessive aux combustibles fossiles traditionnels à faible efficacité et à forte pollution. Dans ce contexte, Il est donc essentiel de développer les technologies énergétiques alternatives performantes, abordables, fiables, non polluantes, et utilisant des ressources abondantes, peu coûteuses et renouvelables.

Les piles à combustible à membrane d'échange de protons (PEMFCs, de l'Anglais proton exchange membrane fuel cells) alimentées par de l'hydrogène (H_2) ou de petites molécules organiques qui sont riches en hydrogène, (comme le méthanol, l'éthanol, l'éthylène glycol, etc.) en raison de leur efficacité élevée, de leur forte densité d'énergie et de leurs émissions faibles ou nulles sont considérées comme des dispositifs de conversion d'énergie alternatifs attrayants pour surmonter nos préoccupations sur l'énergie fossile et l'environnement [1]. Parmi les différents combustibles disponibles pour les PEMFC, l'éthanol est de plus en plus attrayant par rapport à H_2 et à d'autres combustibles organiques [2]. Effectivement, à température ambiante, l'éthanol est à l'état liquide et, à la différence de l'hydrogène, peut être facilement entreposé et transporté

à l'aide de l'infrastructure de l'essence actuelle avec seulement de légères modifications. En outre, il présente plus d'avantages que d'autres combustibles liquides, y compris une faible toxicité, une forte densité énergétique (8.0 kWh/kg contre 6.5 kWh/kg pour le méthanol), une biocompatibilité et une large disponibilité des ressources renouvelables, comme la canne à sucre, le blé, le maïs ou même paille et algues. Malgré ces avantages, l'utilisation de l'éthanol dans les piles à combustible et finalement le déploiement commercial des piles à combustible à éthanol direct (DEFCs, de l'Anglais direct ethanol fuel cells) sont encore entravés par plusieurs défis, en particulier les difficultés liées au développement des catalyseurs anodiques qui sont listés comme suit:

(i) Coût élevé des électrocatalyseurs [3]. Les catalyseurs Pt et à base de Pt sont les catalyseurs les plus couramment utilisés et largement étudiés pour les DEFC, mais en raison du coût et de la rareté de Pt, la quantité élevée de Pt aux électrodes retarde le déploiement à grande échelle des DEFCs;

(ii) Cinétique lente de la réaction d'oxydation de l'éthanol;

(iii) Les difficultés associées à la scission de la liaison C-C et à l'oxydation complète de l'éthanol jusqu'au CO_2 [4, 5]. Il est bien connu que Pt en tant que catalyseur d'anode est très actif en ce qui concerne le clivage de la liaison C-H et l'adsorption dissociative de l'éthanol, mais il ne peut pas accomplir l'oxydation complète libérant 12 électrons en cassant efficacement les liens C-O et C-C à basses températures. Grâce à l'oxydation incomplète (ou partielle) de l'éthanol (oxydation à 2 électrons et à 4 électrons), des sous-produits indésirables, l'acétaldéhyde (CH_3CHO, AAL) et l'acide acétique (CH_3COOH, AA) sont formés respectivement [4, 5]. L'oxydation incomplète de l'éthanol non seulement diminue l'efficacité énergétique à cause du nombre d'électrons échangés inférieur à celui requis pour une oxydation complète, mais aussi génère l'acétate ou (bi) sulfate qui s'adsorbe fortement à la surface du catalyseur et affecte de manière significative la réactivité des catalyseurs.

(iv) La faible durabilité des catalyseurs est un autre problème important pour l'application pratique des DEFCs [6]. Le Pt lui-même a une faible résistance à l'empoisonnement, car plusieurs intermédiaires tels que CO_{ads} pourraient être fortement adsorbés sur leur surface, empoisonnant les catalyseurs et entraînant par conséquent une faible vitesse de la réaction et même une dégradation irréversible de la performance catalytique. D'autre part, la corrosion électrochimique des matériaux de support (par exemple Vulcan XC-72) pendant le fonctionnement des DEFCs à long terme conduit à l'agrégation, la dissolution et l'isolement des catalyseurs, ce qui entraîne une dégradation de la performance de la DEFC entière.

Pour répondre aux problématiques ci-dessus auxquelles les DEFCs sont confrontées, une grande quantité de travail a été axée sur l'exploration des catalyseurs multi-composants par rapport au Pt pur, qui a pour but le développement de catalyseurs performants, sélectifs et stables. De nombreuses tentatives, telles que la combinaison de Pt avec d'autres métaux de transition moins chers pour former des catalyseurs bi et trimétalliques [7-9] ou l'incorporation d'oxydes de métaux au Pt formant catalyseurs nanocomposés ont été réalisées depuis plusieurs années [6, 10]. Une revue de la littérature concernant les études sur les catalyseurs Pt-M et Pt-oxyde de métal (MO_x) est décrite dans la section suivante. Selon le cadre de ce travail, les catalyseurs appliqués en milieu acide seront présentés et discutés exclusivement.

Jusqu'à présent, beaucoup d'efforts ont été centrés sur la modification du platine en ajoutant d'autres métaux de transition (M: Ru, Sn, Mo, Pd, Ir.) pour former des catalyseurs bi ou tri-métalliques [7-9]. Comme dans le cas de l'oxydation du méthanol, il existe deux effets largement reconnus et bien acceptés pour tenir compte de l'amélioration de la performance catalytique pour la réaction d'oxydation de l'éthanol (ROE), soit le mécanisme bifonctionnel [11] et l'effet électronique (ou l'effet ligand) [12]. Selon le mécanisme bifonctionnel, le platine reste le matériau nécessaire pour briser les liaisons chimiques de l'éthanol et que les atomes M voisins pourraient activer H_2O à potentiel plus négatif que le platine pour former des espèces hydroxy adsorbées (OH_{ads}). Ces OH_{ads} facilitent l'élimination des espèces de CO fortement adsorbées sur le Pt. En outre, le métal allié pourrait modifier la structure électronique du Pt voisin, engendrant une diminution de l'énergie de la liaison du CO sur le Pt, ce qui entraînerait un effet d'empoisonnement amoindri du Pt.

Parmi les électrocatalyseurs bimétalliques à base de Pt étudiés, le catalyseur Pt-Sn été considéré comme le plus actif pour l'ROE dans un milieu acide [8], contrastant avec le cas de ROM (Réaction d'oxydation du Méthanol) pour lequel le catalyseur PtRu est connu pour être le plus efficace [13]. Par conséquent, une attention particulière de l'étude des catalyseurs bimétalliques est donnée aux catalyseurs à base de Pt-Sn, y compris l'effet principal influençant l'activité de l'ROE, l'investigation du mécanisme d'oxydation de l'éthanol. La composition du catalyseur, le degré d'alliage et le contenu d'oxydes de Sn ont été identifiés comme les principaux facteurs influençant la performance catalytique vis-à-vis de l'électro-oxydation de l'éthanol [14]. Cependant, jusqu'à présent, il n'y a pas de consensus sur les conditions optimales pour Pt-Sn envers la ROE dans la littérature. Parfois, les résultats sont même contradictoires. Les écarts concernant les catalyseurs Pt-Sn peuvent être attribués à une variété de facteurs tels que la taille, la cristallinité, la forme, la composition des catalyseurs, le contenu de chaque type de phase pour

le Sn (allié ou non allié). De plus, plusieurs méthodes de synthèse peuvent également provoquer des impuretés telles que le solvant organique, agent réducteur qui affecte également les comportements catalytiques. En outre, les conditions des tests électrochimiques telles que la température, la concentration de l'éthanol, etc., peuvent également jouer un rôle dans la performance catalytique. La complexité du processus d'oxydation de l'éthanol est une autre raison importante. À partir des études sur le catalyseur binaires Pt-Sn, il ne fait aucun doute que l'ajout de Sn améliore les performances catalytiques vis-à-vis de l'oxydation de l'éthanol à une surtension plus faible, et augmente l'énergie délivrée. Cependant, les recherches ont montrés que le Pt-Sn ne peut pas accomplir l'oxydation complète de l'éthanol à basses températures et aux potentiels plus bas, mais aide plutôt à produire AAL et AA comme produits principaux à travers un échange de 2 et 4 électrons, respectivement [8, 15]. Il est donc crucial de développer de nouveaux catalyseurs qui présentent une activité et une sélectivité élevées pour la ROE.

En plus de l'étude approfondie sur les catalyseurs bimétalliques, beaucoup d'efforts ont été faits pour explorer un nouveau catalyseur à base de Pt en introduisant divers oxydes métalliques fonctionnels (FMOs, de l'Anglais Functional Metal Oxides) tels que CeO_2, SnO_2, MnO_2, TiO_2, WO_3, etc [6]. Ces FMO sont peu coûteux et abondants par rapport à Pt, et donc l'incorporation de FMO à haute surface spécifique pourrait réduire largement le coût des catalyseurs [16]. D'autre part, l'interaction entre le Pt et le FMO s'est avérée avoir une grande influence sur les propriétés de la chimisorption et le comportement catalytique ultime [17]. En effet, le rôle des FMO a été affirmé pour améliorer la dispersion des nanoparticules de Pt, et/ou pour fournir des espèces d'hydroxyle à des potentiels inférieurs à ceux de Pt pour effectuer l'élimination oxydante de CO_{ads} (le mécanisme bifonctionnel) et/ou pour modifier la structure électronique de Pt et diminuer ainsi la force d'adsorption de CO_{ads} sur Pt (l'effet électronique). Cependant, les performances catalytiques des composés Pt-FMO résultants ont été largement affectées par leur microstructure, leur taille, leur composition qui varient selon la méthode de leur préparation. Afin de bien comprendre le rôle de promotion de FMO dans la composante Pt-FMO vers ROE, il est important d'explorer une approche de préparation permettant de contrôler efficacement la taille, la microstructure et la composition du matériel synthétisé. Parmi les différentes techniques de synthèse des matériaux, le dépôt par ablation laser (mieux connu sous son nom Anglais: pulsed laser deposition, PLD) est une alternative prometteuse [18]. Cette technique est apparue au cours de la dernière décennie comme une méthode de déposition hautement versatile pour la croissance des nanomatériaux et des films minces à partir de presque toute sorte de matériaux condensés y compris les métaux, les isolants, les semi-conducteurs, les polymères, et même les matériaux biologiques, avec une épaisseur ajustable, la cristallinité, la

morphologie et la composition contrôlés pour réaliser les propriétés désirées. Les caractéristiques de la PLD pourraient simplement répondre aux exigences de préparation de différents composés de Pt-FMO. En même temps, les réactifs chimiques ou les ions chimiques ou autres impuretés ne sont pas introduits dans cette approche comparée aux méthodes chimiques, donnant ainsi une surface propre des catalyseurs.

Les objectifs de la thèse

Selon l'introduction et la problématique présentée ci-dessus et la revue de la littérature pertinente sur les catalyseurs à base de Pt pour les DEFC à basse température, notre objectif principal est de développer des électrodes de Pt-FMO nanostructurées et autoportantes avec une activité catalytique plus élevée et étant stables pour les applications de DEFC. Les électrodes autoportantes avec deux types d'architectures sont construites en combinant Pt et FMO de manières différentes sur le substrat.

Vers l'objectif principal, nous suivrons les sous-objectifs suivants:

1. Les couches de catalyseur avec deux architectures construites par FMO et Pt sont fabriquées à l'aide de la technique PLD et CBPLD (du nom Anglais, cross-beam pulsed laser deposition), à savoir l'architecture couche sur couche (de l'Anglais Layer onto Layer, LOL) et l'architecture co-déposée. La première architecture est fabriquée en déposant la couche Pt sur la couche de FMO. La deuxième architecture est obtenue par les ablations simultanées de deux cibles de Pt et FMO. Différents FMO incluant CeO_2, SnO_2, MnO_2 et TiO_2 ont été choisis et comparativement étudiés dans ces deux types d'architectures.

2. Pour chaque architecture, la condition de croissance optimisée pour chaque type de FMO est systématiquement étudiée en faisant varier la pression du gaz dans la chambre de PLD.

3. Les microstructures, les propriétés physiques et l'activité électrochimique vis-à-vis de l'ROE de la couche de catalyseur développée dans les sous-objectifs 1 et 2 sont systématiquement caractérisées. En outre, la corrélation de la structure et la performance électrochimique pour chaque type de catalyseur sont étudiées et discutées afin de nous guider à développer un catalyseur performant.

Organisation de la thèse

Cette thèse de doctorat est composée de 5 parties organisées comme suit:

Le chapitre 1 présente les antécédents et les motivations de ce travail.

Le chapitre 2 commence par la revue de la littérature sur les catalyseurs à base de Pt pour les DEFCs au cours de dernières décennies. Par la suite, les problèmes clés restants dans le développement des catalyseurs à base de Pt sont soulignés. À la fin, les objectifs et l'organisation de la thèse sont introduits.

Le chapitre 3 décrit brièvement la méthodologie de cette thèse, y compris l'introduction des matériaux et les méthodes de synthèse utilisées, les détails des processus de synthèse de divers catalyseurs à base de FMO, puis la description détaillée de diverses techniques de caractérisation physico-chimiques et électrochimiques employées au cours du projet de doctorat.

Le chapitre 4 comprend les 4 articles écrits tout au long de la thèse. Un résumé précède chaque publication afin de souligner les motivations de ce travail.

Le chapitre 5 présente la conclusion générale et propose les travaux futurs.

Méthodes éxperimentales

Les électrodes tridimensionnelles (3D) et autoportantes avec deux types d'architectures sont construites en combinant Pt et FMO dans différentes façons sur le substrat. Ces électrodes sont préparées par une combinaison de techniques de dépôt chimique en phase vapeur (mieux connu sous son nom Anglais, chemical vapor deposition, CVD) et PLD.

Les électrodes 3D et autoportantes comprennent essentiellement trois composants:

Le substrat: le papier carbone (CP, Toray) non traité est choisi comme le substrat de la couche des catalyseurs qui sert de collecteur de courant. Le CP est un réseau de fibres de carbone enchevêtrées de diamètre de 7 à 10 μm (comme le montre de la Figure 3.1). Il est le type de couche de diffusion gazeuse (mieux connu sous son nom Anglais, gas diffusion layer, GDL) souvent intégré dans le MEA (du nom Anglais: membrane electrode assembly) dans les systèmes de piles à combustible, en raison de sa nature poreuse, sa conductivité électrique élevée et sa bonne résistance à la corrosion.

Le support de catalyseur: les nanotubes de carbone (mieux connu sous son nom Anglais, Carbon Nanotubes, CNTs) sont utilisés comme supports de catalyseurs en raison de leur haute conductivité électronique et de leur résistance à l'oxydation/corrosion dans les conditions de fonctionnement des piles à combustible. Les CNTs (présentés à la Figure 3.1) dans notre projet

sont synthétisés par déposition chimique en phase vapeur et les conditions détaillées de préparation seront présentées dans la section du CVD.

Des Catalyseurs: deux architectures ont été considérées et sont présentées dans la Figure R1. Les catalyseurs de l'architecture de LOL sont fabriqués en déposant la couche Pt sur la couche de FMO. Les catalyseurs de l'architecture co-déposés sont obtenus par CBPLD.
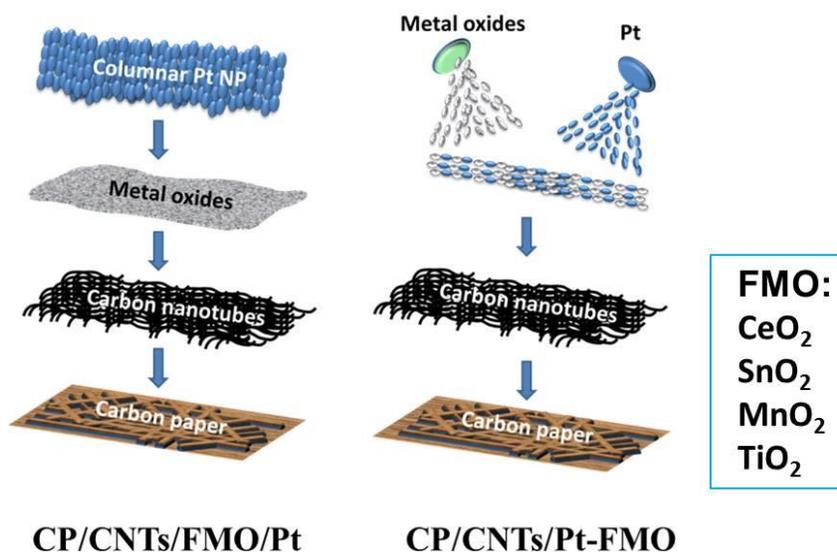
Figure R1 La représentation de deux architectures de film de catalyseur contenant Pt et FMO: l'architecture couche sur couche (gauche), l'architecture co-déposée (droite).

La CVD est une méthode bien établie pour la synthèse des CNTs par décomposition thermique des hydrocarbures (méthane, éthane, acétylène et éthylène, etc.) en présence de catalyseurs métalliques (tels que le nickel, le fer, le cobalt ou une combinaison de ceux tels que le cobalt/Molybdène ou cobalt/fer) [19]. Par rapport à d'autres techniques disponibles telles que la décharge à l'arc, l'ablation par laser, la méthode CVD est une méthode plus simple et plus économique basée sur une mise à l'échelle facile et les équipements limités requis. En outre, la CVD en décomposant des précurseurs d'hydrocarbures en présence de catalyseurs permet de croître des CNTs sous diverses formes: poudres, films minces/épais sur des variétés de substrats, droites ou enroulées, alignées ou enchevêtrées.

Pour la croissance des CNTs, un film continu de Ni a d'abord été déposé par PLD sur un côté du CP. Ce film de Ni a été déposé à température ambiante par ablation d'une cible de Ni polycristallin (99,95%, Kurt J. Lesker Co.) sous vide au moyen d'un laser excimère KrF (longueur d'onde de 248 nm, durée de tir de 17 ns, taux de répétition de 30 Hz). La fluence laser a été fixée à 4 J cm^{-2}, et la distance entre la cible et le substrat a été fixée à 5 cm. Au cours du processus

de déposition, la cible de Ni est maintenue en mouvement de rotation et de translation constant afin d'assurer une ablation uniforme. La configuration de la CVD utilisée dans notre laboratoire pour la croissance des CNTs est illustrée à la Figure 3.6. En ce qui concerne le processus de croissance, le substrat de CP recouvert de Ni a d'abord été placé dans un tube à quartz horizontal, qui est ensuite inséré dans un four. Dans un premier temps, une rampe de température de 30 min est programmée pour atteindre une température 700 °C sous un courant d'hydrogène de 70 cm^3 min^{-1} (sccm) ce qui permet la coalescence et la formation des nanoparticules de Ni à partir du film continu de Ni. Le diamètre des CNTs sont influencés par le diamètre de ces nanoparticules. Lorsque la température atteint 700 °C, la croissance des CNTs est initiée en introduisant l'acétylène, l'argon et l'hydrogène à 20, 140 et 100 sccm, respectivement. Après un temps de synthèse de 35 min, les flux d'acétylène et d'argon sont coupés et le four est refroidi jusqu'à température ambiante sous un débit de 60 sccm de H_2.

La PLD est un processus de déposition physique, qui partage certaines caractéristiques communes avec des épitaxies par jets moléculaires et des dépositions par pulvérisation cathodique. Dans la PLD typique, représentée schématiquement dans la Figure 3.7 (a), un faisceau laser pulsé de courte durée et d'énergie très élevée est focalisé sur une cible du matériau à déposer. Le matériau est vaporisé de la surface de la cible dans une plume de plasma dirigé vers l'avant lorsque l'absorption par la matière d'une énergie supérieure à l'énergie de liaison des atomes. Pour créer une plume de plasma avec un taux d'ablation adéquat, la fluence (énergie du laser (J)/aire du point focal (cm^2)) du laser à travers la zone focale devrait dépasser la fluence seuil du matériau, qui dépend de la longueur d'onde du laser, de la durée et des propriétés intrinsèques du matériau. La plume résultant prend de l'expansion et se propage à une vitesse élevée ver le substrat avant la déposition sur celui-ci. Si l'ablation est effectuée sous vide ou sous une pression faible de gaz, la plume est très restreinte et dirigée vers l'avant. Dans un gaz ambiant d'une pression plus élevée, les molécules de gaz confinent le plasma dans un volume plus petit en augmentant le nombre de collisions entre les composantes ablatées (atomes et cations) et les molécules de gaz, et ainsi diminuant les énergies cinétiques des espèces de propagation. La pression et la masse molaire du gaz introduit sont les paramètres qui affecteront l'énergie cinétique de la matière ablatée et auront une importante influence sur le mécanisme de croissance des films déposés. En outre, le gaz peut participer activement à la chimie de la croissance du film comme espèces réactives (par exemple, O_2, N_2) pendant les collisions entre le plasma et les espèces du gaz. Par exemple, O_2 est nécessaire pour compenser la perte d'un élément plus léger de O assurant le transfert stœchiométrique de la cible au substrat, lorsque le film d'oxydes métalliques est fabriqué.

Un schéma du montage CBPLD est illustré sur la Figure 3.7 (b). Le système comprend deux cibles individuelles, chacune ablaté par un faisceau laser distinct [18]. Cette technique permet la croissance directe des matériaux composés ou des alliages en utilisant deux cibles de nature différente. En tant que la PLD classique, les paramètres de déposition pour la CBPLD sont les mêmes, tels que la pression/la masse du gaz, la distance entre la cible et le substrat, la température du substrat. Par conséquent, cette technique offre la possibilité de produire des matériaux nanostructurés avec la flexibilité nécessaire pour varier tant la stoechiométrie que la morphologie et la structure des films exempts de gouttelettes.

Dans ce projet, les dépôts avec la PLD et la CBPLD sont réalisés à température ambiante dans une chambre en acier inoxydable qui peut être évacuée jusqu'à une pression de 4×10^{-5} Torr avec une pompe turbo. Un laser excimère KrF pulsé (λ = 248 nm, largeur d'impulsion = 17 ns et taux de répétition = 50 Hz) a été utilisé pour toutes les expériences d'ablation. Des cibles à haute pureté de Pt, CeO_2, SnO_2, TiO_2 et MnO_2 de chez Kurt J. Lesker Co ont été utilisées.

a) Catalyseurs FMO/Pt de l'architecture couche sur couche

Une collègue de notre groupe a lancé ce travail en construisant les catalyseurs CeO_2/Pt et SnO_2/Pt d'architecture LOL [20, 21]. À la suite de ces travaux, les mêmes architectures ont été construites en utilisant deux autres oxydes MnO_2 et TiO_2 et les catalyseurs résultants sont représentés par MnO_2/Pt et TiO_2/Pt. La PLD conventionnelle est utilisé pour la préparation des électrodes d'architecture LOL. Le substrat (CP non traité ou CP/CNT) était tourné vers la cible avec la distance cible-substrat de 5 cm, et le faisceau laser était incident à un angle de 45° à la surface de la cible. La cible et le substrat ont été maintenus en mouvement de rotation et de translation constant pour obtenir une ablation uniforme sur toute la cible et une déposition uniforme sur le substrat. Pour les électrodes MnO_2/Pt, les films de MnO_2 ont été déposé en utilisant la fluence de 2.5 J cm^{-2} et le nombre de tirs de 20000, sous vide, sous 0.5 et 2 Torr d'hélium et sous 10 mTorr d'oxygène. En ce qui concerne les électrodes TiO_2/Pt, le film de TiO_2 est déposé en utilisant la fluence de 4 J cm^{-2} et le nombre de tirs de 20000, sous vide, sous 0.5 et 2 Torr d'hélium et sous 10 mTorr d'oxygène. Les films de Pt pour les électrodes supportées par MnO_2 et TiO_2 ont été déposés dans la même condition: la fluence utilisée était de 4 J cm^{-2}, le nombre de tirs était de 20000, sous 2 Torr d'hélium.

b) Co-déposition de catalyseurs binaires Pt-FMO par CBPLD

Quatre types de catalyseurs co-déposés (Pt-CeO_2, Pt-SnO_2, Pt-TiO_2 et Pt-MnO_2) avec des morphologies variées ont été préparés par CBPLD. Pour tous les échantillons synthétisés par

CBPLD, la distance substrat-cible était de 5 cm, sous trois pressions (sous vide, sous 0.5 et 2 Torr d'hélium)

c) Préparation de catalyseurs ternaires de Pt, CeO_2 et SnO_2 par CBPLD

Basé sur le travail sur les co-dépositions de Pt-CeO_2 et Pt-SnO_2, nous avons constaté que le Pt-CeO_2 et Pt-SnO_2 synthétisé sous 0.5T a montré des performances catalytiques intéressantes pour l'oxydation de l'éthanol, ce qui nous a guidé à fabriquer des catalyseurs ternaires composés de Pt, CeO_2 et SnO_2 visant à combiner les avantages de deux types de co-dépositions pour l'oxydation de l'éthanol. Les catalyseurs ternaires ont été préparés avec différentes combinaisons de ces trois composants. Pour tous les dépositions, la fluence a été fixé à 4 Jcm^{-2} et 0,5 T d'hélium a été utilisé. Les conditions détaillées sont présentées au Tableau 3.2.

Caractérisation physico-chimique

Cette partie traite les diverses techniques physiques utilisées pour la caractérisation morphologique et microstructurale des matériaux d'électrode préparés dans ce projet. Les principales méthodes de caractérisation comprennent la microscopie électronique à balayage (MEB), la microscopie électronique en transmission (MET), la diffraction des rayons X (DRX), la spectroscopie photoélectronique de rayons X (SPX) et la microscopie à force atomique (MFA). De plus, l'analyse par activation neutronique (AAN) a été utilisée pour déterminer la charge massique (μg cm^{-2}) de Pt.

Dans cette thèse, deux installations MEB, JEOL-JSM-6300F (INRS) et JEOL-JSM-7401F (localisé dans la salle blanche de l'INRS-EMT) ont été utilisées pour examiner la morphologie de surface des échantillons préparés.

Le MET a été utilisé pour observer la morphologie et la taille des catalyseurs préparés sur le substrat. L'information sur la cristallinité des catalyseurs a été identifiée avec la diffraction électronique en aire sélectionnée (SAED, de l'Anglais selected area eletron diffraction). Le MET à haute résolution (MET-HR) et SAED ont été effectués avec un JEOL-JEM-2100F (École Polytechnique de Montréal) fonctionnant à 200 kV. Les distributions de granulométrie ont été déterminées en mesurant plus de 100 particules individuelles dans des images MET.

Les analyses DRX ont été effectuées pour l'identification de phase du matériau cristallin et l'estimation de la taille des cristallites ainsi que les paramètres du réseau. Un diffractomètre Bruker D8 Advance équipé d'une source de Cu Kα (λ = 0.15406 nm) a été utilisé fonctionnant à

40 kV et 40 mA. Tous les diffractogrammes ont été acquis en incidence rasante avec un angle d'incidence de 2°, un pas angulaire 2θ de 0,04° et un temps d'acquisition de 4 s par pas. Le logiciel Eva V14 a été utilisé pour déterminer les angles de diffraction des pics et leurs valeurs de largeur à mi-hauteur du maximum du pic (FWHM, de l'anglais Full Width at Half Maximum) employé pour estimer la taille des cristallites et les paramètres du réseau.

La spectroscopie Micro-Raman comprend un spectromètre Raman spécialement conçu, intégré au microscope optique, qui permet d'acquérir des spectres Raman d'échantillons microscopiques. L'analyse de phase et structurelle de CNT et de certains oxydes de métaux dans cette thèse a été conduite avec le microspectroscope Raman (montrée à la Figure 3.11) qui est un modèle Renishaw inVia Raman Microscope utilisant un laser à ions Ar^+ de longueur d'onde de 514.5 nm et une polarisation circulaire. Le faisceau du laser est focalisé sur l'échantillon jusqu'à un point de 1 µm de diamètre (Renishaw Imaging Microscope WireTM).

La SPX a été utilisé pour identifier l'état chimique et déterminer la composition à la surface des échantillons. Les mesures ont été effectuées en utilisant un spectromètre VG Escalab 220i-XL. Sur la base de la conductivité de nos échantillons, on a utilisé deux types de sources d'Al (hv = 1486,6 eV), l'une est une source monochromatique d'Al pour les matériaux à plus grande conductivité et l'autre une source polychromatique à double anode d'Al pour des matériaux avec conductivité relativement basse. Pour Les mesures XPS en utilisant la source monochromatique Al K_α, l'anode a été opérée à 10 kV et 20 mA. Tous les échantillons ont été analysés avec une tache de 250×1000 µm située approximativement au centre de l'échantillon. Pour les mesures en utilisant la source polychromatique, l'anode a fonctionné à 15 kV. L'énergie de l'analyseur a été fixée à 100 eV pour les larges balayages en énergie (appelés survol) et à 20 eV pour les balayages à haute résolution, respectivement. La quantification des éléments a été effectuée avec le logiciel CasaXPS (Casa Software Ltd.).

La topographie de surface (rugosité) des films de TiO_2 a été caractérisée par MFA à l'aide d'un microscope de Nanoscope III du Groupe de Digital Instruments Veeco Metrology. Toutes les mesures ont été effectuées en mode taraudage (contact intermittent). La collecte de données et les analyses ont été effectuées à l'aide du logiciel intégrant sur le système NanoScopeTM.

Dans notre travail, la charge massique de Pt est déterminée avec la technique AAN sur tous les échantillons à l'aide d'un réacteur nucléaire SLOWPOKE (École Polytechnique de Montréal). Pour les dépôts de Pt avec 20000 tirs de laser, la charge massique de Pt est de 48 µg cm^{-2}. Pour les dépôts de Pt et Pt-FMO avec 50000 tirs de laser, la charge massique de Pt est de 120 µg cm^{-2}.

Caractérisation électrochimique

Dans le but d'explorer des catalyseurs actifs et stables pour les applications de piles à combustible, la performance électrocatalytique des catalyseurs présente un intérêt primordial. Les diverses caractérisations physico-chimiques, par contre, visent à comprendre les propriétés physico-chimiques et leurs effets sur les performances électrochimiques des catalyseurs, ce qui permet une orientation dans la conception des électrocatalyseurs nouveaux pour les applications de piles à combustible.

Différentes techniques d'analyse électrochimique telles que la voltamétrie cyclique (potentiodynamique) et la chronoampérométrie (potentiostatique) sont utilisées dans ce projet pour évaluer les performances électrocatalytiques des catalyseurs.

Voltamétrie cyclique (de l'Anglais, cyclic voltammetry, CV) est une technique précieuse pour étudier les mécanismes et les taux de processus d'oxydation et de réduction, ce qui permet une caractérisation rapide des réactions électrochimiques se produisant à l'interface entre l'électrode et la solution d'électrolyte. Au cours d'une mesure de la CV, le potentiel de l'électrode de travail est linéairement balayé entre deux limites de potentiel à une vitesse fixe, et la réponse de courant qui circule entre l'électrode de travail et l'électrode auxiliaire est enregistrée en conséquence. Le graphique du courant en fonction du potentiel appliqué est appelé voltamogramme cyclique.

La voltamétrie à balayage linéaire (de l'Anglais, linear sweep voltammetry, LSV) est un autre type de technique de voltamétrie qui fonctionne d'une manière similaire à CV et peut être simplement considérée comme une moitié du CV.

La chronoamperométrie (de l'Anglais, chronoamperometry, CA) est très utile pour évaluer la durabilité d'une électrode à un potentiel d'intérêt pratique pour les piles à combustible. Elle est réalisée en faisant passer instantanément d'un potentiel E_1, où aucune réaction faradique ne se produit (par exemple, le potentiel de circuit ouvert (OCP), à un potentiel E_2, où la vitesse de réaction est limitée par le transfert de matière. Le courant résultant est mesuré en fonction du temps, comme le montre à la Figure 3.17 (b).

Procédures expérimentales pour les mesures électrochimiques

Dans cette thèse, tous les tests électrochimiques sont effectués à température ambiante dans une cellule à trois compartiments avec un potentiostat/galvanostat (PGSTAT) Autolab

d'EcoChemie. Les catalyseurs à base de Pt synthétisés par PLD et CBPLD ont servi comme électrode de travail, un long fil de Pt en forme de spirale a été utilisé comme contre-électrode et un Ag/AgCl (le KCl de 3 M) a été utilisé comme électrode de référence. Avant chaque test électrochimique, l'oxygène dissous est éliminé de la solution d'électrolyte en faisant un bullage d'argon pendant environ 30 min. Initialement, la surface de l'électrode est amenée dans un état reproductible par CV avec une vitesse de balayage de 50 mV s^{-1} dans un électrolyte d'acide sulfurique (H_2SO_4) de concentration de 0.5 M. Cette procédure est également appelée nettoyage électrochimique et processus d'activation des catalyseurs. Ce processus sert également deux autres objectifs. Tout d'abord, les caractéristiques de l'électrode Pt peuvent être examinées dans l'électrolyte vierge, et estimer certains paramètres (par exemple, la surface électroactive réelle) associées au nombre de sites actifs. Deuxièmement, le voltamogramme cyclique résultant sert également de référence aux comportements des catalyseurs en présence d'espèces électroactives (par exemple Ethanol, O_2).

Ensuite, l'étude de l'activité catalytique s'effectue au moyen de LSV, dans un mélange de solutions désaérées 0.5 M H_2SO_4 + 1 M C_2H_5OH pour les réactions d'oxydation de l'éthanol et dans une solution de H_2SO_4 de 0.5 M saturé par O_2 pour les réactions de réduction de l'oxygène, respectivement. Par la suite, les catalyseurs pour l'ROE subissent des tests de durabilité avec au moyen de la chronoamperométrie à long terme à un potentiel fixé.

Résultats et discussion

Dans la thèse, quatre types de FMO (CeO_2, SnO_2, MnO_2 et TiO_2) ont été sélectionnés pour être intégrés dans la couche de catalyseur de deux façons différentes pour développer le catalyseur optimal.

Catalyseurs FMO/Pt de l'architecture LOL

D'abord, les catalyseurs MnO_2/Pt et TiO_2/Pt avec l'architecture LOL ont été préparés et étudiés. Cette étude est fondée sur les travaux de catalyseurs CeO_2/Pt et SnO_2/Pt LOL-nanostructurés effectués précédemment dans notre laboratoire par Amel Tabet-Aoul et al [20, 21]. Afin de comprendre le rôle de la couche de FMO, les microstructures (taille des cristallites, la structure, la rugosité, la porosité, etc.) de la couche sous-jacente de FMO ont été variées en changeant l'atmosphère de gaz pendant la déposition en PLD, tandis que les conditions de préparation pour la couche supérieure de Pt ont été invariables. Quelques soient les conditions

de dépôts, tous les films de TiO_2 et MnO_2 synthétisés se sont révélés amorphes par les caractérisations par XRD. Sur les images SEM, il peut être observé que la morphologie de film de FMO est passée d'une structure dense et compacte à poreuse puis à très poreuse lorsque la pression de déposition variait sous vide (ou 10 mTorr d'O_2) à 0.5 Torr de He jusqu'à 2 Torr de He, respectivement. En accord donc avec les études précédentes, la morphologie de surface des films déposés par PLD dépendait en grande partie de la pression du gaz dans la chambre de déposition. Brièvement, la pression du gaz affectera l'énergie cinétique de la matière ablatée et aura une importante influence sur le mécanisme de croissance des films [22]. En ce qui concerne la morphologie de la couche supérieure de Pt, il est intéressant de noter qu'elle est dictée par la morphologie de la couche sous-jacente de FMO. Lorsque la couche sous-jacente de FMO est lisse, la surface des couches de Pt est relativement plate, composée de particules hautement interconnectées. D'autre part, lorsque la couche FMO est poreuse, les particules de Pt s'assemblent dans des arrangements semblables à un chou-fleur. Tel qu'il peut être observé à la Figure R2, Il peut facilement être noté que la morphologie de la couche Pt est affectée par celle de la couche FMO sous-jacente. Les films de TiO_2 sont passés d'un film dense et compact à des colonnes densément emballées, jusqu'à la structure en forme d'arbre lorsque la pression du gaz passe de sous vide à 0.5 Torr de He jusqu'à 2 Torr de He. En conséquence, les films de Pt déposés sur le dessus ont changé de structure en forme de colonne à une forme ressemblant "choufleur". Cette différence de morphologie résulte de l'angle de déposition, i.e., pour substrat relativement plat, l'angle de déposition est presque normal, alors que, dans le cas d'un substrat rugueux, une partie notable du film croît à l'incidence rasante, c'est-à-dire à des conditions de GLAD (de l'Anglais glancing angle deposition) [23, 24]. En général, la déposition GLAD entraîne la formation de matériaux colonnaires et poreux, tandis qu'une déposition d'incidence normal (ND) conduit à la formation de films plus denses. Régulièrement, la morphologie de la surface de MnO_2 montre la même variation que le TiO_2 avec la pression du gaz, la dépendance morphologique de Pt par-dessus le MnO_2 montre également la même évolution que celle observée sur le film de TiO_2. La mesure par XPS a montré que le Pt était principalement sous forme métallique, comme observé avec les échantillons CeO_2/Pt [20] et SnO_2/Pt [21]. Les études électrochimiques par CV et CA ont démontré que les électrodes MnO_2/Pt (ou TiO_2/Pt) LOL présentaient des performances ROE variées en raison de la différence morphologique. Enfin, la pression du gaz de préparation optimale pour les catalyseurs MnO_2/Pt et TiO_2/Pt d'architecture LOL a été obtenue en fonction de leur activité et de leur durabilité pour ROE.
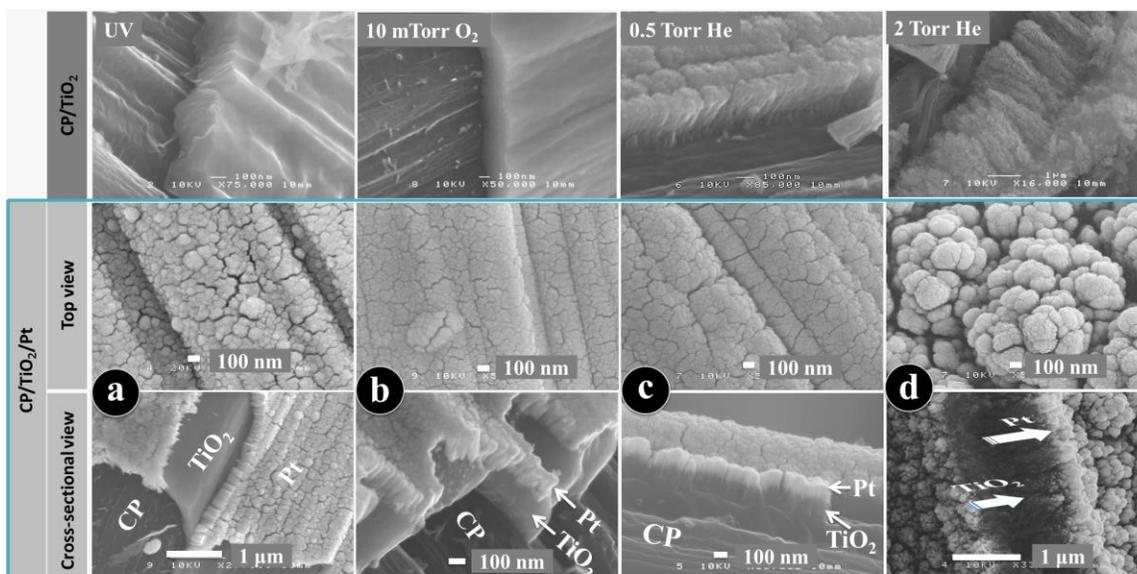
Figure R2. Micrographies SEM des échantillons CP/(TiO$_2$); et des échantillons CP/(TiO$_2$)/Pt (a) CP/(TiO$_2$)$_{UV}$/Pt; (b) CP/(TiO$_2$)$_{10mTO2}$/Pt; (c) CP/(TiO$_2$)$_{0.5THe}$/Pt and (d) CP/(TiO$_2$)$_{2THe}$/Pt.

Catalyseurs Pt-FMO de l'architecture co-déposée

Ensuite, quatre types de catalyseurs Pt-FMO de l'architecture co-déposée (Pt-CeO$_2$, Pt-SnO$_2$, Pt-MnO$_2$ et Pt-TiO$_2$) ont été fabriqués par CBPLD. Au moyen de plusieurs techniques physico-chimiques, nous avons systématiquement étudié la variation de la morphologie à la surface, de la cristallinité, de la taille des particules et de l'état d'oxydation de catalyseurs Pt-FMO co-déposés en fonction de la pression du gaz à l'intérieur de la chambre de dépôt.

En comparant les images SEM de tous les Pt-FMO co-déposées préparés sous différentes pressions du gaz, il a été constaté que la variation de Pt-FMO en morphologie suit la même tendance en fonction de la pression du gaz, indépendamment de la nature de FMO. Un film très lisse et de structure fermée a été observé pour (Pt-FMO) synthétisé sous vide. D'autre part, les films co-déposés sous 2 Torr de He sont clairement rugueux et consistent de grappes de particules. La porosité des films co-déposés sous 0.5 Torr de He se situe entre les deux. Les images SEM pour les catalyseurs Pt-CeO$_2$ [25], Pt-SnO$_2$ [26] et Pt-MnO$_2$ [27] se trouvent respectivement à l'article 1, 2 et 3 du chapitre 4. La Figure R3 présente seulement les images SEM des films Pt-TiO$_2$ co-déposés, qui représentent la même variation morphologique avec le changement de la pression du gaz. Les différences en morphologie observées sur les films Pt-FMO fabriqués par CBPLD sont principalement attribuables à la diminution de l'énergie cinétique des espèces lors de la déposition qui varie avec l'atmosphère dans la chambre de déposition. La

variation de l'énergie cinétique des espèces du plasma induit une modification de la mobilité de surface des espèces déposées. Sous vide, l'absence de collisions entre le plasma en expansion et les molécules de gaz ambiant conduit à une situation où l'énergie cinétique des espèces du plasma est la plus élevée. La plus grande mobilité de surface des espèces déposées se transforme en films plus denses par le réorganisation de surface qui mène à la minimisation de l'énergie, ce qui est le cas ici pour tous les $(Pt-FMO)_{UV}$. Au contraire, la présence du gaz dans la chambre de déposition diminuera l'énergie cinétique des espèces de plasma. En raison de ce fait, le plasma en expansion interagira plus fortement avec les molécules du gaz. Lorsque la pression du gaz dans la chambre de déposition augmente, la probabilité pour les espèces de plasma de perdre une partie de leur énergie cinétique par un contact avec les molécules de gaz sera également augmentée, réduisant ainsi l'énergie cinétique des espèces de plasma. Cette diminution de l'énergie cinétique des espèces de plasma induit moins de diffusion sur la surface ce qui entraine la formation d'un film poreux. Plus détails concernant l'influence de l'atmosphère de la chambre sur les processus physiques de l'interaction laser-matériau se trouvent ailleurs [28, 29].
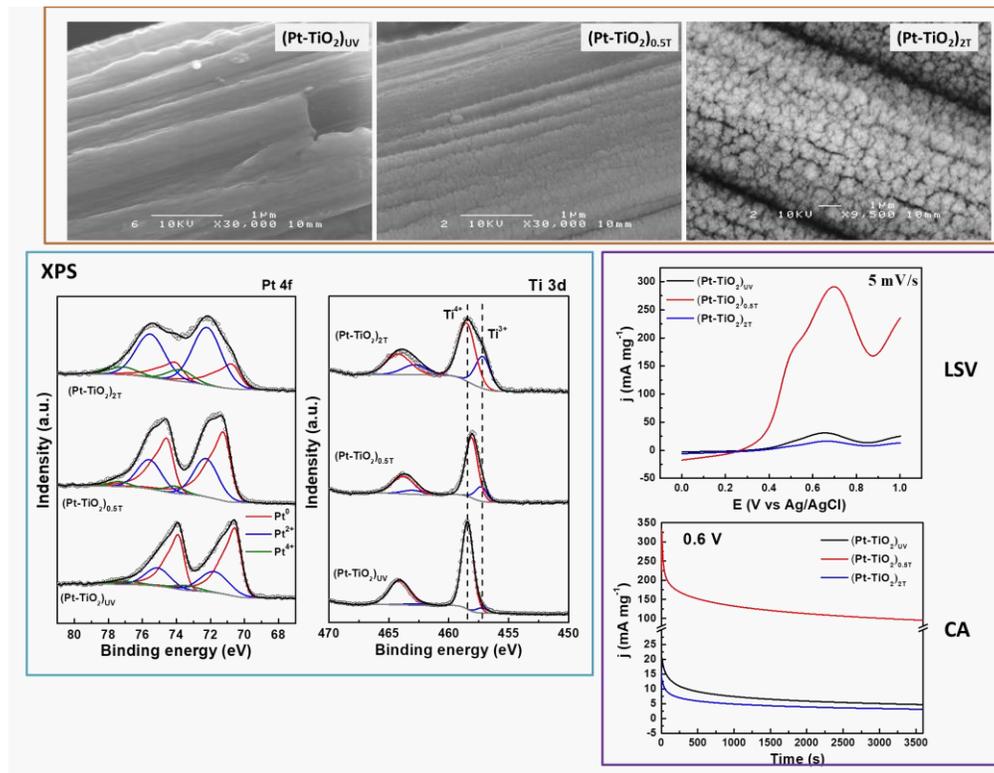
Figure R3 Images SEM, Spectres XPS des niveaux de cœur Pt 4f et Ti 3d, et LSV, CA en solutions de 0.5 M H_2SO_4+1.0 M EtOH.

Par la suite, à partir des analyses TEM, XRD, XPS et Raman, on a observé que l'étendue de l'interaction entre Pt et FMO était influencée par la pression de gaz pendant la déposition. Les spectres XPS des niveaux de cœur Pt 4f et Ti 3d sont présentés à la Figure R3, et les données XPS pour (Pt-CeO$_2$) et (Pt-SnO$_2$) co-déposés se trouvent respectivement à l'article 1 et 2. Les films (Pt-CeO$_2$), (Pt-SnO$_2$) et (Pt-TiO$_2$) co-déposés sous l'atmosphère d'He présentent une forte concentration de Pt^{2+}, tandis que les films co-déposés sous vide présentent une forte concentration de Pt^0. L'état d'oxydation du métal dans FMO révèle des cations mixtes, soit M^{4+} et M$^{x+ (x<4)}$. La taille des grains de FMO dans les échantillons (Pt-FMO) a également été influencée par la pression du gaz, ce qui a été démontré par le changement radical de la réponse Raman. Grâce aux tests LSV et CA sur les (Pt-FMO), le catalyseur fabriqué sous 0.5T d'He a démontré une performance catalytique supérieure et une haute durabilité par rapport à (Pt-FMO)$_{UV}$ et (Pt-FMO)$_{2T}$, attribué à une morphologie de surface idéale adaptée à l'accessibilité de électrolyte et la forte interaction entre Pt et FMO.

En ce qui concerne les catalyseurs (Pt-MnO$_2$) co-déposés, la variation de la morphologie de la surface et de la taille du cristallin Pt pourrait être notée à partir des analyses SEM et XRD. Des tests XRD, Raman et XPS, on peut conclure la présence de MnO$_2$ amorphe dans tous les films (Pt-MnO$_2$). Le rôle de MnO$_2$ envers l'ROE a été démontré en comparant leur performance et leur durabilité dans les tests électrochimiques. Conformément aux discussions de Jindi Cai et al. [30], Nous proposons que: (i) l'excellente conductivité protonique de MnO$_2$ favorise l'oxydation électrocatalytique de l'éthanol par une accélération de la déshydrogénation dans l'oxydation de l'éthanol. (Ii) MnO$_2$ active l'eau adsorbée et puis (iii) fournit de l'hydroxyle pour oxyder les intermédiaires adsorbés (CO$_{ads}$) sur Pt et utilise l'effet synergique entre Pt et MnO$_2$. La meilleure performance électrochimique des catalyseurs CNT/(Pt-MnO$_2$)$_{2T}$ par rapport à celles de CNT/(Pt-MnO$_2$)$_{UV}$ et CNT/(Pt-MnO$_2$)$_{0.5}$, peut être associée à la morphologie de surface de la forme du catalyseur, soit une rugosité plus élevée, ce qui signifie plus de sites actifs disponibles électrochimiquement du catalyseur, qui fournit un hydroxyle additionnel pour éliminer le nombre supplémentaire de CO adsorbé.

Le tableau S1 énumère les résultats électrochimiques des meilleures électrodes à base de FMO. À titre de comparaison, il comprend également les résultats des catalyseurs Pt synthétisés par PLD sur les CNT et le CP. En comparant deux architectures de catalyseurs, on a constaté que la position de FMO dans la couche de catalyseur affectait de manière significative la performance catalytique du catalyseur résultant envers l'oxydation de l'éthanol. Les catalyseurs Pt-FMO co-déposées par CBPLD ont montré une performance électrocatalytique supérieure à

l'oxydation de l'éthanol par rapport à celle avec l'architecture LOL. L'activité électrocatalytique élevée des catalyseurs Pt-FMO optimisés pour la ROE peut être attribuée aux caractéristiques suivantes:

1) Porosité raisonnable offrant une forte cohérence de catalyseurs avec support/substrat et favorable au transport massique de molécules de l'éthanol.

2) Une forte interaction entre Pt et FMO modifie la structure électronique de Pt, ce qui entraîne une plus grande résistance à l'empoisonnement. L'architecture co-déposée pourrait induire une interaction beaucoup plus élevée entre Pt et FMO en trois dimensions par rapport au modèle bidimensionnel de Pt sur FMO. En ce qui concerne l'architecture LOL, le FMO intercalé entre le support de catalyseur et le catalyseur Pt est bénéfique pour la réduction de la taille de Pt et l'augmentation de la dispersion de Pt, mais la structure de la couche ne peut pas fournir suffisamment d'OH_{ads} pour éliminer CO_{ads} sur Pt et ainsi ont présenté des performances inférieures.

3) Les propriétés uniques de FMO génèrent facilement des espèces OH d'abondance qui facilite l'élimination par oxydation des espèces CO_{ads} et améliorent finalement la performance catalytique des catalyseurs à base de FMO.

Tableau S1 Conditions de déposition et résultats électrochimiques des meilleures électrodes de chaque série.

Meilleure électrode	Architecture	Surtension (V vs Ag/AgCl)	Densité de courant de pic (mA/mg$_{Pt}$) (LSV @ 5 mV/s)	Densité de courant à l'état stationnaire (mA/mg$_{Pt}$)
CP/Pt$_{2T}$	-	0.27	182.7	23.9
CNTs/Pt$_{2T}$	-	0.27	242.4	62.5
CNTs/CeO$_2$)$_{2T}$/Pt$_{2T}$	LOL	0.21	220	72.1
CNTs/(Pt-CeO$_2$)$_{0.5T}$	Co-deposition	0.21	292.5	130
CNTs/(SnO$_2$)$_{2T}$/Pt$_{2T}$	LOL	0.25	169.3	66.7
CNTs/(Pt-SnO$_2$)$_{0.5T}$	Co-deposition	0.10	345.7	169.7
CNTs/(MnO$_2$)$_{2T}$/Pt$_{2T}$	LOL	0.13	249.4	61.7
CNTs/(Pt-MnO$_2$)$_{2T}$	Co-deposition	0.08	417.0	137.5
CNTs/(TiO$_2$)$_{0.5T}$/Pt$_{2T}$	LOL	0.22	98.7	33.3
CNTs/(Pt-TiO$_2$)$_{0.5T}$	Co-deposition	0.27	289.0	95.4

Des catalyseurs ternaires constitués de trois substituants Pt, CeO$_2$ et SnO$_2$ qui ont également été préparés afin de combiner l'activité excellente et la durabilité, en particulier les

catalyseurs (Pt-SnO$_2$) supportés par CNT/CeO$_2$, les catalyseurs (Pt-CeO$_2$) supportés par CNT/SnO$_2$ ont été synthétisés. Compte tenu de la mauvaise conductivité électronique de CeO$_2$ et SnO$_2$, l'épaisseur de la sous-couche CeO$_2$ (ou SnO$_2$) a été variée de 5000 tirs de laser à 10000 tirs de laser, tandis que la couche supérieure (Pt-SnO$_2$) (ou (Pt-CeO$_2$) supérieure a été déposée sous les conditions optimisées, soit 0.5 Torr de He et 50000 tirs de laser. Le Tableau S2 présente les résultats électrochimiques des meilleures électrodes de catalyseur ternaire Pt-CeO$_2$-SnO$_2$. Il est observé que les CNT/(CeO$_2$)$_{5kp}$/(Pt-SnO$_2$) et les CNT/(SnO$_2$)$_{5kp}$/(Pt-CeO$_2$) ont fourni une densité de courant plus élevée par rapport à leurs homologues avec une couche d'oxyde plus épaisse. Les catalyseurs CNT/(CeO$_2$)$_{5kp}$/(Pt-SnO$_2$) ont montré l'activité catalytique la plus élevée et la haute durabilité vis-à-vis de la ROE par rapport aux trois autres catalyseurs ternaires. Son courant catalytique s'améliore par rapport à (Pt-CeO$_2$)$_{0.5T}$, en particulier aux potentiels plus négatifs, cependant sa durabilité n'a pas été améliorée. Par conséquent, d'autres travaux doivent être effectués pour obtenir un aperçu du rôle exact du CeO$_2$ et du SnO$_2$ dans le processus d'oxydation de l'éthanol lorsqu'il est combiné avec de Pt. Une telle étude systématique permettra non seulement d'approfondir notre compréhension sur le rôle de FMO dans les propriétés structurelles et électroniques de Pt, mais elle éclaircira également son effet promotionnel en ce qui concerne l'électrooxydation de l'éthanol qui n'a pas encore été établie.

Tableau S2 Conditions de déposition et résultats électrochimiques des meilleures électrodes de catalyseur Pt-CeO$_2$-SnO$_2$ ternaire

Meilleure électrode	Surtension (V vs Ag/AgCl)	Densités de courant à 0.3 V (mA/mg$_{Pt}$) (LSV @ 5 mV/s)	Densités de courants de pics (mA/mg$_{Pt}$) (LSV @ 5 mV/s)	Densité de courant à l'état stationnaire (mA/mg$_{Pt}$)
CNTs**/**(CeO$_2$)$_{2T, 5kp}$**/**(Pt-SnO$_2$)$_{0.5T}$	0.12	30.17	300.8	166.6
CNTs**/**(CeO$_2$)$_{2T,10kp}$**/**(Pt-SnO$_2$)$_{0.5T}$	0.15	6.75	274.6	75
CNTs**/**(SnO$_2$)$_{2T, 5kp}$**/**(Pt-CeO$_2$)$_{0.5T}$	0.19	7.58	301.5	171
CNTs**/**(SnO$_2$)$_{2T, 10kp}$**/**(Pt-CeO$_2$)$_{0.5T}$	0.20	2.17	296.3	82
CNTs**/**(Pt-SnO$_2$)$_{0.5T}$	0.10	49	345.7	169.7
CNTs**/**(Pt-CeO$_2$)$_{0.5T}$	0.21	3.08	292.5	129

Les catalyseurs cathodiques pour l'ORR (de l'anglais Oxygen Reduction Reaction) font face à des défis similaires à ceux des catalyseurs anodiques dans les DEFCs, y compris la lenteur

de la cinétique, une faible durabilité due à la dégradation des catalyseurs et à la réduction incomplète de l'O_2 [31]. Les catalyseurs de Pt modifiés par le FMO pourraient être des candidats potentiels, en raison du faible coût et de l'effet favorisant les FMO vis-à-vis de l'ORR. En plus de l'effet synergique de l'interface Pt-FMO, le déversement d'espèces contenant de l'oxygène à Pt a également été démontré comme facteur principal qui améliore l'électrocatalyse de l'ORR dans les composés Pt-FMO. Dans cette thèse, la performance ORR de Pt supporté sur TiO_2 a été étudiée. Il a été montré que les films de TiO_2 synthétisés augmentaient de façon spectaculaire la surface électro-active de Pt et augmentaient son électro-activité pour l'ORR par rapport à l'électrode Pt. En raison de la restriction dans le temps, l'étudie de ORR sur d'autres catalyseurs synthétisés dans ce projet n'a pas été complétée. Cependant, il pourrait être un bon début pour une étude intensive des catalyseurs à base de FMO pour l'ORR.

REFERENCES

[1] G. Hoogers. *Fuel cell technology handbook*, CRC press, Boca Raton, FL, 2003.

[2] L. Zhang, T. Lu, J. Bao, Y. Tang, C. Li. Electrochem. Commun., 8 (2006) 1625-1627.

[3] X. Teng. Materials and Processes for Energy: Communicating Current Research and Technological Developments, Formatex Research Center, (2013) 473-484.

[4] Y. Wang, S. Zou, W.-B. Cai. Catalysts, 5 (2015) 1507-1534.

[5] G.A. Camara, T. Iwasita. J. Electroanal. Chem., 578 (2005) 315-321.

[6] Z. Zhang, J. Liu, J. Gu, L. Su, L. Cheng. Energy & Environmental Science, 7 (2014) 2535-2558.

[7] G.A. Camara, R.B. de Lima, T. Iwasita. Electrochem. Commun., 6 (2004) 812-815.

[8] C. Lamy, S. Rousseau, E.M. Belgsir, C. Coutanceau, J.M. Léger. Electrochim. Acta, 49 (2004) 3901-3908.

[9] E. Antolini. J. Power Sources, 170 (2007) 1-12.

[10] A. Kowal, M. Li, M. Shao, K. Sasaki, M.B. Vukmirovic, J. Zhang, N.S. Marinkovic, P. Liu, A.I. Frenkel, R.R. Adzic. Nat. Mater., 8 (2009) 325-330.

[11] M. Watanabe, S. Motoo. Journal of Electroanalytical Chemistry and Interfacial Electrochemistry, 60 (1975) 275-283.

[12] N.M. Marković, H.A. Gasteiger, P.N. Ross Jr, X. Jiang, I. Villegas, M.J. Weaver. Electrochim. Acta, 40 (1995) 91-98.

[13] B. Coq, F. Figueras. Coord. Chem. Rev., 178-180 (1998) 1753-1783.

[14] E. Antolini. Int. J. Hydrogen Energy, 36 (2011) 11043-11047.

[15] S. Song, W. Zhou, Z. Zhou, L. Jiang, G. Sun, Q. Xin, V. Leontidis, S. Kontou, P. Tsiakaras. Int. J. Hydrogen Energy, 30 (2005) 995-1001.

[16] Y. Shao, J. Liu, Y. Wang, Y. Lin. J. Mater. Chem., 19 (2009) 46-59.

[17] G.N. Vayssilov, Y. Lykhach, A. Migani, T. Staudt, G.P. Petrova, N. Tsud, T. Skála, A. Bruix, F. Illas, K.C. Prince, V.r. Matolı´n, K.M. Neyman, J. Libuda. Nat. Mater., 10 (2011) 310-315.

[18] R. Eason. *Pulsed laser deposition of thin films: applications-led growth of functional materials*, John Wiley & Sons, 2007.

[19] E.T. Thostenson, Z. Ren, T.-W. Chou. Composites Science and Technology, 61 (2001) 1899-1912.

[20] A. Tabet-Aoul, M. Mohamedi. Phys. Chem. Chem. Phys., 14 (2012) 4463-4474.

[21] A. Tabet-Aoul, F. Saidani, D. Rochefort, M. Mohamedi. Int. J. Electrochem. Sci, 6 (2011) 6385-6397.

[22] E. Irissou, B. Le Drogoff, M. Chaker, D. Guay. J. Appl. Phys., 94 (2003) 4796-4802.

[23] W.J. Khudhayer, N.N. Kariuki, X. Wang, D.J. Myers, A.U. Shaikh, T. Karabacak. J. Electrochem. Soc., 158 (2011) B1029.

[24] L. González-García, I. González-Valls, M. Lira-Cantu, A. Barranco, A.R. González-Elipe. Energy & Environmental Science, 4 (2011) 3426-3435.

[25] Y. Wang, A. Tabet-Aoul, M. Gougis, M. Mohamedi. J. Power Sources, 273 (2015) 904-913.

[26] Y. Wang, A. Tabet-Aoul, M. Mohamedi. J. Electrochem. Soc., 163 (2016) F1272-F1278.

[27] Y. Wang, M. Mohamedi. ChemElectroChem, 3 (2016) 1-8.

[28] E. Irissou, B. Le Drogoff, M. Chaker, D. Guay. Appl. Phys. Lett., 80 (2002) 1716-1718.

[29] A. Pereira, F. Laplante, M. Chaker, D. Guay. Adv. Funct. Mater., 17 (2007) 443-450.

[30] J. Cai, Y. Huang, B. Huang, S. Zheng, Y. Guo. Int. J. Hydrogen Energy, 39 (2014) 798-807.

[31] M.Z.F. Kamarudin, S.K. Kamarudin, M.S. Masdar, W.R.W. Daud. Int. J. Hydrogen Energy, 38 (2013) 9438-9453.

B: Curriculum vitae

SCIENTIFIC PUBLICATIONS OBTAINED DURING THE THESIS

1. Fatemeh Ataherian, **Youling Wang,** Amel Tabet-Aoul and Mohamed Mohamedi. "High capacitance and cycle-life performance of binder-free supercapacitor nanocomposite electrode by direct growth of manganese oxide nanostructures on carbon nanotubes" **ChemElectrochem** 4 (2017) 1-9.

2. Amel Tabet-Aoul, Haixia Wang, **Youling Wang**, and Mohamed Mohamedi. "3D porous sphere-like aggregates of bimetallic PtRh nanoparticles grown onto carbon nanotubes: Efficient and Durable Catalyst for the Ethanol Oxidation Reaction" **Journal of the Electrochemical Society** 164 (2017) F685-F689.

3. Juan Carlos Abrego-Martínez, **Youling Wang**, Luis Gerardo Arriaga Hurtado and Mohamed Mohamedi. "A laser synthesized platinum-silver catalyst for methanol-tolerant oxygen reduction reaction", **International Journal of Hydrogen Energy** (In Press) http://doi.org/10.1016/j.ijhydene.2017.02.165.

4. Juan Carlos Abrego-Martínez, **Youling Wang**, L. H. Mendoza-Huizar, J. Ledesma-Garcia, F. M. Cuevas-Muñiz, M. Mohamedi and L. G. Arriaga. "Mixed-reactant ethanol fuel cell using an electrochemically deposited Ag@Pt tolerant cathode", **International Journal of Hydrogen Energy** 41 (2016) 23417-23424.

5. **Youling Wang**, Amel Tabet-Aoul, Mohamed Mohamedi. "Room Temperature Laser Synthesis of Mixed Pt and Tin Oxide Nanostructures: Optimum Morphology and Significantly Improved Kinetics for Ethanol Electrooxidation" **J. Electrochem. Soc**. 163 (2016) F1272-F1278.

6. **Youling Wang**, Mohamed Mohamedi. "Synthesis, Characterization and Electrochemical Activity of Laser Co-Deposited Pt-MnO$_2$-decorated carbon nanotubes nanocomposites" **ChemElectroChem** 3 (2016) 1-8.

7. Qiliang Wei, Yanqing Fu, Gaixia Zhang, **Youling Wang**, et al. "Highly-ordered microporous carbon nanospheres: A promising anode for high-performance sodium-ion batteries" **RSC advances**, 6 (2016) 84149-84154.

8. **Youling Wang**, Amel Tabet-Aoul, Maxime Gougis, Mohamed Mohamedi. "Cross-beam pulsed laser fabrication of Free-Standing Nanostructured Carbon Nanotubes-Pt-Ceria Anode with unprecedented electroactivity and durability for ethanol oxidation" **J. Power Sources** 273 (2015) 904-913.

9. **Youling Wang**, Amel Tabet-Aoul, Mohamed Mohamedi. "Laser synthesis of hierarchically organized nanostructured TiO_2 films on microfibrous carbon paper substrate: characterization and electrocatalyst supporting properties" **J. Power Sources** 299 (2015) 149-155.

10. **Youling Wang**, Amel Tabet-Aoul, Maxime Gougis & Mohamed Mohamedi. "Nanomaterials and nanotechnology for direct ethanol fuel cells", Proceedings of RIED 2012-1st Scientific Seminar, (2012) 76-78.

CONFERENCE PRESENTATIONS

05/2016: Presented at *The 229th ECS meeting (Poster),* San Diego, USA.

04/2015: Presented at *2014 Energy Materials Nanotechnology (EMN) East Meeting (Oral)*, Beijing, P. R. China.

06/2014: Presented at *The 4th ECS Montreal Student Symposium (Poster)*, Montreal, Canada.

05/2014: Presented at 2014 *Energy Materials Nanotechnology (EMN) East Meeting (Poster),* Beijing, P. R. China.

11/2013: Presented at *6e Colloque annuel du CQMF (Poster),* Shawinigan, Canada.

05/2013: Presented at *The 223rd ECS Meeting (Oral),* Toronto, Canada.

11/2012: Presented at *2012 Materials Research Society (MRS) Fall Meeting (Poster),* Boston, USA.

06/2012: Presented at *The 2nd ECS Montreal Student Symposium (Oral),* Montreal, Canada.

06/2012: Presented at *The 1st RIED Symposium Synergy (Oral),* Montreal, Canada.

04/2012: Presented at *2012 Spring Symposium of The Canadian Section of The Electrochemical Society (Poster),* Montreal, Canada.